Bistable laminates for energy harvesting

Harris, Peter

Award date:
2017

Awarding institution:
University of Bath

Bistable Laminates for Energy Harvesting

submitted by

Peter Joshua Harris

for the degree of Doctor of Philosophy

of the

University of Bath

Department of Mechanical Engineering

July 2017

Acknowledgement

He that dwelleth in the secret place of the most High shall abide under the shadow of the Almighty. I will say of the LORD, He is my refuge and my fortress: my God; in him will I trust. Psalm 91:1–2

First and foremost, a plethora of thanks is due to my longsuffering wife Olivia. Thanks so much for all your work to maintain my sanity and listening to me droning on pedantically over whatever minutiae had grabbed my interest at a given time. A great amount of gratitude is also deserved by my family–specifically my parents and grandparents. I am sure that had it not been for the family business and all the welding, fiberglass layups, holes drilled, and wrenches swung, that I never would have been interested in engineering! I also want to give a specific shoutout to Paul Harris for being a cornucopia of absolutely bizarre topical material, and smooth jams. I also want to give my sincere gratitude to my Hong Kong family. Thanks for being the very best in-laws I could ever hope to have. I am also truly thankful for my supervisor Chris Bowen. Thanks for the patience, guidance, availability of your time, and constant reminding to look at things in the bigger context. Many thanks also to the biomech people–Abdullah Alshuri, Emilie Crosnier, Lisa Coles, Sam Micklewright, Jan Gosiewski, Jason Forder, Faisal Al-Fadhel, and Tim Holsgrove–my first friends at Bath during my PhD for making me feel very welcome right from the start. Great thanks is also due to Sean Plott, Bill Graner, and Sean Bouchard for their witty banter helping me to keep going during crunch time. To the technicians who have helped–Ian Trussler, Nick Gathercole, Clare Ball, Stephen Thomas, and Mathew Ball–thanks for always being very quick in responding to work requests. Thanks also to the optimization people–Peter Dunning, David Betts, João Duro, Mehdi Tavakkoli, Khalid Ismail, Siân Jenkins, Vincent Seow Jiaming Kang, and Chris Brampton–for all the useful discussion on how to best check the reliability of models against experimental data, but also for being extremely encouraging throughout. Also of great importance to me have been the collaborators who opened up new possibilities for research–Grzegorz Litak, Robert Guyer, and Farbod Khoshnoud. The NEMESIS crew has also been a fantastic bunch. Thanks to Dan Zabek, Vana Adamaki, Andrew Avent, Yan Zhang, Marcin Kraśny, Kate Polak Kraśna, James Roscow and Mengying Xie. Being a part of this group has been crazy and wonderful.

Peter “Twitch” Joshua Harris April 2017.

Abstract

This thesis presents novel research in the area of energy harvesting from broadband vibrations. The aim of energy harvesting is to recover energy wasted or unused in the environment to power low-consumption devices on the order of hundreds of microwatts to milliwatts. The motivation is twofold. In providing a localized, self-contained power source, device reliability, flexibility of installation location can be improved, and maintenance costs can be reduced. Furthermore, reduced reliance on batteries will mitigate the environmental impact associated with resource extraction, and disposal. To this end, this thesis investigates bistable laminates with piezoelectric transduction as broadband energy harvesters. Hitherto, a wealth of literature exists in which narrowband energy harvesters have been studied and optimized to operate over a small frequency interval. While these have been successful to the point of having devices commercially available, many situations exist where the dominant frequencies from which energy is to be harvested change with respect to time, or may be dominated by noise, thus not having a truly dominating frequency. Energy harvesters with nonlinear frequency responses have attracted substantial research interest because of their ability to respond over a broader frequency band. Due to complexities of the response of these harvesters, particularly when the intensity of the vibrational input is high, modeling their behavior is difficult. Designing these harvesters is therefore challenging as the relationships between the various design parameters and power output can be highly involved, or require numerical solutions as analytical solutions may not be possible. This thesis helps to address this knowledge gap. Bistable laminates of both cantilever and plate configuration are studied. Parametric studies are undertaken to empirically demonstrate the relationship between power output and parameters such as resistance load, proof mass addition, operation orientation, different shapes, ply angles, and introduction of adjustable magnetic compression. Modeling work is also undertaken to capture the main features of the nonlinear response such as subharmonics, superharmonics, and snap-through. A study is also carried out to quantify the differences of performance between a linear harvester and an equivalent bistable counterpart. As a practical demonstration, some plate-type harvesters are subjected to excitation patterns based on measured train data. Ultimately, this thesis provides an in depth understanding of bistable shape, layup, and design on harvesting performance.

Contents

List of Figures

List of Tables

Chapter 1

Introduction

As demand for energy increases, researchers around the globe are attempting to satisfy the requirement both on the supply side by finding more sources of sustainable energy, and on the usage side by increasing the efficiency of existing processes. Energy sources over a broad spectrum of magnitudes are at varying stages of technological maturity such as hydroelectric power or nuclear fusion, and on the opposite end of the power level spectrum, on the order of micro to milliwatts of power is energy harvesting. Energy harvesting has attracted substantial research interest as power levels of this magnitude are sufficient to power low-consumption devices such as structural autonomous wireless health monitoring sensor systems. The philosophy of energy harvesting is to utilize wasted or unused energy in the surrounding environment to provide a localized power source for a device's operation. It is hoped that energy harvesting will be able to realize several benefits over the incumbent solution of batteries and electrical mains connections. Energy harvesters have the potential to replace batteries which deplete and must be routinely inspected, recharged or replaced. Because the production and disposal of batteries involves several environmentally unfriendly processes, reduction of their use is also beneficial. Furthermore, eliminating the need for human inspection allows for a reduction in operational overhead costs, and opens up possibilities for operation in inhospitable or dangerous environments. Conventional devices which are intended for long-term deployment in harsh environments are often designed to be hermetically sealed making battery replacement impossible, requiring the user to dispose of the device. The provision of self-powering capability allows the overall operational lifetime of the device to be extended and provides autonomous operation. As no mains connections are necessary, the physical area occupied by the different sensor nodes can be expansive. Finally, because the energy being used is essentially wasted from some original primary process, energy harvesting allows for the efficiency of processes to be increased.

1.1 Linear Energy Harvesters

Energy harvesting has been undertaken from a variety of sources such as indoor solar, heat and mechanical vibrations. This thesis' research concerns energy harvesting from mechanical vibrations. Sources of vibrational energy with different levels of available energy are abundant. Much of the vibrational energy harvesting research has focused on improvements on energy harvesters with linear frequency response characteristics. The design of linear energy harvesters typically begins by identifying a potential source of vibrational energy which vibrates at a dominant characteristic frequency. This dominant frequency is measured, and a harvester is built such that the natural frequency of the harvester matches that of the source. A means of converting the mechanical strain energy of the resonating structure into electrical energy, typically piezoelectric or electromagnetic transduction, is implemented. The frequency matching maximizes the displacement of the harvester and therefore the energy harvested. In practice, many vibrational sources do not vibrate with a single fixed dominant frequency. If there is a dominant frequency, it may not be constant and vary with time or operating conditions. Other sources may have several significant frequency components or be some form of noise with no dominant frequency.

1.2 Nonlinear Energy Harvesters

Structures with a nonlinear frequency response are capable of responding over a broader frequency band and are therefore being researched and developed to overcome the shortcomings of linear systems. For this thesis, a type of structure was built from cured, asymmetrically laid stacks of unidirectional carbon fiber pre preg called bistable laminates. The laminates were built from plies laid at two different angles where all the plies of one angle were stacked on top of each other followed by the remaining plies in the second orientation. When cured in an autoclave at high temperature and pressure, the asymmetry of the stacking sequence exploited the inherent disparity of the thermal expansion coefficients in the pre preg's fiber and matrix directions, respectively. This residual strain resulted in significant curvature of the cured laminate as well as the existence of two stable states aligned with the ply angles, hence the term "bistable laminates". Given sufficient energy, the laminate can be made to transition between its stable states, undergoing a sudden phenomenon called "snap-through". Piezoelectric patches were adhered to the bistable laminates to give them the ability to produce electrical power. These bistable laminate vibrational energy harvesters were placed on vibrating surfaces which caused the structure to strain. The piezoelectric patch transduced the mechanical strain into electrical energy allowing energy to be harvested from vibration. The snap-through transition gives bistable laminates a highly nonlinear response to vibrational excitation thereby providing a broader response bandwidth.

Chapter 2

Literature Review

The literature review begins by presenting the levels of power which are demanded by the application of remote wireless sensor networks for their operation. The levels of harvestable energy densities afforded by different energy sources are then shown with vibrational sources demonstrating high energy density. Different transduction methods for harvesting vibrational energy are reviewed with piezoelectric transduction emerging as the preferred method. The performance of linear harvesters is then shown, highlighting the narrowness of their frequency response function. Attempts to extend the frequency range of operation by tuning are described. Different methods for introducing nonlinearity are detailed. Research on bistable laminates for energy harvesting using piezoelectric Macro-Fiber Composites (MFC) patches is then explained. The novel research work of this thesis is contextualized within this body of work.

2.1 Magnitude of Energy Demanded by Sensors

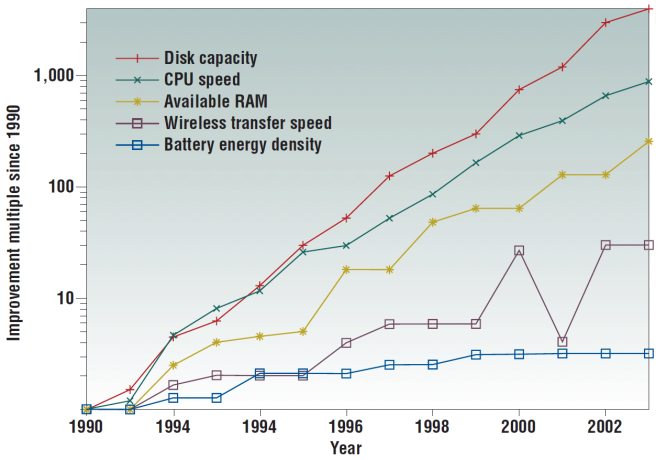

Figure 2-1: Increase of capability of various electronic capabilities over time [1]

Table 2.1: Power demand of sensor node with multiple sensors [10]

Operation Mode	Time [s]	Sensor Power [mW]	Processor Power [mW]	Transceiver Power [mW]	Total Power [mW]	Total Energy [mJ]
Transmitting	0.003908	0	19.965	63.162	83.127	0.325
Receiving	0.000452	0	19.965	71.511	91.476	0.041
Processing	0.02	0	19.965	0.018	19.983	0.400
Reading 1: Temperature	0.0002	0.029	21.054	0.018	21.101	0.004
Reading 2: Light	0.0002	0.109	21.054	0.018	21.101	0.004
Reading 3: Humidity	0.8	1.089	21.054	0.018	22.161	17.729
Reading 4: Vibration	0.02	2.178	21.054	0.018	23.25	0.465
Reading 5: Pressure	0.02	38.5	21.054	0.018	59.572	1.191
Total Active	0.86476					1.191
Sleep		0	0.0363	0.018	0.054	

Global demands for security, communication, information, and data have caused a tremendous escalation in the number of electronic devices in use. As these systems are deployed globally, many of them are powered by battery systems. While operational parameters such as transistor density famously increase according to Moore's law, the increase of energy density of batteries has seen only incremental improvements, as shown in figure 2-1 [1].

While battery operation allows for greater convenience, the extraction of rare earth metals to manufacture them as well as problems from improper disposal have a number of documented associated negative health effects [2–8]. Energy harvesting is a highly active area of research which aims to allow devices to power themselves from wasted or ambient energy in their surroundings with typical outputs on the order of micro to milliwatts. The aim is to improve device reliability and reduce maintenance costs by allowing devices to be deployed long-term with no need of battery checking, replacement, disposal and potential corrosion damage. A potential area of application which is the subject of much research is powering wireless sensor networks for structural health monitoring [9]. One example of the energy scales required for a sensor node was given by Mathúna et. al [10] and is shown in table 2.1.

The power demands of its transmitter, temperature, light, humidity, vibration, and pressure sensors are shown. In order for the sensor node to awaken from its sleep state, and for all the sensors to measure their respective quantities, and transmit the information, 20.16 mJ of energy are expended over 0.86 s resulting in a power demand of 23.3 mW [10]. Depending on how frequently measurements need to be taken and transmitted, the power of the energy harvester could be significantly smaller than this value as a capacitor can be charged up as an accumulator to store the harvested energy for intermittent operation.

Table 2.2 shows the decrease of energy required per day as the proportion of time spent in the sleep state increases. It is possible for a sensor node to consume only 4.73 J per day if a daily sample is sufficient frequency for an application. Figure 2-2 shows the power requirement of the transmitter increasing with respect to transmissions per minute [11].

Table 2.2: Decrease of energy required with increasing time in sleep state [10]

Sleep Time	Sleep Time [s]	Duty Cycle on-time [%]	Duty Cycle on-time [%]	Energy in Sleep Mode [mJ]	Energy in Operation [mJ]	Total Energy Per Cycle [mJ]	Total Energy Per Day [J]
1 s	1	90.48	9.52	0.05	21.59	21.59	1864.95
2 s	2	45.24	54.76	0.11	21.64	21.59	934.83
30 s	30	3.02	96.98	1.63	23.16	21.59	66.71
1 min	60	1.51	98.49	3.27	24.80	21.59	35.71
2 min	120	0.75	99.25	6.53	28.06	21.59	20.21
20 mins	1,200	0.08	99.92	65.34	86.97	21.59	6.25
1 hr	3,600	0.025	99.975	196.02	217.55	21.59	5.22
12 hr	43,200	0.002	99.998	2,532.24	2,373.77	21.59	4.75
24 hr	86,400	0.001	99.999	4,704.48	4,726.01	21.59	4.73

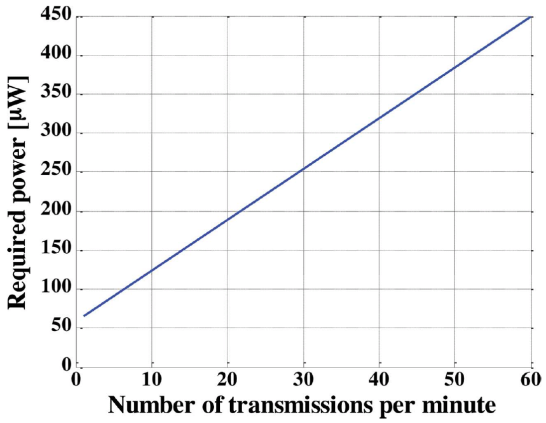

Figure 2-2: Increase of power required with respect to transmission frequency [11] with more transmissions requiring more power.

2.2 Candidate Energy Sources

Several sources of energy have been identified as suitable candidates for energy harvesting research. While for each source, a wide variety of designs of harvesters are realizable within their respective design spaces, indicative values are given here for typical device power densities and the amount of available harvestable energy. The benefits and challenges of harvesting from the various sources is also discussed.

2.2.1 Indoor Solar

Indoor solar energy harvesting is a well-established technology with devices such as calculators having been commercially available for some time [12].

While the power densities afforded by indoor solar energy harvesting are high, as seen in table 2.3, several problems are present as well. Firstly, sunlight is only available intermittently. This implies that for overnight operation, the storage of energy is not trivial. Secondly, solar

Table 2.3: Typical power outputs and device densities for indoor solar energy harvesting [13]

Number	Building Loc.	Calculated Power $[\mu W]$	Power Density $\left[\frac{\mu \mathbf{W}}{\mathbf{cm^3}}\right]$
1	Southampton, UK	110	38
2	Southampton, UK	87	30
3	Southampton, UK	25	9
4	Southampton, UK	28	10
5	San Sebastian, Spain	56	19
6	San Sebastian, Spain	1149	399
7	Warsaw, Poland	244	85
8	Warsaw, Poland	743	258
9	Warsaw, Poland	275	95
10	Warsaw, Poland	681	236
11	Warsaw, Poland	134	47

panels must be kept dust-free for effective operation, thus defeating the purpose of reducing maintenance costs due to cleaning requirements. Lastly, lighting is usually only required in environs where humans are present. If the sensor is to operate remotely, or in an unlit enclosed area, the provision of artificial light solely for the purpose of illuminating photovoltaic cells is inefficient.

2.2.2 Pyroelectricity

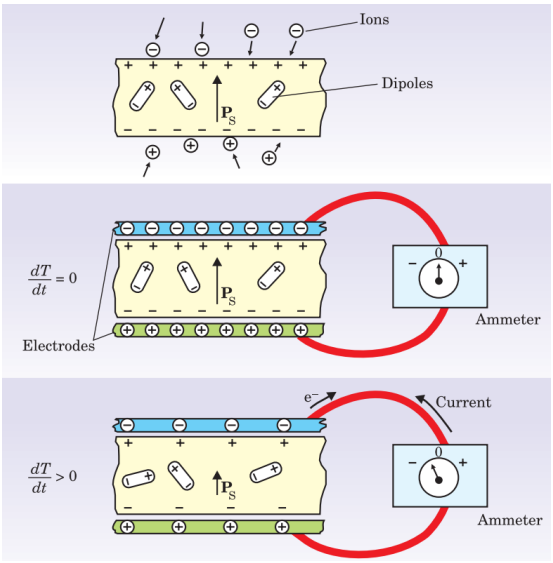

Figure 2-3: Fluctuating temperature causing current resulting from changes of surface charge due to the pyroelectric effect [14]

Thermal sources are another area of great research activity with several methods in use. Pyroelectric energy harvesting requires a fluctuation of temperature in the time domain [17].

Table 2.4: Typical power output densities for pyroelectric energy harvesters utilizing various pyroelectric materials [15]

Pyroelectric Material Number	**Power Density** $\left[\frac{\mu \mathbf{W}}{\mathbf{cm^3}}\right]$
1	100-169
2	12.9
3	13.4
4	6.12
5	1570
6	500
7	750
8	4320
9	2240
10	5960

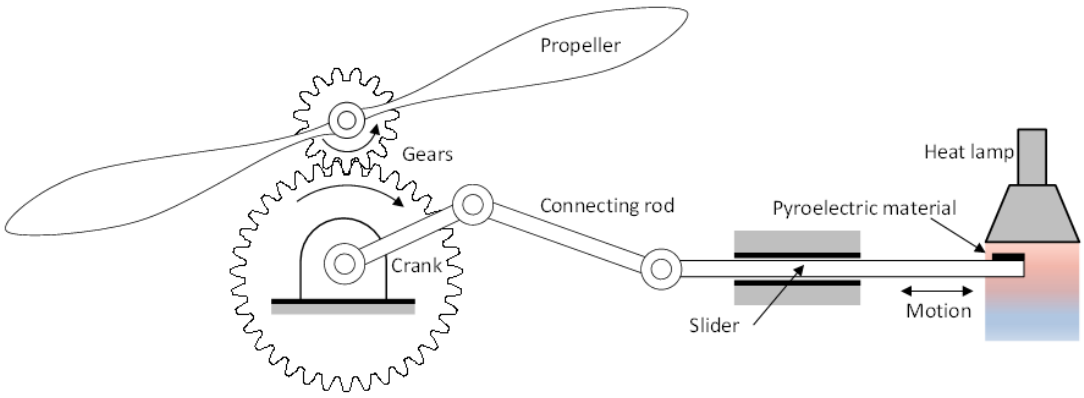

Figure 2-4: A device for increasing the change of temperature experienced by a pyroelectric device [16]

The open-circuit voltage V and short-circuit current i_p developed follow equations 2.1 and 2.2, respectively [18]. Here p is the pyroelectric coefficient specific to the material, ε_{33}^d is the permittivity in the polarization direction at constant stress, h is the material's thickness, and $\frac{dT}{dt}$ is the change of temperature T with respect to time t, and A is the material surface area.

$$V = \frac{p}{\varepsilon_{33}^d} h \frac{dT}{dt} \tag{2.1}$$

$$i_p = Ap\frac{dT}{dt} \tag{2.2}$$

Pyroelectrically active materials have oriented domains such that at the surfaces of the material there is a net charge of opposite polarity on the different surfaces as seen in figure 2-3 [14]. When the material experiences a change in temperature, the domains move resulting

in a change of charge at the surfaces. If there is a net loss of surface attraction, electrons are forced to move, resulting in an electrical current. Depending on whether the domains are becoming more or less oriented with respect to temperature change determines the direction of the flow of the current [19]. Indicative power levels and device densities are shown in table 2.4.

Recent improvements in electrode technology by Zabek et. al [20] reported a device using Polyvinylidene difluoride (PVDF) where the device's energy density was 66.9 $\mu J/cm^3$ for a 20 second cycle from innovative patterning of the electrodes. The main challenge with pyroelectric energy harvesting is finding sources of quickly fluctuating temperature as most device power outputs are quite low, however further research may improve this, such as the wind-driven device in figure 2-4 which moves the pyroelectric element in and out of a heated area [16].

2.2.3 Thermoelectric Energy Harvesting

Thermoelectric energy harvesting has shown much higher potential for energy harvesting with device power densities several orders of magnitude higher than pyroelectricity, as shown in table 2.5 where typical temperature gradients in occupied spaces are analyzed. Thermoelectric materials have mobile charges which are motivated to move with increasing temperature as shown in figure 2-5 a. Open circuit voltage is described by equation 2.3 where V is voltage developed, α is the thermoelectric coefficient specific to the material, and ΔT is the spatial temperature gradient $\frac{dT}{dx}$ [21]:

$$V = \alpha \Delta T \tag{2.3}$$

Table 2.5: Available energy from various thermal sources and thermoelectric device power densities [13]

Number	**Location**	**Calculated Power** $[mW]$	**Power Density** $\left[\frac{\mathbf{mW}}{\mathbf{cm^3}}\right]$
1	Southampton, UK	6	4.3
2	Southampton, UK	> 9	> 6.4
3	Southampton, UK	3	2.1
4	Southampton, UK	1	0.7
5	Southampton, UK	2	1.4
6	San Sebastian, Spain	2	1.4
7	Warsaw, Poland	1	0.7
8	Warsaw, Poland	7	5
9	Warsaw, Poland	9	6.4

Thermoelectric harvesters are a maturing technology with some commercial devices available. While they have been used effectively for energy harvesting, they suffer from the drawback of requiring heat exchangers and being physically large to maintain the temperature gradient as shown in figure 2-5 b. Another method for harvesting energy from heat, thermoacoustic energy harvesting, has research currently underway [24] but this is still in a highly experimental state.

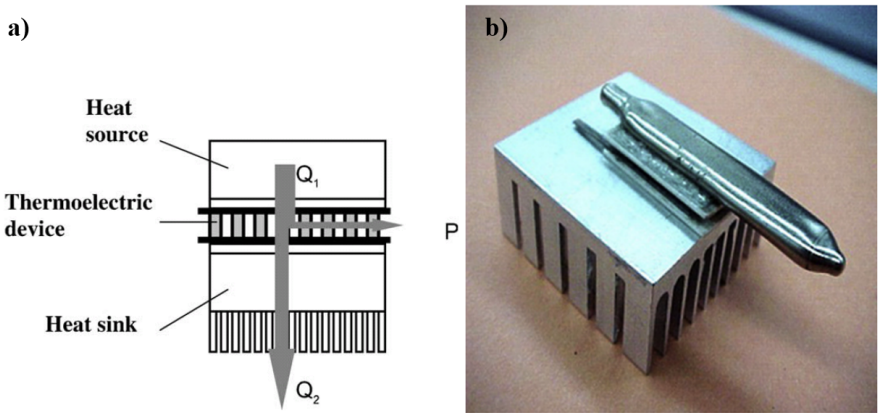

Figure 2-5: a) Diagram of thermoelectric generator [22] b) Photograph of thermoelectric generator [23]

2.3 Vibrational Energy Harvesting

Vibrational energy harvesting is a broad topic and has several sub-disciplines. In general, vibrational energy harvesters consist of a flexible member designed to amplify the small movement of the source and a transducer with converts the mechanical strain energy of the flexible member into useful electrical energy. Vibrational energy harvesters (VEHs) have been applied to several different vibration sources other than just moving surfaces such as human foot-fall [25] and wind energy [26–29]. The main differences amongst VEHs are their transduction method, and whether they are designed to operate in a linear or nonlinear regime. The main types of transducers used are electrostatic, piezoelectric and electromagnetic, although magnetostrictive [30], and electroelastic [31] transducers are also seen. At present some VEHs are commercially available from companies such as Perpetuum, ReVibe, and Kinergizer.

2.3.1 Electrostatic Transduction

Two designs of electrostatic transducers appear in figure 2-6. Electrostatic transducers require a high potential difference to be maintained across the two sets of electrodes shown in light and dark in figure 2-6. As the transducer strains, the gap between the electrodes is changed, resulting in a change of capacitance. Because the voltage has been maintained, energy is produced [32]. The voltage generated is given by equation 2.4 [33]:

$$V_{max} = \frac{C_{max} + C_{par}}{C_{min} + C_{par}} V_{in} \tag{2.4}$$

Here V_{max} is the maximum voltage attained during a strain cycle, C_{max} is the maximum capacitance value, C_{par} is the capacitance of the capacitor put in parallel to maintain voltage, C_{min} is the minimum capacitance from the strain cycle, and V_{in} is the voltage across the electrodes.

Some representative energy densities are shown in table 2.6. As shown, the device power

Table 2.6: Power outputs and device densities for an electrostatic energy harvester [34]

Device Number	**Power Output** $[\mu\mathbf{W}]$	**Power Density** $\left[\frac{\mu\mathbf{W}}{\mathbf{cm^3}}\right]$
1	36	2.42
2	7.4e-06	1.23e-03
3	6	15
4	1760	56
5	2.4	4

densities are quite low, with the highest energy density value reported being two orders of magnitude less than the best pyroelectric efforts in table 2.4. Additionally, the requirement for an external voltage source is a complication.

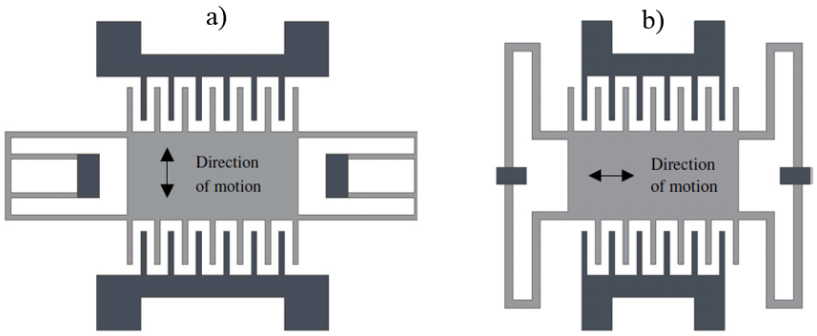

Figure 2-6: a & b) Two possible design realizations of electrostatic transducers depending on orientation of strain field for harvesting [35]

2.3.2 Electromagnetic Energy Harvesting

Electromagnetic energy harvesting requires a magnet and a conducting loop as shown in 2-7b. As the loop moves through the magnetic field, an electromagnetic force is developed according to equation 2.5 Where F_{EM} is the electromotive force, I is induced current, and $\frac{d\varphi}{dt}$ is the rate of change of flux density with respect to time within the loop [36].

$$F_{EM} = I\frac{d\varphi}{dt} \tag{2.5}$$

Figure 2-7a shows an actual harvester where the end mass at the end is the magnet. The magnet is placed at the end of the cantilever because maximum power is produced when the velocity is highest. This approach is well established with commercial devices available. Table 2.7 gives indicative power density levels showing high power outputs and device densities. Electromagnetic induction is well understood, encouraging much research in this area. Because magnetic fields can have unwanted interactions with electrical equipment, and due to the requirements of external framework to house either the magnet or the induction coils, piezoelectric

Table 2.7: Electromagnetic energy harvesting power outputs and device densities [34]

Device Number	**Power Output** $[\mu W]$	**Power Density** $\left[\frac{\mu \mathbf{W}}{\mathbf{cm^3}}\right]$
1	100 (Processed)	6
2	1.5	100
3	5	1.5
4	10 (Processed)	8.06
5	0.33	22
6	530	2208.3
7	680 (Processed)	680
8	830 (Processed)	830
9	0.0004	.0002
10	830	114
11	37	44
12	0.02	0.21
13	2.85	47.5
14	0.12	1.79
15	0.05	0.07
16	1.44	40
17	800 (Processed)	6.4
18	3,500 (Processed)	27
19	40,000 (Processed)	306
20	800	6
21	3,100	23
22	10,800	81

transduction is used in this research.

2.3.3 Piezoelectric Energy Harvesting

Piezoelectric materials have unit cell structures which have a dipole owing to the physically asymmetric nature of their charge distributions [39]. Poling these materials to orient the material domains causes them to align within the material. If the material has a force F applied to it in the poling direction as shown in figure 2-8b, the electrical behavior depends on the resistance placed across the piezoelectric. In the case of an open circuit, where resistance approaches infinity, a charge Q will accumulate across the electrodes based on the amount of force applied F, the dimensions of the piezoelectric element a, b, c and the coupling coefficients g_{ij}. The coupling coefficient g_{ij} is called the piezoelectric voltage coefficient and has the units of volts per unit force. The subscripted i and j refer to the direction of strain to which the coefficient relates. Because of the high resistance, there is no flow of current, and therefore the actual power output is zero. This behavior is described by equation 2.6. The extreme opposite scenario is the short-circuit condition where the resistance approaches zero. Here, the charge is allowed to dissipate immediately leading to high current. Because there is effectively no voltage, this flow of current again results in zero power. This behavior is described in equation

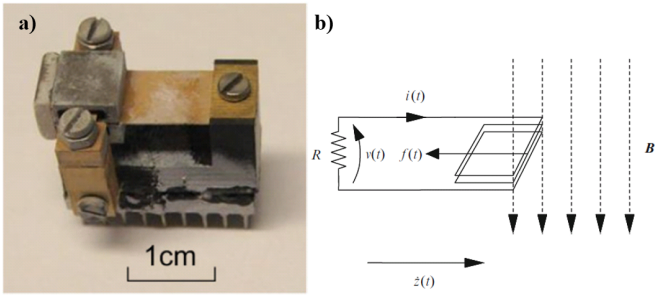

Figure 2-7: a) Example of a cantilever configuration electromagnetic energy harvester [37] b) Diagram of electromagnetic induction [38]

2.7. Here the piezoelectric charge coefficient d_{ij}, which has the units of charge per unit force, is used. The maximum amount of energy harvested per strain cycle E_{max} is given by equation 2.8.

$$V(Q=0) = \frac{c}{ab} g_{33} F \tag{2.6}$$

$$Q(V=0) = d_{33} F \tag{2.7}$$

$$E_{max} = \frac{c}{ab} d_{33} g_{33} F \tag{2.8}$$

If the piezoelectric material is strained normal to the poling direction as shown in figure 2-8, this is referred to as the 31 operating mode. The behavior in open circuit vs. short circuit follow the same principles as 33 operation, and are described in equations 2.9–2.11, along with the maximum harvestable energy, respectively.

$$V(Q=0) = g_{31} F \frac{1}{a} \tag{2.9}$$

$$Q(V=0) = d_{31} F \frac{b}{c} \tag{2.10}$$

$$E_{max} = \frac{1}{a} d_{31} g_{31} F^2 \tag{2.11}$$

The piezoelectric activity of the 31 mode with respect to the 33 mode is approximately equal to the activity of the 33 mode multiplied by the material's Poisson ratio [40], and is therefore lower. For actuation purposes, piezoelectric materials are reversible in that a voltage can be applied and the material will dilate. This allows piezoelectric materials to be applied effectively as both transducers and actuators. Notice that in figure 2-8a the piezoelectric patch is placed at the root of the cantilever. For the electromagnetic harvester, the electromagnetic elements were placed such that their velocity was maximized, but here, the piezoelectric element is placed such that the strain is maximized. Several types of piezoelectric elements have been utilized by different research efforts. One commonly-encountered type is the macro fiber composite (MFC), the properties of which are thoroughly discussed here [41, 42]. The piezoelectrically active

material used is lead zirconate titanate (PZT). It is drawn into long strands, and is sandwiched between copper mesh electrodes. The assembly is embedded in a protective polymer matrix in a useful patch form with some exposed electrodes for electrical connections.

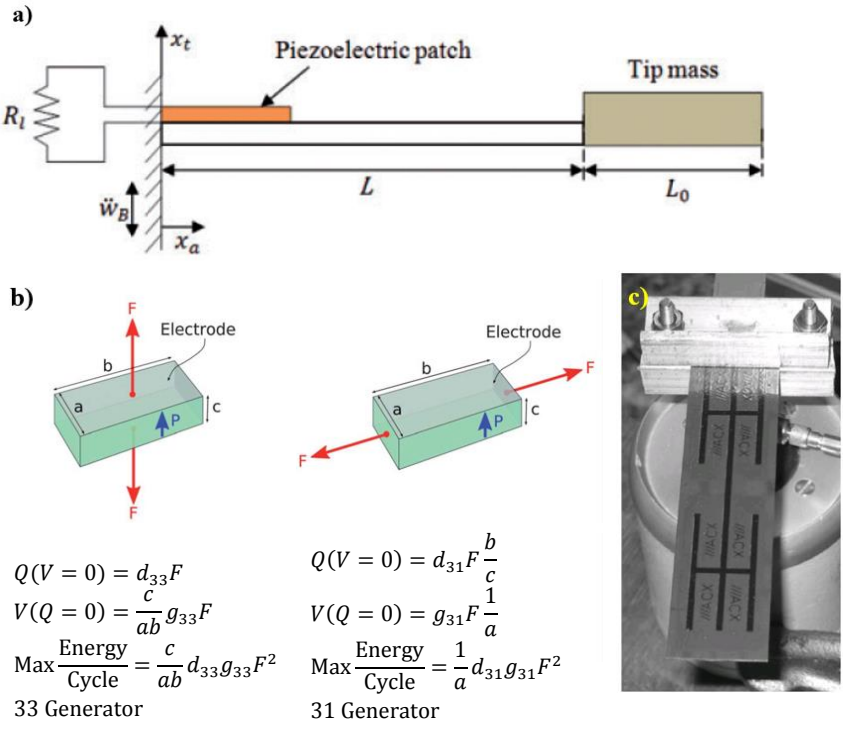

Figure 2-8: Diagram of a typical piezoelectric energy harvester [43] b) Two modes of operation [44]c) Example of a cantilevered piezoelectric energy harvester [45]

Since the first piezoelectric energy harvester was tested in 1984 [46], a broad spectrum of harvester designs have been tested. Bespoke piezoelectric materials for transduction are being researched [47, 48] and are reviewed by Bowen et al [44]. Piezoelectric vibration energy harvesters are reviewed by Kim, et. al [49] and Sodano et. al [50].

As shown in table 2.8, of all the energy sources and transducer types available, vibrational energy harvesting with piezoelectric transduction allows for the highest potential device power density. This is the primary reason why this source and transducer pair are used in this research. Despite this impressive performance, strong arguments can still be made in favor of electromagnetic induction as discussed in [51, 52]. Furthermore, the amount of power can differ depending on the accompanying circuit [53–59]. While a great deal of effort has been expended in this area to develop the electronic interfaces, this research focuses mainly upon the development of the harvester alone. As these electrical systems boost the energy harvested by any harvester by some proportion, it is assumed that maximizing the harvester's performance alone is sufficient.

Table 2.8: Piezoelectric energy harvester power outputs and energy densities [34]

Device Number	**Power Output** $[\mu W]$	**Power Density** $\left[\frac{\mu \mathbf{W}}{\mathbf{cm^3}}\right]$
1	1.5 (Processed)	2.83
2	80	80
3	207	90
4	365	180
5	1,700	145
6	10,000 (Processed)	88
7	300,000	2,650
8	-	15,000
9	180	20
10	2.16	3,510
11	0.25	2.47
12	35.5	82
12	8,000	198
14	1,800	45

2.4 Linear Energy Harvesting System Performance

The main challenge of conventional energy harvesting is that linear structures only response with high amplitude around a very narrow frequency band as seen in figures 2-9a-c [60–62]. A measure of the broadness of the response is to take the peak power output attained by the system, and to find the frequency band over which at least half the peak power is produced. The half power bandwidths for these linear systems are on the order of a few Hertz meaning that any deviation of the source's input frequency will result in a significant drop in harvested power.

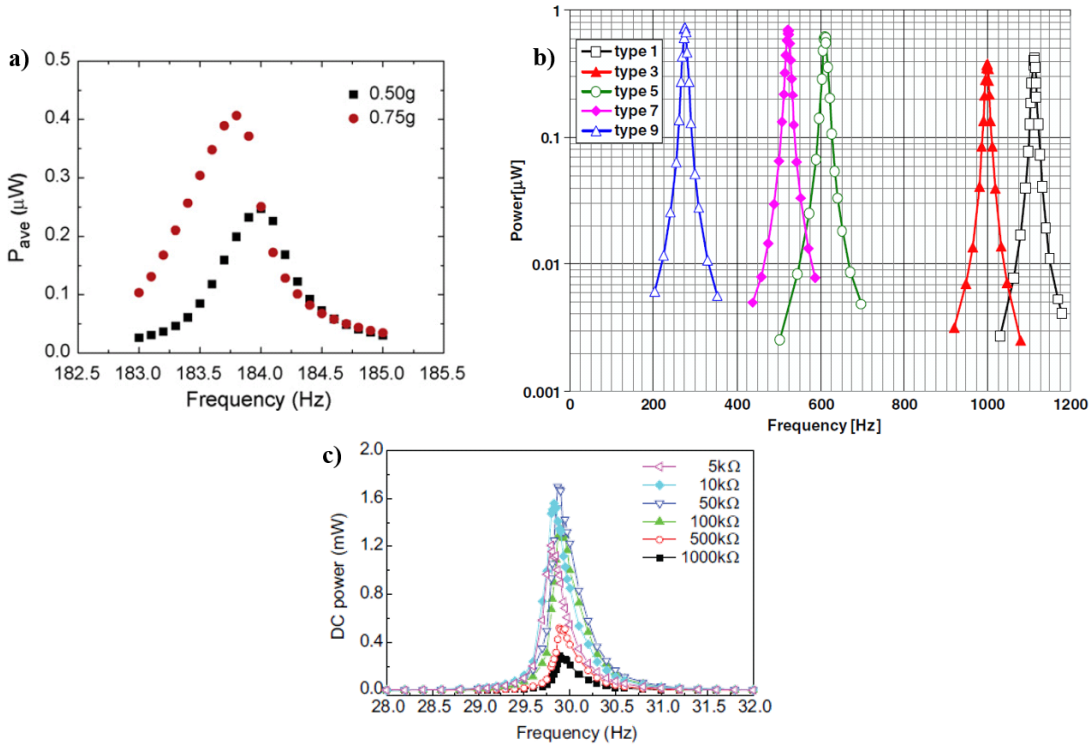

Figure 2-9: Power frequency response at two g levels for a micromachined cantilever linear harvesting device [60]b) Five different cantilever designs of different width, length and end mass [61] c) Power output over a frequency band with changing resistances for a cantilever energy harvester [62]

Linear harvesters are often designed and built to have the lowest possible damping ratio in order to maximize the response amplitude on resonance. While there is some scope for adjusting the damping ratio to decrease the peak power for a slight gain in response bandwidth, this scope is extremely narrow.

2.5 Linear Harvester Frequency Extension

To address the limited bandwidth of linear devices, much effort has been dedicated to extending the operational window of linear harvesters which are reviewed by Zhu, et. al [63].

Several methods have been implemented to allow the natural frequency of harvesters to be tuned. Some methods required manual adjustment of the natural frequency by the user. Some examples of active tuning methods and passive tuning methods have also been reported. Figure 2-10a shows one attempt which moved a magnet using an actuator to exert a force on a cantilever to change its natural frequency [64]. As seen in figure 2-10b, the power output does decrease at the highest extent of the frequency range, but there is an operational range through which the device operates effectively. Similar implementations have been used by others [65, 67–69]. In a rotating energy harvester context, it is possible to have arrangements

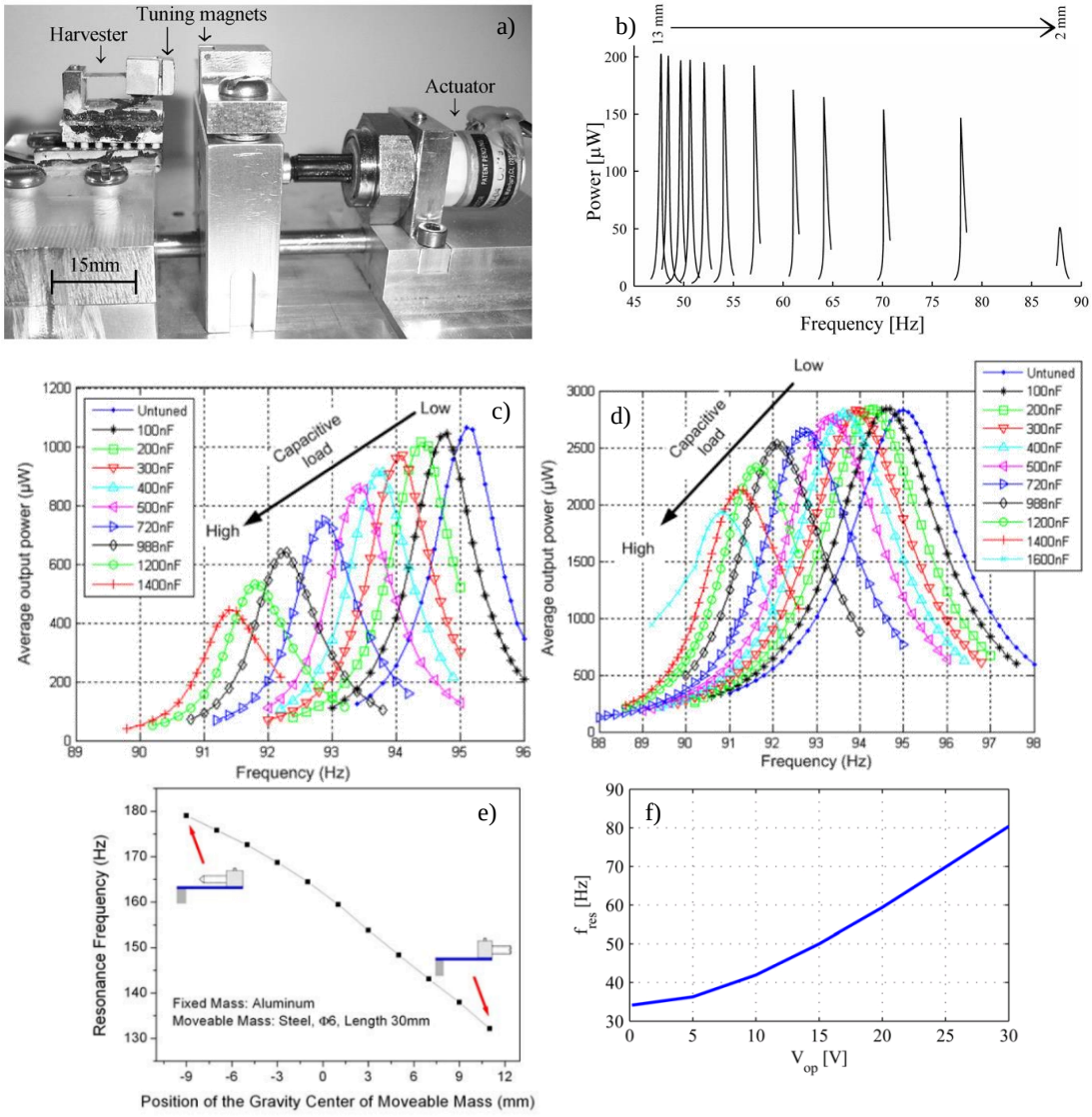

Figure 2-10: a) Harvester's cantilevered magnet, corresponding moveable magnet, and actuator b) Frequency range of operation [64, 65] c) Tuning range for electromagnetic energy harvester with a load resistance of 10 kΩ d) Tuning range as in c) but with load resistance of 4 kΩ [37]e) Natural frequency shift with respect to mass extension coordinate [66]f) Change of natural frequency as increased voltage stiffens actuator [66]

where the centripetal acceleration puts the structure in tension such that the natural frequencies is matched with the driving frequency [70]. If the main structural member is flexible enough, a sliding mass can be positioned on the member. If the harvester is driven off resonance, the mass will tend to move such that it passively changes the natural frequency to being synchronized with the driving frequency [71]. On the electrical side, the capacitance of the device can be altered to change the dynamic characteristics of the harvester as seen in figure 2-10c,d [37]. Figure 2-10f shows a device with a mass on a screw that can be extended to change the amount of polarized mass which changes the natural frequency [72]. Other methods of tuning on the electrical side is that a square voltage wave matching the driving frequency can be applied to the piezo electrodes [73]. Furthermore, it is possible to apply voltages across the piezoelectric transducers to alter the stiffness of the device to adjust the natural frequency [72] as seen in figure 2-10f. Arrays of harvesters have been attempted [74], but this is effectively several harvesters rather than a single device. As seen, the frequency ranges attainable by these tuning methods are substantial. While the manual methods would allow a device to be tuned before deployment, these still assume that the driving frequency is constant. Thus, if the frequency varies with respect to time, periodic manual retuning would be required. The automatic tuning methods from this perspective are more promising, however the consumption of the active tuning methods marginalizes any gains made, and passive methods suffer from slow response times, but are a very interesting alternative. However, all these energy harvesting systems have the implicit assumption that the source is indeed harmonic, whereas many real sources could be multimodal, or be composed of random noise in which case there may be no dominant frequency for tuning. In any case, harmonic characterization of nonlinear systems is still of value as their responses to the simple harmonic cases of repeatable, rather than stochastic inputs, is an excellent method to building an understanding of the response to an arbitrary frequency input.

2.6 Nonlinear Energy Harvesters

Nonlinear energy harvesters are being researched intensely because of their potential to respond over a broader frequency band inherently without external control systems. A nonlinear system in this discussion refers to an energy harvesting device which responds non-proportionately to excitation input in at least some parts operational parametric space. It may be the case for some nonlinear harvesters that they will have a region of linear behavior, but once a certain excitation amplitude is exceeded, the response may cease being proportional and begin operating in the nonlinear regime. An example of a nonlinear frequency response with respect to a linear frequency response appears in figure 2-11 a). As shown, the resonant peak of the linear response is symmetric with a clear maximal value. The nonlinear response by contrast is non symmetric. The frequency response function initially increases with respect to frequency similar to the shape of a linear response, but then a bend is seen in the amplitude and it continues to increase. Following the highest amplitude, the dropoff of response amplitude is more sudden than the linear response. Another characteristic of linear harvesters is that for a harmonic

excitation of frequency ω the response will also be at ω but with a difference of amplitude and phase angle. A nonlinear harvester may respond with multiple frequencies to a harmonic input. The benefits and difficulties between linear and nonlinear systems are discussed in [75–79]. The first main difference between them is the level of certainty from understanding the design space. Because the formulations governing linear energy harvesting systems are more likely to be solvable with known numerical techniques resulting in closed-form analytical solutions, they can be mathematically analyzed rigorously to predict and understand the device behavior. Some governing equations of nonlinear systems can only be analytically solved for trivial cases, and numerical solutions may require advanced computational methods to solve. Some nonlinear systems are only partially understood, or at times have analytical descriptions only solvable using advanced numerical solutions. This implies that the design of these systems requires greater time and effort in analysis and in general it is more difficult to design such a system such that it embodies the required dynamic characteristics for a given vibrational input pattern. While linear systems tend to have higher power outputs, in theory, this is not necessarily the case. The main added benefit of a nonlinear system, then, is not in high power outputs, but broadband performance. Beeby et. al [76] undertook a comparison between linear and nonlinear devices with both electromagnetic and piezoelectric induction, for various sampled vibration spectra which is shown in table 2.9. As seen, the harvesters with piezoelectric transduction produce more energy than their electromagnetic counterparts. Furthermore, for vibration spectra not having distinct driving frequency components, the nonlinear harvesters outperform their linear counterparts.

2.6.1 Duffing Oscillators

Duffing oscillators are a simple example of a nonlinear system. These oscillators can be built relatively easily and can be described by well-known governing equations. The defining characteristic of a Duffing oscillator is that when the system is displaced from its equilibrium position, the restoring force is proportional to the cube of displacement. To provide contrast, a classic linear single degree of freedom vibrational system will have a governing equation such as that shown in equation 2.12.

$$m\ddot{x} + c\dot{x} + kx = A_0 \sin(2\pi f + \phi) \tag{2.12}$$

Where m is the mass of the system, $\ddot{x}$ is acceleration, c is the damping, $\dot{x}$ is velocity, k is the stiffness, x is the displacement, A_0 is the force amplitude of the harmonic forcing function of frequency f and phase angle ϕ. Many types of nonlinear energy harvesters have been researched. Duffing oscillators are an example of a nonlinear energy harvester which has been investigated [80–82]. A single degree of freedom Duffing oscillator has a governing equation of the form shown in equation 2.13:

$$m\ddot{x} + c\dot{x} + k_1 x + k_2 x^3 = A_0 \sin(2\pi f + \phi) \tag{2.13}$$

Where k_1 is the linear stiffness, and k_2 is the cubic stiffness term. In general, a nonlinear

Table 2.9: Linear and nonlinear piezoelectric and electromagnetic energy harvesters applied to different input spectra [75]

Electromagnetic Energy Harvesters—Energy in Joules [J]				
Source	**High Q Linear Harvester**	**Low Q Linear Harvester**	**Bistable Harvester**	**Duffing Oscillator**
White Noise	672	329	349	329
Car Engine z-axis	423	130	34	137
Car Engine x-axis	125	40	25	37
Ferry Engine x-axis	31,455	7,127	179	737
CHP z-axis	431	93	3	93
Helicopter	3,243	817	318	403
Piezoelectric Energy Harvesters—Energy in Joules [J]				
Source	**High Q Linear Harvester**	**Low Q Linear Harvester**	**Bistable Harvester**	**Duffing Oscillator**
White Noise	1,107	1,070	2,549	1,070
Car Engine z-axis	856	683	354	748
Car Engine x-axis	197	158	144	146
Ferry Engine x-axis	27,432	19,975	908	1,565
CHP z-axis	2,808	1,645	66	1,646
Helicopter	3,837	2,375	1,258	1,336

system may have additional terms such as a $\ddot{x}^2$ term, or situations where k is a function of x, i.e. $k(x)$, etc. The frequency response of a Duffing oscillator is contrasted against a linear oscillator in figure 2-11a&b. Modifying equation 2.13 to be compatible with the notation used in [75] results in equation 2.14. If $\beta = 0$, the system is a linear oscillator. The calculated response of the oscillator for several values of β and $\alpha = 0$ are shown in figure 2-11b. As shown in figure 2-11c with increasing acceleration, the natural frequency of the system tends to increase to reflect the change of stiffness characteristic to this variety of nonlinear system.

$$m\ddot{x} + c\dot{x} + x(k_1 - \alpha + \beta x^2) = \text{Force}(t) \tag{2.14}$$

Duffing oscillators are an interesting nonlinear system because the governing equations are well-understood and finding numerical solutions to them is possible. However, research into systems of this sort have shown that harvesters with hardening nonlinearity $k_2 > 0$ with a given linear stiffness k_1 can never have a power output exceeding that of a linear harvester of stiffness $k = k_1$ [84]. Duffing oscillators with $k_2 < 0$ do also exist. Another approach is to use asymmetric end mass systems which are now described.

2.6.2 Asymmetric End-Mass Harvesters

Asymmetric end masses were implemented by Bai et. al to introduce twisting to an otherwise linear cantilever system [85]. The mass magnitudes and their asymmetry are shown in figures

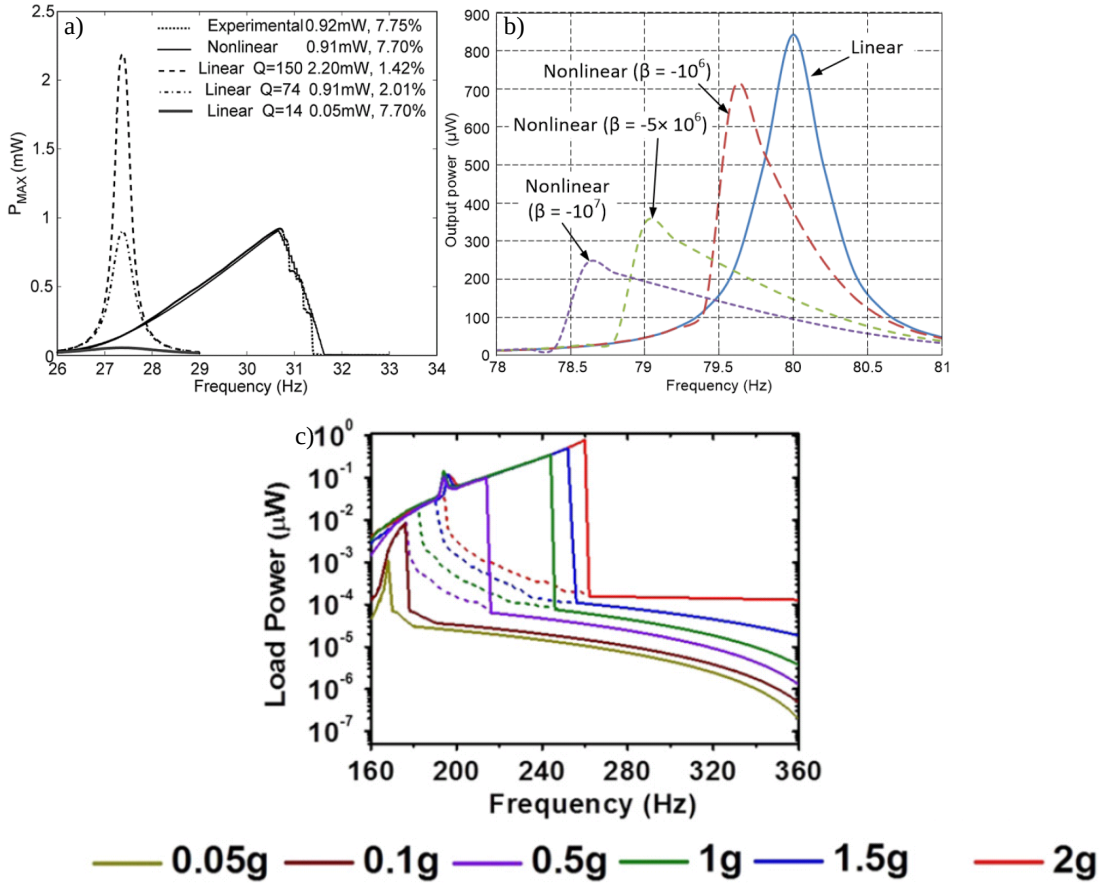

Figure 2-11: a) Linear harvester energy harvesting characteristic and Duffing oscillator experimental and modeling results [80] b) Power output as nonlinear Duffing spring coefficient changes [75] c) Duffing oscillator with different degrees of nonlinearity [83]

2-12 a-c. Figure 2-12 d-f shows the root mean squared (RMS) power outputs for the different configurations. As shown, the device natural frequencies are all different. The natural frequencies all tend to shift down with increasing acceleration demonstrating softening. Because the peak frequency response happens around the natural frequency ω which is given by the relation $\omega^2 = \frac{k}{m}$ where k is stiffness and m is mass, a decrease of ω means that k must be decreasing because m is fixed. Therefore, the fact that the ω is decreasing means that the system is undergoing softening.

While the power outputs are on the order of μW, an interesting feature can be seen in figure 2-12f at about 100 Hz where there seems to be an almost vertical line which could be due to a torsional natural frequency. While stiffening nonlinearity is undesirable, it was shown that softening nonlinearity can allow a nonlinear energy harvester to produce more power than a linear one [87].

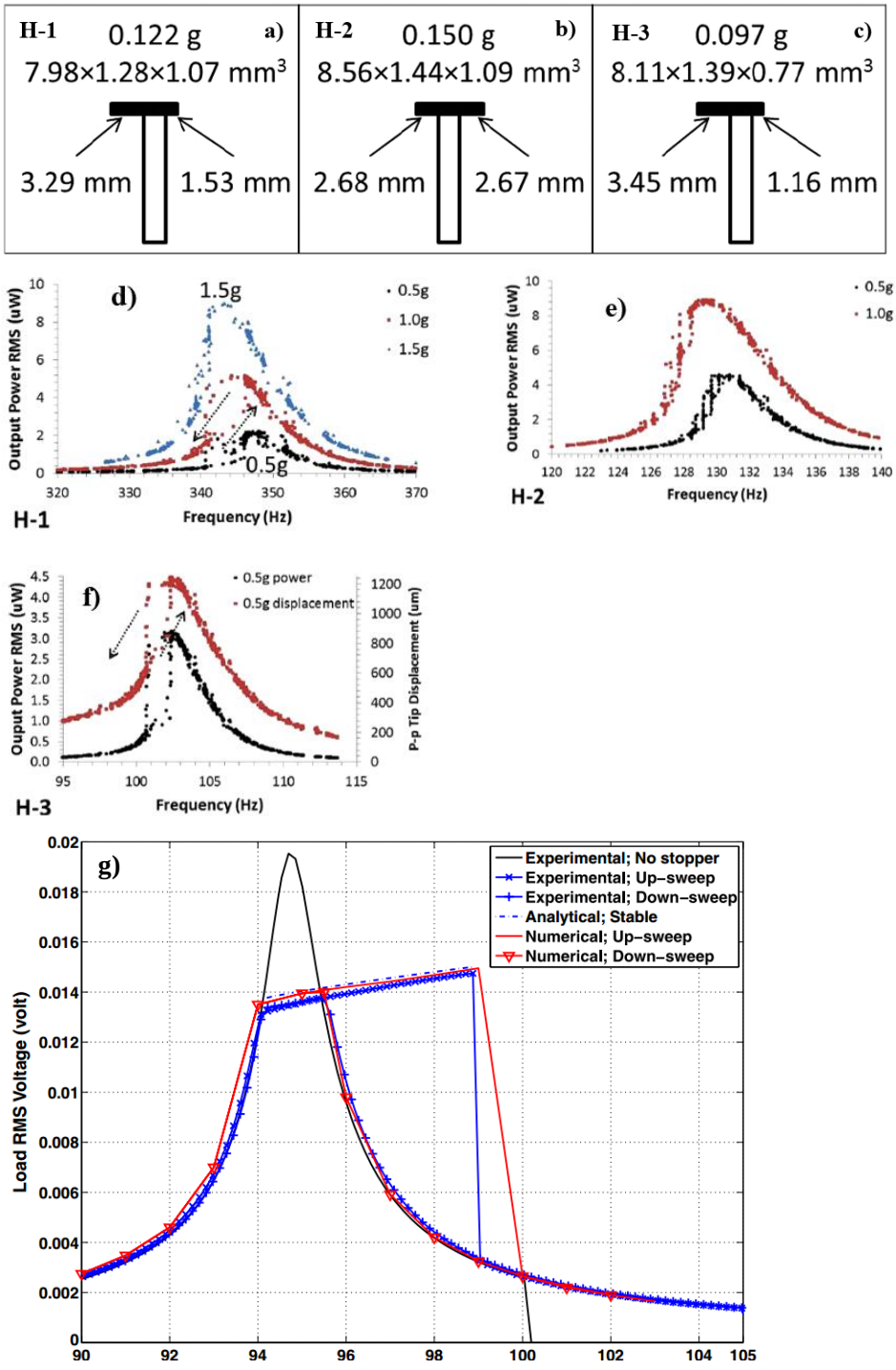

Figure 2-12: a) Mass and location of H-1 energy harvesting cantilever end mass b) Mass and location of H-2 energy harvesting cantilever end mass c) Mass and location of H-3 energy harvesting cantilever end mass d) RMS power generated at indicated frequency for H-1, e) H-2, f) H-3 [85] g) Numerical and experimental power outputs for linear energy harvester and end-stop harvester [86]

2.6.3 Endstops and Coupled Harvesters

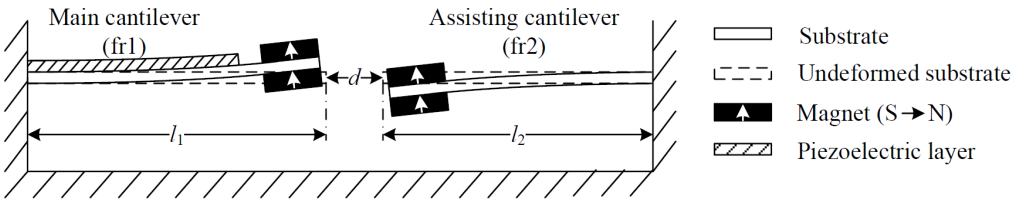

Figure 2-13: a) coupled bistable energy harvester diagram

Endstops [86, 88] and coupling two oscillators against each other, as shown in figure 2-14a has also been attempted as a means to introduce nonlinearity into vibrational energy harvesting systems [89, 90].

As seen in figure 2-12g, the broadness of the response is expanded for the harvester with endstops. It is interesting to note that one nonlinear feature present there is a difference in the power output depending on the sweep direction of the input excitation. However, it is also obvious that the peak power output is significantly decreased since constraining the motion does not allow for higher strains and strain rates to be developed. Figures 2-14c-e show the capacitor charge up times for the coupled harvester system of figure 2-14a as well as the average power outputs. The steepness of the initial charging period is clearly related to the presence of more energy at the higher excitation levels. Again, this is an effective method for inducing nonlinearity to the system, but the presence of two cantilevers again blurs the line of whether this is in fact two devices or not.

2.6.4 Bistability

An interesting nonlinear property which has attracted much attention is multistability. Stability in this context is defined as a systemic state where an attempt to move the system away from this equilibrium state is met with resistance from the system itself. Multistability is the existence of several such states. If sufficient energy is expended, the system may leave one of its stable states and transition to a different one. A transition from one stable state to another is called a "snap-through transition". It is usually associated with high velocity and displacement which is advantageous in an energy harvesting context. While there is some research on systems with high orders of multistability [94–98] most of the research in the energy harvesting realm has been on bistable energy harvesters, i.e. structures with two stable states. Bistability can be induced using several methods. The common thread between all is that forces are either externally imposed or residual stress is imparted such that two strain energy wells exist as seen in figure 2-15c where each of the minima correspond to a stable state and the local maximum between them corresponds to the energy required to cause a state transition. This is referred to specifically as a dual potential well or generally as a strain energy function or

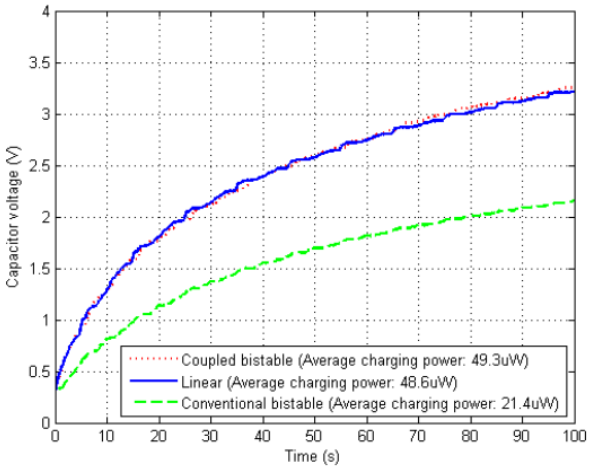

(a) signal 1: 6.9 $m \cdot s^{-2}_{rms}$

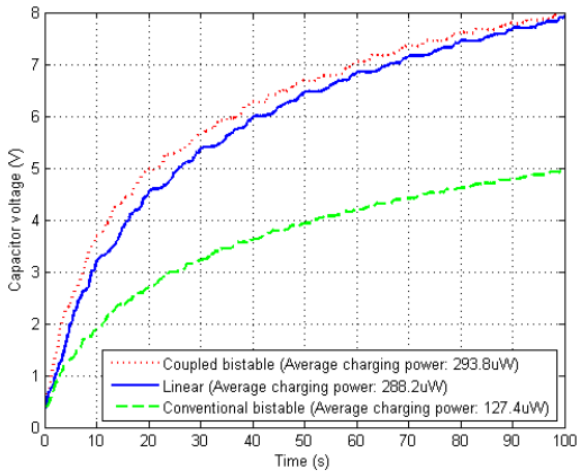

(b) signal 2: 12 $m \cdot s^{-2}_{rms}$

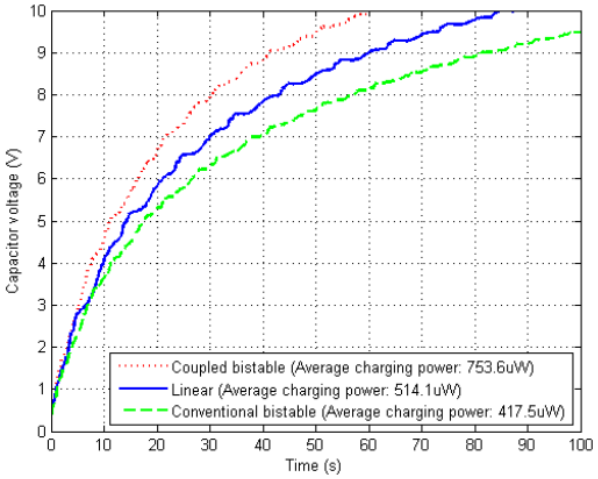

(c) signal 3: 18.3 $m \cdot s^{-2}_{rms}$

Figure 2-14: a-c) capacitor charge-up times for coupled harvester at indicated accelerator levels [89]

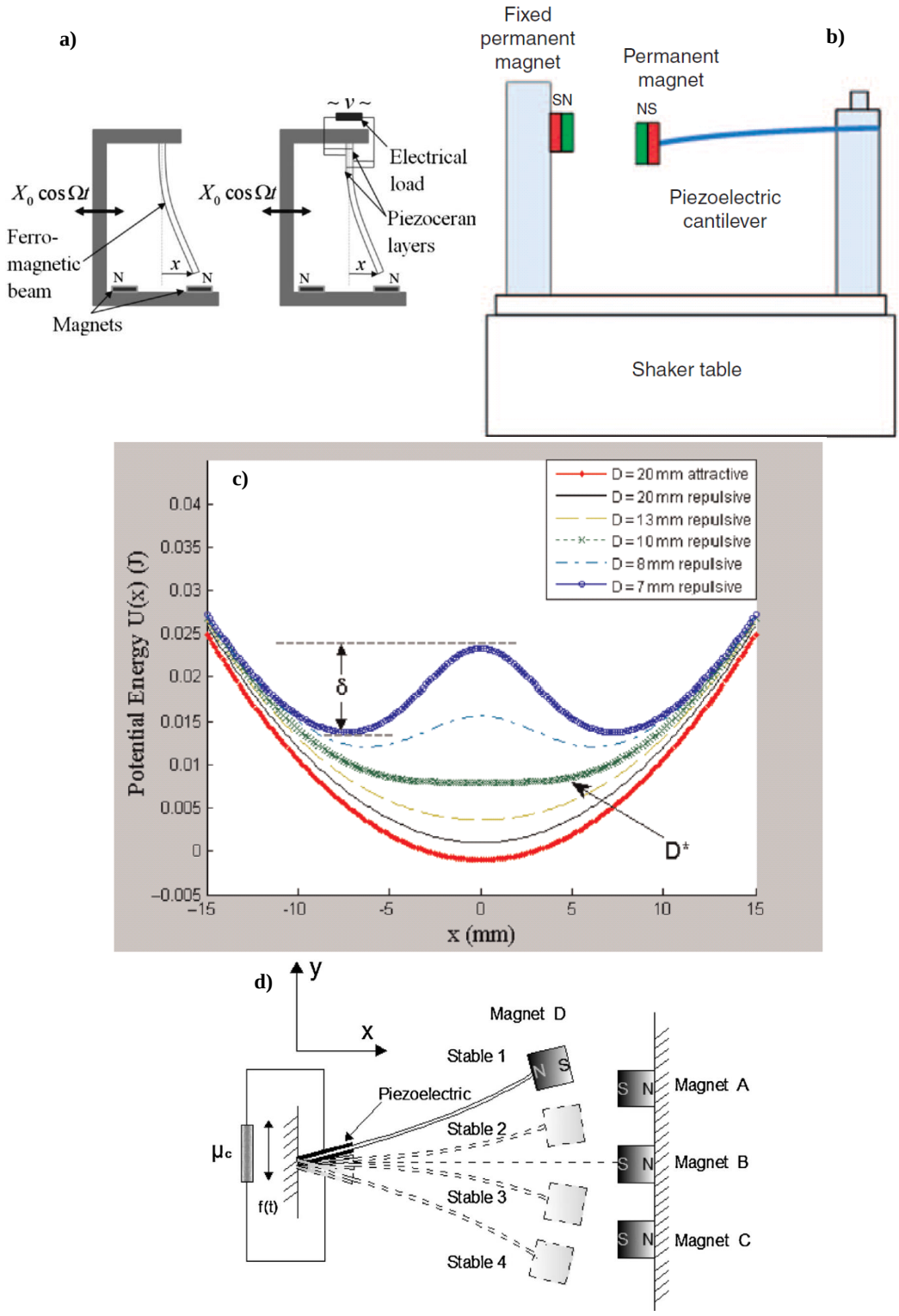

Figure 2-15: a) Magnet attraction bistable cantilevers [91]b) Magnetic repulsion bistable cantilever [92]c): Dual potential well [93]
d) Quadstable magnetic cantilever [94]

strain energy landscape. The simplest bistable energy harvesters are shown in figures 2-15a and 2-15b. Both use external interactions with magnets to induce bistability with one utilizing magnetic attraction of the metal cantilever, and the other using magnetic repulsion. Altering the distance between the magnets of figure 2-15b can change the potential energy function as shown in figure 2-15c. This figure shows the strain energy function resulting from the magnets being at a distance of 20 mm and having minimal interaction. As shown, the strain energy function is parabolic, implying linear stiffness. As the magnets are moved closer, the effort required to move the magnets through their narrowest point increases. The simple addition of magnets has allowed for experimentation with systems having many stable states such as the one shown in figure 2-15d. Springs have also been used to induce bistability, by Wu, et. al [99]. Bistability has also been induced in postbuckled beams, such as the one shown in figure 2-16a [100–103]. Depending on the amount of force exerted upon the end of the beam, the strain energy function can be adjusted as well as seen in figure 2-16b&c [104]. Bistable structures have also been created by carefully engineering the thickness of structural members such as those appearing in figure 2-16d [105]. These areas of high compliance causes behavior similar to hinges. Bistables of this sort can be manufactured easily by stamping from metal sheets, such as the one shown. Optimization studies were carried out to allow for specified activation forces for snap-through to be realized [106] revealing high sensitivities of small changes of geometry and dynamic characteristics. While this does allow for very low per unit cost of manufacture, this approach is not very scalable as making a structure of significant thickness would require very high forces. Thus it would be difficult to design a structure with suitable area for mounting a piezoelectric transducer. Similar to post-buckled members, a snap-through event would also have high damping leading to low efficiency.

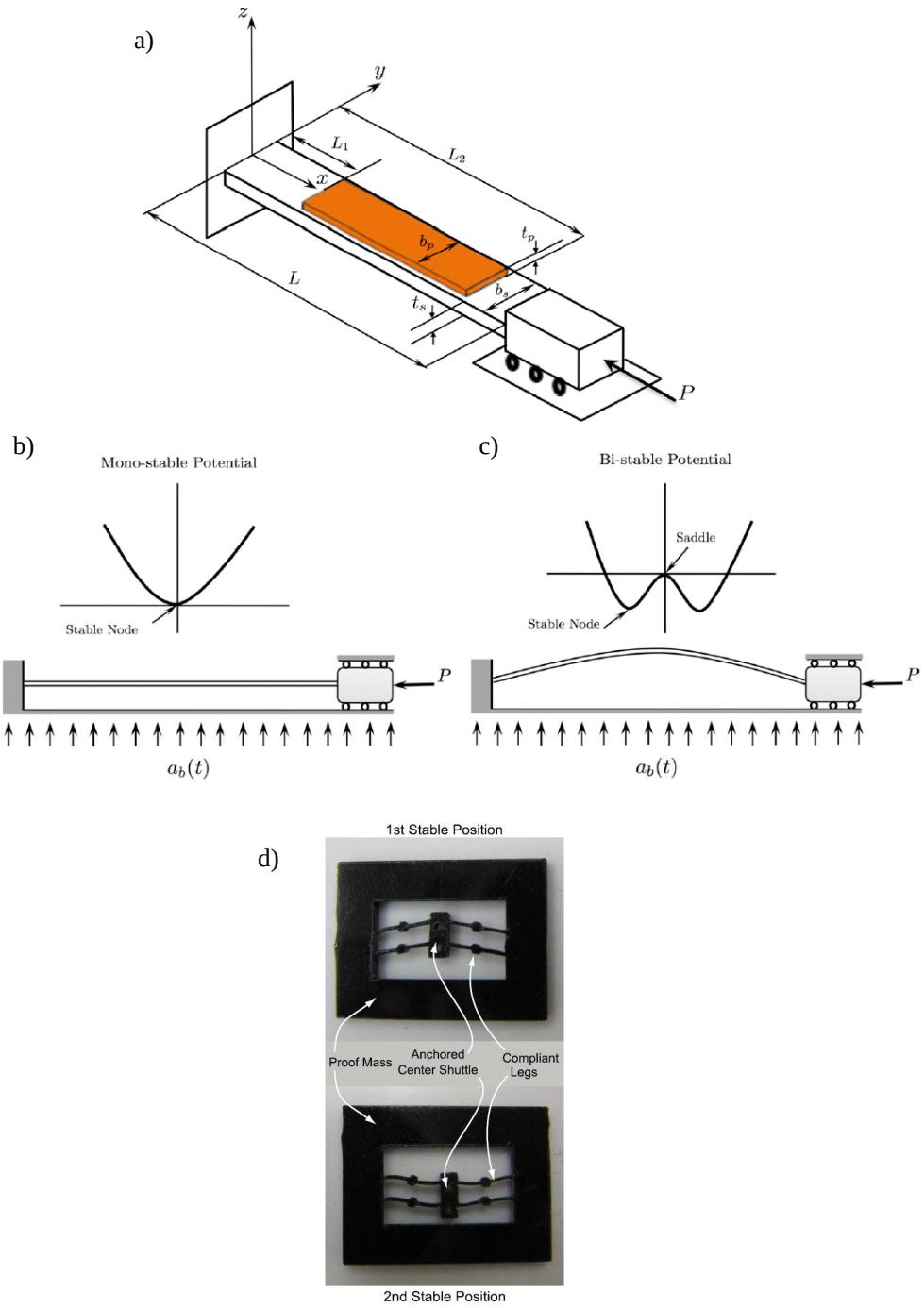

Figure 2-16: a) Bistable buckled beam setup b) strain energy function prior to buckling c) dual potential well after application of end load d) [107] Stamped bistable hinge-type structure [105]

Residual stress in a material has allowed for several types of bistable structures to be investigated. This method is preferred because it does not require the manufacture of an external framework to maintain forces acting on the harvester. It however does not have the

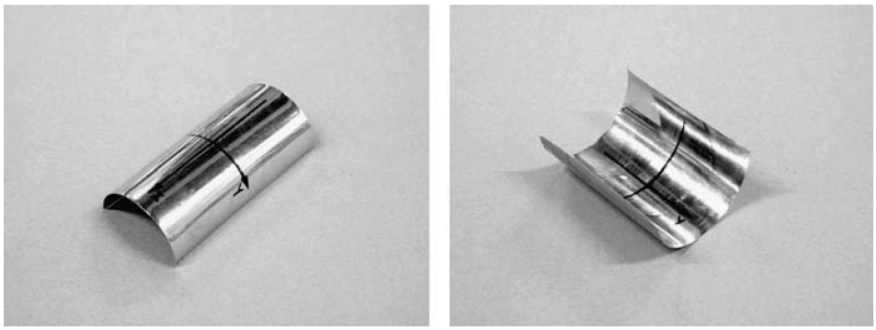

Figure 2-17: 50 x 50 mm bistable metallic tape's static states [108]

ability of tuning upon deployment as the strains are inherent within the material. Prestressing steel has been used to make bistable tapes such as those seen in figure 2-17 and has been used as novelty toys, tape measures, and other applications. They have generally been used effectively for actuation and structural deployment contexts. From an energy harvesting context, the activation forces are again relatively high due to the stiff nature of steel even though they can be made quite thin.

A highly interesting approach to bistability from the standpoint of energy harvesting is in laminate structures [109–111]. This has been done primarily in two ways. The first approach is to put the individual laminae composing the structure in tension, and then to stack them with an asymmetry in the stresses. The laminae are then bound together by some method and the external tension support is released, causing the laminate to be bistable. This pre-tensioning method allows the user great control over the amount of stress present in the final structure, but requires the manufacture of complicated equipment for this which may only allow for a narrow range of sizes to be made. Thus, bistability resulting from the thermal strains of materials is of great interest as the bistable effect comes from properties inherent to the material allowing for great freedom in the shapes and sizes manufactured. In order for sufficient thermal strains to be induced, a material with anisotropic thermal expansion coefficients is required. Unidirectional carbon fiber is such a material, and it has been used by a number of studies. Unidirectional carbon fiber is available in long tape form where it has been already infused with the uncured polymer matrix, referred to as pre-preg. Coupons are cut from the long tapes and are stacked in the correct orientation and thickness for the component being built. The thermal expansion coefficient in the fiber direction is typically negative in sign, implying contraction upon heating, and is approximately on the order of 10^{-6} strain/C°, whereas the matrix's thermal expansion coefficient is positive and on the order of 10^{-7} strain/C° [112]. To mitigate the effects of the anisotropy, stacking sequences are often specified to have plies at different orientations, often with mirrored symmetry about the central ply such that the thermal strains cancel allowing for flat panels to be manufactured. Two different stacking sequences are generally used to make bistable structures. Antisymmetric laminates have a stacking sequence of the form $[+\alpha^{\circ}/-\alpha^{\circ}]_n$ e.g. $[+45^{\circ}/-45^{\circ}]_3 = [+45^{\circ}/-45^{\circ}/+45^{\circ}/-45^{\circ}+45^{\circ}/-45^{\circ}]_{\mathrm{T}}$. The angles are all given using the right-hand convention which sets the positive angles as being counter-clockwise and negative as

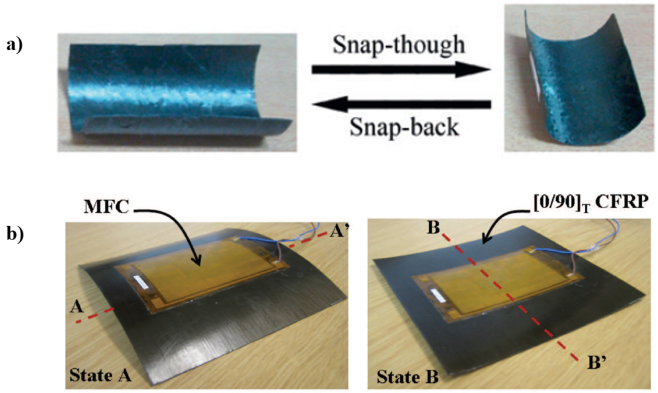

Figure 2-18: a) Antisymmetric bistable laminate states and transition b) [114]Bistable laminate with piezoelectric MFC actuator [115]

clockwise. The subscript$_{\mathrm{T}}$ denotes that it is the total stacking sequence through the thickness. These laminates must be built on a curved tool plate surface of some radius of curvature [113]. This results in a bistable laminate of the sort seen in figure 2-18a with the shown snap-through transition. The other commonly used stacking sequence is of the $[\alpha_n^\circ/(\alpha+90_n^\circ)]_{\mathrm{T}}$. Commonly, the angles chosen are of the form $[0_n^\circ/90_n^\circ]_{\mathrm{T}}$ e.g. $[0_2^\circ/90_2^\circ]_{\mathrm{T}} = [0^\circ/0^\circ/90^\circ/90]_{\mathrm{T}}$. These laminates undergo the snap-through transition seen in figure 2-18b. As shown, the displacement of the apex of the curvature from one state to the apex of the curvature in the second state is large. Because large strains and strain rates are desirable in an energy harvesting context, the latter layup form is preferred.

Bistable laminates of the $[0_n^\circ/90_n^\circ]_T$ variety were first reported in 1981 [116] as classical laminated plate theory suggested that laminates of this variety would cure in a saddle shape. Later work [117] extended the classical laminated plate theory with the von Kármán nonlinearities, offering the first analytical description of the thermal phenomena occurring. Refinements including higher order approximations of the strain fields were derived [118, 119] which allowed for accurate predictions of the out-of plane displacements and curvatures. Because the bistability is brought about by the pulling on either side of the laminate by the contracting matrix where the resistance to the stiffness comes from the thickness of material, the edge length to thickness ratio must be greater than 80-85 [120]. This means that while there is a limit to how small a bistable laminate can be, the upper size boundary is set only by manufacturing capability. Figure 2-19c shows the curvature values with respect to edge length. As shown, over a certain threshold value, these curvatures are constant regardless of the size of laminate. The onset of bistability as seen in the bifurcation is sudden and sensitive to manufacturing tolerances. The overall laminate properties are effected strongly by defects and some environmental factors. In particular, Betts [121] and Brampton [120] investigated the effects of resin thickness nonuniformity and ply thickness variation on the out-of-plane displacement. The effects of slippage between the forming toolplate and cured laminate properties was investigated by [122, 123]. As shown in figure 2-19a the curvature of the side cured in contact with the tool

surface is minimally affected, but the top side's curvature increases with the curvature of the tool surface. The effects of long-term stowage was also investigated [124]. As shown in figure 2-19b, exposure to high temperatures for long periods of time to accelerate the aging process results in a decrease of stiffness.

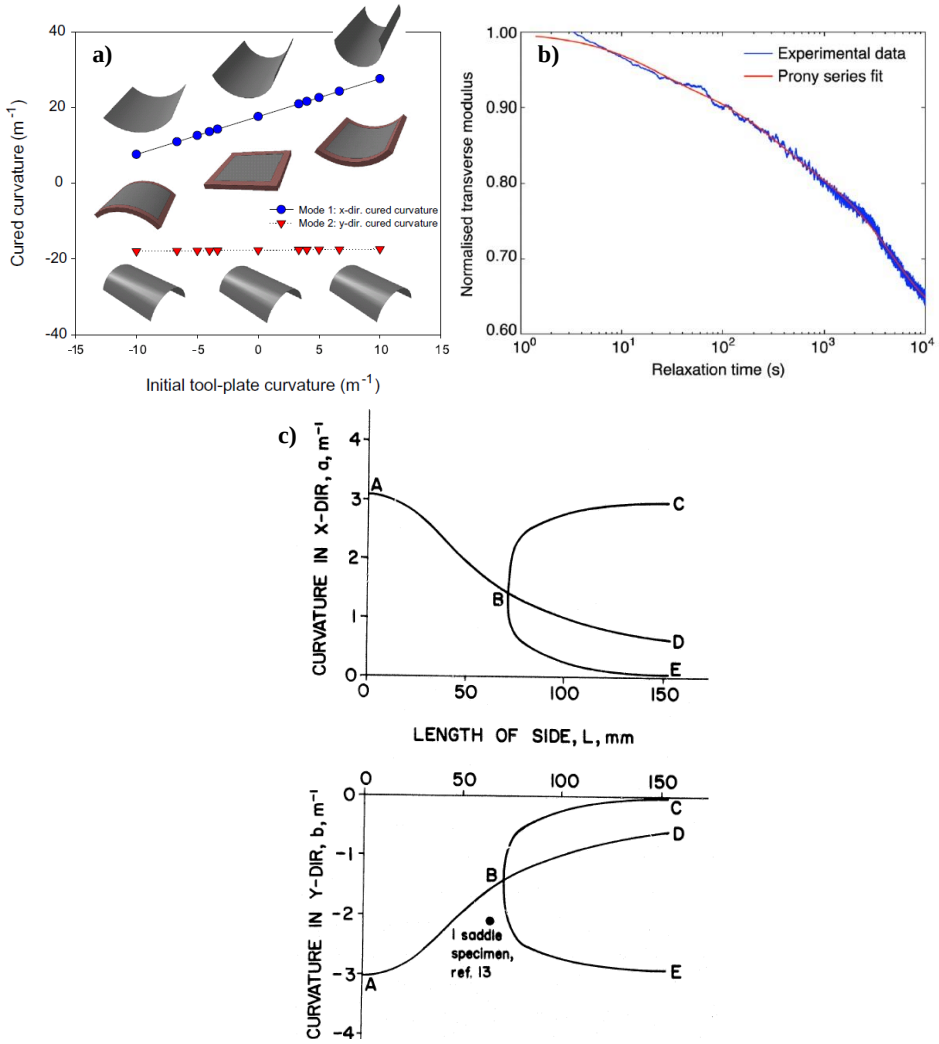

Figure 2-19: a) Tool plate curvature influence on laminate curvature [123]b) Stiffness over time for bistable tube at $60C^{\circ}$ [124]c) curvature on x-axis and y-axis for the two stable states of a bistable laminate with respect to the edge length [117]

The first application for bistable laminates was in an actuation context. Interest was attracted because the actuation distance was substantial and stability in both states did not require a constant input of energy to hold the different configurations–only a one-off actuation energy cost was required to select the needed state. One of the drivers was the idea of seamless control surfaces for aerospace applications [125–129]. Several methods of actuation were tested such as Shape Memory Alloys [130], heat [131, 132], and piezoelectric transducers [133, 134].

An optimization study was carried to find the optimal design for actuation [135]. To increase the stiffness of the laminates in their respective states, metal layers were added between the composite layers [136]. These actuation studies contributed much information to the scientific community regarding the static shapes and some information on the dynamics of single snap-through events.

Interest in the dynamics of bistable laminate systems under forced oscillations logically followed [137, 138]. The first bistable laminates for energy harvesting with piezoelectric transducers was done in 2010 [139] and is shown in figure 2-20a. As shown, four small piezoelectric patches were used to convert mechanical strain into electrical energy. Mass was added at the corners to facilitate snap-through. Examination of the dynamics showed that subharmonic and superharmonic frequency components were significant characteristics of bistable laminates' response to higher forcing levels, and the snap through effort was found to be frequency-dependent [140] with oscillations near resonance most susceptible to state changes. Another investigation found that edge effects were significant in terms of changing the out-of plane displacement and the ringdown of laminates subjected to perturbations was modeled [141]. The mode shapes of bistable laminates were calculated and validated, as well as the conditions needed for snap-through. In addition to the bending modes usually capitalized upon, several twisting modes were also present. Upon snapping through, different dynamic response modes were observed [142]. In general, when excited, the response of a bistable oscillator can be classified as one of four modes. Energetically, the smallest response is when the system is driven such insufficient energy is supplied to escape the occupied well. This is referred to as a single well response. In order to analyze recorded time histories of driven oscillators, Poincaré plots are sometimes used to visually determine the mode. A Poincaré plot, sometimes referred to as a phase portrait, is typically done by plotting the derivative of a dynamic quantity on the vertical axis and the undifferentiated quantity on the horizontal axis. The Poincaré plots appearing in figure 2-21 a-d show velocity and displacement. Figure 2-21 a shows the shape of Poincaré plot associated with single-well oscillation. If enough energy is supplied that the oscillator undergoes snap-through from one state to another, it may be the case that the snap-through events follow a pattern e.g. 3 oscillations in one well, a snap-through, 4 oscillations in the other well, followed by snap-back, in a continuous cycle. This mode's corresponding Poincaré plot appears in figure 2-21b. This response mode is called periodic intermittent. Depending on the forcing conditions, the snap-through and snap-back may not have any set pattern, and the response of the system can be chaotic. This dynamic mode's corresponding Poincaré plot appears in figure 2-21c. This is the chaotic intermittent response mode. Finally, it can be the case where the system continuously snaps between states in a limit cycle oscillation. This is referred to as continuous snap through, and its corresponding Poincaré plot appears in figure 2-21d. A modal map showing the frequencies and accelerations where these different modes are observed appears in figure 2-21e. Bistable laminates for energy harvesting has been the focus of a narrow range of researchers, and is reviewed here [143, 144]. A study determined that the optimal shape and number of plies to maximize the amount of energy harvested from a single snap-through event of a centrally supported plate was square and two, respectively [145, 146].

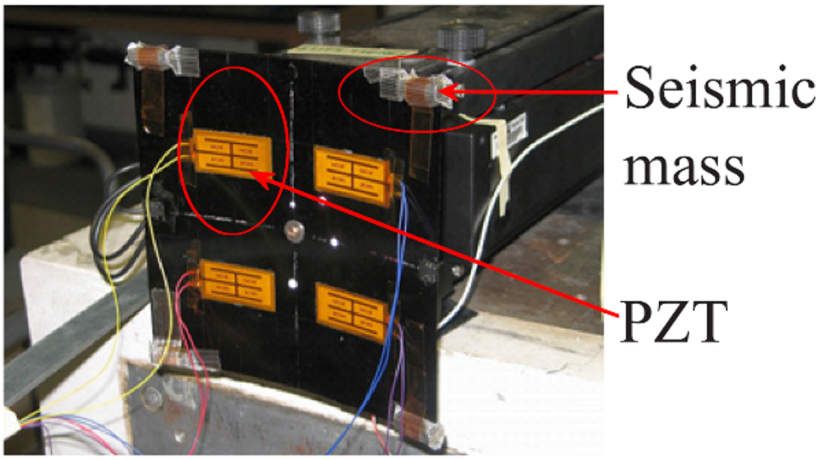

Figure 2-20: a) Bistable laminate for energy harvesting [147]

This optimization study shed light on the sort of tradeoffs and considerations for this type of harvesters. Firstly, it established that there was a tradeoff between piezoelectric coverage and power. Usually, laminates are cured at high temperature, and after cooling, a piezoelectric patch is attached. While more active piezoelectric area usually increases the amount of energy harvested, there are diminishing returns on this. Most researchers harvesting energy from plate-type structures seek to maximize the energy harvested from the first bending mode, which in the case of centrally supported laminates means that the highest strain concentrations are near the bolthole, and decrease in the direction of the laminate edges. It was established that the stiffness of the piezoelectric material is sufficient that under some coverage ratios, the curvature of the laminates can be significantly changed, as well as the excitement required to cause snap-through. Thus, the interaction between the piezoelectric material and the substrate is significant. This study only considered square and rectangular laminates and aimed to maximize the energy harvested from a single snap-through event.

Research expanded beyond rectangular laminates and some arbitrarily shaped plates were studied. Based off of formulations for the strain energy function in [118] two extensions of note are mentioned here. Betts' formulation included a binary grid with values of zero or one where zero represents a void and one represents the presence of material [148]. This discretization allows the representation of arbitrary shapes. This study was accompanied by experimental results to compare the predicted power against the measured power and to confirm the predictions of the static shapes produced by the model [148,149] Tavakkoli further extended this formulation by adding full piezo-mechanical coupling [150]. The change of stiffness of the piezo based on the electrical boundary condition was taken into account. The most recent analytical model of bistable laminates used a 4^{th} order polynomial was used to more closely represent the shape of the laminates which allowed anticlastic curvature to be represented [151]. This allowed for closer agreement with finite element results. The bistable plates were driven through different frequencies and accelerations and the dynamic responses were observed [152]. A derivation by Taki et. al refined the assumption of the out-of-plane curvature [153]. Prior to

this, it was assumed that the cured shape of the laminate could be approximated by a parabolic section whereas here a 4^{th} order polynomial was used to more closely represent the shape of the laminates which allowed for the presence of anticlastic curvature, but only for square laminates.

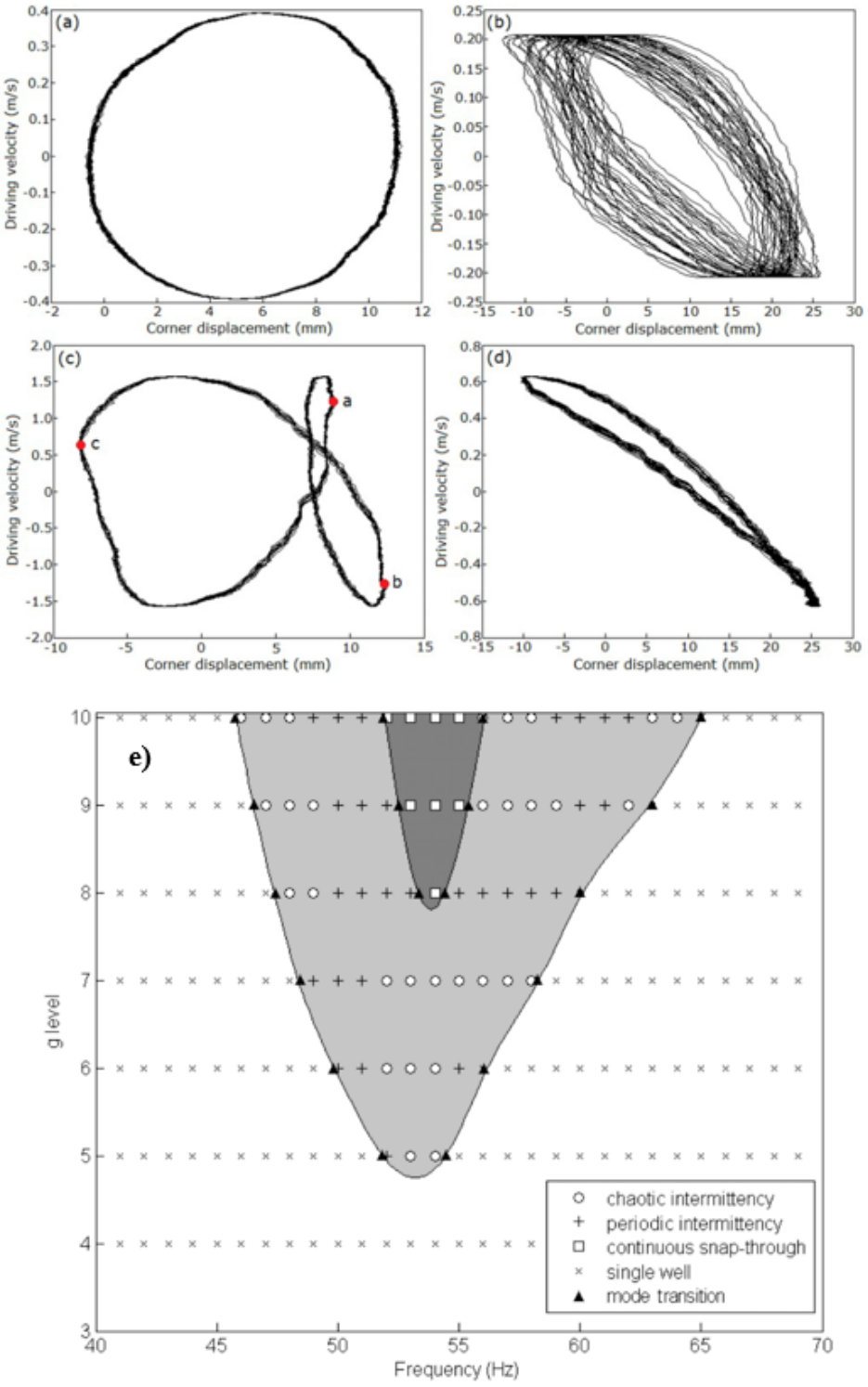

Figure 2-21: a) single well oscillation b) chaotic oscillation c) periodic intermittent d) continuous snap-through [154] e) modal map of laminate tested at indicated frequencies and g levels

Bistable laminates were also built in cantilever form such as the one shown in figure 2-22, and evaluated for their suitability. A two-ply harvester was manufactured, tested and modeled [155, 156]. Cantilevered bistables were found to be advantageous as their well-known strain distributions under deflection allowed for intuitive placement of the piezoelectric patches. The natural frequency of the cantilever could be adjusted effectively by changing the length. The acceleration level required for snap through was reduced.

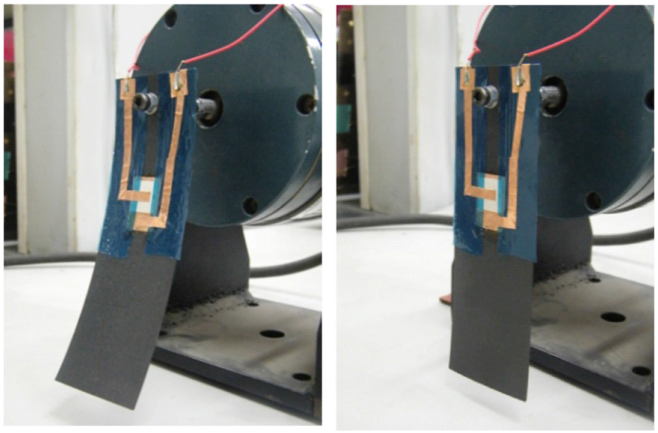

Figure 2-22: Bistable cantilever's two states [157]

2.7 Thesis Scope

The research contained in this thesis has made original contributions to science in the area of bistable laminates with piezoelectric transduction for energy harvesting from vibrations. The relevant publications are included in the appendix [59, 149, 158–162]. The primary objective of this thesis is to investigate the efficacy of changing various design parameters to tailor the dynamic characteristics of bistable energy harvesters for improved energy harvesting from vibrations in terms of operational frequency bandwidth and power output. This is done by changing the design parameters through a range of values and characterizing the change of the power output as well as other dynamic characteristics. The secondary objective is to study the response of the bistable harvesters to better understand the dynamic behavior especially under high-amplitude excitation. In the following chapters, work is presented on both plate-type and cantilever-type harvesters.

- Chapter 3 presents several contributions on providing an experimental comparison between a bistable cantilever system and an equivalent linear one, which is achieved by interchanging a single pair of laminae. The design parameters of interest are the operation orientation, adjustment of the electrical boundary condition, and the introduction of an end mass.

    1. A bistable laminate cantilever energy harvester and an equivalent linear cantilever energy harvester are built and subjected to the same acceleration levels and the

power output over a load resistor is measured

2. The bistable energy harvester was tested in both the vertical and horizontal operating orientations
3. The electrical boundary condition is varied through a range of values and the change of power output is observed at both high and low acceleration levels
4. A small end mass was added to the cantilever tip and the harvester was tested at different frequency and acceleration levels
5. The dynamic modes of the bistable is analyzed using a sophisticated numerical technique to distinguish different behavioral regimes

It is concluded that:

1. The bistable energy harvester's peak power is just over half of the linear system at the high forcing levels, but the frequency band of operation is four times broader
2. The operation orientation was not very effective in changing the behavioral dynamics implying the self weight of the harvester at this scale to be a small factor
3. The peak power output is shown to be maximized around resistance values where the load impedance is matched to the piezoelectric transducer's capacitance
4. Despite changes of natural frequency due to nonlinear softening, it is not to an extent where active tuning of the load resistance would realize substantial gains
5. The addition of an end mass reduced the acceleration needed for snap-through from 5g to 4g
6. Baselines for analysis in terms of orders of magnitude of power output, snap-through acceleration, and natural frequency are established

- Chapter 4 explores the efficacy of changing the shape of a square, centrally-mounted plate-type bistable laminate energy harvester. Three different shapes are built from the same material and for two, 20% of the material by area is removed. A model is derived to attempt to capture their behavior and is validated against experimental results. The dynamic behavior of the plate is then studied.

  1. A model is derived featuring full electromechanical coupling between the piezoelectric patch and bistable laminate, and the capability to accept arbitrary shapes as an input is implemented
  2. Validation results are gathered and compared against model results for low and high acceleration levels both in the form of time-domain data as well as averaged (RMS) values
  3. The dynamic behavior is then analyzed and the emergence of some nonlinear features are studied

  It is concluded that:

1. The removal of material successfully reduced the acceleration level required to initiate snap-through from greater than 11g for the case of the square to 7g for a saltire shape, but power was decreased by nearly one half
2. The removal of material from square to a cruciform shape improved power, but did not have significant effect on the bandwidth of operation
3. The model's prediction for out-of-plane curvature of the laminates is tested and shown to agree within approximately 16%
4. The predictions of the natural frequencies for the different states and different shapes are within 13%
5. The main nonlinear features such as subharmonics, superharmonics, antiresonances, and snapthrough of the different shapes are present in the model
6. The general trends of the natural frequency's value with respect to differences of operating state and material removal were correctly represented

- Chapter 5 continues the investigation of plate-type bistable laminate energy harvesters. The efficacy of changing the layup to non-orthogonal configurations is studied as a means of controlling stiffness and therefore broadening the response of the harvesters.

  1. A series of laminates are constructed where the second ply angle is reduced such that the bistable laminate approaches monostability
  2. The emergence of nonlinear characteristics in the response of a nonorthogonal laminate is characterized
  3. Different metrics are calculated from the harvesters' responses and presented

  It is concluded that:

  1. The snap-through acceleration is effectively reduced from greater than 11g to 2g
  2. The damping ratio is shown to vary linearly with respect to acceleration input
  3. The broadness of the response of the non-orthogonal outputs is shown to be twice that of the orthogonal harvester
  4. Matching the natural frequency of the two states is shown to be important for effective broadband harvesting
  5. The gradual emergence of nonlinear features in the response is shown

- Chapter 6 returns to the concept of bistable laminate cantilever energy harvesters. Repelling magnets are set up to superimpose a second bistable strain energy landscape upon the existing bistable strain energy landscape. The efficacy a varying compressive pre-load on the bistable cantilever is assessed.

  1. A simple 1DOF empirical model is derived and the relevant experimental parameters are experimentally identified

2. Frequency tests are undertaken at different acceleration levels and varied magnetic gap distances

It is concluded that:

1. Adjusting the magnetic gap allowed for a trading off between peak power and broadness of response
2. The magnet successfully reduced the acceleration required for snap through from 3g to 2g
3. The 1DOF model is able to follow the trend of natural frequency with respect to magnetic gap distance, as well as the approximate forcing parameters required for snap-through

- Chapter 7 presents two practical demonstrators

1. A cantilever was placed in a wind tunnel for energy harvesting from wind
2. Some harvesters are subjected to excitations based on sampled train bogey vibrations
3. Design criteria for the train context are set and a target power output is set

It is concluded that:

1. It is possible to harvest energy from the wind with bistable cantilevers
2. The small-angle energy harvesters offer good potential to harvest energy from real vibrational scenarios supplying sufficient power for running sensors at the rate of approximately 1 reading every 5 seconds

- Chapter 8 presents the conclusions and discusses future research directions

Chapter 3

Linear and Bistable Laminate Cantilever Energy Harvesters

This chapter seeks to address three main objectives. The first objective is to experimentally compare the performance of a linear cantilever energy harvester against a bistable counterpart and demonstrate that the bistable provides broadband performance. This is done by fabricating a linear and a bistable cantilever which are as similar as possible in terms of construction, and subjecting them to comparable vibrational tests. The second objective is to establish the efficacy of adjusting certain design parameters and to investigate their relationship with the power output. In this chapter, the load resistance is varied at different acceleration levels to determine the efficacy of resistance tuning. The operation orientation is also tested with harvesting in the vertical orientation and in the horizontal orientation to see if the effects of gravity are a significant contribution to the harvester's performance. An end mass is adhered to the end of the cantilever to study the efficacy of small proof masses to this bistable cantilever system. The third objective was to establish a sense of typical orders of magnitude of different quantities for this scale of device such as power outputs, natural frequencies and acceleration amplitude required for snap through. As shown, natural frequencies in the region of 15 Hz and upwards are expected, power outputs are anticipated in the order of milliwatts, and snap-through is expected at about 5g.

3.1 Introduction

The aim of energy harvesting is to provide power for a device locally in order to improve device reliability and reduce maintenance costs. Devices for the conversion of vibrational energy to electrical power have received increasing interest in the past decade, with a particular application of autonomous low power devices such as wireless sensor nodes. A variety of transduction methods have been considered including electrostatic generation [163], electromagnetic induction [164] and the piezoelectric effect [147]. The piezoelectric effect has a number of advantages

including ease of integration within a system, higher strain energy densities compared to electrostatic and electromagnetic systems and a purely solid-state conversion between electrical and mechanical energy [152]. In many cases piezoelectric energy harvesting devices have been designed to operate in the linear regime where the resonance of the system is exploited to maximize the displacement of the structure in a function analogous to a mechanical amplifier. Commonly, simple linear cantilevered beam configurations [165] are used as their properties are well known. Devices with high quality factors are possible with high power outputs, but only within a narrow band, as was discussed in chapter 2, section 4. While this approach is suitable for energy harvesting contexts in which the source is harmonic and is time-invariant, in practice this is often not the case. An alternative approach is to exploit nonlinear dynamics, such as bistability, to improve the power harvesting capability. Because of the inherent complexity of the frequency responses of nonlinear energy harvesting systems, finding optimal designs is not trivial. A common nonlinear piezoelectric energy harvesting device is a bistable cantilever system where the bistability is induced using an external arrangements of magnets. An alternative method presented by Arrieta, et al. employs a piezoelectric element attached to the surface of a composite laminate with an asymmetric stacking sequence [147]. Such an approach is aimed at exploiting the inherent bistability arising from anisotropic thermal properties of laminate composites. Figures 3-1a, b) shows the two stable equilibrium states of a square bistable $[0°/90°]_{\mathrm{T}}$ Carbon Fiber Reinforced Polymer (CFRP) laminate with a Macro Fiber Composite (MFC) piezoelectric element attached to its center. Figure 3-1c shows the double-well strain energy profile for the range of curvatures of a bistable composite obtained via an analytical model, where the two minima represent the two stable equilibria, State 1 and State 2 (inset of Figure 3-1c) and the saddle point in the center shows the unstable equilibrium [152]. The energy hill that needs to be traversed to 'snap-through' from one state to the other is also apparent in Figure 3-1c.

Bistable laminates have been extensively studied for morphing or adaptive structure concepts [91, 166, 167] since snap-through between stable states can result in a large deflection. Because of the structure's bistability, it is able to bear a load in its two states without external assistance and therefore requires energy only for the transition. For harvesting applications, a conformable piezoelectric element is attached to the laminate surface to generate electrical energy by the direct piezoelectric effect as the structure is repeatedly deformed as a result of mechanical vibrations. The onset of snap-through events is thought to lead to large and rapid variation in strain leading to high power outputs achieved over a broad frequency range [147]. Experimentally, such harvesting devices have been shown to exhibit high levels of power extraction over a wide range of frequencies; for example, approximately 30 mW was achieved for an acceleration forcing level of 2.0 g, and there are opportunities for further optimization to increase the power output [118] by tuning the laminate lay-up and geometry. However, what is less clear is how the power output compares quantitatively between linear and bistable energy harvesting devices. While the essence of the argument has been qualitatively presented, a quantitative comparison between the energy harvesting capability of the two systems is more difficult. Particularly, the criteria for what constitutes the equivalent nonlinear device for a

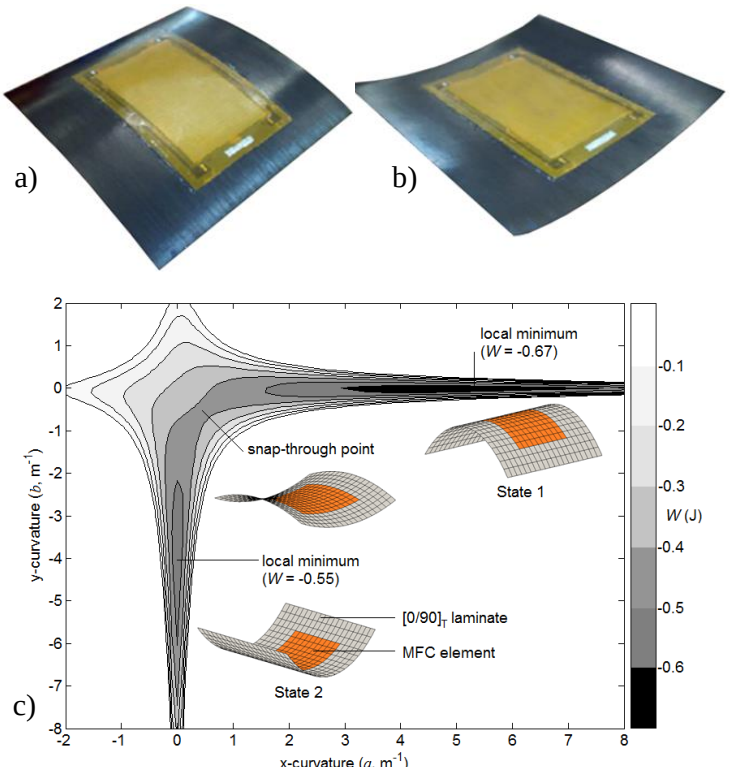

Figure 3-1: a) First stable state of $[0°/90°]_{\mathrm{T}}$ laminate with MFC piezoelectric patch b) second state c) corresponding strain energy profile

given linear device and vice/versa for meaningful comparison is difficult to prescribe. [75,80,83] have attempted such an experimental comparison with devices that are designed to have "tunable nonlinearity". These devices are essentially linear devices where the extent of nonlinearity can be adjusted. This work uses a similar approach. Here, two cantilever energy harvesters are compared. The only main difference between them is that one pair of the carbon fiber reinforced polymer plies (CFRP) are interchanged to introduce bistability. The manufacturing process of the harvesters is described, especially with regards to how electrode fatigue is mitigated. Subsequently, the natural frequencies of the harvesters are characterized and a range of frequencies are selected around them. Sweeps through the frequency band are done at a range of accelerations and the RMS powers are shown and nonlinear features in the response are identified.

3.2 Composite Manufacture

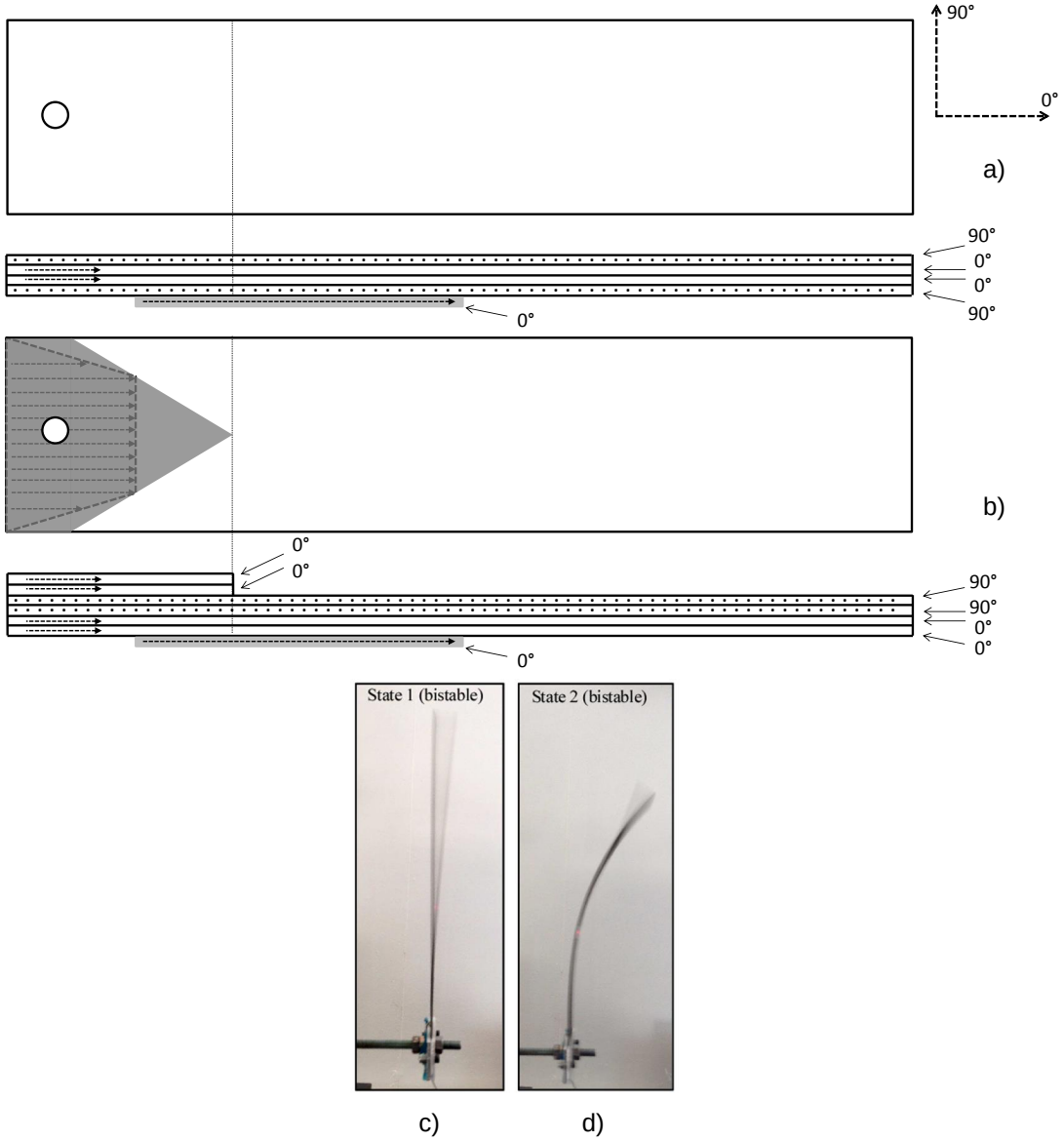

Figure 3-2: Harvester lay-ups a) linear and symmetric $[0^{\circ}_{\mathrm{MFC}}/90^{\circ}/0^{\circ}/0^{\circ}90^{\circ}]_{\mathrm{T}}$, b) bistable and asymmetric $[0^{\circ}_{\mathrm{MFC}}/0^{\circ}/0^{\circ}/90^{\circ}/90^{\circ}]_{\mathrm{T}}$. The cantilevers were clamped at the left hand side. Bistable states: c) State 1 d) State 2

Two cantilevered beams were made using unidirectional CFRP, HexPly M21 UDM 194 (Hexcel) with a Young's modulus (E_{11}) of 178 GPa and shear modulus (G_{12}) of 5.2 GPa [146]. The ply layup for the linear beam was $[0^{\circ}_{\mathrm{MFC}}/90^{\circ}/0^{\circ}/0^{\circ}90^{\circ}]_{\mathrm{T}}$, as shown in Figure 3-2a, and the bistable beam was $[0^{\circ}_{\mathrm{MFC}}/0^{\circ}/0^{\circ}/90^{\circ}/90^{\circ}]_{\mathrm{T}}$, as shown in Figure 3-2b where 0° is along the span of the beams. The beam dimensions were 280 mm long and 60 mm wide and the ply thickness

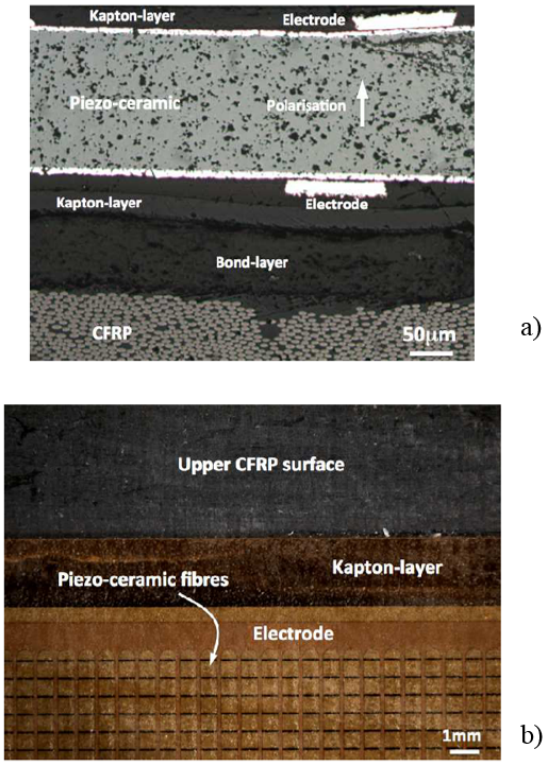

Figure 3-3: a) Cross-section of MFC-carbon epoxy laminate b) top-down view of piezoelectric showing piezoelectric fibres and electrode structure

was between 0.185 and 0.195 mm after curing. To ensure the clamped end of the bistable cantilever remained flat in its two stable states, two additional plies were added at one end to make the clamped region symmetric, giving it the following localized stacking sequence $[0^{\circ}_{\mathrm{MFC}}/0^{\circ}/0^{\circ}/90^{\circ}/90^{\circ}/0^{\circ}/0^{\circ}]_{\mathrm{T}}$, as seen in Figure 3-2b. Figures 3-2c, d) show the two states of the bistable beam. In order to convert mechanical vibrations of the laminate beams into electrical energy, a MFC piezoelectric element (M8528-P2, Smart Materials) of dimensions 105 x 34 mm was bonded to the surface of the laminate at 35 mm from the root. The MFC is based on a lead zirconate titanate (PZT) ferroelectric ceramic which is polarized through its thickness with a manufacturer's specified capacitance of 172 nF [168]. Figure 3-3a shows a cross section of the MFC bonded onto the CFRP showing the piezoelectric fiber in the MFC, and the upper and lower electrodes used to collect the harvested charge and the bond layer. Figure 3-3b shows a top down view of the MFC attached to the CFRP where the piezoelectric fibres and the upper mesh electrode can be observed.

Figures 3-4a, b) show the strain field throughout the bistable cantilever with the maximal strain occurring at the root. It was found that under high acceleration, the copper electrodes at the clamped end were subject to fatigue failure as shown in figure 3-4c. To mitigate the problem, prior to applying adhesive to the MFC, a small section of tape was added to mask off an area of the electrode. Because this small region was not adhered to the CFRP substrate

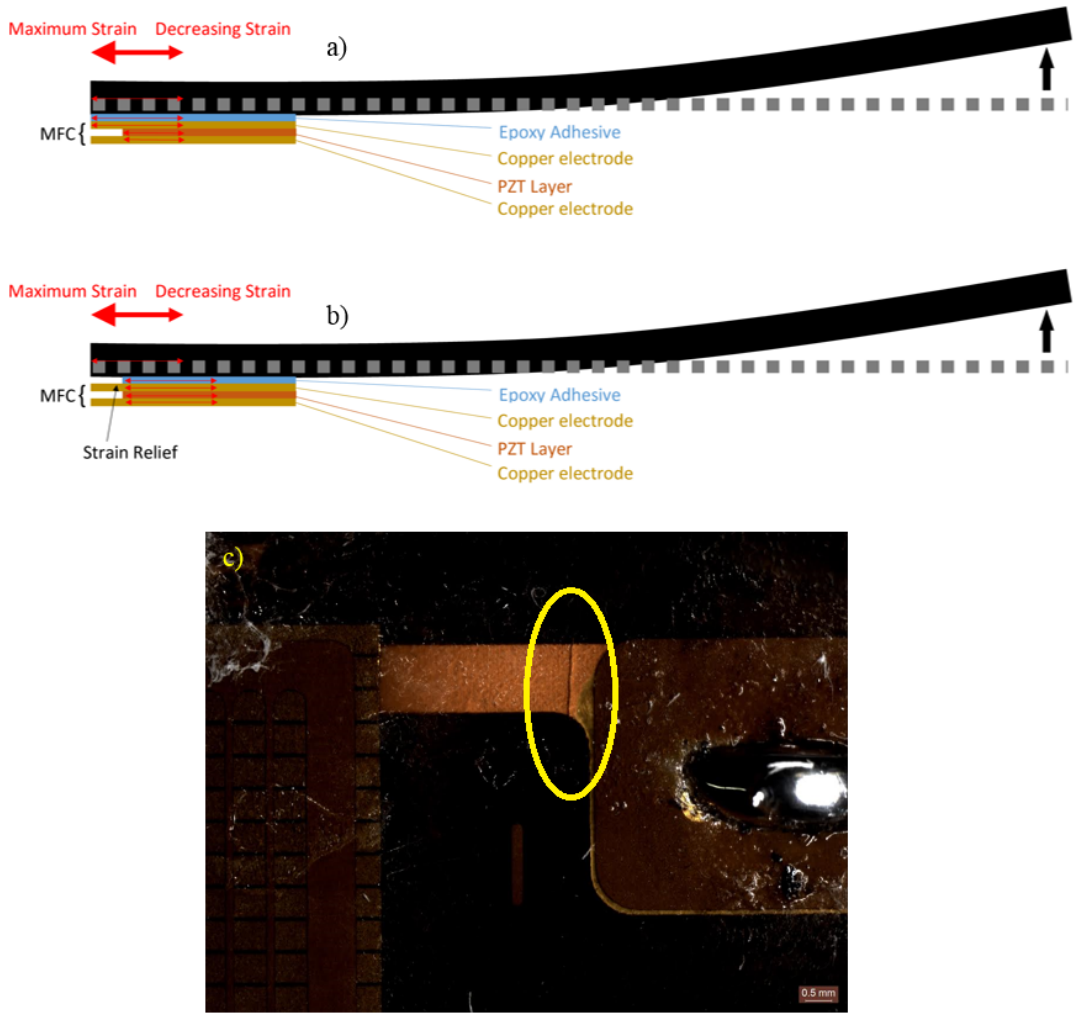

Figure 3-4: a) Full-length adhesion method of the MFC patch to the bistable. b) Fatigue relief adhesion method with shorter adhesive strip c) fatigue crack in electrode

as shown in figure 3-4b the amount of strain transfer was made negligible, thus allowing the electrode to perform for a longer duration. Because the length of the electrode was slightly longer than the piezoelectrically active portion of the MFC patch as shown in figure 3-4, the amount of non-active area was also small, as shown in figures 3-4b.

3.3 Composite Characterization

3.3.1 Characterization Experimental Setup

The first 30 mm of the beams were bolted between two aluminum plates to induce the clamped boundary condition, as shown in figure 3-5a, which also shows the overall dimensions. The energy harvester (i.e. the laminate-MFC combination) was mounted to an electrodynamic

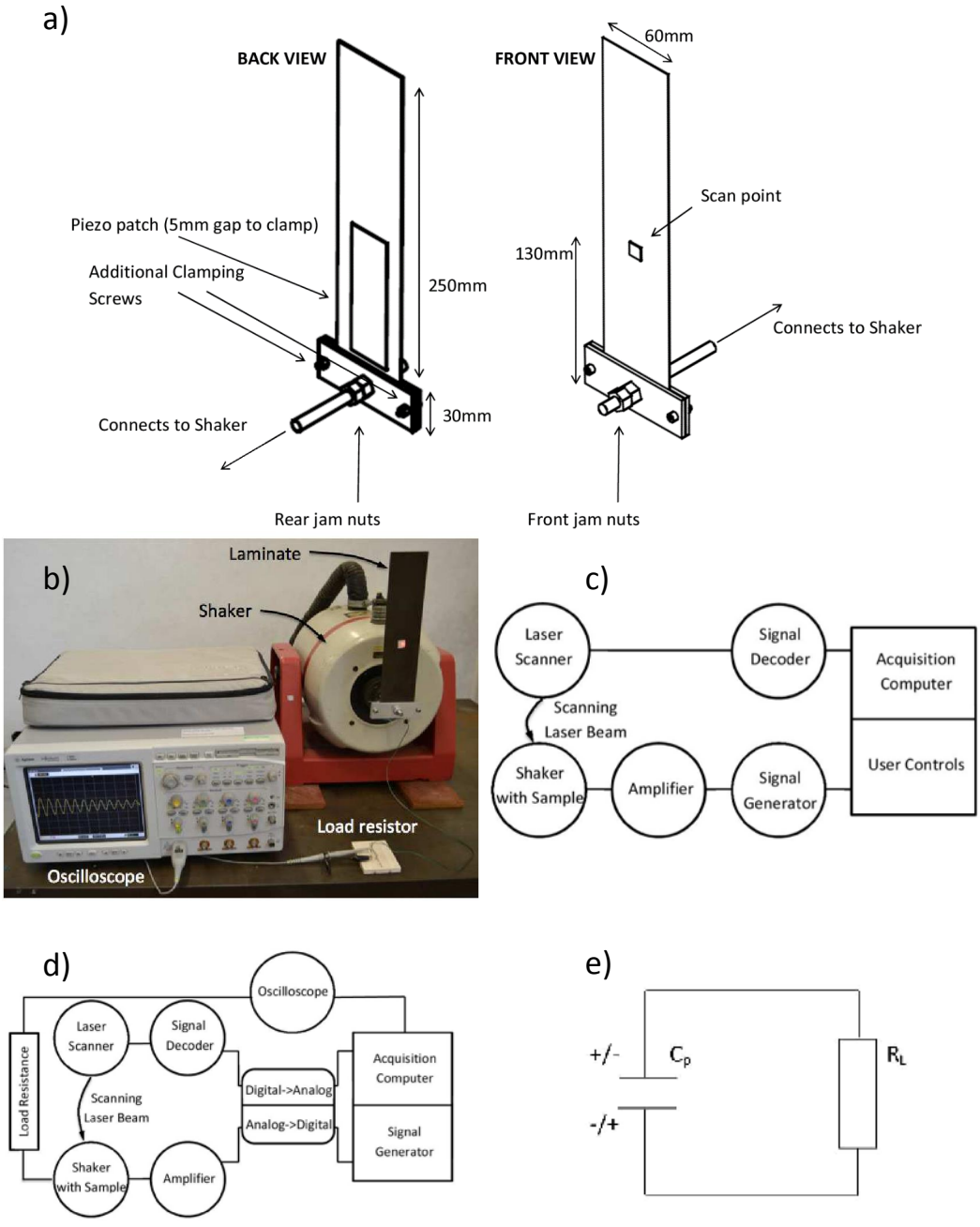

Figure 3-5: Experimental setup: a) clamped cantilever beam; b) cantilever energy harvester on shaker and reflective tape and a load resistor; c) schematic of the experimental setup for frequency response function; d) experimental schematic for power versus frequency, g-level and load resistance e) energy harvesting circuit

shaker (LDS V455) as shown in figure 3-5b. When undertaking frequency sweeps at constant peak acceleration for power generation, the shaker signal was generated in LabVIEW (National Instruments NI-USB-6211 DAQ) which determined the signal amplitude to provide a desired g-level at a particular frequency. This was achieved by initially measuring the velocity, and then calculating the acceleration of the central shaker attachment for a range of drive frequencies (10–200 Hz) and shaker input voltages (0.05–5.0 V) and generating a calibration table for any chosen g-level. The shaker input in terms of drive frequency and input voltage was driven via an audio amplifier (Europower EP1500). In order to characterize the frequency response function of the energy harvester, an input signal was generated using Polytech's 'PSV Acquisition' software (Ver. 8.82). The structural response of the harvester was monitored by a laser vibrometer (Polytec PSV-400-M4 with VD-09 decoder) to measure the displacement and velocity of one point of the harvester 130 mm from the clamped end. Reflective tape was adhered to the harvester to improve the signal return of the scanning laser, as shown in Figures 3-5a and b. Figure 3-5c shows a schematic of the experimental arrangement to characterize the frequency response. In order to characterize harvested power it was necessary to attach a resistive load to the piezoelectric element while undergoing vibration. A load resistor was attached across the MFC and the potential difference across it was measured using an oscilloscope (Agilent 54835A). The optimal load resistance (R_L) for maximum power at a particular frequency (f) was obtained by matching the load impedance to the capacitative load of the piezoelectric (C_p = 172nF); this is reached at the condition where $2\pi f R_L C_p = 1$. For the initial phase of testing, a single load resistance was used which for the linear harvester R_L = 21 kΩ (2^{nd} bending mode at 43 Hz) and for the bistable R_L = 36 kΩ (1^{st} bending mode at 26 Hz). Figure 3-5d shows a schematic of the experimental arrangement for power characterization and Figure 3-5e shows the harvester electrical circuit diagram. Additional test procedures are also detailed where relevant throughout the chapter.

3.3.2 Dynamic Modes of Linear and Bistable Cantilever Beams

Table 3.1: Mode Shapes and Associated Frequencies for Linear and Bistable Harvesters

Mode	Mode Shape	Linear Beam	Bistable Beam
1st bending	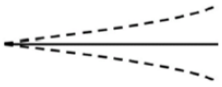	9 Hz	26 Hz
2nd bending		43 Hz	176 Hz
3rd bending		129 Hz	> 200 Hz (not observed)

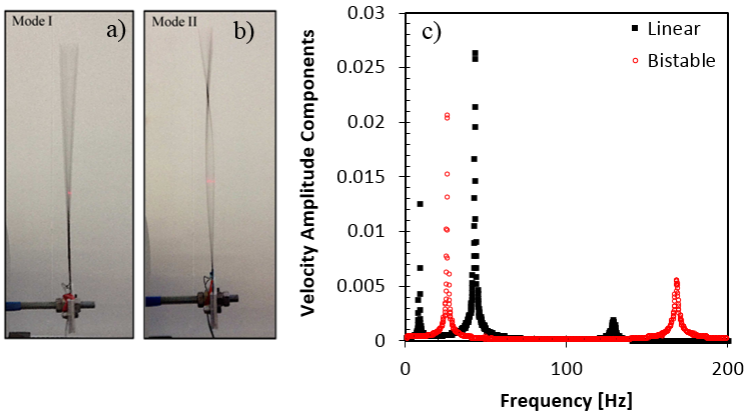

Figure 3-6: Mode shapes: a) First bending mode; b) Second bending mode c) Fast Fourier Transform (FFT) of the velocity of the linear and bistable cantilevered beams

The frequency response function of the energy harvesters were initially characterized to examine the resonant frequencies of the beams. A frequency range from 1–200 Hz which covers a typical frequency range of a bridge with traffic and ground transport was analyzed [169]. To characterize the response of the linear and bistable beams, they were both subjected to the same perturbation input, and their free vibration response recorded in the time domain and then transformed into the frequency domain using a fast Fourier transform. The perturbation was a burst 'chirp' signal which swept through frequencies of 310–340 Hz in approximately 0.32s. From the start of the chirp, the scanner was set to delay measurement for 0.55s, giving the laminate 0.23s to transition into a free response and the shaker's shank to come to a complete stop. During the experiment, velocity data was collected for 6.4 seconds with a sampling frequency of 1.28 kHz. The shaker was driven with a constant voltage of 3.5V resulting in an RMS acceleration of 47g and a maximal value of over 70g. Snap-through of the bistable beam during chirp characterization was not observed during this testing phase. Figure 3-6c shows the fast Fourier transform (FFT) of the velocity measurements at the scan point of Figures 3-5a and 3-5b of the linear and bistable cantilever beams from 1–200 Hz. As the velocity measurement was taken in the center of the width, torsional or rolling modes around the axis along the span of the beam were not identified. Table 3.1 summarizes the resonant modes and Figures 3-6a and b shows the first and second bending modes; the displacement of the third mode was too small to be observed visually. Within the experimental range of 1–200 Hz, three resonant modes were observed for the linear beam while two modes were observed for the bistable beam. Noting that the velocity was measured at the location just lower than the center of the beam, the amplitudes of the modes are consistent with the corresponding mode shapes.

As shown in Figure 3-6, the frequency at which the bistable encounters the different bending mode orders was consistently higher than those of the linear harvester. This is due to higher stiffness of the bistable cantilever since the bistable harvester had an extra two layers in the clamping region and the asymmetric nature of the bistable layup leads to a curvature of the

cantilever about the longitudinal axis, further increasing the bending stiffness.

3.4 Investigation of Harvested Power with Frequency

To demonstrate the differences between high and low excitation for both of the harvesters, sweeps from 15 Hz to 200 Hz were carried out at 1g and 6g acceleration for both the linear and bistable energy harvester, as shown in figure 3-7a, b. To highlight in detail the regions of maximal power output, near the natural frequencies, more detailed frequency sweeps with an increment of 0.2 Hz were undertaken as shown in Figures 3-7 c-f for the linear and bistable system at 1g, 2g, 4g and 6g. The lower bound of frequencies when performing sweeps such as these was 15 Hz due to the electric current limitations of amplifier powering the shaker system. This limits the investigation for the power harvesting characteristics of the linear first mode which is at 9 Hz. The power characterization investigations are therefore focused on the second and third modes of the linear harvester.

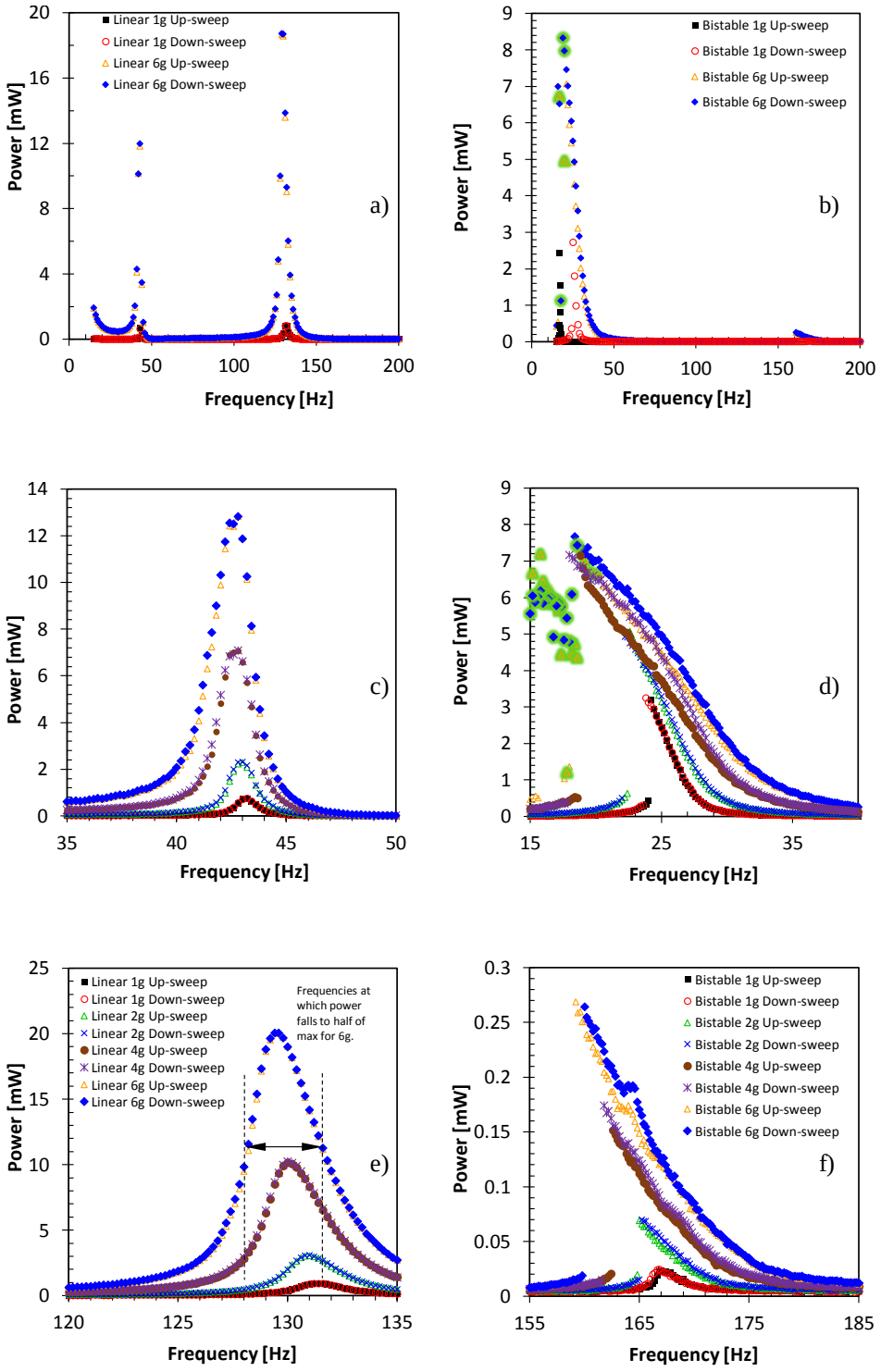

Figure 3-7: Power versus frequency for 1g, 2g, 4g and 6g for linear beam: a) frequency range 15–200 Hz; c) detailed view of 2nd mode; and e) detailed view of 3rd mode, power versus frequency and 1g, 2g, 4g and 6g for bistable beam: b) frequency range 15–200 Hz; d) detailed view of 1st mode; and f) detailed view of 2nd mode

3.4.1 Nonlinear Features in Frequency Response

Measurements were undertaken by both increasing frequency ('up-sweep') and decreasing frequency ('down-sweep') to further characterize any nonlinear behavior. Upon changing to each frequency, 0.2s was allowed for the harvester to attain a steady-state response before the velocity data was recorded for 4.8 seconds. From the set of data at each frequency, the peak velocity value and a root mean squared (RMS) voltage were measured. The harvesting power for a specific frequency and g-level was calculated using Equation 3.1.

$$P_{\mathrm{RMS}} = \frac{V_{RMS}^2}{R_L} \tag{3.1}$$

It can be seen that for the linear harvester, there is a small decrease in the natural frequency of less than 2 Hz for the 2$^{\mathrm{nd}}$ and 3$^{\mathrm{rd}}$ bending modes when the excitation is gradually increased from 1g to 6g (see figures 3-7c and 3-7e). The small decrease in natural frequency with increasing excitation is likely due to some softening (nonlinearities) inherent to the CFRP material [170, 171].

For the bistable beam, there is a difference in power output between the upward and downward frequency sweeps at higher g-level (see Figure 3-7b,d,f). This is particularly apparent for the 1$^{\mathrm{st}}$ bending mode at 6g in Figure 3-7d, where the curve becomes asymmetric and leans towards lower frequencies ('horning') due to softening at higher excitation levels and is a characteristic of nonlinear systems [172]. Snap-through events are shown in Figure 3-7b, and 3-7d by highlighted data points.

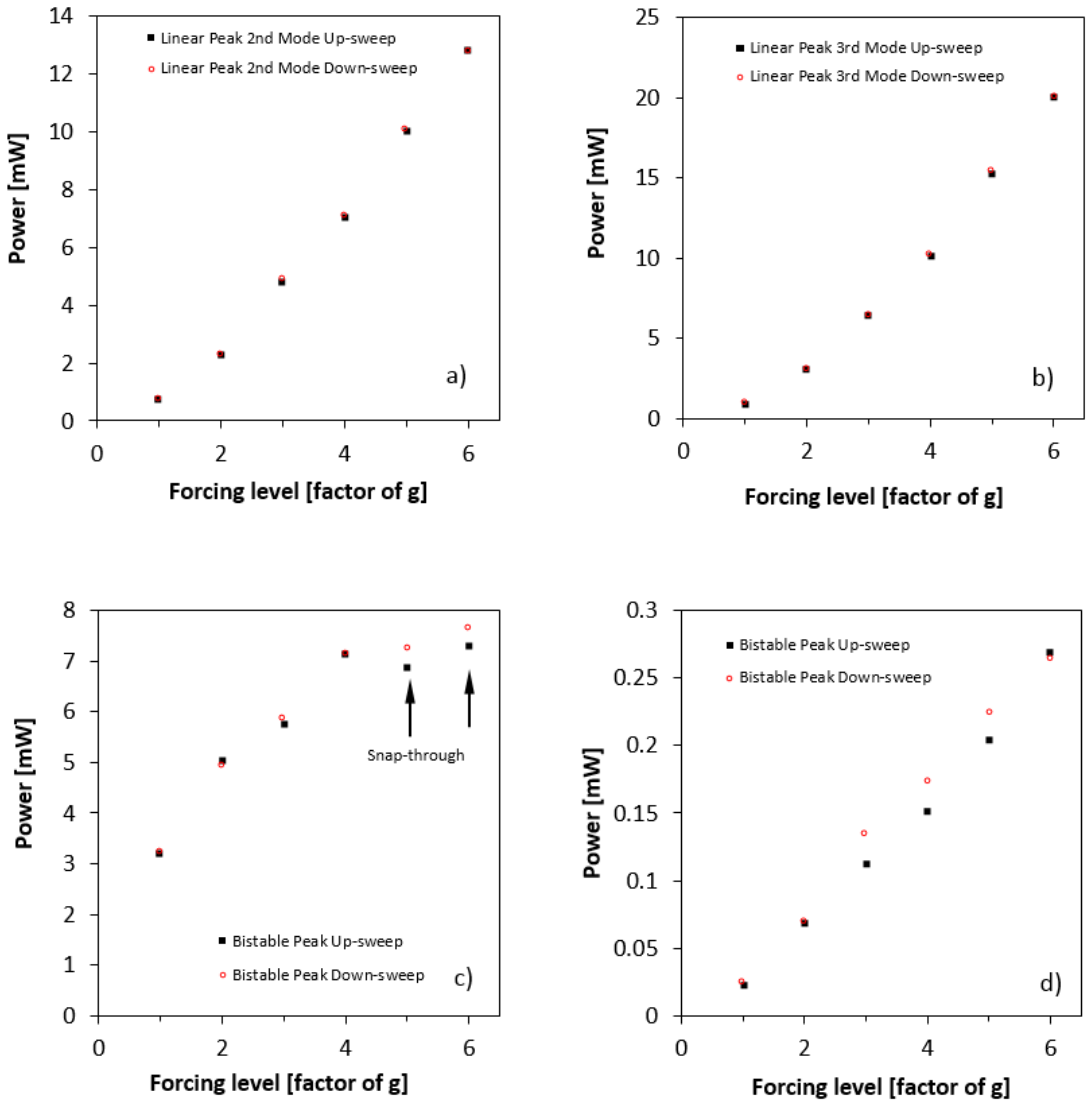

Figure 3-8: Maximum power output at modes over a range of input acceleration for linear beam: a) second mode; and b) third mode. Maximum power output at modes over a range of input acceleration for bistable beam: c) first mode; and d) second mode

Figures 3-8a and 3-8b show the increase of peak power for the 2nd and 3rd modes of the linear harvesting beam respectively. The relationship between peak power and excitation level is approximately linear. A small degree of nonlinear behavior in the power versus excitation level is observed; this may be due to the fact that both CFRP and PZT exhibits a small degree of nonlinear behavior [170, 171, 173]. Based on a linear relationship of peak power against the excitation level for the data in Figures 3-8a and b, the R^2 is 0.992 and 0.981 for the second and third bending modes respectively. Here R^2 refers to the goodness of the fit that a polynomial of a given order has with the data it aims to describe. A value of 1 indicates that the polynomial is able to touch all the points in the dataset, and is therefore a perfect fit, whereas a low value

of R^2 indicates that it the polynomial's curve never passes close to any of the datapoints. A quadratic relationship leads to R^2 values of 0.999 for both cases. Thus, the power increase over the range is slightly greater than expected by a linear approximation and any softening of the harvester leads to higher strain in the MFC, resulting in higher power output.

Figures 3-8c 3-8d show the increase of peak power for the 1st and 2nd modes of the bistable harvester respectively at increasing excitation (g-level). The relationship between the excitation level, the degree of softening and the hysteretic behaviour of the power output of the harvester is more complex than the linear system. With reference to the first bending mode, at 1g the 'up-sweep' and 'down-sweep' power levels are almost coincident since at low excitation levels the bistable harvester exhibits almost linear behavior. At increasing excitation level the structure exhibits nonlinear behaviour ('softening'), as seen in Figure 3-7d. In this case there is an area of instability underneath the 'overhang' in Figure 3-7b) where limited power data are recorded. The is due to the fact that on the up-sweep, the state of the system tends to stay on the lower fold until sufficient energy is achieved for the system to switch to the upper fold. During the down-sweep the system tends to stay on the higher of the two-folds and stays at a higher state of excitation for a greater duration until energy dissipation causes a jump down to the lower fold. The increase of the degree of softening at higher excitation explains why the peak power outputs diverge for both the up-sweep and down-sweep.

3.4.2 Bandwidth Analysis

In practical applications the frequency of the excitation can change significantly with respect to time, implying that a meaningful comparison requires more than just a comparison of peak power outputs and that the broadness of the power generation capability must be quantified. The frequencies on either side of the maximum at which the power output level reduces to half the maximum value, Full Width Half Maximum (FWHM) is often used to evaluate the broadband nature of harvesters [152, 174]. An example is illustrated in Figure 3-7e.

Table 3.2 summarizes the peak power and bandwidth for the different modes at excitation levels of 1g and 6g. It shows that at an excitation level of 1g, the bistable harvester in Mode 1 generates higher power, at greater band-width than the linear harvester. While the power of Mode 2 of the bistable is small, it is a relatively broad response; also shown in Figure 3-7e. At a 6g excitation level, the peak power for the Mode 2 and Mode 3 of the linear harvester is highest and exceeds the power for the Mode 1 and Mode 2 of the bistable harvester, but only over a narrow frequency range [see FWHM bandwidth in Table 3.2 and Figure 3-7a]. As the excitation level increases the FWHM increases and at a 6g excitation, Mode 1 of the bistable produces the widest FWHM (see Table 3.2 and figure 3-7b indicating the potential of bistable systems for increasing the broadness of the response.

Table 3.2: Figures of Merit for the Modal Orders and Harvester Types

	Linear		Bistable		g-level
	Mode 2	Mode 3	Mode 1	Mode 2	
Peak Power [mW]	0.738	0.930	3.19	0.023	1
FWHM [Hz]	1.1	2.7	1.9	3.3	
Peak Power [mW]	2.29	3.04	5.06	0.069	2
FWHM [Hz]	1.4	3.0	3.3	3.5	
Peak Power [mW]	7.07	10.15	7.14	0.15	4
FWHM [Hz]	1.8	3.4	6.6	5.1	
Peak Power [mW]	12.83	20.07	7.3	0.268	6
FWHM [Hz]	2.1	3.8	8.4	6.6	

3.5 Investigation of Harvested Power Sensitivity to Operating Parameters

As shown in the previous section, the bistable energy harvester's mode 1 is able to respond with half the peak power over a frequency band four times wider than the linear counterpart's mode 2 at 6g. In order to understand how the harvested energy changes with respect to changes of operating parameters such as the presence of an added mass, different physical orientation, or different electrical resistances, experiments are undertaken to observe changes of power.

3.5.1 Investigation of Harvested Power and Mass Addition

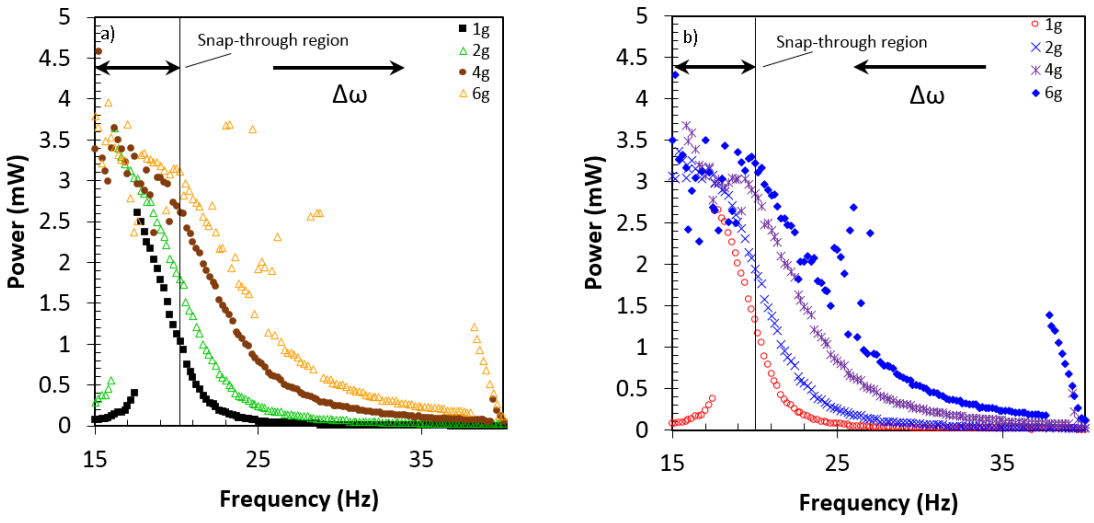

Figure 3-9: a) Upsweeping power tests and b) downsweeping power tests at 1, 2, 4, and 6g

In the case of a linear system, the addition of mass to the end of a cantilever system has the effect of decreasing the natural frequency. For the case of a bistable nonlinear system, the effects of adding mass are more complex. While the natural frequency does decrease, the added mass increases the available inertia for the excitation to push against, thus changing the excitation conditions required for snap-through.

A 4.1 gram mass of vacuum bag sealing putty was affixed 20 mm from the free end of the cantilever. It was subjected to the accelerations and frequencies shown on figure 3-9a and 3-9b. As highlighted in figure 3-8c, when no mass is present, snap-through occurs at 5g. The addition of mass allows the snap-through acceleration to be decreased to 4g. The natural frequency is depressed as expected. The full frequency response of the system could not be experimentally observed in completeness as at the higher forcing levels, snap-through occurred at the lowest frequency attainable by the rig. It is seen that the amount and location of small end masses is able to significantly change the dynamic characteristics of the bistable system. While the power developed at the different acceleration levels is lower here than those of figure 3-7, the ability to control the conditions required for snap-through is advantageous. If snap-through can be attained at lower excitation levels, then this allows the designer to utilize a trade-off between peak power and broad-band power output. Another route for tailoring the excitation level for snap-through is given in Chapter 6 by adding magnets in repulsion.

3.5.2 Investigation of Harvested Power and Operation Orientation

Having established that the addition of a small mass is sufficient to significantly alter the dynamic characteristics of the system, the orientation of the harvester was rotated 90° to the horizontal orientation according to the convention in figure 3-10a and 3-10b to see if gravitational effects were significant.

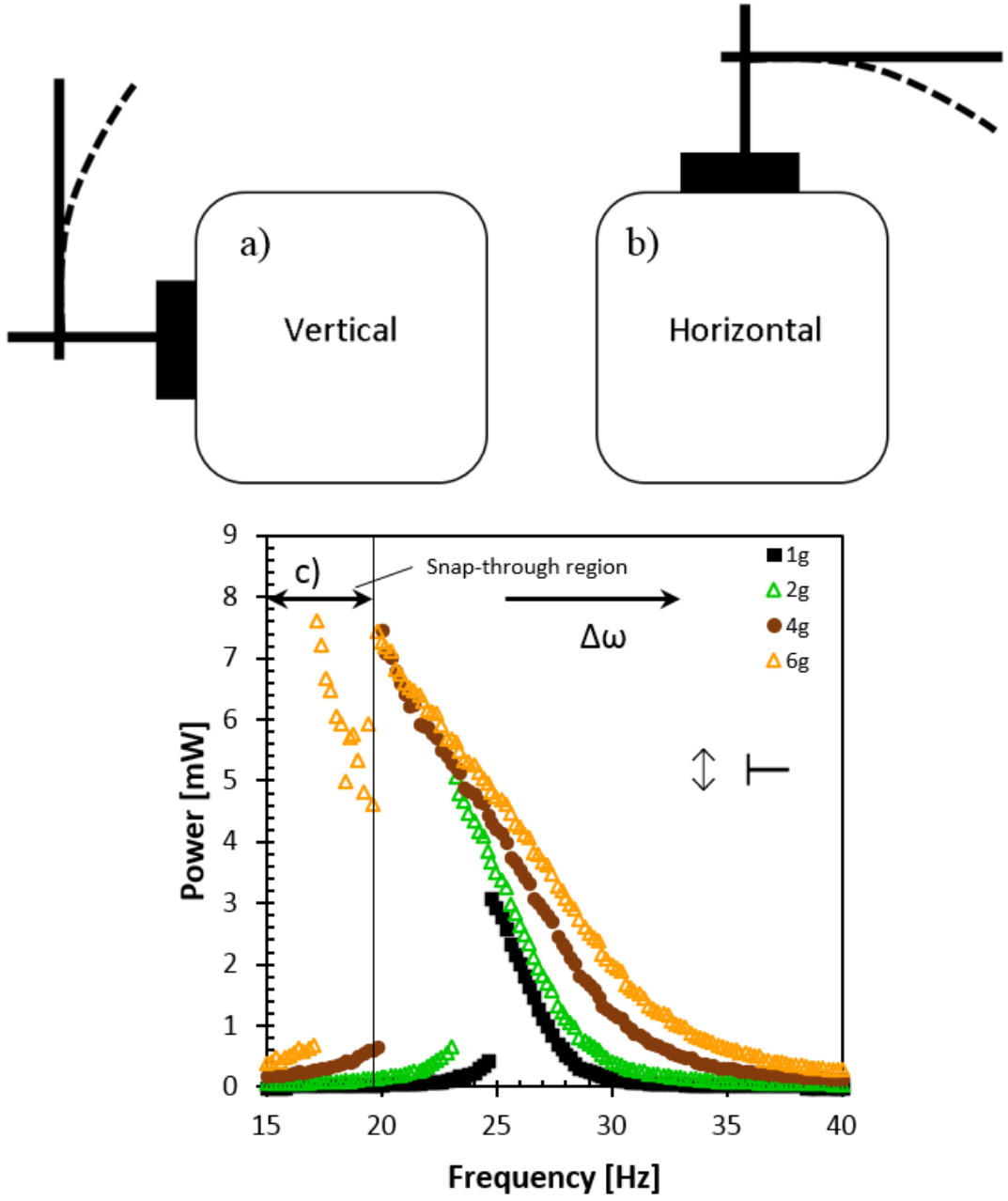

Figure 3-10: a) vertical vs b) horizontal naming convention; c) Power output of horizontally oriented cantilever

The laminate was subjected to the indicated accelerations and frequencies in figure 3-10c. Comparing this figure against figure 3-7d which was tested in the vertical orientation shows that the power and natural frequencies are not significantly changed. The acceleration required for snap-through is also unchanged at 6g, and the frequency band over which snap-through is observed is approximately the same as well. Thus, despite the sensitivity of the dynamic

characteristics to the presence of a small proof mass, the harvester's power output appears unchanged by changes of physical orientation from 0° to 90°.

3.5.3 Investigation of Harvested Power and Load Resistance

As mentioned in section 3.3, the load resistance is selected based on the natural frequency of the device, and the piezoelectric patch's capacitance. Also previously discussed in section 3.4, one of the nonlinear features observed in the bistable harvester is nonlinear softening, which results in lower natural frequencies at higher excitation levels. To experimentally investigate the dependence of the bistable harvester's power output upon the electrical boundary condition, several tests are undertaken. First, as a basic verification, the bistable harvester is driven at its natural frequency at 1g where the response is nearly linear, and a range of resistances are tested. The same is done at 6g where softening is significant. To illustrate the point in finer detail, the bistable harvester is then driven through a range of frequencies at different resistance values again at 1g and 6g. The harvester is then rotated from operating in a vertical orientation to a horizontal orientation. Figure 3-11a shows the peak power attained at 1g at the resistances indicated. As expected, the peak power is observed at approximately the value predicted. Figure 3-11b shows the same for 6g with snap through. The value resistance value giving peak power is slightly lower than that of figure 3-11a but the difference of power level resulting from 36 kΩ vs 40 kΩ is very slight despite being at extreme ends of the operation scope.

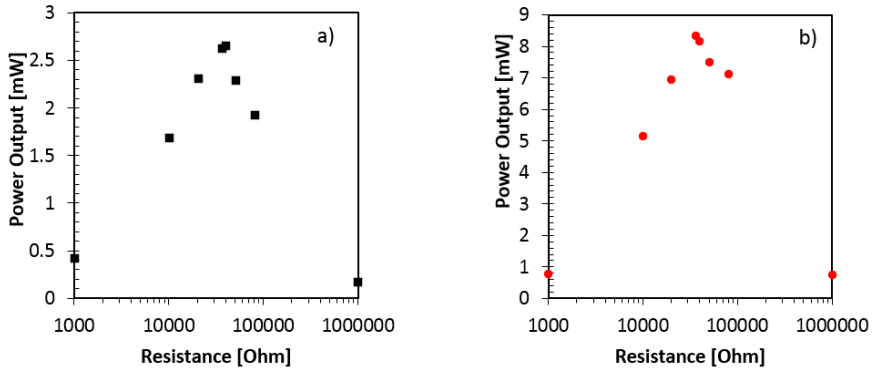

Figure 3-11: a) peak power at 1g for vertical harvester b) peak power at 6g for vertical harvester

To add further detail to the discussion, full frequency sweeps are carried out at the resistances and forcing levels. To further illustrate the points made in section 3.4, vertical and horizontal orientations are tested. As shown, whether operating in the horizontal or vertical position, the 30-40 kΩ range of load resistances yields the highest power outputs. In figures 3-12 a)-h) the 1kΩ resistor appears to be shifted higher than the other resistances, but this an artifact due to how the voltages are post-processed. While the findings here suggest that a slightly reduced load resistance is advantageous at higher forcing levels, the small increase in power in figure 3-11 suggests that the added complexity of a form of resistance tuning mecha-

nism would likely not lead to significant increase of power. In this case the AC power has been characterized by dissipating the piezoelectric charge generated through a load resistor; however in real applications there is often a need to provide DC power, e.g. to charge a battery or operate a microelectronic device. As a result, a typical energy harvesting system may consist of the piezoelectric transducer, AC-DC conversion, a DC-DC converter, and a battery charging and power management module [175]. This need for power conditioning can lead to additional losses; for example Lefeuvre et al. determined overall efficiencies of 71–79% that included the rectifier losses, buck-boost converter losses and control consumption [176] while experiments by Kong et al. [177] indicated 58–72% of the available power could be harvested around the fundamental resonance of the harvester.

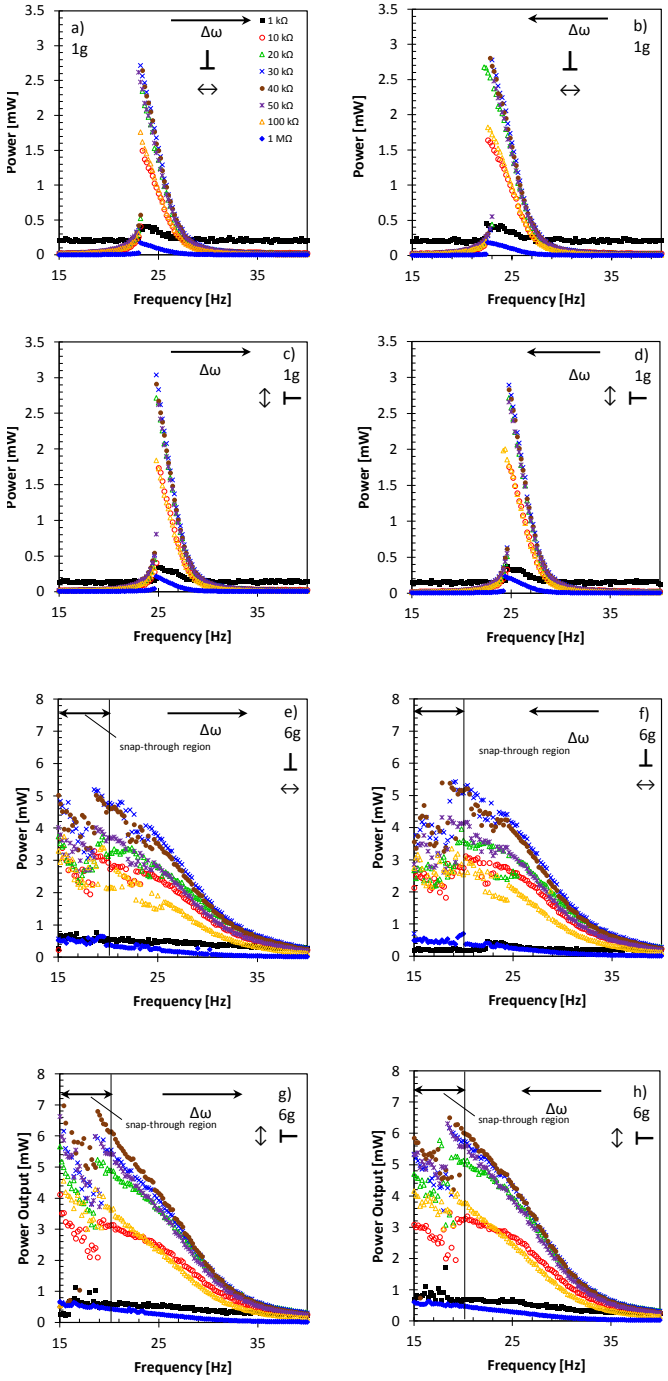

Figure 3-12: Vibration harvester at a) 1 g excitation with various resistances sweeping upwards and b) downwards through a range of frequencies in the vertical orientation and c) horizontal sweeping up and d) horizontal and sweeping down through the same range of resistances and frequencies e) at 6 g excitation with various resistances sweeping upwards and f) downwards through a range of frequencies in the vertical orientation and g) in the horizontal orientation with increasing frequency and h) with decreasing frequency

3.6 Conclusion

This chapter set out to address three objectives. The first was to compare the performance of a bistable laminate energy harvester against a linear energy harvester to establish whether or not bistability was advantageous. The finding of this investigation was that the linear harvester developed twice as much peak power, but over a quarter of the frequency bandwidth when compared against the bistable energy harvester. The main benefit sought in using bistable energy harvesters is the ability to harvest energy over a broad range of frequencies. The second objective was to investigate the efficacy of the three design parameters: changing the load resistance at different operating conditions, the operation orientation and the addition of a small proof mass. The highest power output was observed when the impedance matching criterion was met. It was also seen that despite changes of the natural frequency depending on forcing level as well as the different oscillatory modes, a fixed resistance value was found to be sufficient. It is surmised that an active load resistance adjustment device would not yield substantial power gains. The operational orientation of the harvester from a vertical to horizontal state did not appear to have significant impact on the power produced, implying that the self weight of the harvester is not a major contributor to the dynamics at this scale. The addition of a small proof mass changed both the natural frequency and snap-through acceleration by 1g. The power-frequency data suggested that while snap-through occurred at lower g allowing for some broadening, the peak power output seemed to decrease. The third objective was to establish a sense of typical orders of magnitude of different quantities such as device dimensions, power outputs, natural frequencies and accelerations required to trigger snap-through which are likely to be encountered throughout this work. As shown, natural frequencies in the region of 15 Hz and upwards are expected, power outputs are anticipated on the order of milliwatts, and snap-through is expected at about 5g.

While it is unlikely for the peak power output of a linear harvester to be exceeded by a bistable energy harvester, nonetheless the logical way forward is to increase the bistable's power output and to extend the bandwidth of the device. One possible avenue for increasing the power output is to use a larger piezoelectric transducer. Because the strain field of the cantilever beam is such that the strain is maximized at the clamp and decreases from there, using a longer MFC patch would result in minimal power gain. Due to the high aspect ratio of the cantilever, a small change of width would result in a large change of length, implying a large device, if the relative dimensions are to be kept constant. Bistable laminates in plate form have also been used for energy harvesting from vibrations. These harvesters tend to be square, and as such are more easily scalable in terms of device size to accommodate larger MFC patches. The next chapter investigates the benefits of changing the shape of bistable plate-type harvesters by removing material.

This major findings of this chapter can be summarized:

- The bistable energy harvester's peak power is nearly half that of the linear system at the same forcing levels, but the frequency band of operation is broader. At 6g, the power of the bistable is 7.3 mW against the linear harvester's 12.8 mW, but the bandwidth is four

times as great at 8.4 Hz vs 2.1 Hz.

- The operation orientation was not very effective in changing the behavioral dynamics implying the self weight of the harvester at this scale to be a small factor
- The peak power output is shown to be maximized around resistance values where the load impedance is matched to the piezoelectric transducer's capacitance
- Despite changes of natural frequency due to nonlinear softening, it is not to an extent where active tuning of the load resistance would realize substantial gains
- The addition of a 4.1g mass altered the response of the harvester in that the acceleration reduced from 5g to 4g at a lowered natural frequency.

Chapter 4

Arbitrarily Shaped Bistable Laminate Energy Harvesters

The previous chapter demonstrated that a bistable energy harvester is capable of responding over a wider frequency range than its linear counterpart, but also that it does so at a cost of peak power output. Here, plates are considered because they are able to utilize more surface coverage by a piezoelectric patch. While bistable plates have been researched by others, this chapter seeks to address two novel points. The first objective is to establish the efficacy of changing the planiform shape of a bistable plate-type centrally-supported harvester and to investigate the relationship between these changes of planiform shape and the power output. Three different geometries are analyzed: a cross (+), or cruciform shape, a saltire or x shape, and a square shape. They are all made from the same substrate material, with the same piezoelectric transducers, and the cruciform and saltire both have 20% material removed. These two laminates are compared against the harvesting capability of a square which serves as the control case in this scenario. Secondly, an analytical model is presented. The model is used to predict the nonlinear features and power outputs resulting from the bistable laminate energy harvester's response at different frequencies and accelerations. The chapter is structured with the model's derivation first because this model is used to predict the static shapes and power outputs of the laminates. This is followed by experimental results and validation. Some experimental data is then analyzed in detail.

4.1 Introduction

Modeling of bistable laminates both with and without piezoelectric transduction has been undertaken to understand their dynamical response to excitation. The main feature of bistable laminates which makes modeling non-trivial is the snap-through transition. From the literature, the modeling efforts began with the static shapes, progress to single-well dynamics, and then were expanded to cross-well oscillation.

Static modeling of the stable shapes of bistable laminates is well established [118], in which the curved shapes of asymmetric laminates due to the high temperatures experienced during manufacturing (curing process) are modeled based on a nonlinear extension to classical laminated plate theory. The mid-plane strains and out-of-plane displacement profile are assumed to conform to second order polynomials. The process of identifying the stable static shapes is performed by finding the values of the coefficients of these assumed shapes by minimization of the total potential energy of the system. This modeling approach has been validated experimentally and using finite element analysis [118, 130, 178].

The approach to modeling the single-well case used by Vogl [179] was to first assume a static curvature, a_0. As the laminate vibrated in response to excitation of frequency ω, it was assumed that this curvature would vary sinusoidally between some bounds in the time domain leading to the expression $a(t) = a_0 + a_1 \sin(\omega t)$. This limited the response of the bistable to the linear regime–that is the frequency of the response of the laminate will only be equal to that of the excitation. Arrieta et. al extended this work by including nonlinear stiffness based on experimental measurements made by tracking the motion of a point on an oscillating bistable laminate [140]. They also developed a model analyzing single well dynamics by using all non-zero combinations of sinusoidal functions to approximate the laminate curvatures rather than considering a single point's displacement [137]. In order to implement the model, several parameters are required to be found experimentally.

Diaconu et. al presented an analytical model of a bistable laminate with no piezoelectric element undergoing a single snap-through event [141]. This model added inertia and damping to the classic Rayleigh-Ritz [180] strain energy minimization formulation by applying Hamilton's principle [181]. Snap-through was induced by exerting point forces at the corners of the laminate and then integrating forward through time. Arrieta et. al continued by including snap-through in a model by using a piecewise representation of the restoring force [138]. A jump discontinuity was implemented to approximate snap-through. They then presented an experimental study on the excitation parameters under which snap-through occurs and found that the excitation amplitude required was minimized around the natural frequencies [182]. This analysis was used for both actuation [183] and energy harvesters [184]. The resulting model assumed the cured shape of the laminates were parabolic in shape, like Dano and Hyer [118]. This model was able to predict the frequencies at which the amplitude of excitation required for snap-through was minimized, but did not predict the excitation levels required to trigger snap-through.

For the purpose of designing a bistable laminate energy harvester, the ideal model would receive as its inputs the properties of the materials composing the laminate, electrical boundary condition, the device's dimensions and shape, and the excitation pattern. The output would be the electrical power output in the time domain. This way, the behavior of a laminate could be predicted without having to build it. The model presented in the following section attempts to fulfill these requirements. This is the same model presented by Tavakkoli et. al in [150]. The only empirical information required is the damping ratio of the device.

4.2 Analytical Model

4.2.1 Constitutive Equations for Piezoelectric Layer

The following modeling work was done in collaboration with Dr. Seyed Mehdi Tavakkoli at the University of Bath. In general, constitutive equations for piezoelectric materials are divided into the converse and direct effects and may be expressed as,

$$\boldsymbol{\sigma} = \mathbf{C}\boldsymbol{\varepsilon} - \mathbf{e}\mathbf{E} \tag{4.1}$$

$$\mathbf{D} = \mathbf{e}\boldsymbol{\varepsilon} + \boldsymbol{\eta}\mathbf{E} \tag{4.2}$$

respectively, where $\boldsymbol{\sigma}$ and $\boldsymbol{\varepsilon}$ are stress and strain fields, respectively, $\mathbf{C}$ is the elasticity matrix, $\mathbf{e}$ is the electromechanical coupling coefficients matrix, $\mathbf{E}$ is the electrical field vector, $\mathbf{D}$ is the electrical displacement vector and $\boldsymbol{\eta}$ is the permittivity matrix. In this work, the piezoelectric plate is assumed to be polarized in the thickness direction $e_{36} = 0$ and the electrical and displacement fields are uniform across the thickness and aligned in the direction normal to the mid-plane $D_1 = D_2 = 0$. In addition, by assuming $\sigma_{33} = 0$ for plate structures and using the Kirchhoff plate theory [185], the constitutive relation can be summarized and expanded as follows,

$$\begin{bmatrix} \sigma_{11} \\ \sigma_{22} \\ \sigma_{12} \\ D_3 \end{bmatrix} = \begin{bmatrix} C_{11} & C_{12} & C_{16} & e_{31} \\ C_{21} & C_{22} & C_{26} & e_{32} \\ C_{61} & C_{62} & C_{66} & 0 \\ e_{31} & e_{32} & 0 & -\eta_{33} \end{bmatrix} \begin{bmatrix} \varepsilon_{11} \\ \varepsilon_{22} \\ \varepsilon_{12} \\ -E_3 \end{bmatrix} \tag{4.3}$$

Since the Kirchhoff theory is used, shear forces perpendicular to the mid plane are assumed to be negligible. Axial forces $\mathbf{N}$ and bending moments $\mathbf{M}$ are defined by the expressions,

$$\mathbf{N} = \langle N_{11} N_{22} N_{12} \rangle^T = \int_{t_1^p}^{t_2^p} \boldsymbol{\sigma}^0 dz \tag{4.4}$$

$$\mathbf{M} = \langle M_{11} M_{22} M_{12} \rangle^T = \int_{t_1^p}^{t_2^p} z\boldsymbol{\sigma} dz \tag{4.5}$$

where $t_2^p - t_1^p$ is the thickness of the piezoelectric layer, z is the axis along the thickness and $\boldsymbol{\sigma}^0$ and $\boldsymbol{\sigma}$ are the membrane and bending parts of section stress defined as,

$$\begin{cases} \boldsymbol{\sigma}^0 &= \mathbf{C}\boldsymbol{\varepsilon}^0 \\ \boldsymbol{\sigma} &= z\mathbf{C}\boldsymbol{\kappa} \end{cases} \tag{4.6}$$

where $\boldsymbol{\varepsilon}^0$ and $\boldsymbol{\kappa}$ are the in-plane strains and curvatures, respectively. By substituting equation 4.3 into equations 4.4 and 4.5, the converse piezoelectric effect equation for a cross-ply laminate in a general and compact form may be expressed as,

$$\begin{bmatrix} \mathbf{N} \\ \mathbf{M} \end{bmatrix} = \begin{bmatrix} \mathbf{A} & \mathbf{B} \\ \mathbf{B} & \mathbf{D} \end{bmatrix} \begin{bmatrix} \boldsymbol{\varepsilon}^0 \\ \boldsymbol{\kappa} \end{bmatrix} - (t_2^p - t_1^p) \begin{bmatrix} \mathbf{I}_3 \\ \frac{(t_2^p + t_1^p)}{2} \mathbf{I}_3 \end{bmatrix} \begin{bmatrix} e_{31} \\ e_{32} \\ 0 \end{bmatrix} \mathbf{E}_3 \tag{4.7}$$

where $\mathbf{A}$, $\mathbf{B}$ and $\mathbf{D}$ are the membrane (extensional), bending and coupling stiffness matrices, respectively, and $\mathbf{I}_3$ is the identity matrix. By integrating from both sides of the sensing equation over the thickness the following is obtained,

$$(t_2^p - t_1^p) D_3 = [e_{31} e_{32} 0](t_2^p - t_1^p) \left[\mathbf{I}_3 \tfrac{t_2^p + t_1^p}{2} \mathbf{I}_3 \right] \begin{bmatrix} \boldsymbol{\varepsilon}^0 \\ \boldsymbol{\kappa} \end{bmatrix} + \eta_{33} E_3 (t_2^p - t_1^p) \tag{4.8}$$

where the thickness can be cancelled from both sides and finally, the constitutive equations 4.1 and 4.2 are rewritten in a compact form for piezoelectric plate structures as follows,

$$\begin{cases} \bar{\mathbf{N}}^p = & \mathbf{Q}^p \bar{\boldsymbol{\varepsilon}} - t^p \mathbf{e}' E_3 \\ D_3 = & \mathbf{e}'^T \bar{\boldsymbol{\varepsilon}} + \eta_{33} E_3 \end{cases} \tag{4.9}$$

where,

$$\bar{\mathbf{N}}^p = \begin{bmatrix} \mathbf{N}^p \\ \mathbf{M}^p \end{bmatrix}, \bar{\boldsymbol{\varepsilon}} = \begin{bmatrix} \boldsymbol{\varepsilon}^0 \\ \boldsymbol{\kappa} \end{bmatrix}, \mathbf{Q}^p = \begin{bmatrix} \mathbf{A}^p & \mathbf{B}^p \\ \mathbf{B}^p & \mathbf{D}^p \end{bmatrix}, \mathbf{e}' = \begin{bmatrix} \mathbf{I}_3 \\ \frac{\bar{t}}{2} \mathbf{I}_3 \end{bmatrix} \begin{bmatrix} e_{31} \\ e_{32} \\ 0 \end{bmatrix}, \bar{t} = t_1^p + t_2^p, t^p = t_2^p - t_1^p \tag{4.10}$$

In geometrically nonlinear problems, it is convenient to separate the linear and nonlinear parts of strain field,

$$\bar{\boldsymbol{\varepsilon}} = \bar{\boldsymbol{\varepsilon}}^L + \bar{\boldsymbol{\varepsilon}}^{NL} \tag{4.11}$$

Therefore, the constitutive equations for geometrically nonlinear piezoelectric plates in equations 4.12 and 4.13 can be expressed in terms of linear and nonlinear strains as follows,

$$\bar{\mathbf{N}}^p = \mathbf{Q}^p \bar{\boldsymbol{\varepsilon}}^L + \mathbf{Q}^p \bar{\boldsymbol{\varepsilon}}^{NL} - t^p \mathbf{e}' E_3 \tag{4.12}$$

$$D_3 = \mathbf{e}'^T \bar{\boldsymbol{\varepsilon}}^L + \mathbf{e}'^T \bar{\boldsymbol{\varepsilon}}^{NL} + \eta_{33} E_3 \tag{4.13}$$

Similarly the constitutive equation for bistable laminates may be expressed as follows,

$$\bar{\mathbf{N}}^s = \mathbf{Q}^s \bar{\boldsymbol{\varepsilon}} \tag{4.14}$$

where superscript s stands for substructure. In addition, in order to examine the linear and

nonlinear parts of the relation separately, using equation 4.11 the following can be written,

$$\bar{\mathbf{N}}^s = \mathbf{Q}^s \bar{\boldsymbol{\varepsilon}}^L + \mathbf{Q}^s \bar{\boldsymbol{\varepsilon}}^{NL} \tag{4.15}$$

4.2.2 Approximating Functions

The in-plane strain field and out-of-plane displacement component (deflection) are approximated based on Hyer's model [118] which can be written in matrix form as,

$$\begin{bmatrix} \varepsilon_x^0 \\ \varepsilon_y^0 \\ \gamma_{xy}^0 \end{bmatrix} \approx \begin{bmatrix} 1 & x^2 & xy & y^2 & 0 & 0 & 0 & 0 & 0 & 0 & 0 \\ 0 & 0 & 0 & 0 & 1 & x^2 & xy & y^2 & 0 & 0 & 0 \\ 0 & 0 & \frac{x^2}{2} & 2xy & 0 & 2xy & \frac{y^2}{2} & 0 & 2 & x^2 & y^2 \end{bmatrix} \begin{bmatrix} d_1 \\ d_2 \\ \dots \\ d_{11} \end{bmatrix} + \begin{bmatrix} 0 \\ 0 \\ f \end{bmatrix} = \bar{\boldsymbol{\phi}}\boldsymbol{d} + \mathbf{f} \approx \boldsymbol{\varepsilon}^{0^L} + \boldsymbol{\varepsilon}^{0^{NL}} \tag{4.16}$$

$$f(x,y) = (ab - \frac{1}{2}c^2)xy + \frac{1}{4}acx^2 + \frac{1}{4}bcy^2 \tag{4.17}$$

$$w(x,y) \approx \frac{1}{2}(ax^2 + by^2 + cxy) \tag{4.18}$$

where $d_1, \dots, d_{11}$ are in-plane strain coefficients of the plate and a, b and c are curvature coefficients. Also, $\boldsymbol{\phi}$ and $\mathbf{f}$ are the linear and nonlinear parts of the approximation functions in Hyer's model, respectively. Using the in-plane strain field approximation in equation 4.16, $\bar{\boldsymbol{\varepsilon}}^L$ and $\bar{\boldsymbol{\varepsilon}}^{NL}$ from equation 4.11 may be expressed in terms of elongation coefficients $\mathbf{d}$ and curvature coefficients $\mathbf{a}$ in a matrix form as follows,

$$\bar{\boldsymbol{\varepsilon}}^L = \begin{bmatrix} \boldsymbol{\varepsilon}^{0^L} \\ \boldsymbol{\kappa} \end{bmatrix} \approx \begin{bmatrix} \bar{\boldsymbol{\phi}} & 0 \\ 0 & -\mathbf{I}_3 \end{bmatrix} \begin{bmatrix} \mathbf{d} \\ \mathbf{a} \end{bmatrix} = \boldsymbol{\Phi}\mathbf{X} \tag{4.19}$$

$$\bar{\boldsymbol{\varepsilon}}^{NL} = \begin{bmatrix} \boldsymbol{\varepsilon}^{0^{NL}} \\ \mathbf{0} \end{bmatrix} \approx \begin{bmatrix} 0 & 0 & f & 0 & 0 \end{bmatrix}^T = \begin{bmatrix} \mathbf{f} \\ \mathbf{0} \end{bmatrix} \tag{4.20}$$

where $\mathbf{X}$ is the in-plane deformations and curvatures vector. The linear and nonlinear strains can be used for approximating internal forces in both the piezoelectric layer and bistable structure.

4.2.3 Dynamic Governing Equations

To satisfy a dynamic equilibrium of the system based on a bistable laminate with bonded piezoelectric elements, the potential energy of the structure under dynamic conditions is minimized according to Hamilton's principle as follows, where T is the kinetic energy, U is the strain energy, W_{ie} is the piezoelectric internal electrical energy and W_{nc} is the non-conservative work of the system. Each energy term in equation 4.21 is derived for a nonlinear piezoelectric composite plate in the following sections.

$$\delta \int_{t_1}^{t_2} (T - U + W_{ie} + W_{nc}) dt = 0 \tag{4.21}$$

Strain Energy of the System, U

The strain energy of the system is calculated by adding the strain energies of the substructure and the piezoelectric layer. The substructure strain energy can be divided into mechanical and thermal strain energies. In the piezoelectric layer the converse piezoelectric component of the constitutive equation comprises two mechanical and electrical parts, therefore the piezoelectric strain energy may be separated into mechanical and electrical strain energies. Therefore, the total strain energy of the system may be written as follows,

$$U = U^s + U^p = U^{m,s} + U^{th,s} + U^{m,p} + U^{e,p} \tag{4.22}$$

where superscripts s, p, m, th, and e stand for substructure, piezoelectric, mechanical, thermal and electrical strain energies, respectively. The substructure and piezoelectric strain energies may be expressed as,

$$U^s = U^{m,s} + U^{th,s} = \frac{1}{2} \int_{A^s} \bar{\mathbf{N}}^{s^T} \bar{\boldsymbol{\varepsilon}} dA^s - \int_{A^s} \bar{\mathbf{N}}^{th^T} \bar{\boldsymbol{\varepsilon}} dA^s \tag{4.23}$$

$$U^p = U^{m,p} + U^{e,p} = \frac{1}{2} \int_{A^p} \bar{\mathbf{N}}^{p^T} \bar{\boldsymbol{\varepsilon}} dA^p \tag{4.24}$$

Substituting $\bar{\mathbf{N}}$ from this constitutive equations of 4.12 and 4.13 obtains,

$$U^s = U^{m,s} + U^{th,s} = \frac{1}{2} \int_{A^s} (\mathbf{Q}^s \bar{\boldsymbol{\varepsilon}}^L + \mathbf{Q}^s \bar{\boldsymbol{\varepsilon}}^{NL} - 2\mathbf{Q}^s \boldsymbol{\alpha} \Delta T)^T (\bar{\boldsymbol{\varepsilon}}^L + \bar{\boldsymbol{\varepsilon}}^{NL}) dA^s \tag{4.25}$$

$$U^p = U^{m,p} + U^{e,p} = \frac{1}{2} \int_{A^s} (\mathbf{Q}^p \bar{\boldsymbol{\varepsilon}}^L + \mathbf{Q}^p \bar{\boldsymbol{\varepsilon}}^{NL} - t^p \mathbf{e}' E_3)^T (\bar{\boldsymbol{\varepsilon}}^L + \bar{\boldsymbol{\varepsilon}}^{NL}) dA^p \tag{4.26}$$

where ΔT is the temperature change and $\boldsymbol{\alpha}$ is the thermal expansion coefficients vector. Since the deformations and voltage are the unknowns in the above strain energy terms, the variation of the strain energy of the system in Hamilton's principle is calculated based on,

$$\partial U = \frac{\partial U}{\partial \mathbf{X}} \delta \mathbf{X} + \frac{\partial U}{\partial v} \delta v \tag{4.27}$$

where $\mathbf{X}$ is the in-plane deformations and curvature coefficients vector and v is the voltage

Piezoelectric Internal Electrical Energy, W_{ie}

The internal electrical energy W_{ie} in the piezoelectric layer may be expressed as

$$W_{ie} = \frac{1}{2} \int_{V^p} \mathbf{E}^T \mathbf{D} dV^p \tag{4.28}$$

where $\mathbf{E}$ is the vector of electric field and is defined as $\mathbf{E} = E_3 = -\frac{v}{t^p}$ Substituting the respective terms from the constitutive relations of 4.12 and 4.13 gives,

$$W_{ie} = \frac{1}{2}\int_{V^p} E_3(\mathbf{e}'^T\bar{\boldsymbol{\varepsilon}}^L + \mathbf{e}'^T\bar{\boldsymbol{\varepsilon}}^{NL} + \eta_{33}E_3)dV^p \tag{4.29}$$

Variation of the internal electrical energy in Hamilton's principle is derived using,

$$\delta W_{ie} = \frac{\partial W_{ie}}{\partial \mathbf{X}}\delta\mathbf{X} + \frac{\partial W_{ie}}{\partial v}\delta v \tag{4.30}$$

Kinetic Energy of the System

The total kinetic energy term in equation 44 can be written as follows,

$$T = \frac{1}{2}\int_{V^s} \rho^s \dot{\mathbf{u}}_a^T\dot{\mathbf{u}}_a dV^s + \frac{1}{2}\int_{V^p} \rho^p \dot{\mathbf{u}}_a^T\dot{\mathbf{u}}_a dV^p \tag{4.31}$$

where ρ^s and ρ^p are the densities of the substructure and the piezoelectric layer, respectively and $\mathbf{u}_a$ is the absolute displacement vector including the base excitation and deformations of the laminate, expressed as follows,

$$\mathbf{u}_a = \begin{bmatrix} u_x^0 - z\frac{\partial w}{\partial x} & u_y^0 - z\frac{\partial w}{\partial y} & w + w_b \end{bmatrix} \tag{4.32}$$

where u_x^0, u_y^0 are in-plane displacements and assumed to be zero, w_b is the base excitation function and w is the deflection of the laminate and approximated as

$$w \approx \frac{1}{2}\left(ax^2 + by^2 + cxy\right) = \begin{bmatrix} \frac{x^2}{2} & \frac{y^2}{2} & \frac{xy}{2} \end{bmatrix}\begin{bmatrix} a \\ b \\ c \end{bmatrix} = \mathbf{g}^T\mathbf{a} \tag{4.33}$$

Substituting equations 4.32 and 4.33 into equation 4.31 and taking variation of the kinetic energy gives,

$$\int_{t1}^{t2} \delta T dt = \int_{t1}^{t2} \left(\ddot{\mathbf{a}}^T\mathbf{M} - \ddot{w}_b\mathbf{M}_b\right)\delta\mathbf{a}dt \tag{4.34}$$

where $\mathbf{M}$ and $\mathbf{M}_b$ are the inertial and base excitation mass matrices, respectively, defined as

$$\mathbf{M} = \int_V \rho\left(z^2(\mathbf{G}_x + \mathbf{G}_y) + \mathbf{G}\right)dV \tag{4.35}$$

$$\mathbf{M}_b = \int_V \rho\mathbf{g}^T dV \tag{4.36}$$

where

$$\mathbf{G}_x = \mathbf{g}_{,x}\otimes\mathbf{g}_{,x}; \mathbf{G}_y = \mathbf{g}_{,y}\otimes\mathbf{g}_{,y}; \mathbf{G} = \mathbf{g}\otimes\mathbf{g} \tag{4.37}$$

and $\mathbf{g}_{,\mathbf{x}}$ indicates $\frac{\partial \mathbf{g}}{\partial \mathbf{x}}$. Applying the superposition principle, the total mass matrices including substructure and piezoelectric mass matrices can be derived,

$$\mathbf{M} = \mathbf{M}^s + \mathbf{M}^p = \int_{V^s} \rho^s \left(z^2(\mathbf{G}_x + \mathbf{G}_y) + \mathbf{G} \right) dV^s + \int_{V^p} \rho^p \left(z^2(\mathbf{G}_x + \mathbf{G}_y) + \mathbf{G} \right) dV^p \quad (4.38)$$

$$\mathbf{M}_b = \mathbf{M}_b^s + \mathbf{M}_b^p = \int_{V^s} \rho^s \mathbf{g}^T dV^s + \int_{V^p} \rho^p \mathbf{g}^T dV^p \quad (4.39)$$

Non-conservative work, W_{nc}

The final term in equation 4.21, the non-conservative work due to electrical charge output is defined as follows

$$\delta W_{nc} = \delta W_{nc}^p = Q(t)\delta v(t) \quad (4.40)$$

Governing Equation

By having all terms of Hamilton's principle, as seen in equation 4.21, as multipliers of virtual inplane deformation and curvature coefficients ($\delta\mathbf{X}$) and virtual voltage (δv) and factorizing $\delta\mathbf{X}$ and δv, their multipliers should be zero in the time interval t_1 to t_2. Consequently, the governing equations of the problem are derived as follows,

$$\begin{bmatrix} \mathbf{0} & \mathbf{0} \\ \mathbf{0} & \mathbf{M} \end{bmatrix} \begin{bmatrix} \ddot{\mathbf{d}} \\ \ddot{\mathbf{a}} \end{bmatrix} + \begin{bmatrix} \mathbf{K}_{11} & \mathbf{K}_{12} \\ \mathbf{K}_{21} & \mathbf{K}_{22} \end{bmatrix} \begin{pmatrix} \mathbf{d} \\ \mathbf{a} \end{pmatrix} + \begin{bmatrix} \boldsymbol{\theta}_d \\ -\boldsymbol{\theta}_a \end{bmatrix} v = \begin{bmatrix} 0 \\ \mathbf{M}_b \ddot{w}_b \end{bmatrix} \quad (4.41)$$

$$-\boldsymbol{\theta}_d \dot{\mathbf{d}} + \boldsymbol{\theta}_a \dot{\mathbf{a}} + C_p \dot{v} + \frac{v}{R} = 0 \quad (4.42)$$

where $\mathbf{d}$ and $\mathbf{a}$ are the in-plane strain coefficients vector and the curvatures, respectively, and,

$$\mathbf{K}_{11} = \int_{A^s} \bar{\boldsymbol{\phi}}^T \mathbf{A}^s \bar{\boldsymbol{\phi}} dA^s + \int_{A^p} \bar{\boldsymbol{\phi}}^T \mathbf{A}^p \bar{\boldsymbol{\phi}} dA^p \quad (4.43)$$

$$\begin{aligned} \mathbf{K}_{12}^T(\mathbf{a}) = &\int_{A^s} -\mathbf{a}^T \mathbf{B}^s \bar{\boldsymbol{\phi}} + \mathbf{f}^T \mathbf{A}^s \bar{\boldsymbol{\phi}} dA^s + \\ &\int_{A^s} -\mathbf{a}^T \mathbf{B}^p \bar{\boldsymbol{\phi}} + \mathbf{f}^T \mathbf{A}^p \bar{\boldsymbol{\phi}} dA^p \end{aligned} \quad (4.44)$$

$$\begin{aligned} \mathbf{K}_{21}^T(\mathbf{a}) = &\int_{A^s} -\bar{\boldsymbol{\phi}}^T \mathbf{B}^s + \bar{\boldsymbol{\phi}}^T \mathbf{A}^s \mathbf{f}_{,\mathbf{a}} dA^s + \\ &\int_{A^p} -\bar{\boldsymbol{\phi}}^T \mathbf{B}^p + \bar{\boldsymbol{\phi}}^T \mathbf{A}^p \mathbf{f}_{,\mathbf{a}} dA^p \end{aligned} \quad (4.45)$$

$$\mathbf{K}_{22}^{T}(\mathbf{a}) = \int_{A^s} \mathbf{a}^T\mathbf{D}^s - \mathbf{f}^T\mathbf{B}^s - \mathbf{a}^T\mathbf{B}^s\mathbf{f}_{,\mathbf{a}}dA^s + \int_{A^p} \mathbf{a}^T\mathbf{D}^p - \mathbf{f}^T\mathbf{B}^p - \mathbf{a}^T\mathbf{B}^p\mathbf{f}_{,\mathbf{a}} + \mathbf{f}^T\mathbf{A}^p\mathbf{f}_{,\mathbf{a}}dA^p - \int_{A^s} \Delta T\bar{\boldsymbol{\alpha}}((\mathbf{A}^s + \mathbf{B}^s)\mathbf{f}_{,\mathbf{a}} - (\mathbf{B}^s + \mathbf{D}^s))dA^s \tag{4.46}$$

$$\boldsymbol{\theta}_d = \int_{A^p} \mathbf{e}^T\bar{\boldsymbol{\phi}}dA^p \tag{4.47}$$

$$\boldsymbol{\theta}_a = \int_{A^p} \mathbf{e}^T\left(\tfrac{\bar{\mathbf{t}}}{2} - \mathbf{f}_{,\mathbf{a}}\right)dA^p \tag{4.48}$$

where $\mathbf{f}_{,\mathbf{a}}$ denotes $\frac{\partial \mathbf{f}}{\partial \mathbf{a}}$. The in-plane strain coefficients $\mathbf{d}$ can be obtained from equation 4.41 in terms of curvatures $\mathbf{a}$. Substituting $\mathbf{d}$ into equation 4.42 gives,

$$\mathbf{M}\ddot{\mathbf{a}} + \mathbf{K}(\mathbf{a}) + \left(\mathbf{k}_{\theta 1}^{T}(\mathbf{a})\boldsymbol{\theta}_d - \boldsymbol{\theta}_a\right)v = \mathbf{M}_b\ddot{w}_b \tag{4.49}$$

$$-\boldsymbol{\theta}_d^T\mathbf{k}_{\theta 2}(\dot{\mathbf{a}}) + \boldsymbol{\theta}_a\dot{\mathbf{a}} + (C^p + C_d)\dot{v} + \frac{v}{R} = 0 \tag{4.50}$$

where,

$$\begin{aligned} \mathbf{K}(\mathbf{a}) &= \mathbf{K}_{22}(\mathbf{a}) - \mathbf{K}_{21}(\mathbf{a})\mathbf{K}_{11}^{-1}\mathbf{K}_{12}(\mathbf{a}) \\ \mathbf{k}_{\theta 1}(\mathbf{a}) &= -\mathbf{K}_{21}(\mathbf{a})\mathbf{K}_{11}^{-1} \\ \mathbf{k}_{\theta 2}(\dot{\mathbf{a}}) &= -\mathbf{K}_{11}^{-1}\mathbf{K}_{12}(\dot{\mathbf{a}}) \\ C_d &= \boldsymbol{\theta}_d^T\mathbf{K}_{11}^{-1}\boldsymbol{\theta}_d \end{aligned} \tag{4.51}$$

where $\mathbf{K}(\mathbf{a})$ is the mechanical tangential stiffness matrix, $\mathbf{k}_{\theta 1}^{T}(\mathbf{a})\boldsymbol{\theta}_d$ and $\boldsymbol{\theta}_a$ are the nonlinear electromechanical vectors related to axial deformations coefficients $\mathbf{d}$ and curvatures $\mathbf{a}$, respectively. In addition, the electromechanical nonlinear term $\boldsymbol{\theta}_d^T\mathbf{k}_{\theta 2}(\dot{\mathbf{a}})$ in the sensing, or piezoelectric "direct effect", equations of 4.49 and 4.50 can be interpreted as the product of coupling coefficients and acceleration in the linear case. It is noted that in Hyer's model $\mathbf{e}^T\mathbf{f}_{,\mathbf{a}} = \mathbf{0}$, therefore, the nonlinear term in $\boldsymbol{\theta}_a$ vanishes and equation 4.47 can be simplified as,

$$\boldsymbol{\theta}_a = \int_{A^p} \frac{\bar{t}}{2}\mathbf{e}^T dA^p \tag{4.52}$$

4.3 Laminates with Arbitrary Shapes

In this section the above model is generalized to consider arbitrary planiforms. To achieve this, a Cartesian design domain is considered and discretized into a number of regular elements, as shown in Figure 4-1. A fine grid therefore provides a close approximation to a shape defined by a smooth boundary. Each element is considered to be represented either by one for solid areas

or zero for voids, which becomes the multiplier for elemental properties. Since every element should satisfy the dynamic equilibrium condition of equation 4.21 in order to have equilibrium of the whole structure, the expressions derived in the previous section can be applied for each element. Therefore, the tangential stiffness and mass matrices in equation 4.41 may be written in the form of,

$$\mathbf{K} = \sigma_{e=1}^{n} \mu_e \mathbf{K}_e; \mathbf{M} = \sigma_{e=1}^{n} \mu_e \mathbf{M}_e \tag{4.53}$$

where μ_e is the binary elemental multiplier, one for solid elements and zero for voids. It is noted that the density of the grid has no discernable effect on computation time as no solving is performed on an element by element basis. Furthermore a single shape function is used and thus no continuity conditions between elements are required.

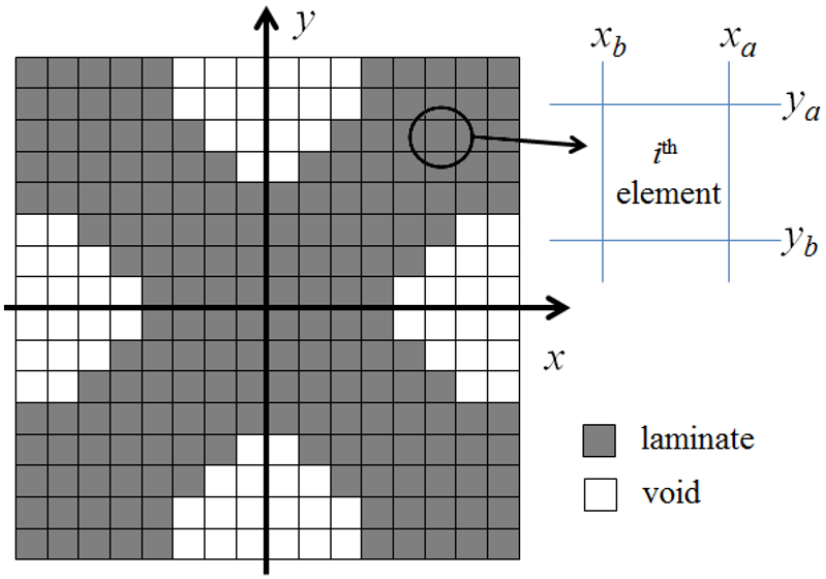

Figure 4-1: Discretization of an example bistable laminate planform [148]

The majority of the research done on vibrational energy harvesting with bistable laminates has been done with variants of the $[0°/90°]_T$ square design. The research on cantilevers in chapter 3 suggests that changes to the mass of the energy harvester can have a significant effect upon its dynamics. Because removing material will change both the mass and the structure's stiffness, the influence upon the dynamics should be significant. Therefore changing the shape of the harvesters is an easy way to tailor the stiffness of the harvester for a given application's vibrational characteristic. The derivation of this model and the ensuing experimental work is intended to be an investigation into a largely unexplored area of the design space which will facilitate further study in this area.

4.4 Experiment Setup

The dynamic response and electrical output of a square, a cruciform and a saltire were investigated using the analytical model and compared with experimental measurements. The square Carbon Fiber Reinforced Polymer (CFRP) laminate has dimensions 200 x 200 x 0.35 mm and a cruciform and a saltire are cut from the square laminate with 20% of the total area removed, shown in Figure 4-2. The laminates are of stacking sequence $[0^{\circ}_{\mathrm{MFC}}/0^{\circ}/90^{\circ}]_{\mathrm{T}}$ and the material properties are defined in Table 4.1. Bonded to the top surface of the laminates is a single Macro Fiber Composite (MFC) piezoelectric element (M-8557-P2, [168]) where the dimensions of the active area are 85 x 57 x0.3 mm, and polarized through its thickness with an experimentally measured capacitance of 330 nF. Material properties of the laminates and the piezoelectric layers are defined in Table 4.1.

Table 4.1: Laminate and piezoelectric material properties

Property	M21/UDM194 (laminate) [150, 186]	M8557-P2 (piezoelectric) [168]
Longitudinal Elastic Modulus E_{11} [GPa]	178	30.3
Transverse Elastic Modulus E_{22} [GPa]	8.15	15.9
Shear Modulus, G_{12} [GPa]	5.2	5.5
Poisson's Ratio, ν_{12}	0.35	0.31
Longitudinal Thermal Expansion Coefficient, $\alpha_1[\,^{\circ}\mathrm{C}^{-1}]$	-9×10^{-8}	N/A
Transverse Thermal Expansion Coefficient, α_2, $\alpha_1[\,^{\circ}\mathrm{C}^{-1}]$	2.65×10^{-5}	N/A
Piezoelectric Constant d_{31}[C/N]	N/A	170×10^{-12}

In addition to these values, the damping ratio for all the harvesters was measured experimentally. The damping ratios were calculated by analyzing the "ring-down" from steady state excitation using the logarithmic decrement method. The harvesters were subjected to sinusoidal excitations of different acceleration as the damping ratio is a function of forcing level. For each forcing level, the harvesters were excited at the natural frequency for that forcing level to compensate for softening.

The energy harvesters are mounted from their centres to an electrodynamic shaker (LDS V455), Figure 4-3a. The shaker signal is generated in LabVIEW (National Instruments NI-USB-6211 DAQ) which sets the signal amplitude to match a desired g-level. This is achieved by measuring the acceleration of the central shaker attachment for a parameter sweep of drive frequency (20-80Hz) and shaker input voltage (0.01-0.5V) and generating a lookup table for any chosen g-level. The shaker input in terms of drive frequency and input voltage is passed via a power amplifier (Ling Dynamic Systems LDS 1000). A load resistor is attached across the MFC and the voltage across it measured using an oscilloscope (Agilent 54835A). The load resistance (R_{load}) remains fixed for each laminate throughout this chapter, corresponding to an optimal impedance match (for capacitance C_p = 330nF) at around natural frequencies of the laminates; i.e. the condition $\omega R_{load} C_p = 1$ where ω is the angular frequency. The structural

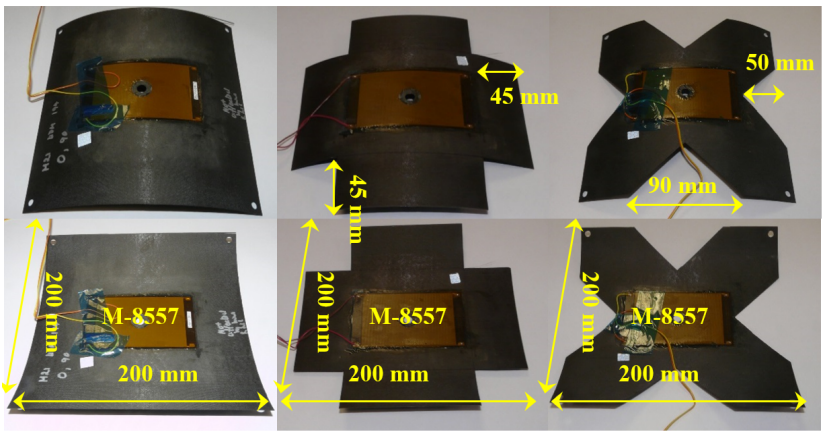

Figure 4-2: Bistable composite specimens with different shapes. A piezoelectric element $[0^{\circ}_{\mathrm{MFC}}/0^{\circ}/90^{\circ}]_{\mathrm{T}}$ is attached to the surface of the laminate.

response of the harvester is monitored by a laser vibrometer (Polytec PSV-400-M4 with VD-09 and DD-09 decoders) measuring displacement and velocity of point A of the plate 50mm in from both edges as shown in Figure 4-3b. Specific test procedures are detailed where relevant throughout the chapter.

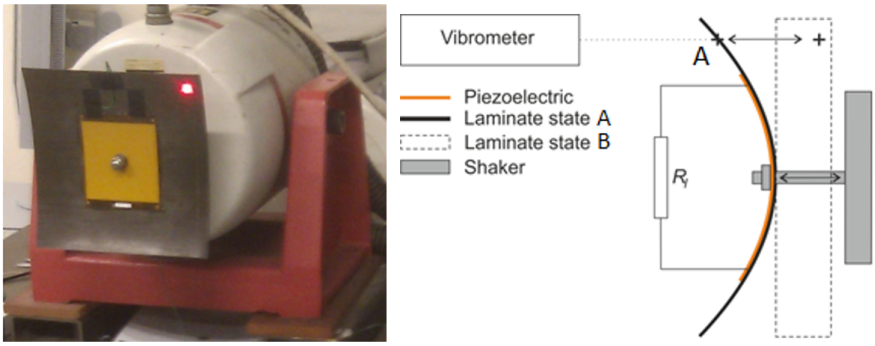

Figure 4-3: An example harvester mounted to an electrodynamic shaker and schematic representation of the experimental test setup

4.5 Results and Discussion

4.5.1 Static Shape Comparison

The laminate curvatures predicted by the model are compared against experimental measurements in this section. The out-of plane displacements in state B of a quarter section of the laminates were measured using a profilometer; the stable states are defined in Figure 4-4. A line spacing of 1 mm was used between measurements with a small number of voids in the profile plots; these were points at which the profilometer failed, returning erroneous readings due to lack of signal return.

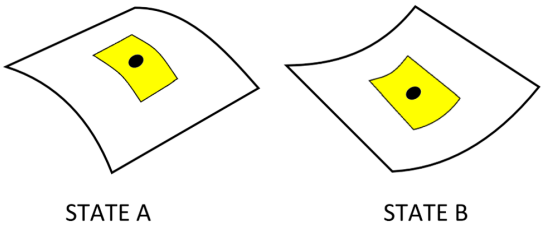

Figure 4-4: Stable states A and B defined with reference to the position and orientation of the piezoelectric element

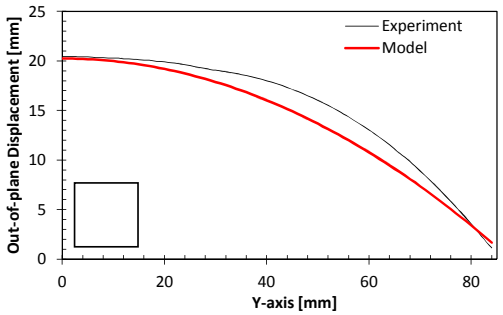

(a)

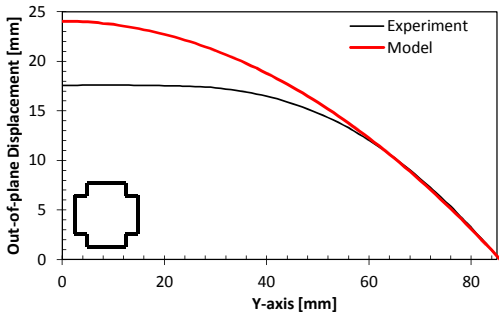

(b)

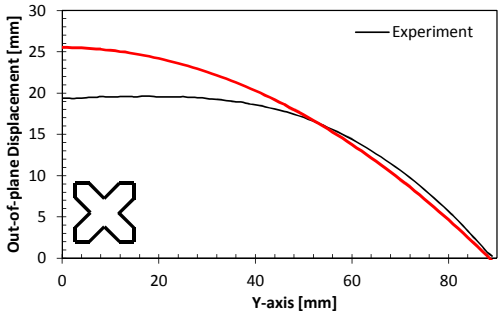

(c)

Figure 4-5: a) Curvature profile predicted by model and experiment for square laminate b) cruciform c) saltire

As indicated in Figure 4-5 the curvature of the measured profiles of the laminates are comparable to those predicted by the model, with the exception of the region around the MFC piezoelectric material. The main reason for this is that the model assumes a parabolic shape as a part of the shape function in section 4.2.2, equation 4.18. Thus, the addition of an MFC patch acts to reduce the overall curvature compared to a bare laminate. In practice, the additional stiffness of the piezoelectric also acts to induce local flattening (e.g. see Figure 4-5b and 4-5c). A surface was fitted to the experimental data using the least squares method (LSQ) on a function of the same form as the model's shape function and the major curvature values are compared in table 4.2. In the calculation, in addition to the failed scan points, any points scanned which were not on the laminate were also eliminated from the analysis. The R^2 value for all the fits was approximately 0.90 and the difference with a maximum of 16%.

Table 4.2: Static shape comparison error

Shape	Model Curvature Prediction [mm^{-1}]	LSQ Curvature Experiment [mm^{-1}]	%Difference
Square	0.00263	0.00239	-10.04
Cruciform	0.00243	0.00239	-1.67
Saltire	0.00239	0.00206	-16.02

4.5.2 Electro-Mechanical and Harvesting Performance

In this section, the dynamic behavior of the modeled harvesters are compared against experimental results. The numerical results were obtained by a MATLAB implementation of the model described in Section 4.2. For this comparison, the voltage signal generated by the piezoelectric patch during vibration is examined for energy harvesting. For each of the three laminate shapes, data are shown at a specific frequency and forcing level; the particular vibration frequency and level are chosen to demonstrate the various modes of oscillation of the bistable system and the comparison of experimental data and model predictions. At each such excitation case, a small section of the overall recorded timestream is initially shown and is followed by a Fourier transform of the entire time series to examine the frequency respose of the device. Finally, a phase diagram is shown where the voltage-time is differentiated with respect to time to examine the modes of vibration such as sinlge well, periodic and chaotic snap-through.

Square Laminate

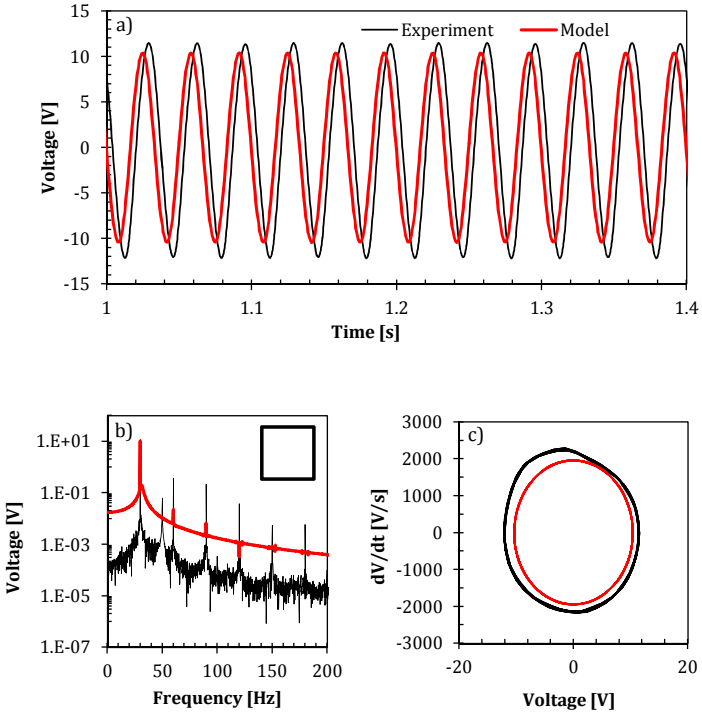

Figure 4-6: a) voltage vs. time, b) FFT plot and c) voltage phase portrait for square laminate and excitation parameters of 30 Hz and 3g

For the square laminate, two conditions of frequency and forcing levels are shown in Figures 4-6 and 4-7, as conditions of 3g/30Hz and 11g/28Hz respectively. Figure 4-6a shows the 3g/30Hz case at which the voltage-time values are in close agreement between experiment and model; in this low vibration level condition the laminate is vibrating in a stable and single state (state A). The Fourier transform of the voltage in Figure 4-6b shows that at this low level of excitation the driving frequency is clearly observed in the experimental data along with the first, second and third harmonics at double, triple and quadruple the driving frequency, respectively. The model also shows a similar behavior along with the higher-frequency activity harmonics. In all the experimental data, a peak is seen at 50 Hz due to the operation of other electrical equipment in the laboratory room at the time of the test. The phase portrait of $\frac{dV}{dt}$ and V in figure 4-6c reveals a circle for both the experiment and model, indicating a linear system with the laminate oscillating in a stable state.

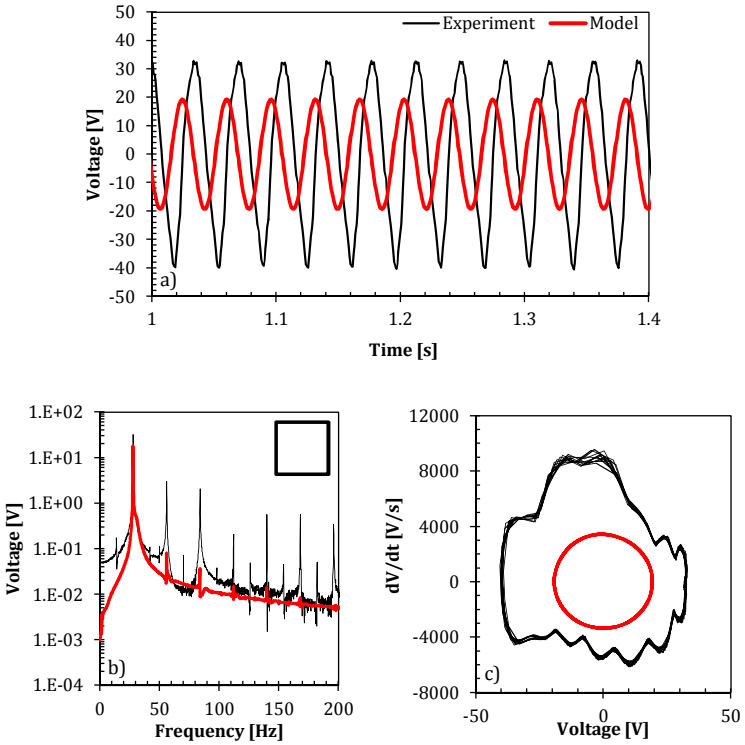

Figure 4-7: a) Voltage vs. time, b) FFT plot and c) voltage phase portrait for square laminate and excitation parameters 28 Hz and 11g

At a high level of excitation (11g/28Hz), complete snap-through of the square laminate from state A to state B was not observed in either the model or experiments; this is the due to high stiffness and curvature. For this higher level of vibration, the voltage-time data shows less agreement between experiment and model but the predicted magnitudes of voltage are of comparable size; see Fig 4-7a. Within the frequency domain (Figure 4-7b), both super and sub-harmonic activity are present. A subharmonic is when a structure is excited by a harmonic source, and there is a significant component of the structure's response at an integer fraction of the driving frequency, ω_d eg $\frac{1}{2}\omega_d$ $\frac{1}{3}\omega_d$ $\frac{1}{4}\omega_d$, etc. Often, these subharmonics are accompanied by superharmonic activity where peaks can be seen at integer multiples of the lowest observed subharmonic peak. In contrast to the low force case, frequency components were observed not only at integer multiples of the fundamental, but also at 2.5, 3.5, etc. in both experiment and model. Within the phase portrait (Figure 4-7c), the onset of nonlinearity in the experimental data is shown by a noticeable lack a symmetry, whereas this is not noticeable in the model's prediction. The phase portrait diagram of the experimental data show significant deviation from linear behavior indicating the onset of nonlinear behavior. This is also observed in the voltage-time data (Figure 4-7a) which also shows some asymmetry, but no snap-through events from state A to B were observed during the experiments.

Cruciform Laminate

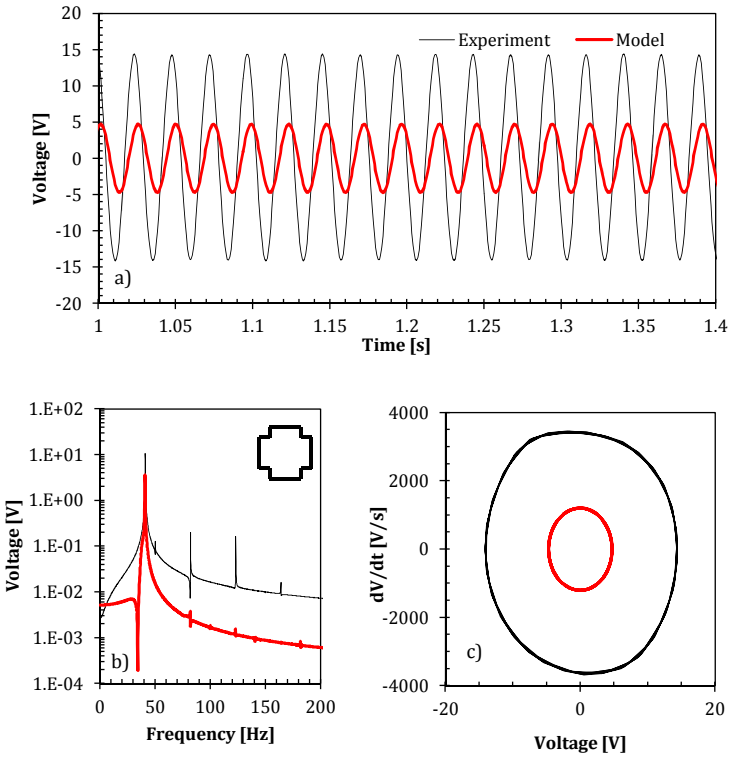

Figure 4-8: a)Voltage vs. time, b) FFT plot and c) voltage phase portrait for cruciform laminate and excitation parameters of 41 Hz and 3g.

In the case of the cruciform, the low-excitation case of 3g/41Hz is initially considered. Figure 4-8a shows the voltage-time response with the model predicting lower peak voltage compared with the experiment. As observed for the square laminate system, harmonic activity is seen for both model and experimental data (Figure 4-8b). An antiresonance is seen in the model just below the fundamental frequency, whereas this appears just prior to the first harmonic in the experimental data. The circular phase portraits in figure 4-8c of both experiment and model show that at this low forcing level the laminate is oscillating in a single state.

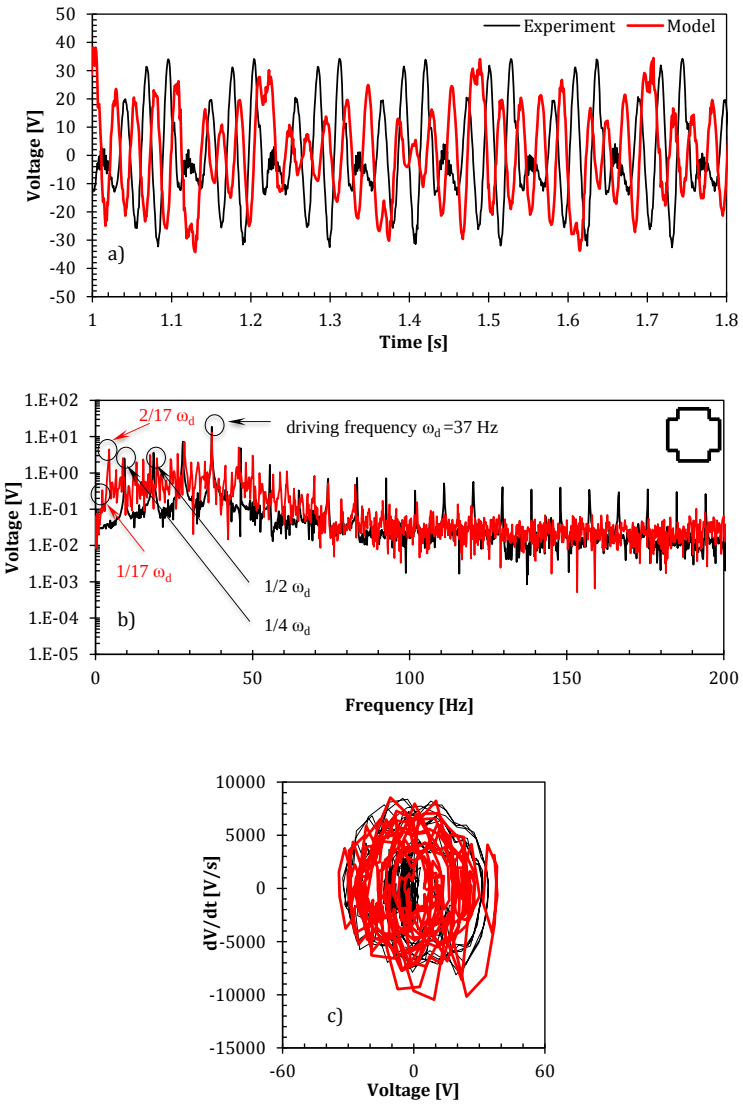

Figure 4-9: a) Voltage vs. time, b) FFT plot and c) voltage phase portrait for cruciform laminate and excitation parameters of 37 Hz and 12g

At a higher vibration of 12g/3 Hz, snap-through is encountered for both the experimental and modeled data as seem in the voltage-time domain data (Figure 4-9a). Snap-through appears intermittent and periodic from the voltage-time response for both the experiment and model. The experimental measurements' lowest peak (Figure 4-9 51) is seen at 9.22 Hz, which is approximately one-fourth of the driving frequency of 37 Hz. From this $\frac{1}{4}^{\text{th}}$ subharmonic onwards, the subsequent peaks appear at integer multiples of this frequency. The phase portraits (Figure 4-9c) indicate the trace of the experimental data recurs upon itself regularly. The additional frequencies present in the model causes the recurrences to overlap to be unclear, but overlaying the traces of the model and the experiments suggest that the voltage values are of comparable magnitude, as also seen in Figure 4-9a.

Saltire Laminate

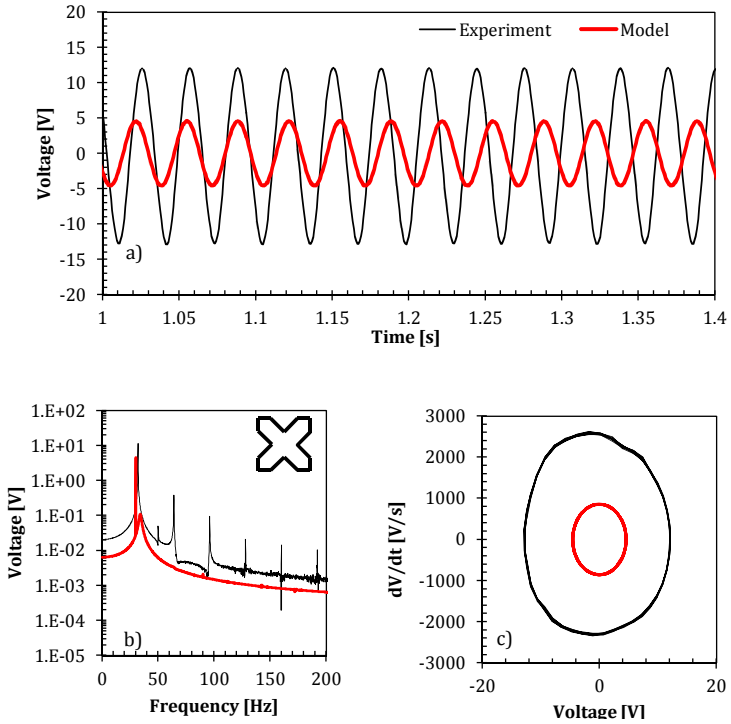

Figure 4-10: a) Voltage vs. time, b) FFT plot and c) voltage phase portrait for saltire laminate and excitation parameters of 32 Hz and 3g

For the low vibration conditions of the saltire at 32Hz/3g, the voltage-time series data in Figure 4-10a of the model is lower than the experiment, but both indicate the laminate to oscillate in a single state. The FFT plot (Figure 4-10b) shows harmonics within the experimental data but these are small in the model. The phase portrait indicate single well oscillation in both experiment and model with higher voltages in the experimental, indicating oscillation in a single state and linear in behavior. At higher vibration levels 9g/33 Hz the model voltage exceeds that of the experiment (Figure 4-11a), but both model and experiment appear to snap-through intermittently and periodically. The Fourier transform of the voltage time stream again yields interesting subharmonic and super-harmonic behavior similar to what was seen in figure 4-9b. The first peak for the model is seen at 4.125 Hz, which is close to $\frac{1}{8}^{\text{th}}$ of the driving frequency of 33 Hz. Peaks then occur at multiples of this frequency. The experimental results' first peak occurs at 2.97 Hz. This is at $\frac{1}{11}^{\text{th}}$ of the driving frequency. Once again, subsequent peaks occur at intervals of this frequency. In figure 4-9b, the model responds to a lower frequency subharmonic than what is measured experimentally. In figure 4-11b, the opposite is the case with the experiment's response beginning at a lower frequency.

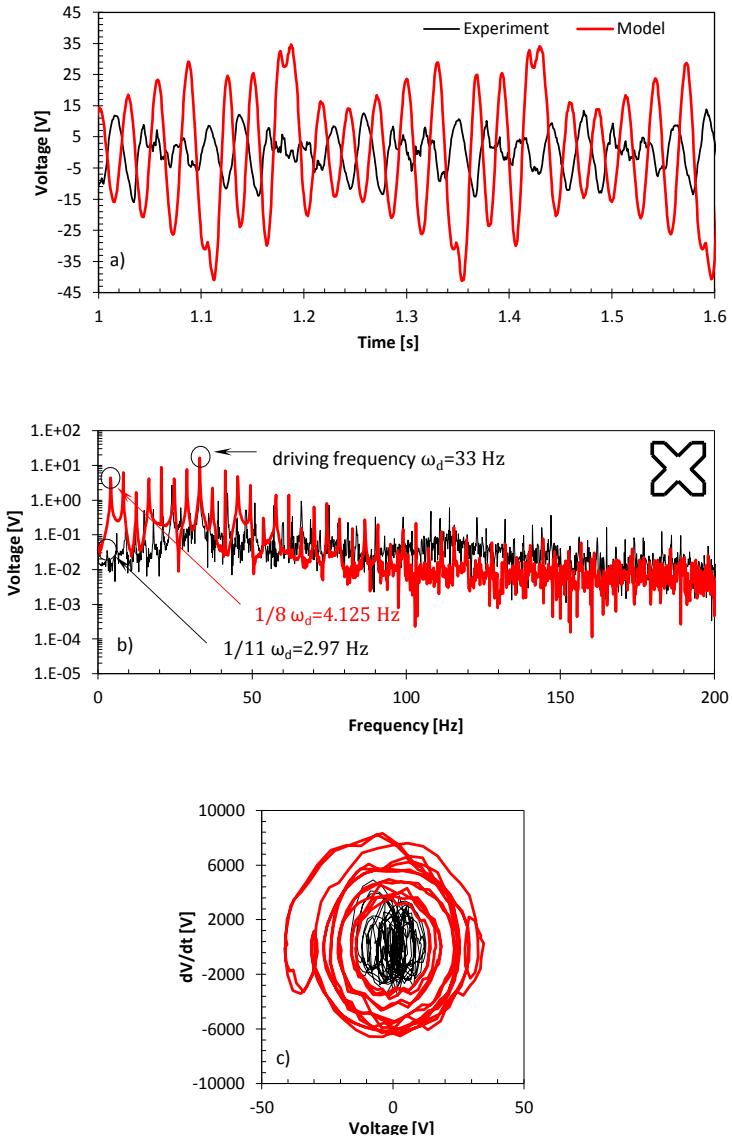

Figure 4-11: a) Voltage vs. time, b) FFT plot for excitation parameters of 33 Hz and 9g c) voltage phase portrait for saltire laminate and excitation parameters of 33 Hz and 9g

The above shows that in some cases the model can predict the onset on snap-through and the intermittent nature of the snap-through events at higher vibration levels. At lower levels at excitation, the onset of multiple frequency components at integer multiples of the driven frequency are seen however their relative magnitudes are lower in the model. The onset of nonlinear behavior is observed at lower vibration levels in the experiments rather than the model and this may be due to the higher curvatures of the laminates in the model, as shown in Figure 4-5. When snapping through, both the model and experiments show periodicity in their responses.

4.6 Power-Frequency Performance

This section examines the harvested power versus frequency and compares experimental and modeling results. The laminates were mounted to a computer controlled electromagnetic shaker. The forcing level was held constant and the frequencies were stepped through the indicated range (20-60Hz). An impedance matching resistor was placed across the piezoelectric. At each frequency, 0.2 seconds were allowed to ensure that the harvester was oscillating in a steady state before calculating the RMS power based on the measured voltage across the load resistor. This was also done numerically, and the results are shown together for comparison. For the 1g data for both State A and State B are shown for comparison of the respective natural frequencies.

Square Laminate

As shown in Figure 4-12a, the peak power output of the square generally increases with respect to forcing level. Peak power increases with acceleration. The peak power of the model appears to level-off after an acceleration level of 7g. This is due to the fact that the model predicts the onset of snap-through at lower forcing levels than is seen experimentally; for example as in Figure 4-12g. The reason for this is perhaps due to how the nonlinear stiffness of the laminate is implemented for when the laminate is undergoing high deformations. This is seen more clearly in Figure 4-12 which shows power versus frequency for different vibration levels. Figure 4-12b and c show the low vibration response in state A and state B respectively. The accuracy of the natural frequency predicted for state A and state B have an error of -3% and 13%, respectively. This difference of natural frequency of the two stable states is due to the asymmetry of the stable states resulting from the rectangular shape of the piezoelectric patch and that it located on one side of the laminate; the model predicts that the natural frequency in state B is higher than that of state A. Figures 4-12d through g show the increase of power at increasing acceleration. Figure 4-12e is of special interest as the model predicts snap through here at 30 Hz, causing the bend in the shape of the resonance peak. This results a reduction of peak power, but a broadening over the frequency band.

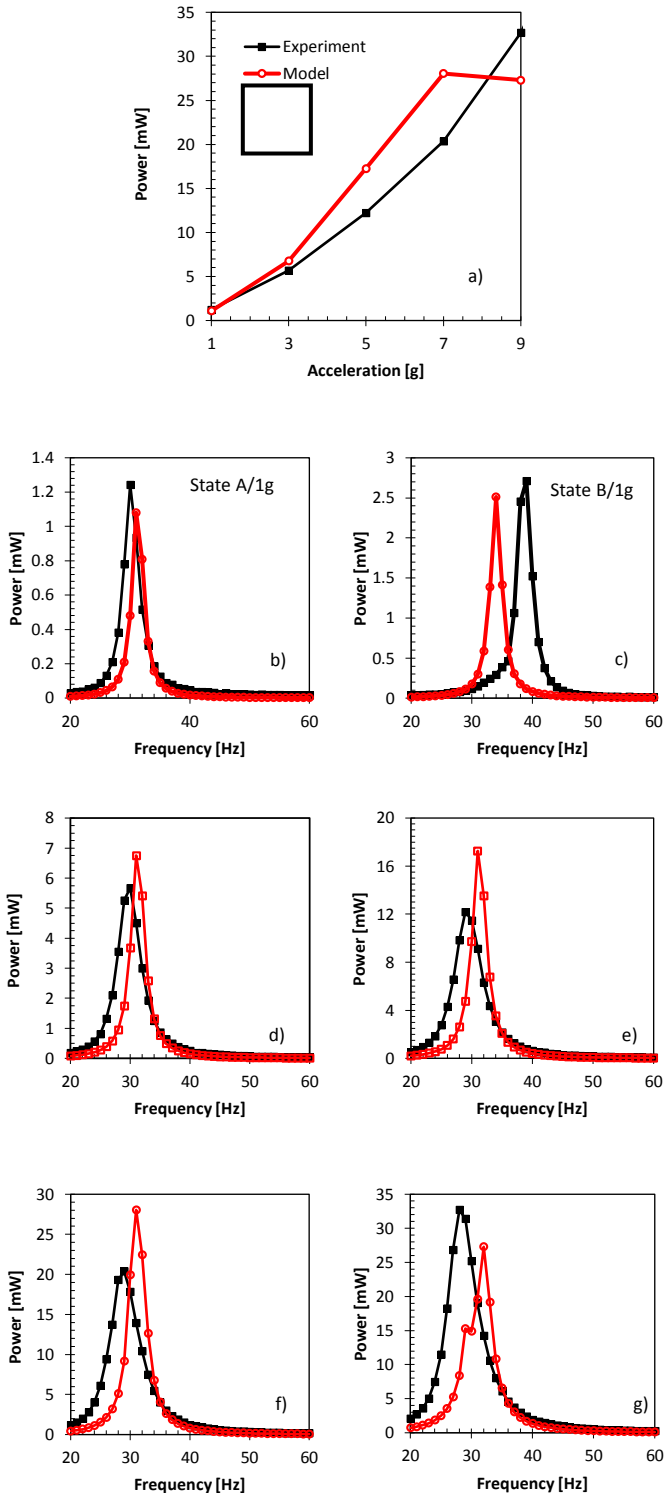

Figure 4-12: a) Peak power for increasing acceleration for square laminate. State A unless stated. b) RMS power at frequency at 1g c) RMS power at frequency at 1g for state B d) RMS Power at 3g for e) RMS Power at 5g for f) RMS Power at 7g for g) RMS Power at 9g

Cruciform Laminate

Figure 4-13a shows the peak power with acceleration level for the cruciform laminate. While the experimental data shows a gradual increase in power with acceleration level the model flattens at higher acceleration levels due to onset of snap-through. Similar to the square laminate, the discrepancy between power and model grows with excitation, and the model predicts snap-through at lower forcing levels. The power output is approximately double that of the square harvester. It is possible that in removing material, the overall structure is more lightly damped, resulting in a higher Q-factor. The natural frequencies seen here are higher than those seen for the square laminate for the model and the experiment. Since the resonant frequency of the harvester is equal to $\sqrt{\frac{k}{m}}$, the higher resonant frequency of the cruciform device indicates that the effects of mass (m) reduction on removing material from the corners of the laminate is greater than those of decrease in stiffness (k). Removing material from the corners reduces the mass of the harvester, but does not reduce the area of the laminate providing resistance to bending. Figures 4-13b and 4-13c show the power versus frequency at a low level of vibration (1g) for the laminate in state A and state B respectively. The error in natural frequency prediction is -9.5% for state A and -6.7% for state B. Again in figures 4-13d and e through 4-13f and g, the power and location around the natural frequency are shown for increasing acceleration levels.

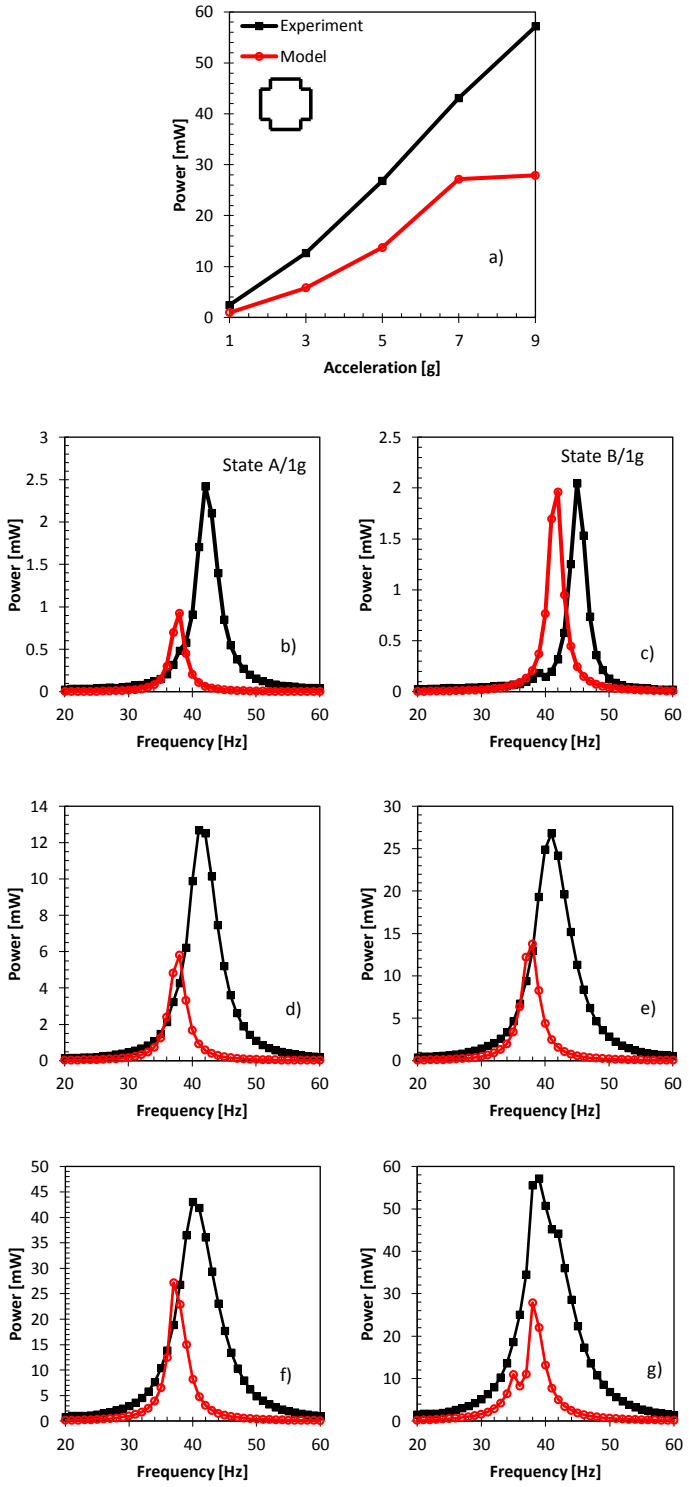

Figure 4-13: a) Peak power for increasing acceleration for cruciform laminate. State A unless stated b) RMS power at frequency at 1g c) RMS power at frequency at 1g for state B d) RMS Power at 3g for e) RMS Power at 5g f) Saltire RMS Power at 7g g) RMS Power at 9g

Saltire Laminate

Figure 4-14a is the peak power as a function of vibration level for saltire laminate and shows that the model and the experimental values encounter snap through at the same forcing level after 5g. There is a divergence after this point, although the overall shape is correct in the change in power at higher acceleration. The experiment is run continuously from frequency to frequency. As such, the initial conditions from the end of a previous frequency impact upon the results of the subsequent frequency. Even though 0.2 seconds are left for ringup, the systems dynamic history especially for frequencies with snap-through still has an effect on the behavior at the next frequency. In the model, each frequency is considered separately with the assumed initial conditions of being stationary prior to excitation. In practice, this carrying forward of the behavior means that once a laminate has begun snapping through, it will tend to continue snapping through over a broader range of frequencies than might be seen if the laminate were to be tested at each frequency individually.

Figure 4-14b and c shows the power versus frequency for the laminate vibrating at a low level of vibration (1g) is state A and state B.The natural frequency error is 3% in state A, and is correct within 1 Hz for state B. Again, the natural frequency of the saltire is higher than that of the square, despite the area resisting bending being significantly decreased; this again suggests that the mass has decreased more quickly than the effective stiffness. Figures 4-14c-g show power versus frequency at increasing vibration levels. The onset of snap-through is clearly seen in figures 4-14f and g in the experimental data by a drop in peak power. In the model data the power begins to increase in frequency as in the non snap-through case, but then suddenly decreases, at excitation parameters such as 29 Hz at 7g and 28 Hz at 9g. From this frequency onwards, the peak power is diminished, but activity is seen over a broader frequency band until the harvester is far enough from the natural frequency to resume single-well behavior (39 Hz at 7g and 38 Hz at 9g). A decrease in power is also observed in the experimental data; this may be a result of the two natural frequencies (Figures 4-14 b and c) contributing to the overall response as the laminate is snapping between the two states. Clearly removing material form the center edges and ensure material/mass remains at the corners to maximise the forcing function reduced the vibration level needed for snap-though.

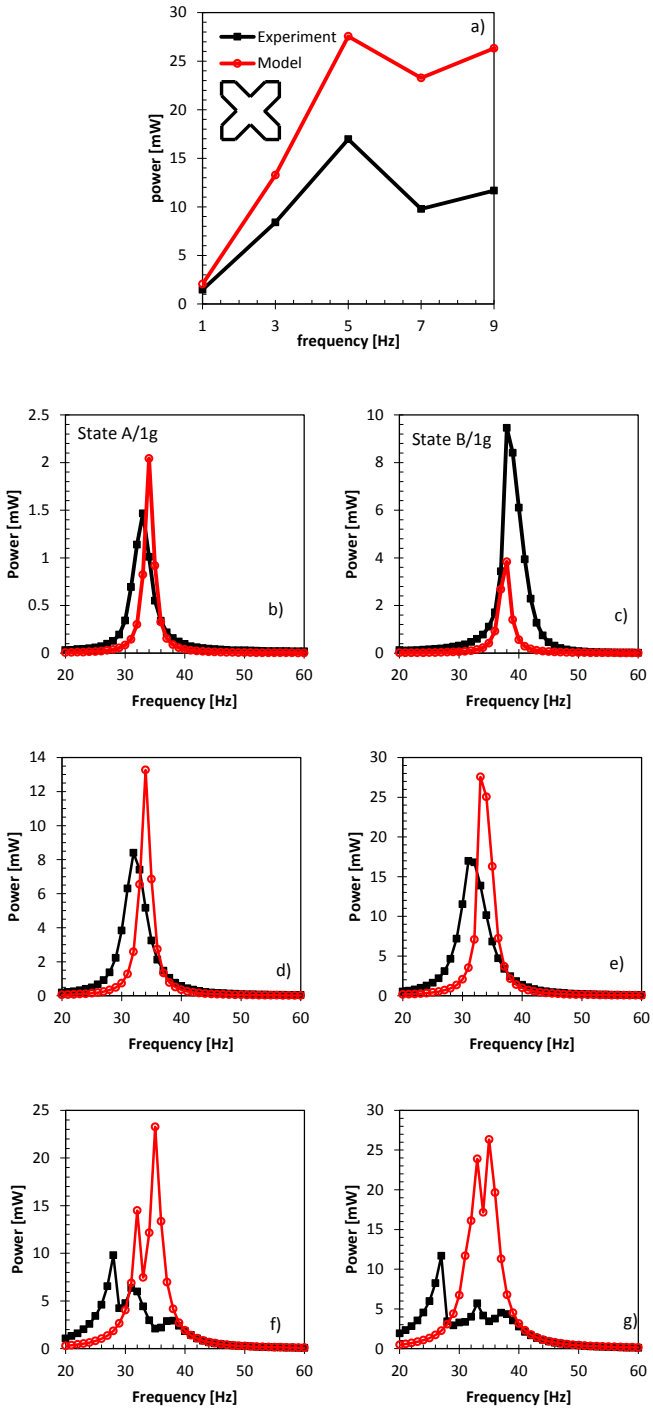

Figure 4-14: a) Peak power for increasing acceleration for saltire laminate. State A unless stated b) RMS power at frequency at 1g for saltire c) RMS power at frequency at 1g for state B d) RMS Power at 3g e) RMS Power at 5g e) f) RMS Power at 7g g) RMS Power at 9g

For the three laminate shapes, the natural frequencies are within 13% for both state A and state B at low vibration levels (1g), with larger errors for prediction of peak power. The experiments here have highlighted the sensitivity of the system to initial conditions. Beyond the scope of this chapter, but certainly of importance of the sensitivity of the power output to manufacturing defects, changes in composite over time (moisture absorption), uncertainty in the exact ply angles, and variations in the thickness of the carbon fiber substrate, damping ratios, adhesion layers between the piezoelectric and laminate and possible frequency dependence as well as forcing level dependence of the harvesters.

4.7 Conclusions

This chapter set out to address two objectives. The first objective was to establish the benefit of changing the planiform shape and to understand the relationship between shape and the power output. It was demonstrated that this design parameter did have some benefit. The snap-through acceleration was decreased, from greater than 11g for the square to 7g for the saltire, but this forcing level is still at high acceleration, compared to the cantilevers of chapter 3 which experienced snap-through at 5g. The power output was increased from 30 mW for the square to 60 mW in the case of the cruciform, but was decreased to about 20 mW for the saltire. The cantilever of chapter 3 had a power output of about 7 mW. In both cases of the cruciform and the saltire, the natural frequency increased. The second objective was to compare the model's results against experimental results. An analytical two degree of freedom model was derived with full electromechanical coupling. A method for representing arbitrary shapes using a discretized grid was implemented. The static shape predictions for the cured laminates was compared against experimental profilometry measurements. Because of the assumption of the shape function, the overall curvature was flattened by the addition of an MFC patch, but remained parabolic whereas the experimental data showed significant local flattening. Under dynamic excitation, the model was able to capture the main qualitative characteristics of the system. The model's predictions of the natural frequencies' value for both states was comparable to the experimentally-derived values. Under increased levels of excitation, the model qualitatively predicted correctly the emergence of nonlinear features. Specifically, the model showed antiresonances, superharmonics and subharmonics. Furthermore, the model did exhibit snap-through. The model correctly showed that the removal of material more significantly affected the mass rather than the stiffness of the laminates as reflected by the increase of natural frequency. The model correctly predicted that removal of material did indeed reduce the acceleration required for snap-through. While the power output predictions were comparable between the model and experiments, the fidelity was not to the extent that it can be used as an exact design tool. It is conjectured that the strain energy landscape could be strain-rate dependent. In terms of efficacy, changing the overall shape of the harvester was able to change the dynamic behavior of the non-square harvesters. While the forcing level required to snap the cruciform laminate through did not decrease substantially, the saltire laminate saw a more significant decrease. Because the corners were cut out of the cruciform laminate, the effective

area resisting any bending motion to transition between states was still largely the same as a square laminate. Since the saltire tended to decrease this effective bending resistance, and still maintain mass at the extremities, each of the arms acted more like cantilevers. This suggests that the optimal shape of a bistable laminate for energy harvesting would possibly be some variant of the saltire. While these investigations on the effects of changing the planiform shape were successful in decreasing the acceleration required for snap-through, the excitation required is still high. In order for planiform-type bistable laminate energy harvesters to be a competitive alternative, this will need to be addressed. Thus, the efficacy of a different design parameter should be investigated. Some possible avenues of research could be to try different substrate materials. It may also be possible to abrade the substrate so that it is thinner to tailor the dynamics. A third option may be to change the angles of the laminae to decrease the stiffness of the harvester which will be discussed in the next chapter, as it is the easiest of these three to implement.

This major findings of this chapter can be summarized:

- The removal of material successfully reduced the acceleration level required to initiate snap-through from greater than 11g for the square to 7g for the saltire
- The power output of the cruciform laminate was nearly double over that of the square (58 mW vs 33 mW), and the saltire was slightly reduced with respect to that of the square (27 mW)
- The model's prediction for out-of-plane curvature of the laminates is tested and shown to agree within approximately 16%
- The predictions of the natural frequencies for the different states and different shapes are within 13%
- The main nonlinear features such as subharmonics, superharmonics, antiresonances, and snap-through of the different shapes are present in the model
- The general trends of the natural frequencies' value with respect to differences of operating state and material removal were correctly represented

Chapter 5

Arbitrary Ply Angle Bistable Laminate Energy Harvesters

The original intention for investigating square laminates for energy harvesting was to exceed the power outputs seen by bistable cantilevers. While their power outputs were exceeded, the accelerations required for snap-through and therefore broadband energy harvesting were impractically high. This chapter sets out two objectives to address this problem and expand the understanding of the dynamics of the harvesters. The first is to establish the benefits of changing the second ply angle of a plate-type bistable energy harvester (ie other than 90° as seen in chapters 3 and 4). The second is to observe the emergence of nonlinear effects in the response of specific harvesters of interest at increasing acceleration. This chapter presents experimental results of non-orthogonal, $[0^\circ_{\mathrm{MFC}}/0^\circ/\theta^\circ]$, bistable laminates for broad-band energy harvesting which are characterized by subjecting them to harmonic excitation of varying frequency and acceleration. While varying the planiform shape of the harvesters was shown to have some effectiveness in tailoring the response, the acceleration levels required for snap-through were still very high, thus the efficacy of the ply angle is investigated as a design parameter. The root mean squared (RMS) power as a function of frequency and vibration level is used as a basis of comparison and analysis and harvester performance is assessed in terms of peak power, cumulative power, and full half-power bandwidth. Nonlinear features in the frequency response are noted for different laminate geometries. A series of excitation parameters are chosen for the $[0^\circ_{\mathrm{MFC}}/0^\circ/30^\circ]_{\mathrm{T}}$ laminate to showcase the gradual emergence of nonlinear features. The relationship between natural frequency and θ° indicates that as the ply angle is reduced, the mismatch in thermal strain is decreased and the stiffness and level of bistability is diminished; this leads to laminates with a low θ° exhibiting nonlinear effects and snap-through from one stable state to another at lower vibration levels. The variation of the laminate lay-up is therefore an effective method to tailor the response of broadband energy harvesters based on bistable laminates.

5.1 Introduction

As presented in chapter 4, despite removing material from the bistable laminate energy harvester, the excitation level required to cause snap through was too high for many practical applications. In order to reduce the snap through acceleration further, the relationship between the power output and second ply angle θ_2° in the stacking sequence $[0^\circ_{\mathrm{MFC}}/\theta_1^\circ/\theta_2^\circ]_{\mathrm{T}}$ will be studied experimentally and using the model derived in chapter 4. The effects of changing θ_2° have been touched upon in the literature. Betts [121] studied and modelled the cured static shapes of some non-orthogonal laminates, and Diaconu [141] undertook some investigations into their dynamics, but neither attempted to harvest energy using them.

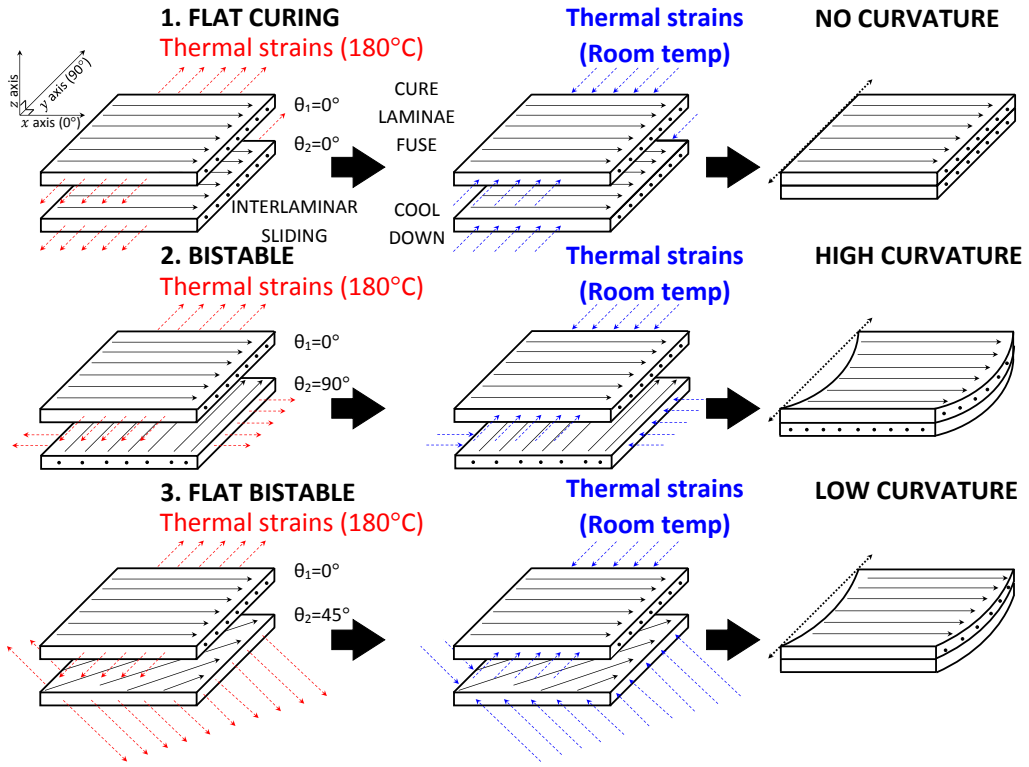

Figure 5-1: Thermal strain orientations for $[0^\circ/0^\circ]_{\mathrm{T}}$, $[0^\circ/90^\circ]_{\mathrm{T}}$, and $[0^\circ/45^\circ]_{\mathrm{T}}$ laminates

The underlying phenomenon which brings about bistability is the inequality of the thermal expansion coefficients in the matrix and the fiber directions. When the plies are laid at right angles $[\theta^\circ/(\theta^\circ + 90^\circ)]_{\mathrm{T}}$ to each other, the effects of the disparity are maximized, causing the greatest possible out of plane displacement, as illustrated in figure 5-1. The extreme opposite case would be a $[\theta^\circ/\theta^\circ]_{\mathrm{T}}$ laminate. This configuration would have no curvature because the laminae would thermally expand and shrink together at the same rate while curing resulting in no strain direction bias at the top and the bottom of the laminate. Therefore, a laminate with a stacking sequence in between these extreme cases should have intermediate behavior. The out of plane displacement should decrease from the $[\theta^\circ/(\theta^\circ + 90^\circ)]_{\mathrm{T}}$'s maximum, and the

excitation required for snap through should be reduced as well.

5.2 Model Predictions

As stated in chapter 4, equation 4.18 of the out-of-plane displacement w static shape of a bistable laminate can be described by

$$w(x,y) = \frac{1}{2}\left(ax^2 + by^2 + cxy\right)$$

where x, y are the x and y coordinates, and a, b, and c are the curvature coefficients. Intuitively, larver values of these coefficients lead to more out-of-plane displacement of the laminate. Therefore, as θ_2 approaches equality with θ_1, it is expected that these coefficients' values will decrease. Figure 5-2a demonstrates this. Here, θ_1 is set to zero degrees, and the coefficients' values are calculated for a range of values of θ_2 from 90° to 0°. For illustrative purposes, a numerical representation of a laminate is shown in figure 5-2b to demonstrate how these coefficient values affect the shape of the laminate. The curvature coefficient values in figure 5-2a are for a single state If the opposite state were considered, the a and b coefficients would exchange values, as the two states are symmetric. However, because of the rectangular shape and anisotropy of the piezoelectric patches, the states will not be perfectly symmetric in practice. the curvature values are maximized at $[0°/90°]_{\mathrm{T}}$ and decrease as the angle between the plies decreases. Starting from between $\theta_2 = 26°$ and $\theta_2 = 25°$ onwards, the curvature values all approximately equal each other, indicating a loss of bistability. The model can be used to predict the curvature of these laminates over a range of values of θ_2, as well as to estimate the shapes of the dual potential wells at these points. The dual potential wells of three different values of θ_2 are superimposed in figure 5-3. The two stable states are referred to as the fiber tension (FT) and matrix compression (MC) states, as shown, based on the predominant direction of strain in the patch.

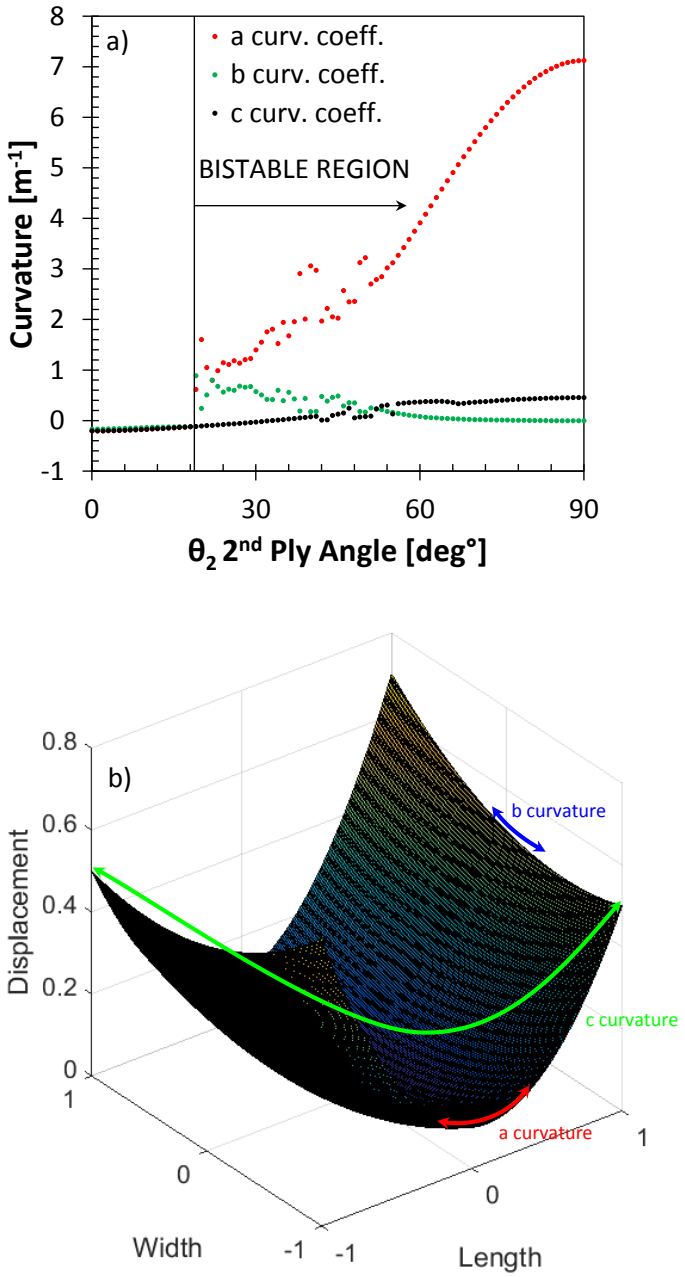

Figure 5-2: a) Curvature coefficients $a, b,$ and,c variation with respect to θ_2 b) Illustrative laminate showing where the curvature values correspond

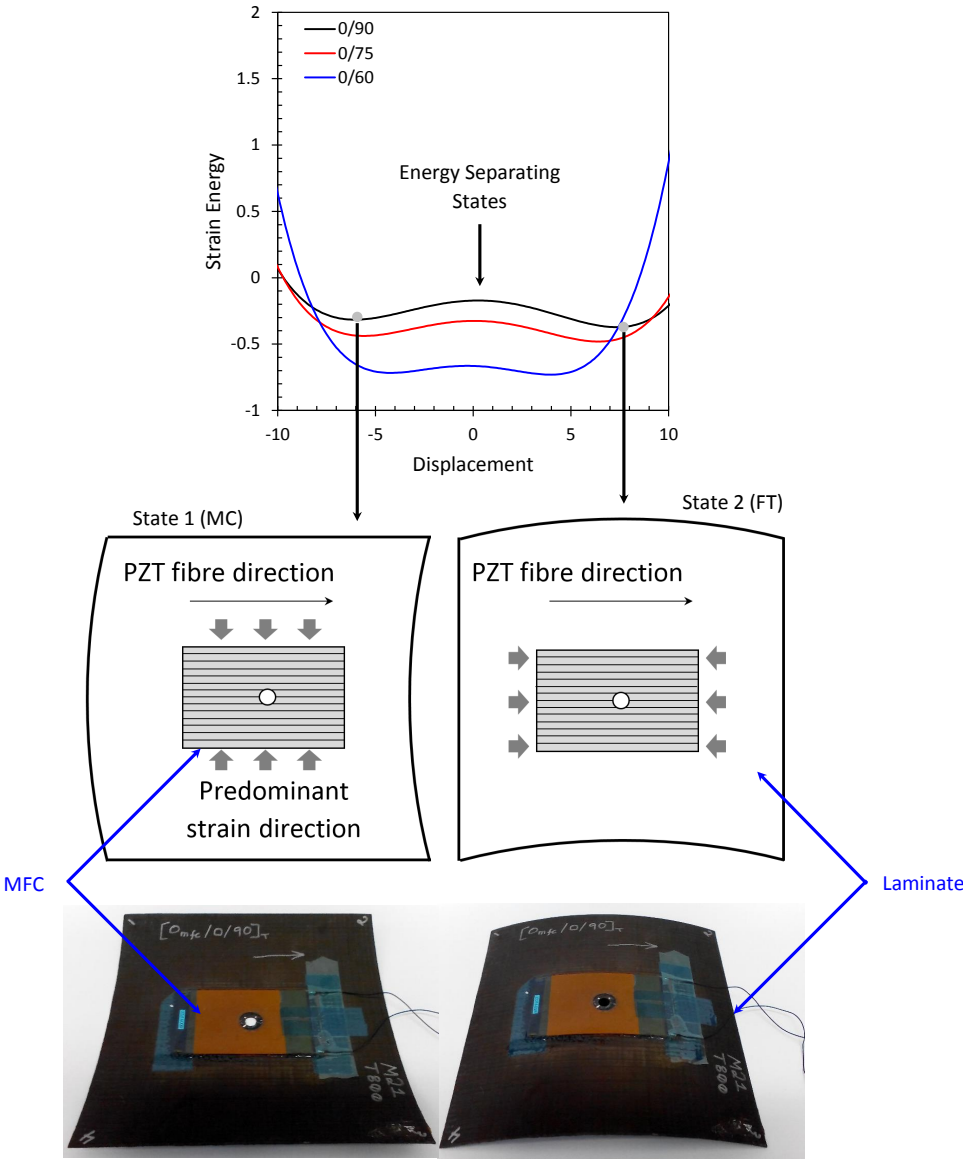

Figure 5-3: Dual potential well and corresponding matrix compression (MC) and fiber tension (FT) stable states. Size of laminates are 200 x 200 mm for scale

As indicated, the lowest points in the two dips correspond to the two stable states of the laminates as this is where the strain energy is minimized. The displacement is the distance from the x, y plane to the highest point of the laminate. Thus, the difference between the horizontal, coordinates of the graph of figure 5-3 is the distance through which the laminate travels as it snaps through. As θ_2 decreases, the distance between the two minima also decreases in agreement with the flattening predicted by a reduction of curvature as seen in the figure. The first derivative of the strain energy is the force exerted by the system as a function of

displacement, and the second derivative is stiffness. The dual potential wells' shapes around the minima are also less curved, suggesting a reduction of stiffness and therefore lower natural frequencies. The separation maximum between the two minima is lower, meaning that less energy is required to cause a snap-through transition from one state to the other.

Electrical power P is given by the simple relation $P = IV$ where I is current and V is voltage. If a piezoelectric patch on a bistable laminate harvester is strained by some amount ε, then the voltage developed will be proportional to this strain: $V \propto \varepsilon$. At the same time, the current developed will be proportional to the strain rate: $I = \frac{\mathrm{d}\varepsilon}{\mathrm{d}t}$. Substituting these quantities into the initial power equation gives that $P \propto \varepsilon \frac{\mathrm{d}\varepsilon}{\mathrm{d}t}$. Some experimental results illustrating these relations appear in appendix 1. Because θ_2 is reduced, the overall snap through displacement is decreased, limiting ε. However, because the stiffness is also decreased, the number of snap through events should be high, leading to high $\frac{\mathrm{d}\varepsilon}{\mathrm{d}t}$. Therefore, the power output should be high.

5.3 Experiment

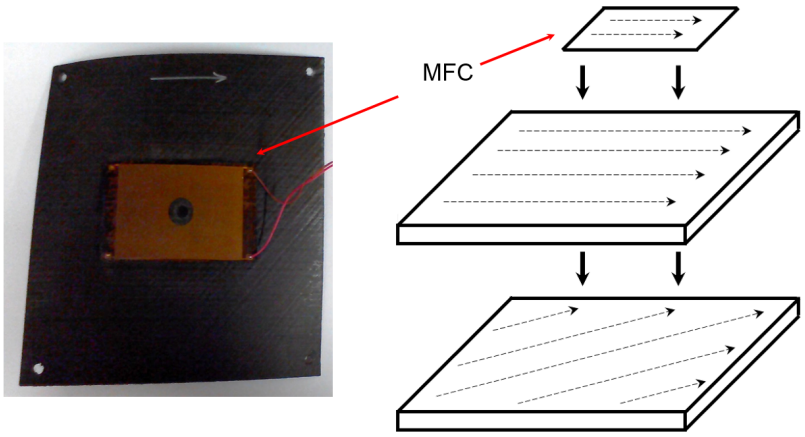

Figure 5-4: Non-orthogonal energy harvester with a stacking sequence $[0^\circ_{\mathrm{MFC}}/0^\circ/45^\circ]_{\mathrm{T}}$. Black material is the $[0^\circ/45^\circ]_{\mathrm{T}}$ carbon fiber reinforced polymer laminate and orange region is the piezoelectric MFC. Arrows indicate carbon or piezoelectric fiber orientation

Seven bistable laminates with a variety of two-ply stacking sequences were built for this work and combined with with MFC piezoelectric patches. The piezoelectric patches used were Smart Materials M-8557-P2 patches [168] with a piezoelectrically active area of 85 x 57 mm. The patch consisted of longitudinally-oriented lead zirconate titanate (PZT) fibres embedded in a polymer matrix as the active layer with planar copper mesh electrodes fixed to the top and bottom, forming a dielectric with a typical capacitance of 300 nF. Due to the difference of stiffness of the piezoelectric patch in the fiber direction with respect to the matrix direction of the MFC (E_{11}=30.3GPa, E_{22}=15.9 GPa, respectively [152]), the patch is included in the stacking sequence where the angle stated refers to the orientation of the PZT fibers, as detailed in figure 5-4. To enable the device to be attached to an electromechanical shaker for char-

acterization, a 17 mm diameter hole was laser cut in the middle of the patch and sanded to ensure that no residual copper would cause a short circuit across the piezoelectric layer. The laminates examined were $[0^{\circ}_{\text{MFC}}/0^{\circ}/90^{\circ}]_{\text{T}}$, $[0^{\circ}_{\text{MFC}}/0^{\circ}/75^{\circ}]_{\text{T}}$, $[0^{\circ}_{\text{MFC}}/0^{\circ}/60^{\circ}]_{\text{T}}$, $[0^{\circ}_{\text{MFC}}/0^{\circ}/45^{\circ}]_{\text{T}}$, $[0^{\circ}_{\text{MFC}}/0^{\circ}/40^{\circ}]_{\text{T}}$, $[0^{\circ}_{\text{MFC}}/0^{\circ}/30^{\circ}]_{\text{T}}$, and $[0^{\circ}_{\text{MFC}}/0^{\circ}/20^{\circ}]_{\text{T}}$ and an example device is shown in figure 5-4. All laminates were of dimension 200 x 200 mm and used an M21-T800 pre preg resin and fiber system and cured in an autoclave at 180°C at a pressure at 7 bar. Upon curing, an 8 mm hole was drilled through the composite plates for mounting onto the shaker. The piezoelectric patch was adhered to the laminate with epoxy glue such that the central hole was concentric with the laminate's hole. These were allowed to cure overnight with a heavy weight placed on top to ensure a thin, continuous bonding layer between the piezoelectric and the laminate. Upon addition of the piezoelectric patch, the $[0^{\circ}_{\text{MFC}}/0^{\circ}/30^{\circ}]_{\text{T}}$, $[0^{\circ}_{\text{MFC}}/0^{\circ}/20^{\circ}]_{\text{T}}$ harvesters lost their ability to maintain their position in their second state, but there was still a noticeable snap-through event, and are still considered bistable. All other devices were exhibited two stable states. The natural frequencies for each harvester was experimentally measured, as well as the capacitance for each piezoelectric patch. Based on the average natural frequency for the FT and MC states, the load resistance was calculated using the principle of impedance matching to maximize the power output, as discussed in [158]. All laminates were subjected to acceleration and frequency controlled sinusoidal excitation on a calibrated Ling Dynamic Systems electromechanical shaker. For the frequency ranges indicated, the shaker increased the driving frequency in increments of 0.2 Hz and at each frequency, the shaker would dwell for 5 seconds. The voltage over the impedance matched load resistor was measured using an oscilloscope, discarding the initial 0.2 seconds of data to allow for a steady state to be reached by the harvester. From this, the RMS power output was calculated. Frequency-stepping tests were undertaken from 1g to 7g. Snap-through was observed for the $[0^{\circ}_{\text{MFC}}/0^{\circ}/45^{\circ}]_{\text{T}}$, $[0^{\circ}_{\text{MFC}}/0^{\circ}/40^{\circ}]_{\text{T}}$, $[0^{\circ}_{\text{MFC}}/0^{\circ}/30^{\circ}]_{\text{T}}$, and $[0^{\circ}_{\text{MFC}}/0^{\circ}/20^{\circ}]_{\text{T}}$ harvesters. Unless stated otherwise, all data is assumed to be from the MC state.

5.4 Results and Discussion

5.4.1 Frequency Sweeping

An example of a typical response of the laminate-MFC combination at low and high vibration levels is shown in Figures 5-5a and 5-5b, respectively. Figure 5-5a shows the RMS power at 1g for the $[0^{\circ}_{\text{MFC}}/0^{\circ}/40^{\circ}]_{\text{T}}$ laminate and the frequency increasing (upsweep) and frequency decreasing (downsweeps) response. A small difference in power output depending on the sweep direction is seen. The difference of natural frequency between the two states of the harvester is 7.8 Hz and is due to the geometric asymmetry of the two curved states, the rectangular shape of the MFC patch, and its anisotropy. As a result of this difference, on transitioning from one state to the other at higher vibration amplitudes, as in Figure 5-5b, the laminate was then off-resonance with a corresponding decrease in its vibrational response such that there was insufficient energy to return to its original state by a cross-well oscillation.

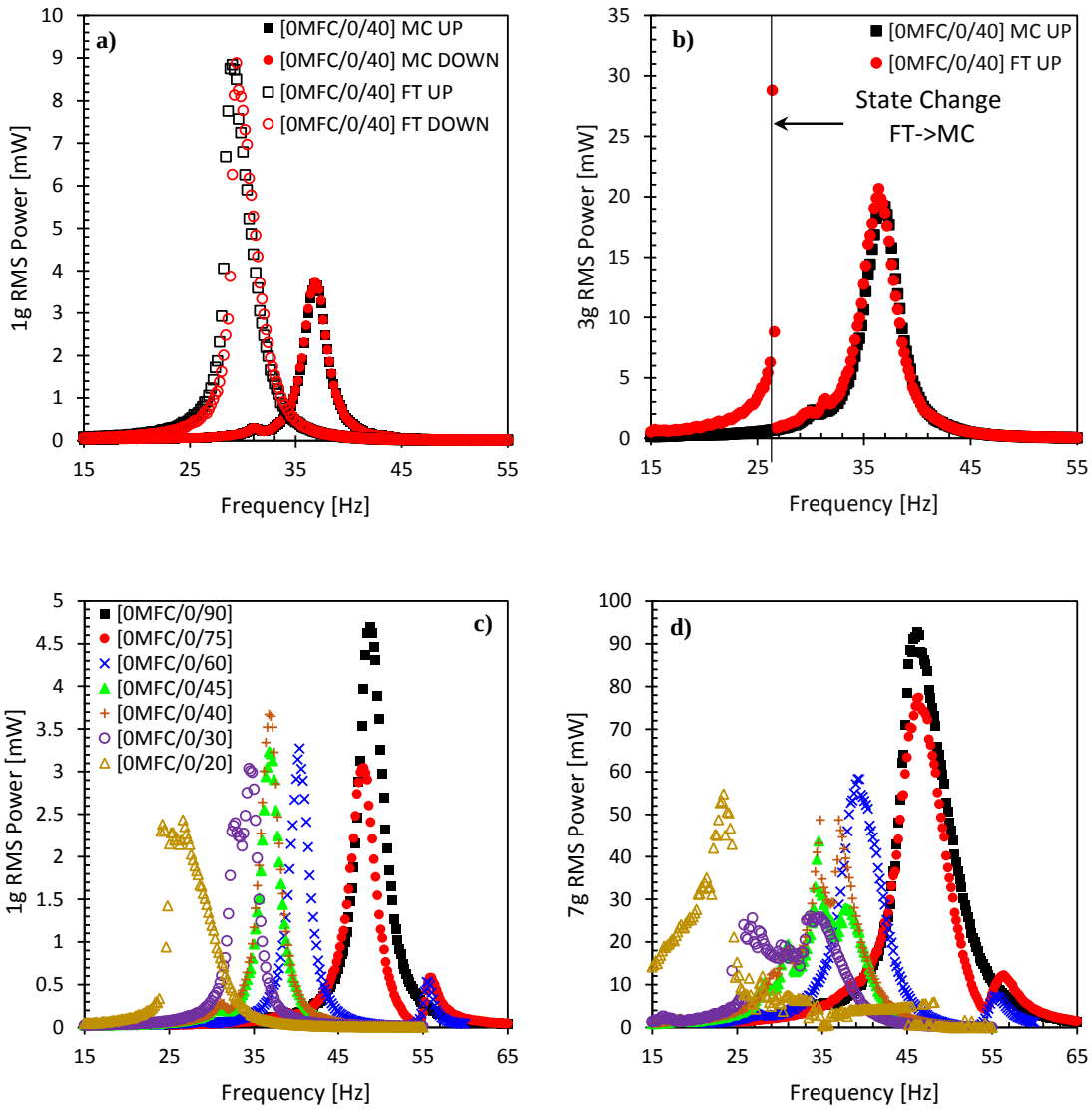

Figure 5-5: RMS power as a function of frequency at a vibration level of a) 1g and b) 3g for the $[0^{\circ}_{\mathrm{MFC}}/0^{\circ}/40^{\circ}]_{\mathrm{T}}$ harvesters, c) 1g for all harvesters and d) 7g for all harvesters

Figure 5-5c) shows the power vs. frequency for the different harvesters at 1g with the highest power output occurring at the respective natural frequencies. As expected, due to the reduction in stiffness, the smaller the ply angle harvesters have lower natural frequencies. The laminates with a second ply angle of 40° and higher show effectively linear behavior at this forcing level. The $[0^{\circ}_{\mathrm{MFC}}/0^{\circ}/30^{\circ}]_{\mathrm{T}}$ harvester has a two small peaks and the $[0^{\circ}_{\mathrm{MFC}}/0^{\circ}/20^{\circ}]_{\mathrm{T}}$ exhibits an flat, broad response. Figure 5-5d) shows the behavior of the harvesters at 7g. The peaks of the $[0^{\circ}_{\mathrm{MFC}}/0^{\circ}/90^{\circ}]_{\mathrm{T}}$, $[0^{\circ}_{\mathrm{MFC}}/0^{\circ}/75^{\circ}]_{\mathrm{T}}$, and $[0^{\circ}_{\mathrm{MFC}}/0^{\circ}/60^{\circ}]_{\mathrm{T}}$ still have mostly linear behaviour. Nonlinear effects are noticeable now in the $[0^{\circ}_{\mathrm{MFC}}/0^{\circ}/45^{\circ}]_{\mathrm{T}}$, and$[0^{\circ}_{\mathrm{MFC}}/0^{\circ}/40^{\circ}]_{\mathrm{T}}$ harvesters. At the lower acceleration level, they exhibited a clear resonance peak, whereas here, double

peaks are seen similar to that of $[0^\circ_{\text{MFC}}/0^\circ/30^\circ]_{\text{T}}$ at 1g. Snap-through is also prevalent in the $[0^\circ_{\text{MFC}}/0^\circ/30^\circ]_{\text{T}}$ and $[0^\circ_{\text{MFC}}/0^\circ/20^\circ]_{\text{T}}$ harvesters. This explains the broadness of power output of these harvesters' frequency response. Comparing figures 5-5c) and 5-5d) shows the general trend that maximum power is produced by the harvesters with the highest ply angle, and the trend is generally downward especially for low g. It is possible that the reason for this is that the stiffer substrate is more able to effectively strain the piezoelectric patch. Therefore, the more compliant laminates do not develop the same power levels. The $[0^\circ_{\text{MFC}}/0^\circ/20^\circ]_{\text{T}}$ harvester in this context has an unusually high power output. It may be that the compliance is such that the piezoelectric is more or less strained directly by the shaker. Thus, the focus of the remaining discussions will be placed upon the $[0^\circ_{\text{MFC}}/0^\circ/90^\circ]_{\text{T}}$, as it is a basis for comparison due to its prevalence in the literature [59, 139, 142, 145, 146, 155, 158, 160, 162, 184, 187–190] and the $[0^\circ_{\text{MFC}}/0^\circ/30^\circ]_{\text{T}}$, $[0^\circ_{\text{MFC}}/0^\circ/20^\circ]_{\text{T}}$ for their interesting dynamical behaviour.

5.4.2 Gradual Emergence of Nonlinearity in the $[0^\circ_{\text{MFC}}/0^\circ/30^\circ]_{\text{T}}$ and $[0^\circ_{\text{MFC}}/0^\circ/90^\circ]_{\text{T}}$ harvesters

To observe in greater detail the gradual emergence of nonlinear features in the $[0^\circ_{\text{MFC}}/0^\circ/30^\circ]_{\text{T}}$ harvester, several measurements were taken at 30 Hz and increasing acceleration levels from 1 to 7g. The dynamic response of the harvesters moves from being approximately linear to highly nonlinear as the acceleration increases in that the frequency content of the harvester's response contains many frequencies other than the single frequency input of the excitation. The $[0^\circ_{\text{MFC}}/0^\circ/90^\circ]_{\text{T}}$ harvester is also tested at increasing levels of vibration, and the damping ratio is shown to not be constant over the range.

Superharmonics and Subharmonics

The Poincaré plot of figure 5-6 is circular, and the time domain plots appear sinusoidal. In the frequency domain, apart from a small component at double the driving frequency, the frequencies of the response are dominated by the driving frequency. Upon increasing the acceleration to 3g, the Poincaré plot begins to bulge as seen in figure 5-7 . This bulging indicates that the stiffness is different in one direction which is why there is higher displacement in the positive part of the displacement-time graph of figure 5-7 a). The displacement's FFT plot of figure 5-7 b) shows that the second harmonic component has grown. The velocity is now obviously not a simple harmonic response as seen in figure 5-7 c). Figure 5-7 d) shows some higher superharmonic activity. At 4g, as seen in figure 5-8 there is the strong presence of nonlinear components in the responses. The displacement FFT in figure 5-8 b) shows a "smearing" of frequencies especially around the driving frequency. The nonlinear effects are again more readily apparent in the velocity-time plot of figure 5-8 c). In the FFT of the velocity in figure 5-8 d), the superharmonic components are still present as at 3g, but here, there is additionally smearing around not only the driving frequency, but also around the superharmonics themselves. These superharmonics can also be seen in the waviness of the Poincaré plot in figure 5-8 e). At 5g, the laminate underwent periodic intermittent snap-through. This is shown in figure 5-9. While the

periodicity is not immediately apparent from inspection of velocity, the displacement-time plot in figure 5-9 a) shows a repeating pattern. For both the displacement and velocity FFT plots in figure 5-9 b) and d), respectively, It is more clear that the response is periodic rather than chaotic. At this level of excitation, in addition to superharmonic activity, subharmonic activity can be seen. There is a small peak at 5 Hz in both plots, or at $\frac{1}{6}^{th}$ of the driving frequency.

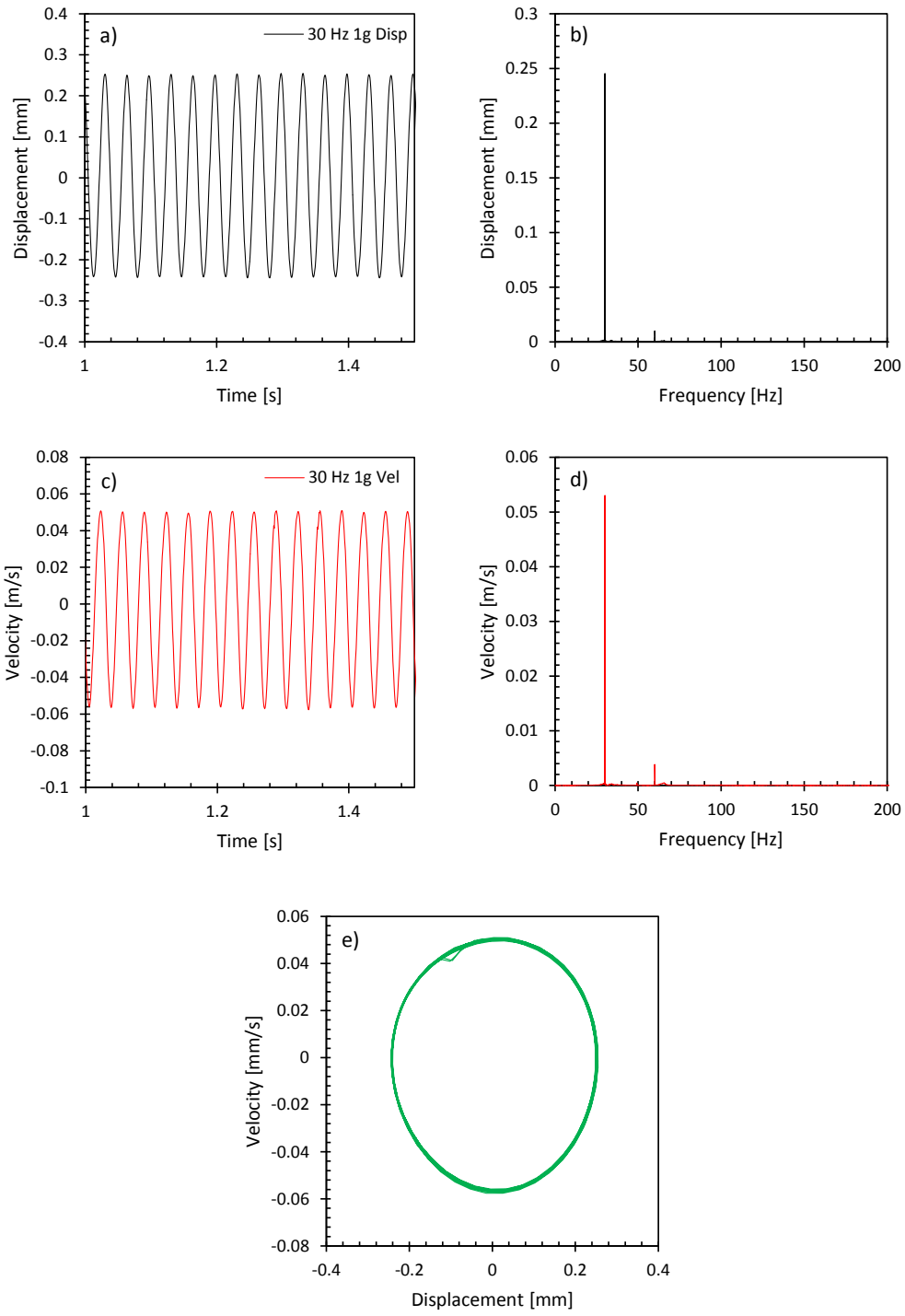

Figure 5-6: Displacement in a) time and b) frequency domain, velocity in c) time and d) frequency domain, and e) phase portrait of $[0^{\circ}_{\mathrm{MFC}}/0^{\circ}/30^{\circ}]_{\mathrm{T}}$ harvester at 30 Hz and 1g

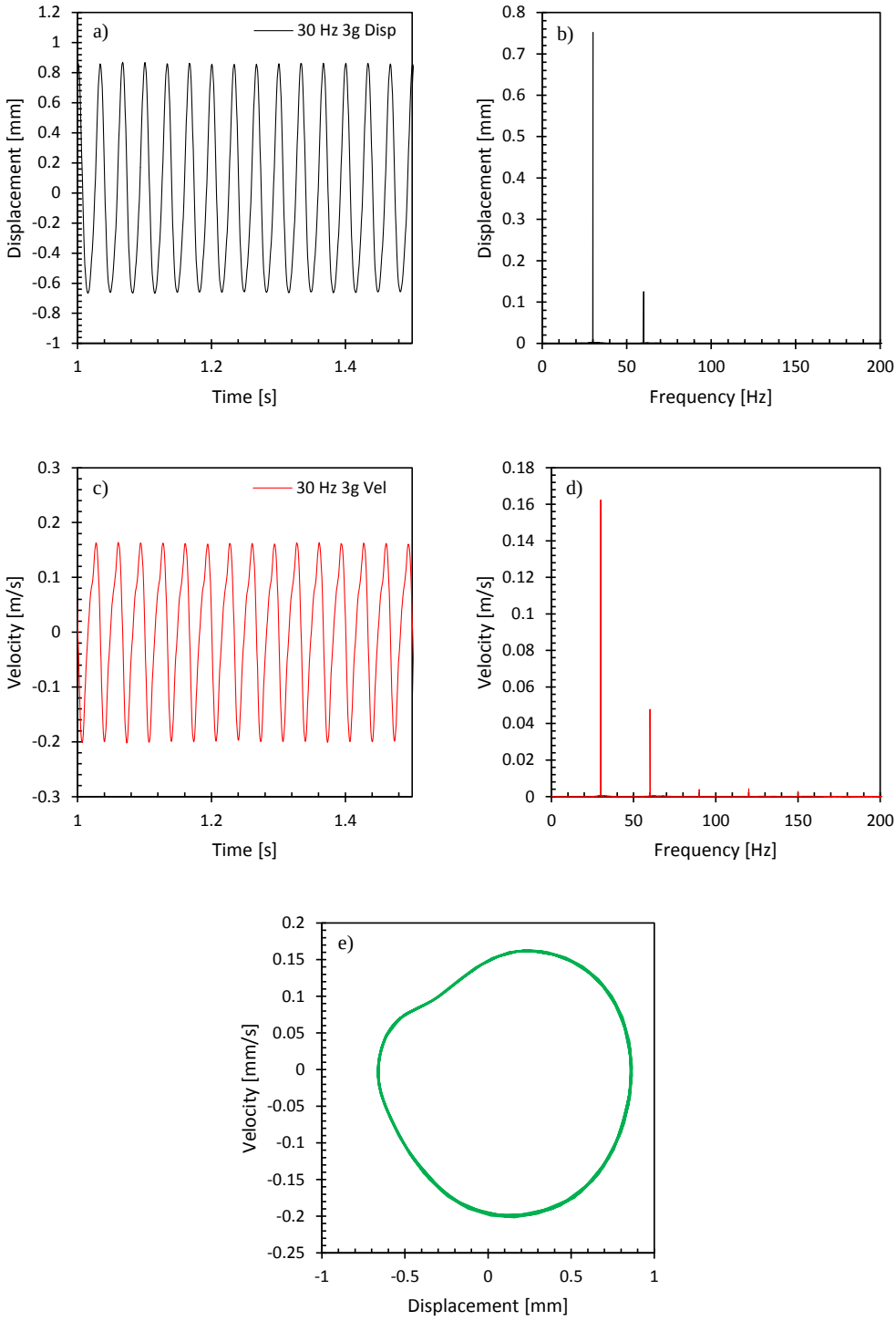

Figure 5-7: Displacement in a) time and b) frequency domain, velocity in c) time and d) frequency domain, and e) phase portrait of $[0^{\circ}_{\mathrm{MFC}}/0^{\circ}/30^{\circ}]_{\mathrm{T}}$ harvester at 30 Hz and 3g

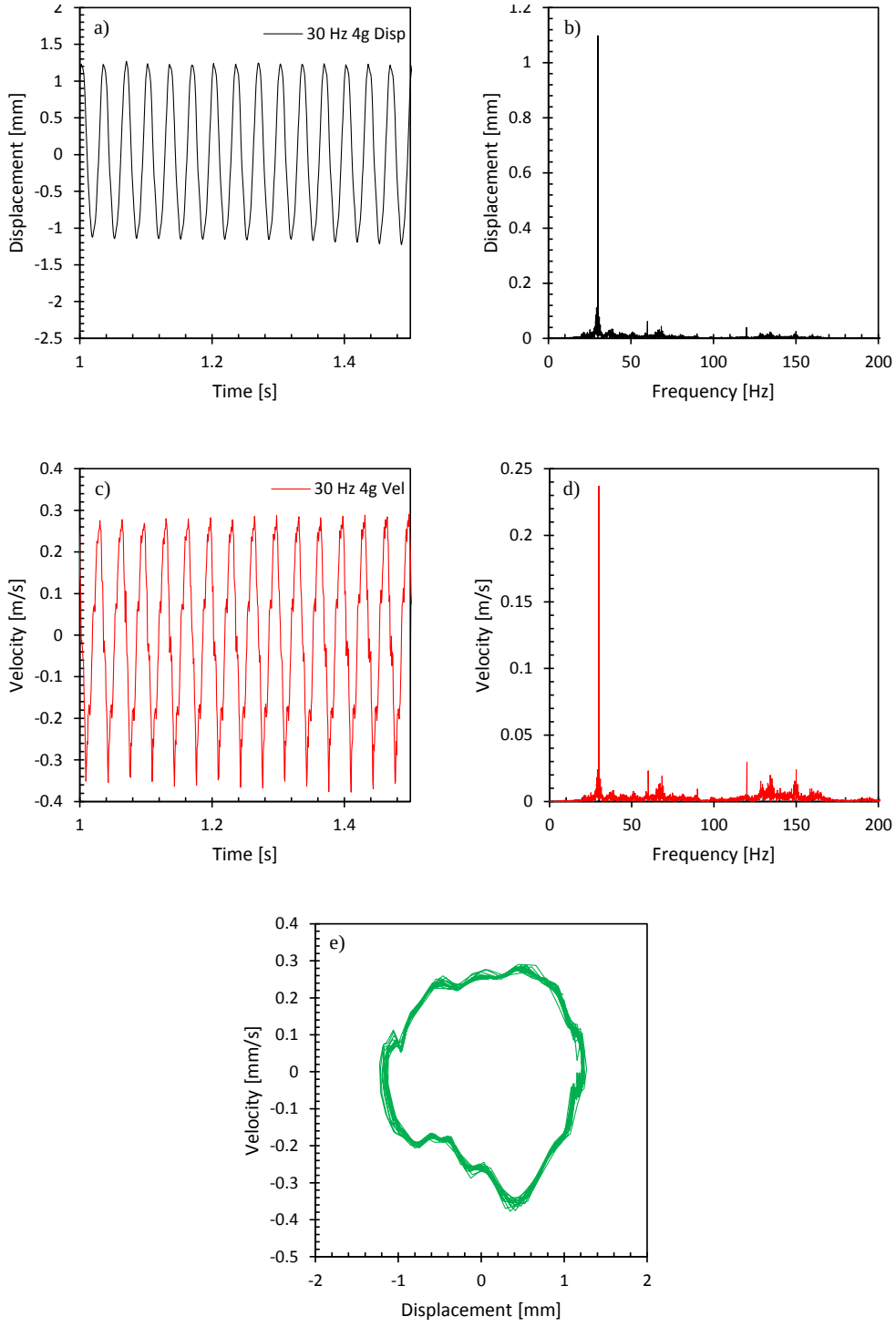

Figure 5-8: Displacement in a) time and b) frequency domain, velocity in c) time and d) frequency domain, and e) phase portrait of $[0^{\circ}_{\mathrm{MFC}}/0^{\circ}/30^{\circ}]_{\mathrm{T}}$ harvester at 30 Hz and 4g

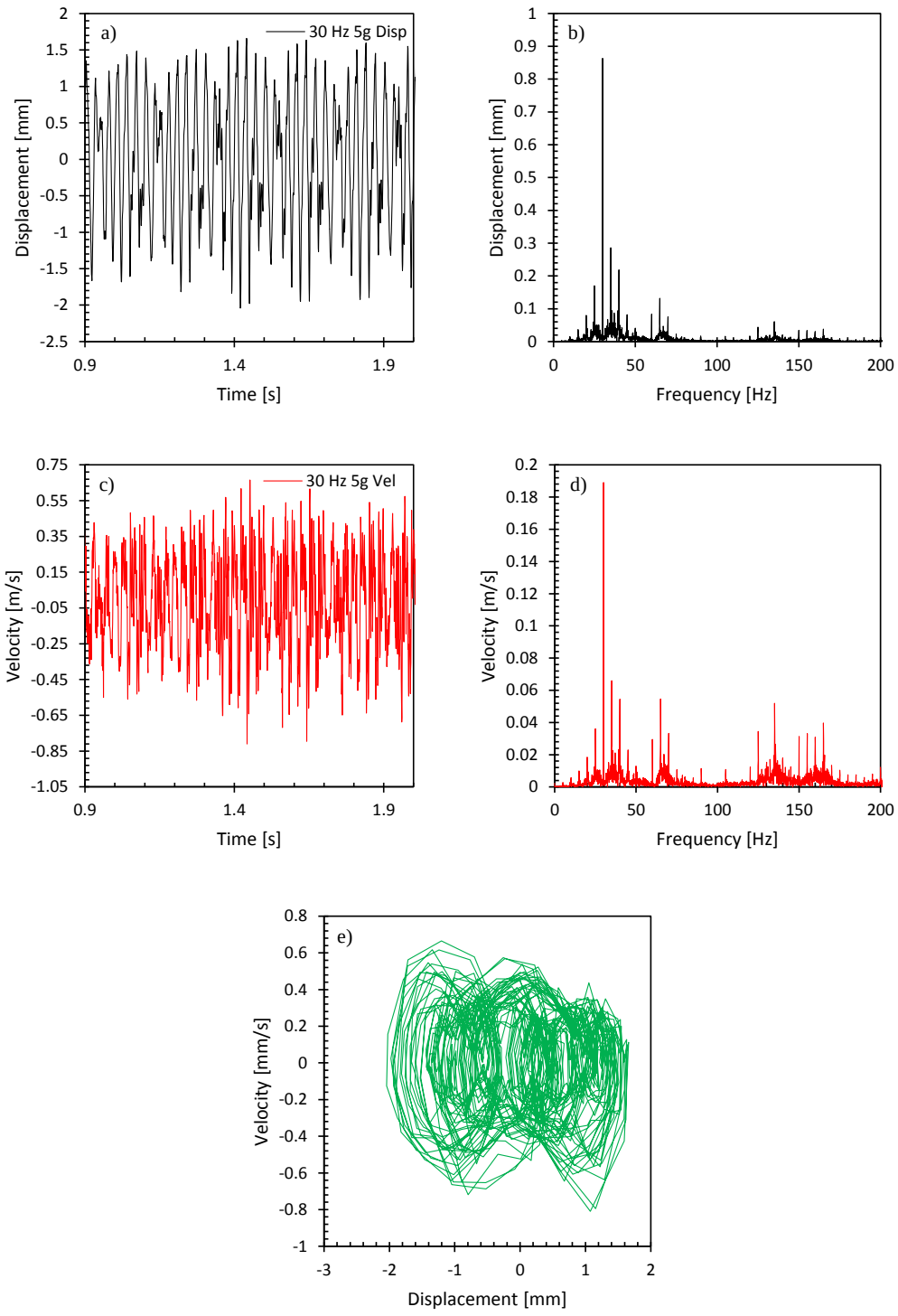

Figure 5-9: Displacement in a) time and b) frequency domain, velocity in c) time and d) frequency domain, and e) phase portrait of $[0^{\circ}_{\mathrm{MFC}}/0^{\circ}/30^{\circ}]_{\mathrm{T}}$ harvester at 30 Hz and 5g

Nonlinear Damping

Another nonlinear feature exhibited by bistable laminate energy harvesters is that the damping increases with acceleration level. The $[0^{\circ}_{\mathrm{MFC}}/0^{\circ}/90^{\circ}]_{\mathrm{T}}$ was excited at its natural frequency and time was given to approach a steady state. The shaker was then switched off, and the ringdown of the harvester was captured, as shown in figure 5-10 a). This test was carried out at increasing g levels. Each ringdown was analyzed using the logarithmic decrement technique to calculate the damping ratio ζ. The method was repeated for the $[0^{\circ}_{\mathrm{MFC}}/0^{\circ}/45^{\circ}]_{\mathrm{T}}$ but due to snap-through, the test could only be done for a limited range of accelerations. The damping ratios at increasing g is shown in figure 5-10 b) and 5-10 c). As shown, both are increasing over the range. It is likely that there are several contributing parameters to this behavior. As the displacement increases, the geometric nonlinearities will be more present. It is also likely that interactions with the air will begin to be more significant as the wind generated by the laminates becomes noticeable. Finally these high displacements could also increase the amount of hysteretic damping within the material.

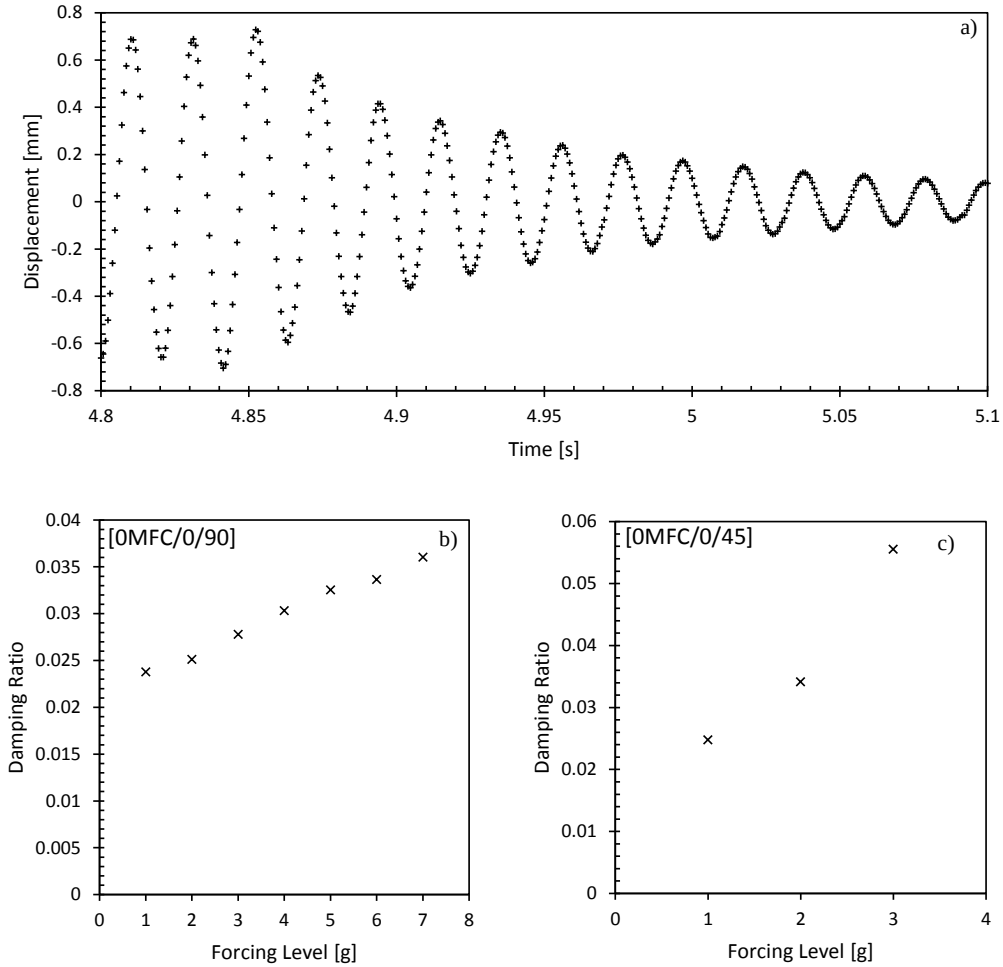

Figure 5-10: a) Example of ringdown event b) Damping at increasing acceleration for $[0^{\circ}_{\mathrm{MFC}}/0^{\circ}/90^{\circ}]_{\mathrm{T}}$ c) Damping at increasing acceleration for $[0^{\circ}_{\mathrm{MFC}}/0^{\circ}/45^{\circ}]_{\mathrm{T}}$

5.4.3 Energy Harvesting Performance Comparison of $[0^{\circ}_{\mathrm{MFC}}/0^{\circ}/90^{\circ}]_{\mathrm{T}}$, $[0^{\circ}_{\mathrm{MFC}}/0^{\circ}/30^{\circ}]_{\mathrm{T}}$, and $[0^{\circ}_{\mathrm{MFC}}/0^{\circ}/20^{\circ}]_{\mathrm{T}}$

Figures 5-11 (a, b) shows nonlinear softening of the $[0^{\circ}_{\mathrm{MFC}}/0^{\circ}/90^{\circ}]_{\mathrm{T}}$ harvester occurring with the maximum power observed at slightly lower frequencies for higher forcing levels; no snap-through between stable states was observed for this laminate. The spacing between the lines at the increasing acceleration levels is proportionate indicating linear behavior. In the case of the $[0^{\circ}_{\mathrm{MFC}}/0^{\circ}/30^{\circ}]_{\mathrm{T}}$ harvester, see figures 5-11 (c, d), the power-frequency response is bimodal. This may be due to two natural frequencies associated with different modes nearly coinciding. Snap-through was observed at vibration levels of 4g and higher for this harvester configuration. This is significantly reduced from the harvesters of chapter 4 where the square underwent snap through at accelerations higher than 11g and the saltire at 7g. This is also lower than the cantilevers of chapter 3, which experienced snap through at 5g. While the increase of power

with respect to forcing level has a clear, approximately proportional relationship in the case of the $[0^{\circ}_{\mathrm{MFC}}/0^{\circ}/90^{\circ}]_{\mathrm{T}}$, figures 5-11 (c, d) show that the nature of the relationship is less linear in the case of the $[0^{\circ}_{\mathrm{MFC}}/0^{\circ}/30^{\circ}]_{\mathrm{T}}$. The overall trend is generally increasing, but peak power is observed at 6g rather than 7g. Broadening and softening is clearly seen as the low frequency boundary moves downwards significantly over the range of forcing levels. The $[0^{\circ}_{\mathrm{MFC}}/0^{\circ}/20^{\circ}]_{\mathrm{T}}$ harvester underwent snap-through from vibration levels of 2g, see figure 5-11 (e, f). The peak power output exceeded that of the $[0^{\circ}_{\mathrm{MFC}}/0^{\circ}/30^{\circ}]_{\mathrm{T}}$. Due to the low frequencies associated with this configuration, the shaker was unable to operate throughout the full range of frequencies required for full characterization. As a result of the constant acceleration scheme implemented, high displacements are required at lower frequencies as well as high power demands on the shaker's driving amplifier. From vibration levels of 4g onwards, the harvester underwent cross-well oscillations from the lowest frequency available for the given forcing levels. In order to better understand and compare the harvesters, several parameters are calculated and now discussed. Maximum (peak) power output for the different acceleration levels for the three laminate configurations are shown in figure 5-12a) to indicate the maximum peak performance. The power generated at each forcing level is then summed up using a trapezoidal integration scheme and the bounds of the integral are set at the frequencies where the power output falls to one-tenth of the peak power output, this data is shown in figure 5-12b). This indicates the overall performance for the harvesters at the different forcing levels. The peak power of the $[0^{\circ}_{\mathrm{MFC}}/0^{\circ}/30^{\circ}]_{\mathrm{T}}$ increases as the vibration level increases but levels off from the onset of snap-through at 4g onwards. The $[0^{\circ}_{\mathrm{MFC}}/0^{\circ}/20^{\circ}]_{\mathrm{T}}$ is continually increasing throughout the range with a jump in power between 5g and 6g. The summed power plot in figure 5-12b) shows the continual increase of power for the $[0^{\circ}_{\mathrm{MFC}}/0^{\circ}/90^{\circ}]_{\mathrm{T}}$ harvester. It also shows that despite the decreasing peak power of the $[0^{\circ}_{\mathrm{MFC}}/0^{\circ}/30^{\circ}]_{\mathrm{T}}$, in terms of summed power, it is continually increasing over the range due to broadening and the harvested power being distributed across a larger range of frequencies. Since the true value of the $[0^{\circ}_{\mathrm{MFC}}/0^{\circ}/20^{\circ}]_{\mathrm{T}}$ harvesters summed power is greater than could be measured due to the frequency range of the shaker, the highlighted points are likely to be closer to the $[0^{\circ}_{\mathrm{MFC}}/0^{\circ}/90^{\circ}]_{\mathrm{T}}$ summed power than shown in figure 5-12b.

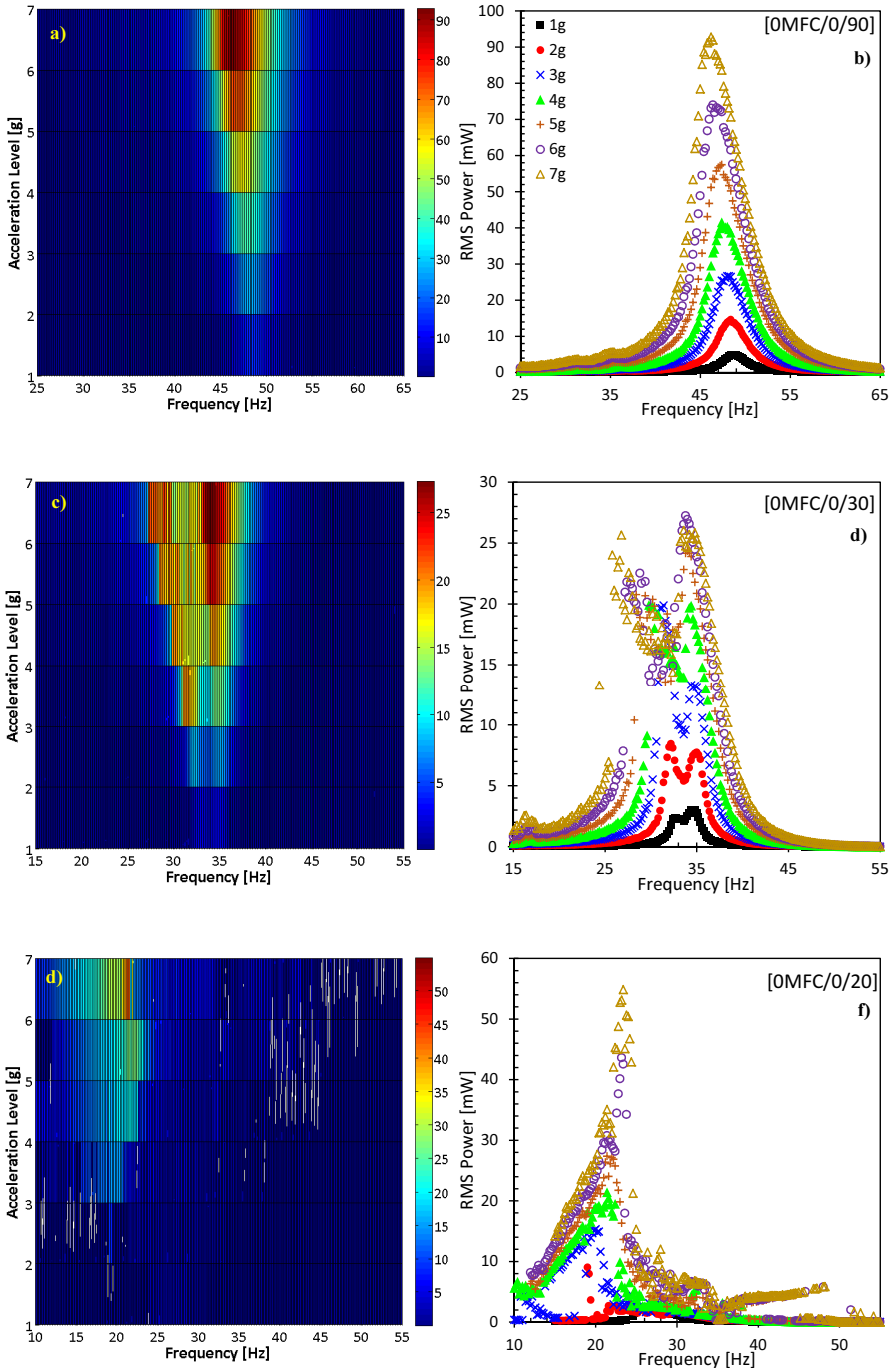

Figure 5-11: a), c), e) power maps of the $[0^{\circ}_{\mathrm{MFC}}/0^{\circ}/90^{\circ}]_{\mathrm{T}}$, $[0^{\circ}_{\mathrm{MFC}}/0^{\circ}/30^{\circ}]_{\mathrm{T}}$, $[0^{\circ}_{\mathrm{MFC}}/0^{\circ}/20^{\circ}]_{\mathrm{T}}$ as a function of frequency and vibration amplitude b), d), f) corresponding power versus frequency for the harvesters.

Thus, despite having lower power output, the actual energy harvested for the $[0^{\circ}_{\mathrm{MFC}}/0^{\circ}/20^{\circ}]_{\mathrm{T}}$

is similar to the $[0^{\circ}_{\mathrm{MFC}}/0^{\circ}/90^{\circ}]_{\mathrm{T}}$. The half power bandwidth in figure 5-12c) shows a slight upward trend with increasing vibration level for the $[0^{\circ}_{\mathrm{MFC}}/0^{\circ}/90^{\circ}]_{\mathrm{T}}$ harvester, Significant broadening is not expected as its behavior is mostly linear. This harvester the narrowest bandwidth at about 6 Hz. The $[0^{\circ}_{\mathrm{MFC}}/0^{\circ}/30^{\circ}]_{\mathrm{T}}$ harvester has a strongly increasing half power bandwidth, especially from the onset of snap-through at 4g onwards. The broadness of 7g is nearly twice that of the $[0^{\circ}_{\mathrm{MFC}}/0^{\circ}/90^{\circ}]_{\mathrm{T}}$ harvester. Due to the more erratic behavior of the $[0^{\circ}_{\mathrm{MFC}}/0^{\circ}/20^{\circ}]_{\mathrm{T}}$ with wide fluctuations of power, there is no clear trend. Nevertheless the performance parameters show particularly strong performance at 4g and 5g. These values of peak power and power bandwidth are significantly higher than the cantilevers of chapter 3. The peak power seen by the linear harvester was 20 mW over a bandwidth of 3.8 at 6g for the third mode, and only 12.8mW at 2.1 Hz for the second mode which occurs within this frequency range. The $[0^{\circ}_{\mathrm{MFC}}/0^{\circ}/90^{\circ}]_{\mathrm{T}}$ harvester's peak power value was over 4 times this value, and at higher bandwidth at just under 6 Hz. The bistable cantilever had slightly higher bandwidth at 8.4 Hz, but at 7.3 mW. The main reason for the difference in power output is because the piezoelectric area is larger here (85x57 mm vs 85x28 mm) and is also more effectively strained based on the mode shape of the laminates and the location of the patch relative to the clamping point. The $[0^{\circ}_{\mathrm{MFC}}/0^{\circ}/30^{\circ}]_{\mathrm{T}}$ is responding at nearly 6 times the bandwidth of the linear cantilever.

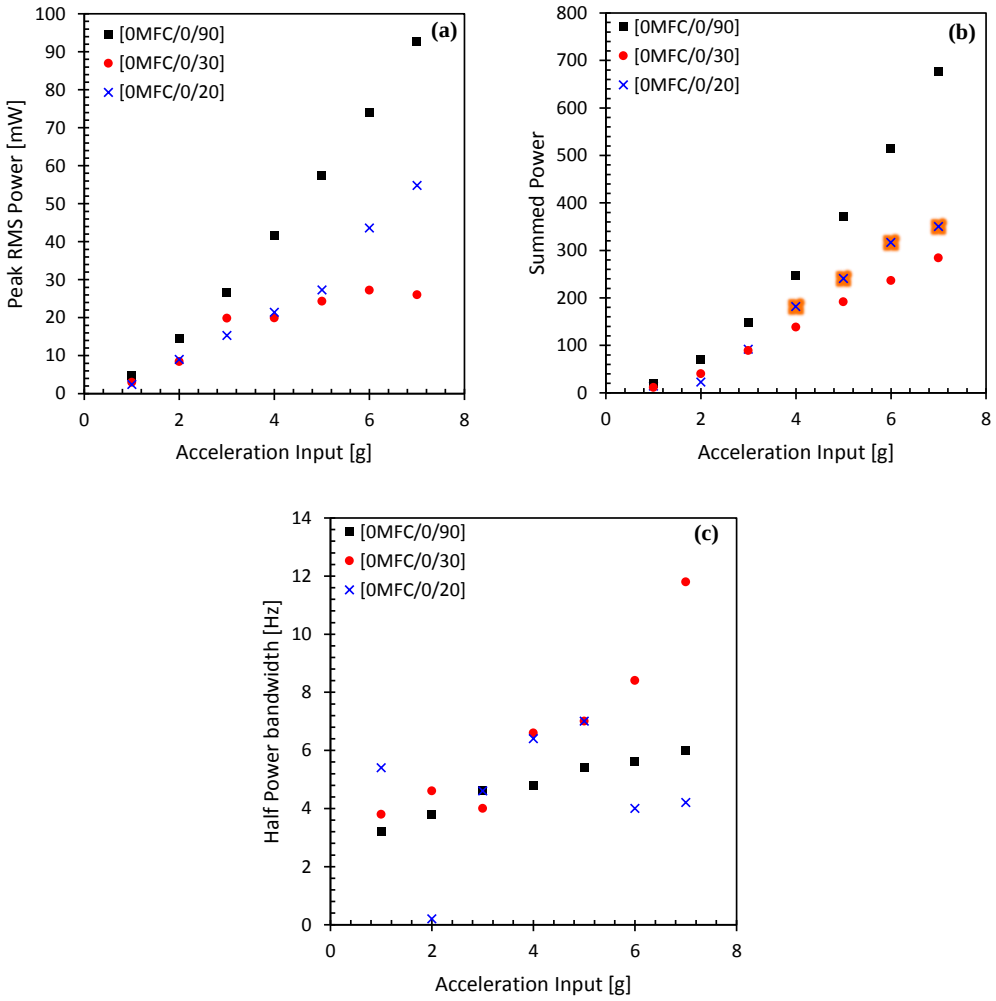

Figure 5-12: a) peak power of harvesters b) summed power of harvesters c) operational bandwidth of harvesters

5.5 Conclusions

This chapter has examined non-orthogonal laminates for nonlinear energy harvesting. The first objective of establishing the benefit of changing the second ply angle was addressed by showing that adjusting the ply angle is an effective approach in reducing the acceleration required to trigger cross-well oscillatory dynamic modes. The snap through acceleration was decreased from over 11g for a $[0^\circ_{\mathrm{MFC}}/0^\circ/90^\circ]_{\mathrm{T}}$ to 4g for a $[0^\circ_{\mathrm{MFC}}/0^\circ/30^\circ]_{\mathrm{T}}$ and 2g for a $[0^\circ_{\mathrm{MFC}}/0^\circ/20^\circ]_{\mathrm{T}}$.The relationship of this design parameter with respect to harvested power was investigated and it was shown that the decrease of stiffness from the smaller angle between plies reduces the natural frequency from approximately 50 Hz for the stiffest laminate ($[0^\circ_{\mathrm{MFC}}/0^\circ/90^\circ]_{\mathrm{T}}$), to 25 for the $[0^\circ_{\mathrm{MFC}}/0^\circ/20^\circ]_{\mathrm{T}}$. The results indicate that there is trade-off between the peak power output and the bandwidth of the harvesters. Despite lower power output, the total energy

harvested of the small angle harvesters is still comparable to the high-angle harvesters. The broadness of the response was increased from 6 to 12 Hz. The second objective was studying the gradual emergence of nonlinear effects. The Poincaré study showed a departure from a round, harmonic response to an egg-shaped response as the stiffness bias in the two directions became more apparent. The presence of subharmonics could be seen in the jaggedness of the orbits, and finally some cross-well oscillatory cases were examined. The damping ratio was seen to increase over the forcing range. The small angle laminates are shown to exhibit nonlinear features in their response to frequency at lower excitation levels. Additionally, frequency matching between the two states of bistable harvesters is proposed as a means of increasing harvester performance.

This chapter has presented an effective method whereby the acceleration required for snap-through was reduced. However, both this method and the method of removing material presented in chapter 4 are permanent. Once the energy harvester is deployed and in use, there is no way of re-tuning should there be a significant change in the excitation parameters. The next chapter returns to cantilevers and introduces a novel method using magnets whereby the characteristics of a bistable cantilever can be adjusted non-permanently

This major findings of this chapter can be summarized:

- The snap-through acceleration is effectively reduced from greater than 11g to 2g by reducing the angle between the laminate's two plies
- The broadness of the response of the non-orthogonal outputs is shown to be nearly twice that of the orthogonal harvester at 12 Hz rather than 6 Hz because snap-through was encountered at lower acceleration levels
- The gradual emergence of nonlinear features were shown such as the damping ratio is shown to vary linearly with respect to acceleration input, showing a gradual transition from the linear behavior regime to the nonlinear regime

Chapter 6

A Doubly Bistable Cantilever Energy Harvester

This chapter returns to cantilever bistable laminate energy harvesters. In chapter 3, the addition of a proof mass allowed for the snap-through acceleration to be reduced from 5g to 4g. Here, a new method whereby this snap-through acceleration can be non-permanently adjusted is presented. This chapter seeks to address two objectives. The first objective is to assess the benefit of superimposing a secondary, magnetically-induced bistable field upon the already existing bistable field inherent to the cantilever resulting from thermal interactions. This secondary field is imposed by putting a magnet at the tip of the cantilever, and constructing a frame outside the cantilever with an identical magnet aligned to put the cantilever into compression. This magnetic gap is adjusted to investigate the relationship between the magnetic gap and the energy harvesting performance of the cantilever. The second objective is to model the behavior of the cantilever using an empirical single degree of freedom model. This model is derived and the relevant parameters are experimentally identified. The model's output is compared against experimental results.

6.1 Introduction

This chapter extends the work of chapter 3 by presenting a novel non-permanent method for tuning the dynamic characteristics of a cantilever bistable laminate energy harvester. The ability of two magnets in repulsion to create a dual potential well was utilized to tailor the response of a bistable cantilever highly similar in construction to that of chapter 3. The objective was to sum together the potential wells of the cantilever's inherent thermally induced bistability with the bistability resulting from the magnetic interactions. A magnet was fixed to the tip of the cantilever, and an identical magnet was anchored to a frame with the poles oriented to repel. The anchored magnet was set at the end of a threaded shank. This allowed for the fine adjustment of the vertical position of the upper magnet and therefore the gap between

the magnets. By modifying the gap's distance, the extent of the magnetic field's participation can be varied from negligible to dominating the bistable field of the cantilever. This allows for the natural frequency of the harvester-magnet system to be located anywhere within a range where the lower bound is set by the non-magnetic case of solely the cantilever, and the higher bound is set by the magnet's properties. In chapters 4 and 5, methods for changing the dynamics of the harvester were introduced, but these were permanent. The aim of this method is to introduce a finely adjustable, non permanent means of altering the dynamics of the harvester.

6.2 Experimental Characterization and Measurements

Since the benefit of a bistable energy harvesting system stems from its nonlinearity and broadband response, the major contributing factors giving rise to device nonlinearities are investigated. The main factors that contribute such a response are first, the forces resulting simply from the magnetic interactions and second, the bistable strain energy landscape of the system. Both the magnetic interaction and nonlinear strain energy landscapes are characterized by measurement of their force-deflection functions experimentally. The construction of the bistable energy harvester is then detailed. Subsequently, the damping ratio of the cantilever is determined by applying the logarithmic decrement method (LDM) to the measured open-circuit voltage, which is the method used in chapter 5. Since the extent of nonlinearity due to the presence of the magnet is tunable by adjusting the separation distance between the magnets, the effects of this upon the energy harvesting capability is then investigated by undertaking sweeps through the frequency range of interest at constant acceleration. The control of the measurement system is presented as well as the measurement of the root mean squared (RMS) power for each frequency/acceleration combination in the explored parametric space. These sweeps are evaluated against a control case where there is no magnetic interaction.

6.2.1 Measurement of Transverse Magnetic Force as a Function of Magnet Separation

The transverse magnetic force as a function of the separation distance between the magnets was measured by mounting a neodymium magnet vertically and fixing it to a digital load cell (see Figure 6-1a). The second magnet was fixed to a vertical rail such that the gap between the magnets in the horizontal direction and their relative displacement in the vertical direction could be adjusted, as shown. A range of magnet separations (gap widths) at different vertical displacements were recorded, and the results are shown in Figure 6-1b).

6.2.2 Manufacture of the Bistable Cantilever Energy Harvester

The bistable cantilever energy harvester was manufactured from carbon fiber reinforced plastic (CFRP) plies of unidirectional UDM 194 carbon fiber in an M21 epoxy matrix. This is the same cantilever that was used in chapter 3, but shortened and with an added receptacle fixed

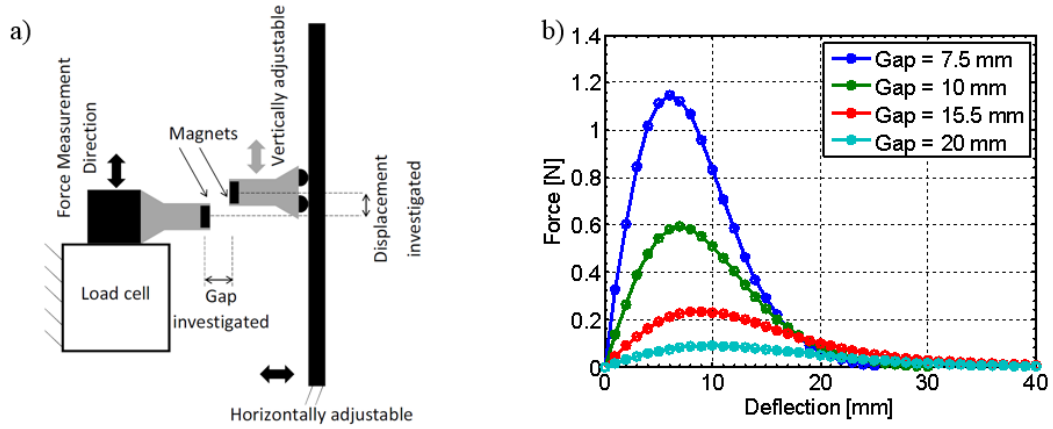

Figure 6-1: a) Schematic of method used for measuring magnetic force-deflection function and (b) the force deflection function of the magnets at the indicated gap distances and displacements

to the end to hold the magnet. A smart materials piezoelectric M8528-P2 Macro Fiber Composite (MFC) patch was attached to the cantilever using an epoxy adhesive for transduction of mechanical strain energy into electrical energy, as shown in Figure 6-2. The MFC is based on a lead zirconium titanate (PZT) ferroelectric ceramic which is polarised through its thickness. This is in contrast to most MFC configurations with an interdigital electrode (IDE) where the polarization direction is along the fiber length and is characterized by a low efficiency. In this case the M8528-P2 device is polarized through thickness by continuous upper and lower electrodes. Compared to an IDE based device such a configuration has more uniform electric field distribution, and high device capacitance, leading to low peak voltages as a result of the piezoelectric charge [158].

As a result of the construction of the MFC patch with lead zirconate titanate (PZT) fibers running along the longitudinal axis and being embedded in a polymer matrix, the resulting anisotropy requires that the directionality of the patch be also stated in any stacking sequence. The cantilever's free length was 210 mm with an additional 30mm for clamping between two aluminum plates. The width of the laminate was 60 mm, and the ply thickness between 0.185mm and 0.195mm. In the clamped region (left hand side of Figure 6-2a), two additional plies were included to make the beam locally monostable so that the clamping would not restrict the curvature of the cantilever. Thus, the stacking sequence at the clamped end is $[0^{\circ}_{\mathrm{MFC}}/0^{\circ}/0^{\circ}/90^{\circ}/90^{\circ}/0^{\circ}/0^{\circ}]_{\mathrm{T}}$ but the sequence for the majority of the beam is $[0^{\circ}_{\mathrm{MFC}}/0^{\circ}/0^{\circ}/[90^{\circ}/90^{\circ}]_{\mathrm{T}}$. A small fixture was adhered at the end of the cantilever to receive the magnet, as shown on the right of Figure 6-2 a). To investigate the change of the energy harvesting characteristic with respect to magnetic separation distance a metal tubular structure was constructed such that another magnet, with the same characteristics as that fixed to the cantilever tip, could be affixed to the end of a bolt for easy adjustment of the vertical

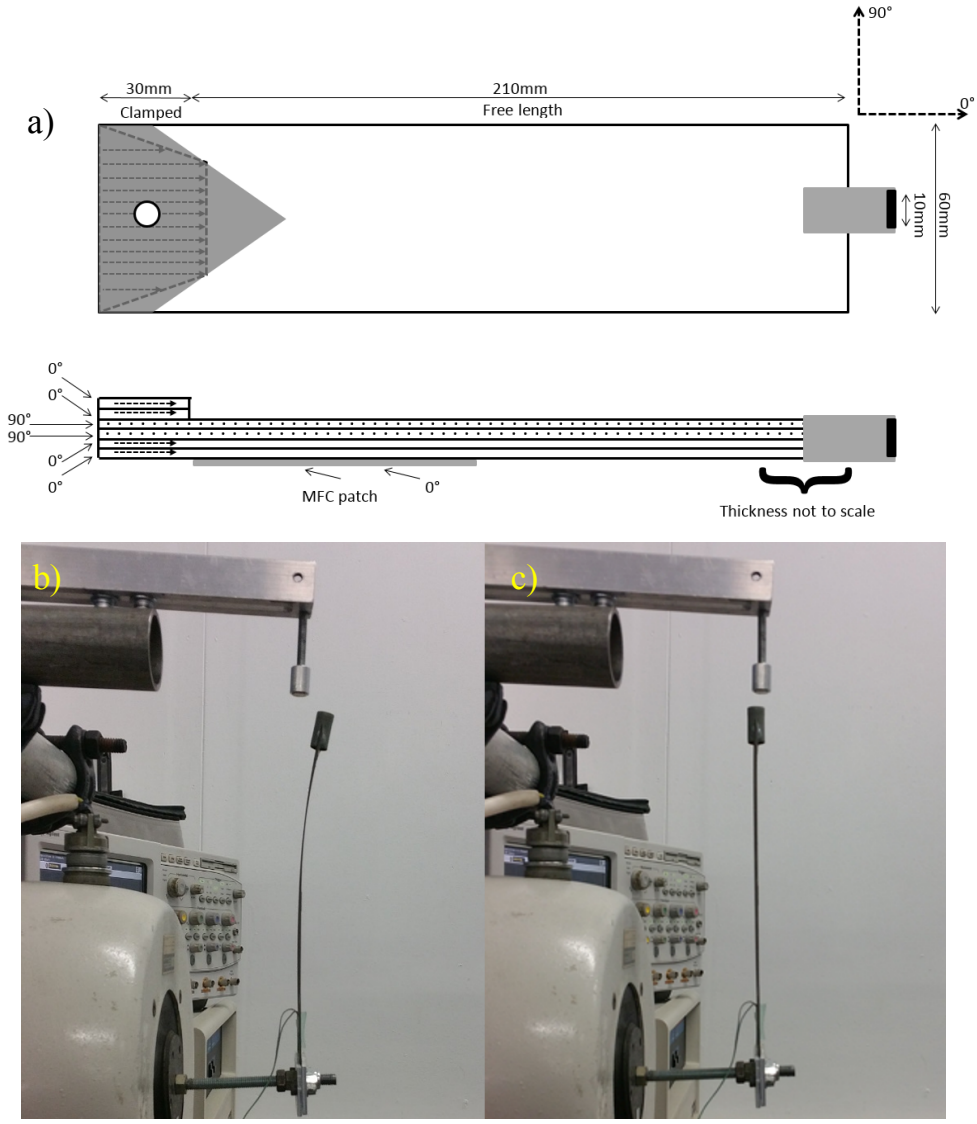

Figure 6-2: a) Detail of the ply orientations, magnet location and MFC location b) Stable state 1 and c) Stable state 2

displacement, as shown in Figures 6-2b) and 6-2c).

6.2.3 Calculation of Damping Ratio Using the Logarithmic Decrement Method (LDM)

Since the open circuit voltage of the energy harvester can be used as a reliable proxy for the tip displacement, and its ease of measurement, this quantity was used for determining the damping ratio of the system. An oscilloscope probe was placed across the electrode terminals of the MFC, and the harvester's aluminium clamping plates were held firmly. The harvester was perturbed and the ring-down of the voltage with time was recorded. Several such tests were carried out; one example of which appears in Figure 6-3.

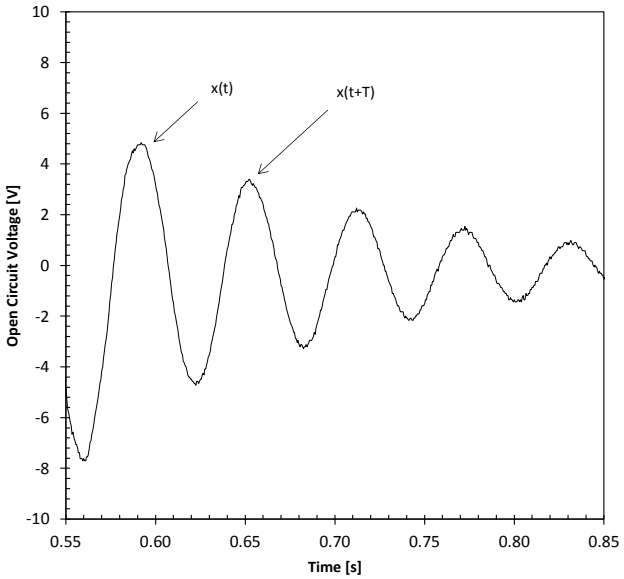

Figure 6-3: Open circuit voltage of harvester ring-down

The damping ratio ζ was calculated using the equations 6.1 and 6.2 from [191]:

$$\delta = \ln \frac{x(t)}{x(t+T)} \tag{6.1}$$

$$\zeta = \frac{\delta}{\sqrt{4\pi^2 + \delta^2}} \tag{6.2}$$

Where $x(t)$ refers to the magnitude of one local maximum, and $x(t+T)$ corresponds to the magnitude of the next local maximum as shown in Figure 6-3. Twenty values of δ were found from five runs, and ζ was calculated to be 0.0634.

6.2.4 Measurement of the Force-Deflection Characteristics of the Bistable Cantilever and its Hysteresis

The force deflection curve was measured on an Instron 3365 tensile tester with a 100 N load cell. In Figures 6-4a) and 6-4b), a positive displacement is defined to be displacement towards the second, or curved state. A negative displacement is in the opposite direction.

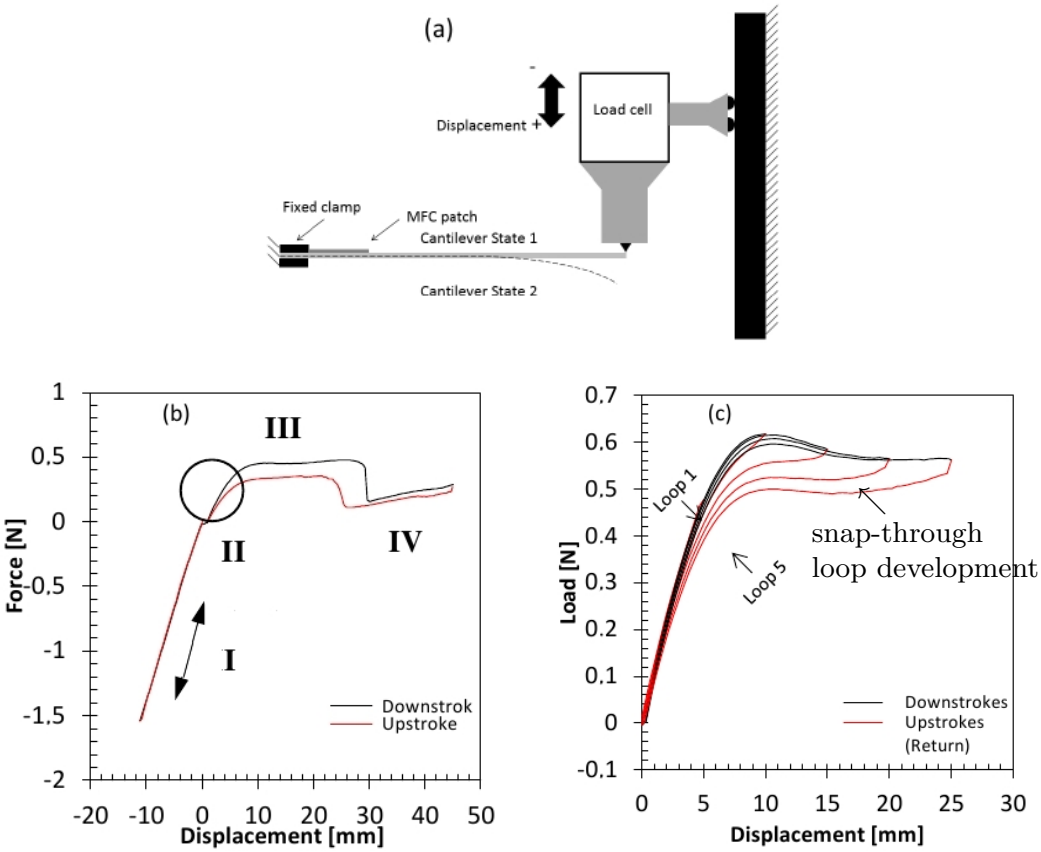

Figure 6-4: a) Schematic of bistable cantilever's orientation used during tensile testing. b) Composited displacement-force function for the bistable cantilever harvester. Region I is the region in which the cantilever is bent in the direction opposite to snap through Region II is the region magnified in Figure 6-4c. Region III is the snap through and snapback section. Region IV is the cantilever being stressed in state 2. c) loading/unloading curves just prior to snap-through

The cantilever was immobilized and the cross head was moved downwards at a rate of approximately 4 mm/s and then returned upwards to the starting position, recording the load cell force on both the downward and upward motions. For the positive displacement portion of the graph, 20 up-and-down loops were compiled to produce Figure 6-4b, and nine loops were undertaken for the negative side. To compile multiple results together for robustness, each individual loop was first considered separately. As a result of slight differences in the descent

rate at each time step, the loops could not be simply averaged together. Thus, for each loop, a linear interpolation was done between all the measured points such that the interpolated points all had exactly the same x-coordinate, but with a y-coordinate specific to that particular loop. These interpolated loops were then averaged together to produce Figure 6-4b). To investigate the hysteresis up to the point of snap-through (Figure 6-4c), first a cross-head displacement of 5 mm was undertaken and the displacement was then gradually increased by 5 mm increments to 25 mm.

6.2.5 RMS Power Frequency Sweeps

Four magnet separation distances of 20, 15.5, 10 and 7.5 mm were investigated and compared against the condition of no magnetic interaction, as shown in Figure 6-5.

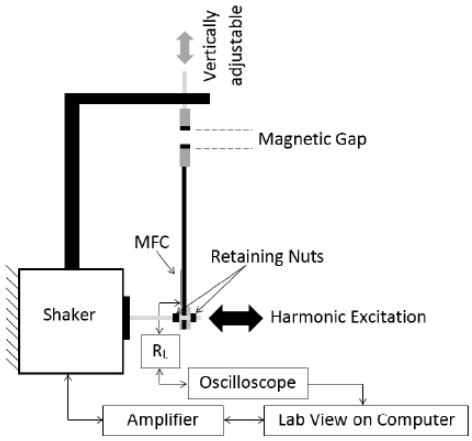

Figure 6-5: Supporting frame with vertically adjustable magnet and electromechanical shaker. Control and voltage acquisition equipment schematically represented

For the case of no magnetic interaction, the magnet was present within the cantilever's tip to maintain experimental consistency, but the second magnet, which was mounted to the frame, was removed. At each of the magnet separations, the harvester was harmonically excited from 12 to 30 Hz in increments of 0.2 Hz. At each frequency step ($\Delta\omega$), a voltage signal over a load resistor was measured using an Agilent oscilloscope and an RMS power was calculated. The shaker was calibrated using a Lab View routine to deliver constant acceleration at required frequencies. The LDS 455 shaker was calibrated by exciting the shaker with a sine wave of controlled amplitude and frequency running through the LDS PA 1000 amplifier. A matrix of voltage amplitudes and frequencies were sent to the shaker, and the response was measured using a Polytech laser differential Vibrometer which measured the velocity using the PSV-400-M4 scanning head, OFV-5000 controller and VD-09 velocity decoder. The peak acceleration was calculated from the velocity data and saved in the calibration file using a LabView routine running on a computer. When a specific acceleration is required at a desired frequency, another routine interpolates between the nearest voltages to deliver the needed acceleration magnitude.

At each frequency, the acquisition system ignores the first 0.2 seconds of data to allow the harvester to be in a steady state. Approximately five seconds of voltage data is then acquired by the oscilloscope over the load resistor, so that the RMS power can be calculated from the RMS voltage. Each of the forcing levels was repeated five times, and the results were averaged for robustness. The results of these power sweeps appear in figure 6-6. The matching load resistor was found using the impedance matching formula $R_L = 1/2\pi fC$ [192]. Here, R_L is the load resistance value required to maximize power output, C is the capacitance of the MFC patch, and f is the natural frequency of the cantilever. The patch capacitance was measured to be 156.5 nF, and the natural frequency found to be 21 +/-1Hz, giving the value of the optimum load resistor to be 48 kΩ, which was used throughout the harvesting experiments.

The frequency sweeps shown in figure 6-6 have been carried out with increasing frequency. For the case of no magnet, i.e. an infinitely large magnetic gap, snap-through of the cantilever was observed at 3g (Figure 6-6b). As the magnetic separation was decreased, the acceleration required to induce snap-through oscillations was decreased. At a magnetic separation of 15.5 and 10mm, snap through was observed at 2g (Figure 6-6b), as compared with 5g for chapter 3. Interestingly, at a magnetic gap of 10 mm, the potential fields of the magnets and thermal stresses coincided such that the system was effectively tristable. At the magnetic gap of 7.5mm, the magnetic interaction was strong enough that no snap-through was observed at any forcing level. In addition to the results shown, the decreasing frequency sweeps were recorded but are not shown for sake of clarity and brevity.

The peak power outputs for the different forcing levels and different gap distances are shown in table 6.1 for both upsweep (increasing frequency) and downsweep (decreasing frequency). Where the addition of magnetic interaction has increased the peak power level with respect to the baseline of no magnet, or led to a reduction in harvested power, this is shown by the + and - signs in the parenthesis in table 6.1. A trend emerges wherein the closer magnetic separations, in particular 10mm and 15.5mm, improve the peak power output at higher excitation levels of 2g and 3g. The broadband energy harvesting capability of the system is measured based on the bandwidth at which at least half the maximal power output is generated. Since the lower frequency bound for half-maximum power could not always be observed, the higher-frequency extent of the harvested power was considered. Given the asymmetry of the shape of the RMS power generated, this is the more informative dimension as the onset of power generation is usually sudden and then gradually decreases with increasing frequency.

6.3 Mechanical Model

The modeling work undertaken in this section was done in collaboration with Dr. Mustafa Arafa of the American University in Cairo. Chapter 4 presented an analytical model where the strain energy as a function of displacement was calculated based on the material properties of the piezoelectric patch and carbon composite substrate. At the end of the chapter, it was concluded that the method used possibly resulted in an oversimplified representation of the strain functions. The model presented here uses empirical data as its inputs to circumvent such

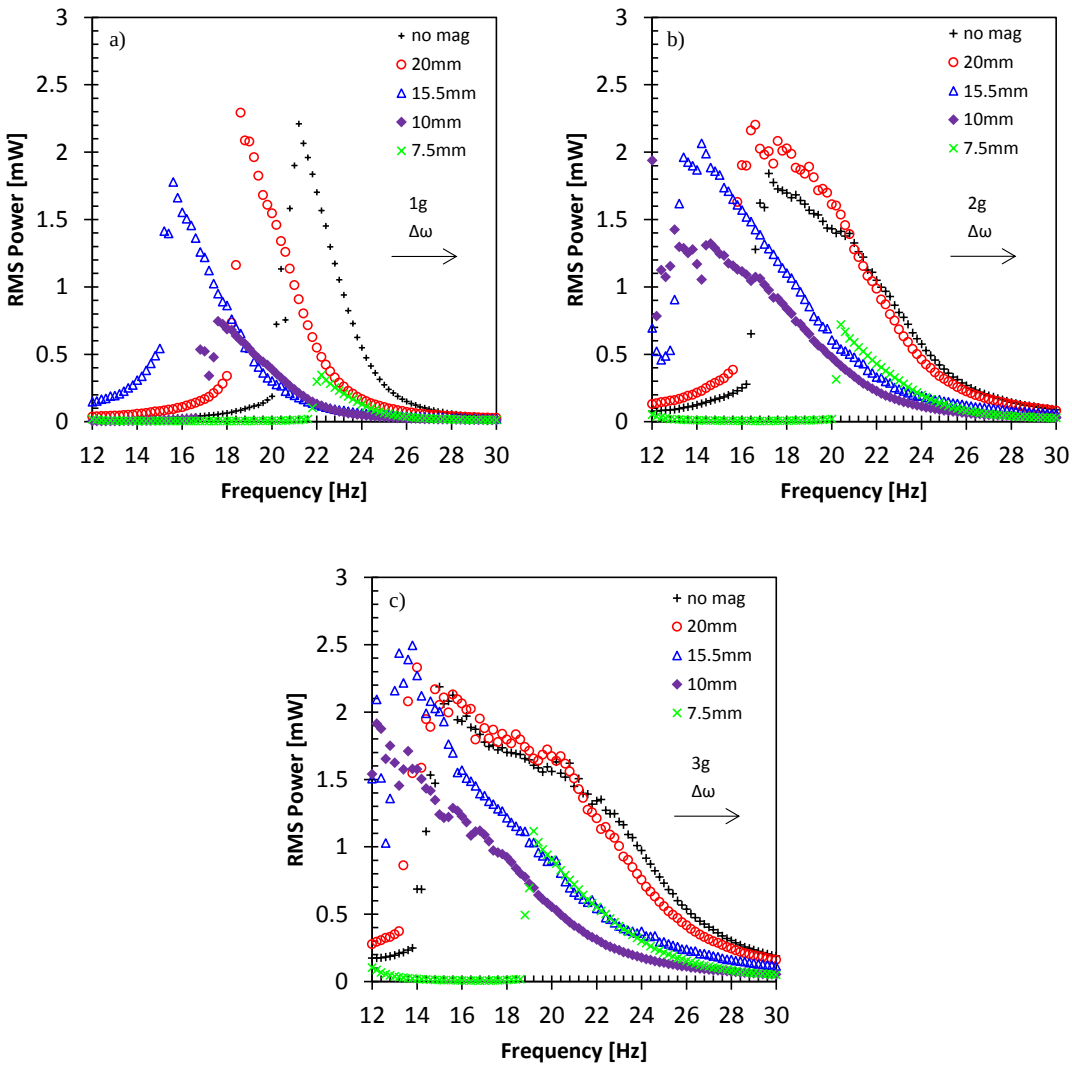

Figure 6-6: RMS power from frequency sweeps at a) 1g, b) 2g, c) and 3g

errors resulting from simplifications. The implementation is more simple than the analytical model, but has the disadvantage that it can only model existing laminates that have been characterized. Figure 6-7 shows a schematic illustration of the force-deflection characteristic curve for the bistable cantilever beam, based on the experimental data in Figure 6-4. Starting with zero initial deflection (point A), loading causes the deflection to follow branch AB. At point B, the beam undergoes snaps-through, leading to an abrupt reduction in the force (point C), from which point a further increase in the deflection occurs along branch CD. Upon load reversal (point D), the beam exhibits a hysteretic behavior featured by a force reduction from point D to E. Subsequent reduction in deflection (unloading) causes the characteristic to follow branch EF. The beam snaps back at point F*, wherein the force suddenly increases to the value corresponding to point G*. A further decrease in the deflection occurs along branch G*A

Table 6.1: Effect of magnetic gap distance on peak power output for the considered g levels for increasing and decreasing frequency sweeps

Upsweep–Frequency Increasing ($\Delta\omega > 0$)						
Gap [mm]	**1g Max Power**	**Bandwidth [Hz]**	**2g Max Power**	**Bandwidth [Hz]**	**3g Max Power**	**Bandwidth [Hz]**
∞	2.31 [mW]	1.6	1.84 [mW]	5.4	2.19 [mW]	8.2
20	+3.73%	2	+19.58%	4.8	+6.59%	8
15.5	–19.54%	2.2	+12.17%	4	+14.08%	4
10	–66.27%	2.4	+5.32%	5.2	+19.07%	5.2
7.5	–84.32%	1.2	–60.87%	2	–49.03%	2.6
Downsweep–Frequency Decreasing ($\Delta\omega < 0$)						
Gap [mm]	**1g Max Power**	**Bandwidth [Hz]**	**2g Max Power**	**Bandwidth [Hz]**	**3g Max Power**	**Bandwidth [Hz]**
∞	2.44 [mW]	2	1.95 [mW]	6.6	2.2 [mW]	8.4
20	–7.78%	2.4	+13.87%	5.2	+3.25%	8.6
15.5	–22.19%	3.4	+8.78%	5.4	+11.00%	5.8
10	–69.19%	2.6	–7.29%	5	+105.14%	5.6
7.5	–85.11%	1.6	–63.38%	2.6	–47.94%	3.6

back to the initial state. Load reversals after the snap through (BC) and before the snap back (F*G*) are exhibited by a hysteretic load cycle DEFG. Similarly, following the unloading path from G* to A, then reversing the load direction at point H (before reaching point A) results in a hysteretic behavior shown by an increase in the force from H to J, after which the loading cycle follows branch AB.

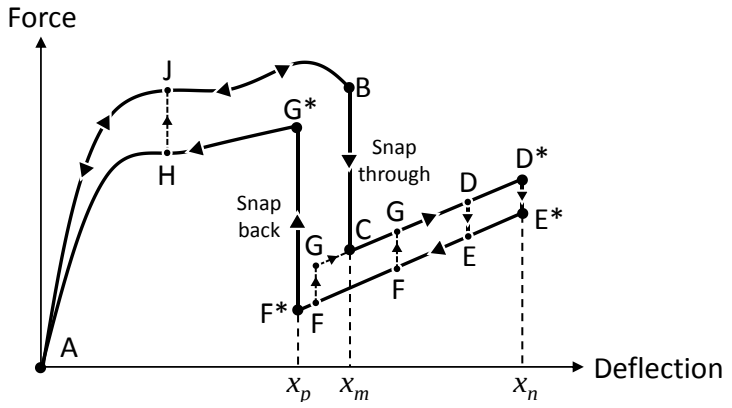

Figure 6-7: Force-deflection characteristic curve for bistable beam

Referring to Figure 6-7, if the tip of the bistable beam is gradually deflected from the undeformed position (A), the restoring force follows path AB until it undergoes snap-through when the displacement reaches x_m. Load reversal before reaching snap-through was observed

to yield inner hysteresis loops (Figure 6-7c) that originate from the point of load reversal, but these will be neglected in the present study. At snap-through the restoring force drops abruptly from B to C and further deflection of the tip causes the restoring force to follow path CD. Load reversal after point C, as in D or D*, results in a drop of the restoring force to E or E*, respectively. Subsequent reduction in the tip displacement results in a reduction in the restoring force along path EF until another cycle reversal takes place at point F, which causes the restoring force to increase to G and onwards to D again. If no cycle reversal takes place along path EF, a snap-back occurs at a deflection x_p causing the force to follow F*G* and on to H. Further cycle reversals cause an increase in the restoring force back to the upper branch AB. As such the restoring force depends not only on the current value of deflection, but also on the velocity sign and number of snaps in the history of motion. The load-deflection characteristics in the negative x indicate an essentially linear behavior, as previously shown in Figure 6-4, so no hysteresis or snap-through occurs. The rule-base listed in Table 6.2 is implemented to obtain the restoring force, depending on all the possible combinations of displacement and motion history.

A single degree of freedom equivalent model is developed to study the dynamics of the base excited cantilever beam. While a distributed-parameter model generally represents a better simulation of the system dynamics, the lumped parameter model is useful for a fundamental understanding of the problem and the effect of the design parameters. The cantilever beam is idealized as a mass supported by a spring and damper to a harmonically excited base which simulates the shaker, as shown in Figure 6-8. In this model the absolute displacement of the beam tip is equivalent to the mass displacement, x, and the displacement of shaker is denoted as y. As the mass m is displaced, the forces acting on it are the nonlinear restoring force, ϕ, the forces due to magnetic repulsion, F_m, and a damping force that is introduced to account for material damping. The magnetic force is assumed to take place in the transverse direction, since the compressive force exists only in the unstable equilibrium state and are otherwise insignificant compared to the transverse component.

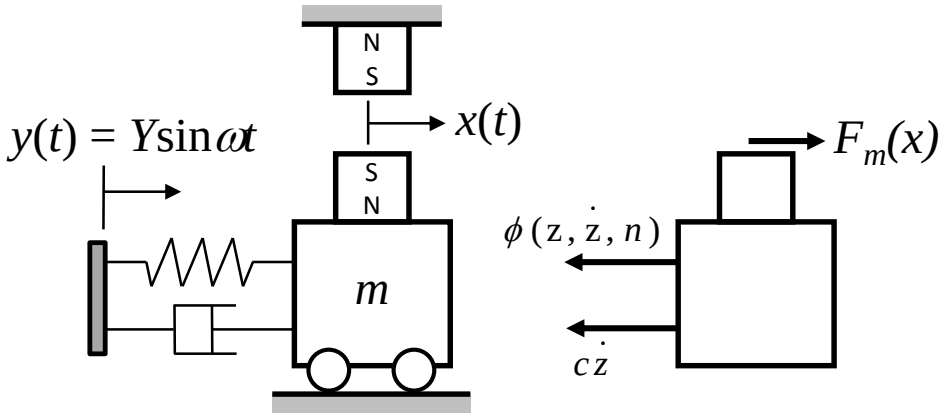

Figure 6-8: Schematic of the single degree of freedom model.

Table 6.2: Rule-base for calculating the nonlinear restoring force

No. of snaps	Displacement	Velocity sign	Branch to obtain restoring force
0	$0 \leq x \leq x_p$	+	A → B
		-	B → A
	$x_p < x \leq x_m$	+	A → B
		-	B → A
	$x_m < x \leq x_n$	Not possible	N/A
Odd	$0 \leq x \leq x_p$	Not possible	N/A
	$x_p \leq x \leq x_m$	+	G → D
		-	E → F
	$x_m \leq x \leq x_n$	+	C → D
		-	E → F
Even	$0 \leq x \leq x_p$	+	A → B
		-	G* → A
	$x_p \leq x \leq x_m$	+	A → B
		-	N/A
	$x_m \leq x \leq x_n$	Not possible	N/A

The equation of motion governing the mechanical behavior can be written as:

$$m\ddot{z} + c\dot{z} + \phi\left(z, \dot{z}, n\right) = F_m(x) + m\omega^2 Y \sin\left(\omega t\right) \tag{6.3}$$

where z is the motion of the mass relative to the base,

$$z = x - y \tag{6.4}$$

The equivalent mass is given by:

$$m = m_t + 0.23 m_b \tag{6.5}$$

where m_t is the tip mass and m_b is the total beam mass. It is noted that the magnetic force F_m depends on the absolute displacement x and is interpolated from the results of Fig. 1b, and ϕ is the restoring force that is obtained according to the rule base outlined in Table 6.2. The equation of motion is integrated in the time domain using the Newmak scheme to obtain time history plots of the mechanical displacement z as a function of the driving level and magnetic separation. A chirp signal is generated numerically to simulate the up-sweep excitation from 10 Hz to 30 Hz in 50 seconds. The relative displacement can be used to examine the mechanical behavior, especially the bistable response, as a function of the design and operating parameters. Figures 6-9, 6-10 and 6-11 show the time-domain plots of the tip displacement, as well as the corresponding phase plots, for excitation levels of 1g, 2g, and 3g, respectively. It can be observed that as drive level increases the resonance frequency decreases, which is attributed to the nonlinear softening behavior. This is clear for the case of no magnet,

where the resonance frequency drops from 18.4 Hz (1g) to 16.6 Hz (2g) to 15.2 Hz (3g) versus the values of 21.2 Hz (1g), 17.2 Hz (2g) and 14.8 Hz (3g) as measured experimentally. A similar trend can also be observed for the case of a magnetic gap of 20 mm. For these cases the bistability is weak and the beam does not undergo snap-through, since the displacement plots do not cross the horizontal red and green lines that denote snap-through and snapback, respectively. It can also be observed for these two cases that as the magnets are brought closer to the beam, the resonance frequency drops. A further reduction in the magnetic separation results in a bistable behavior, as illustrated by the elliptical trajectories in the phase plane plots. It can be inferred that a magnet separation of 10 mm is favorable at 1g and 2g excitation levels. At 3g, a magnetic separation of 15.5 mm as well as 10 mm provide amplified displacements and hence are expected to yield significant power output, as compared to the case of no magnet.

6.3.1 Discussion

In discussing the experimental and modeling results, the control case of the cantilever harvester system with no magnet is considered first. Experimentally, softening behavior was observed with increasing acceleration as evidenced by the decreasing of the natural frequency (Figure 6-6) and this behavior was also seen in the model prediction (Figures 6-9—6-11). The prediction of the natural frequencies from the model and those measured experimentally are in -13, -3, and 3% agreement at 1, 2, and 3g, respectively. Since the piezoelectric response of MFC was not included in the formulation of the model's governing equations, the RMS power values cannot be compared and making inferences of broadening from the displacement-time history alone is difficult. Experimentally, as the magnetic separation decreased, the performance with respect to the control case (equivalent to the magnetic separation being infinite) reaches a maximum and then decreases. The magnets were successfully used to alter the natural frequency of the system from 21.2 to 15.6 Hz before significant power reduction occurred. The model also showed a decrease in natural frequency as the gap narrowed (Figures 6-9—6-11). The experimental results demonstrated that snap-through was achieved at lower excitation inputs with narrower magnetic gap distances, up to 7.5 mm. The extent of the magnetic interaction is such that at the narrowest gap, the harvester did not snap-through at any forcing level. At this magnetic separation distance, the starting position of the cantilever was offset forward noticeably on the experimental rig. The model was able to predict this offset of initial starting stance, but predicted this offset to occur at a magnetic separation of 10 mm. The model was able to predict the excitation level required for snap through in most situations, but there were some discrepancies. Experimentally, snap-through was observed for both the 15.5mm and 10 mm magnet separations at 2g while the model predicted snap-through for only the 10 mm case. For the 3g case, snap-through does not occur for the non-magnetic and 20 mm cases, but is predicted for the 15.5 and 10 mm cases, whereas experimentally, snap-through was observed for all cases except 7.5 mm. Possible reasons for this discrepancy are that the model is a SDOF system in rectilinear coordinates while the true path of the cantilever's tip is more similar to circular arc. This also implies that the magnets are not moving parallel to each other, meaning that

the lines of action of the magnetic forces as well as their magnitude would require multi-axial characterization. As shown in Table 6.1, the effect of the magnets on the broadband response of the harvester is less straightforward. At 1g, the magnetic proximity is able to improve the bandwidth, but at the cost of peak power output. At higher g levels, there is a small cost of bandwidth, but with significant gains in harvested power. The higher the excitation input, the narrower the magnetic separation that is required to maximize the power output.

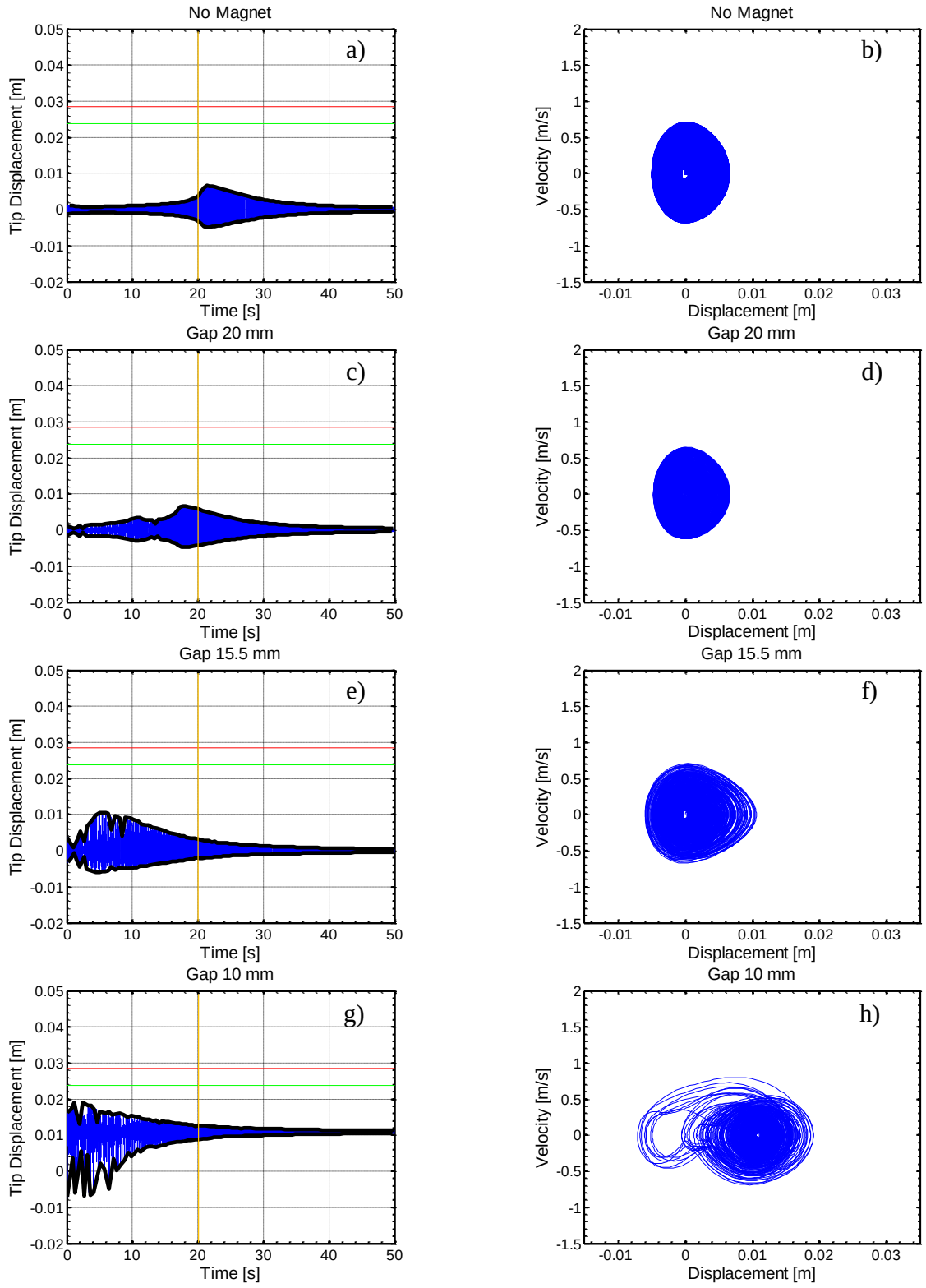

Figure 6-9: Time history plots of the tip displacement and corresponding phase plots at an excitation level of 1g.

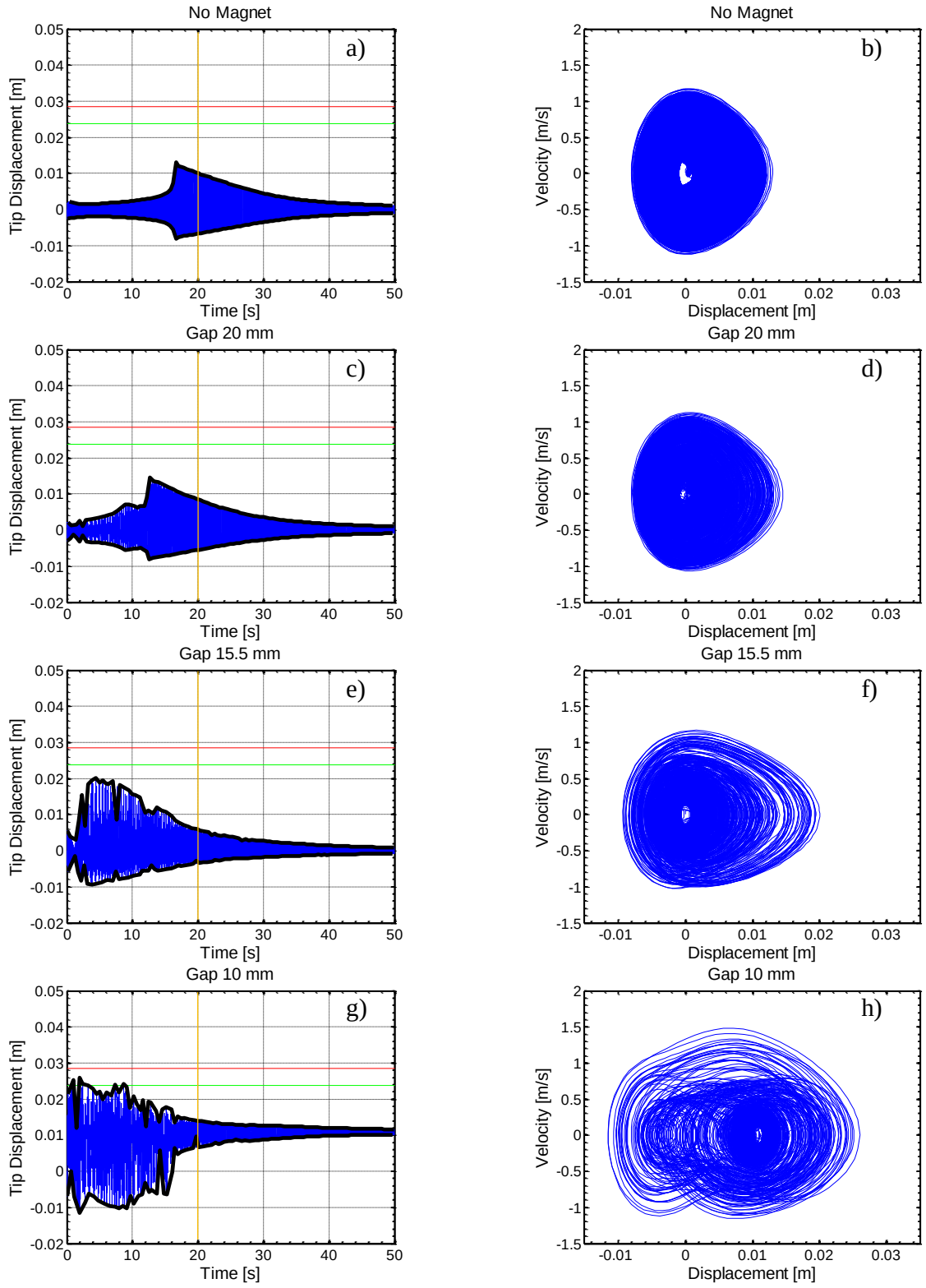

Figure 6-10: Time history plots of the tip displacement and corresponding phase plots at an excitation level of 2g

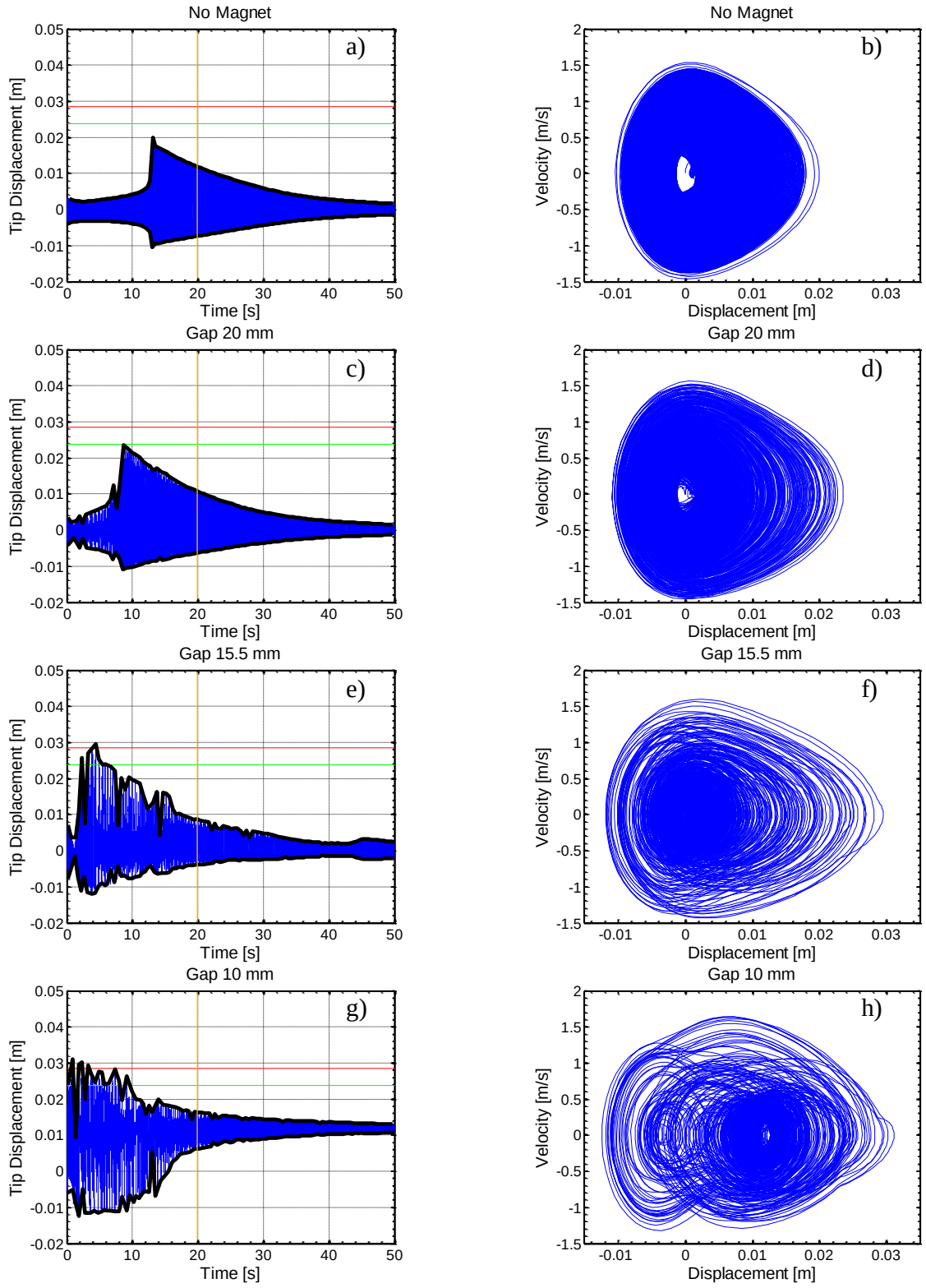

Figure 6-11: Time history plots of the tip displacement and corresponding phase plots at an excitation level of 3g

6.4 Conclusion

This chapter sought to address two objectives. The first was to establish the benefit of using a secondary magnetically superimposed bistable field upon a cantilever which was already bistable due to thermal interactions for energy harvesting. The primary goal was also to investigate the relationship between the design parameter of the magnetic gap spacing and the energy harvested. The introduction of magnets was shown to strongly affect the dynamic behavior of the harvester. The approach enables the modification of the natural frequency of the harvester without removal of material and the magnets were able to increase the bandwidth at low acceleration levels, but at some cost of peak power, and were able to increase peak power at higher excitation levels, but at the cost of some bandwidth. In doing so, the design of the cantilever bistable laminate energy harvesters has been improved. The second objective was to model the behavior of the cantilever using an empirical reduced single degree of freedom system having the form of the Duffing equation for a double-well potential system. The model parameters were experimentally identified such as the load-deflection characteristic of the bistable beam. The model was more simple to implement, but was limited to being implementable only for harvesters which have been built and tested. Hysteresis was shown to be significant at low levels of excitation. The dynamics of the beam were investigated using bifurcation diagrams and shows that the qualitative behavior given by the experimentally measured response is predicted well by the simple single degree of freedom model.

This major findings of this chapter can be summarized:

- Non-permanently adjusting the magnetic gap allowed for a trading off between peak power and broadness of response, giving flexibility to the user for different operational profiles
- The magnet successfully reduced the acceleration required for snap through from 3g to 2g, allowing for broadband energy harvesting even at low acceleration levels
- The single degree of freedom model is able to follow the trend of natural frequency with respect to magnetic gap distance, as well as the approximate forcing parameters required for snap-through and is therefore a potentially useful design aid

Chapter 7

Demonstrators: Energy Harvesting from Train-based Frequency Spectra and Wind Energy Harvesting

The objective of this thesis' research has been the development of bistable laminates for energy harvesting from vibrations. Pursuant to this, several design parameters were identified and investigated in the preceding chapters to study their effects upon the nonlinear dynamics of the harvesters especially where these pertain to the energy harvesting capability of the different harvester configurations. In order to characterize and understand the relationships and behavior of the energy harvesters and their design parameters, harmonic testing at different frequencies and acceleration levels was undertaken. While this has helped develop the theoretical understanding and shown what degrees of sensitivity are associated with different design parameters, these tests are still dissimilar to excitation patterns likely to be encountered in practice. For practical applications, a source of vibrational energy such as ground transport will not exhibit a single clear harmonic frequency. This chapter revisits previously investigated configurations of bistable laminate energy harvesters and shows their energy harvesting capability when subjected to real vibrational input. Two different practical scenarios are considered. The first of the practical applications presented is a bistable cantilever harvesting energy from the wind. Various angles with respect to windflow and different windspeeds were tested in a windtunnel, and energy was successfully harvested. The second practical application presents the results of several plate-type bistable harvesters being tested on a shaker where the shaker's excitation pattern was based off of data sampled from the bogies of trains. Four practical design considerations are set, and harvesters are designed and built to address these considerations. It is shown that not only was energy successfully harvested, but also that these harvesters

are mechanically sufficiently robust to withstand the high accelerations associated with this application.

7.1 Energy harvesting from wind with bistable cantilevers

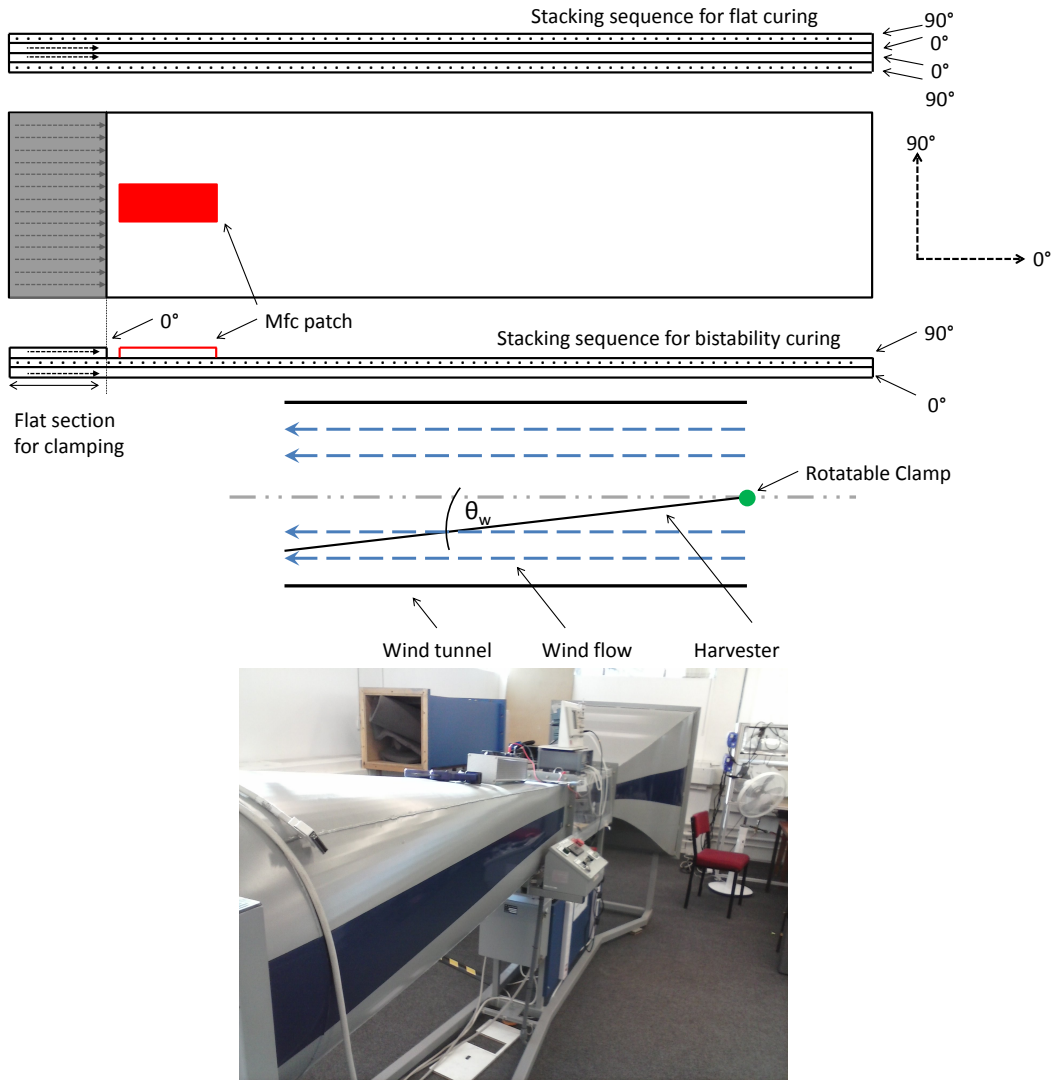

Figure 7-1: Construction of bistable cantilever, orientation in windtunnel, and windtunnel itself

The tests in the following section were carried out in collaboration with Brunel University London at their Uxbridge campus. Using a bistable laminate cantilever as an energy harvesting device for wind energy is attractive because the solid-state nature of piezoelectric transduction of mechanical strain into electrical energy removes the need for moving parts. A cantilever similar in construction to those of chapter 3 and 6 was made, as is shown in figure 7-1. To

make the clamped base cure flat to facilitate clamping, the stacking sequence was $[0°/90°/0°]_T$ and for the free length of the bean, $[0°/90°/0°_{MFC}]_T$. A rotatable clamp was constructed to be used as a fixture to hold the cantilever steady at set angles with respect to windflow θ_W within the wind tunnel as shown in figure 7-1. θ_W was varied through a range of values, as well as the wind speed. An initial characterization was done to find the excitation parameters of θ_W and wind speed which caused snap-through. A calibration point was set at a windspeed of 20 $\frac{m}{s}$m/s and $\theta_W = 25°$ as this was the first point where snap through was observed in the experimental parameter range.

At this calibration point, a range of resistances was tested to find the load resistor maximizing the RMS power output. The results are shown in figure 7-2 a). As shown, maximum power is seen at 9 kΩ.

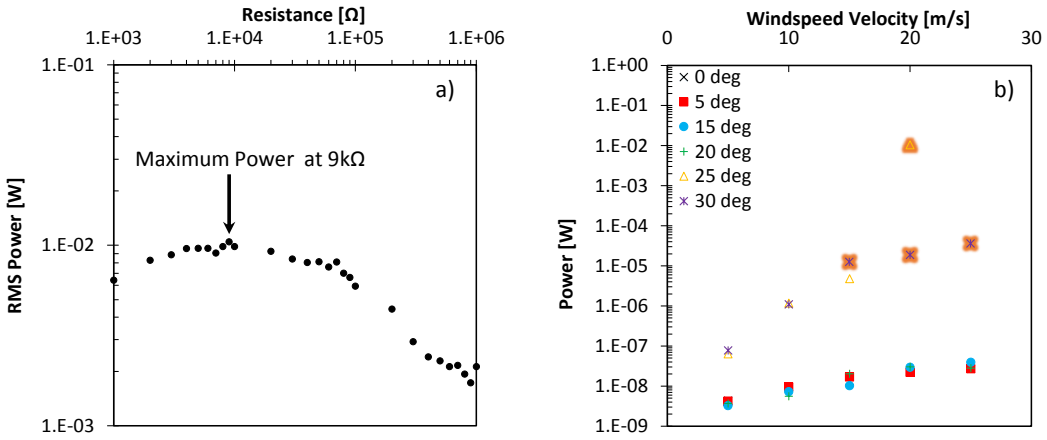

Figure 7-2: a) RMS powerover three decades of resistances with peak power obtained at 9 kΩ b) Power obtained at various windspeeds and values of θ_W at 9 kΩ

Figure 7-2b) shows the power output for the different values of θ_W and wind velocity with the highlighted points indicating snap-through. As expected, the general trend is for higher wind speeds to result in higher power output. Also, intuitively, as θ_W increases, it is increasingly easy to cause snap-through as As shown, there is a increase of power for the $\theta_W = 25°$ and $\theta_W = 30°$ angles with respect to the others. There is also a significant increase in power at the onset of snap through. In particular, at $\theta_W = 30°$ there is a transition to snap-through between windspeeds of 10 and 15 $\frac{m}{s}$ There is an order of magnitude increase of power here. For $\theta_W = 25°$, The snap-through transition happens between 15 and 20 $\frac{m}{s}$. There is an increase of power here of 4 orders of magnitude. This jump is bigger than the increase seen at $\theta_W = 30°$ because this was the excitation parameter set used for calibration. Due to the construction of the MFC patch and its proximity to the wind tunnel motor, there was significant ingress of electrical noise as seen in figure 7-3. These figures show the frequency content of the voltage across one of the load resistors. As can be seen, there are some distinct peaks indicating activity at those frequencies. At high resistances approaching open circuit,the signal-to-noise ratio is

high. As the resistance decreases and the voltage developed by the piezo decreases, the height of the main peak becomes less distinct with respect to the noise floor.

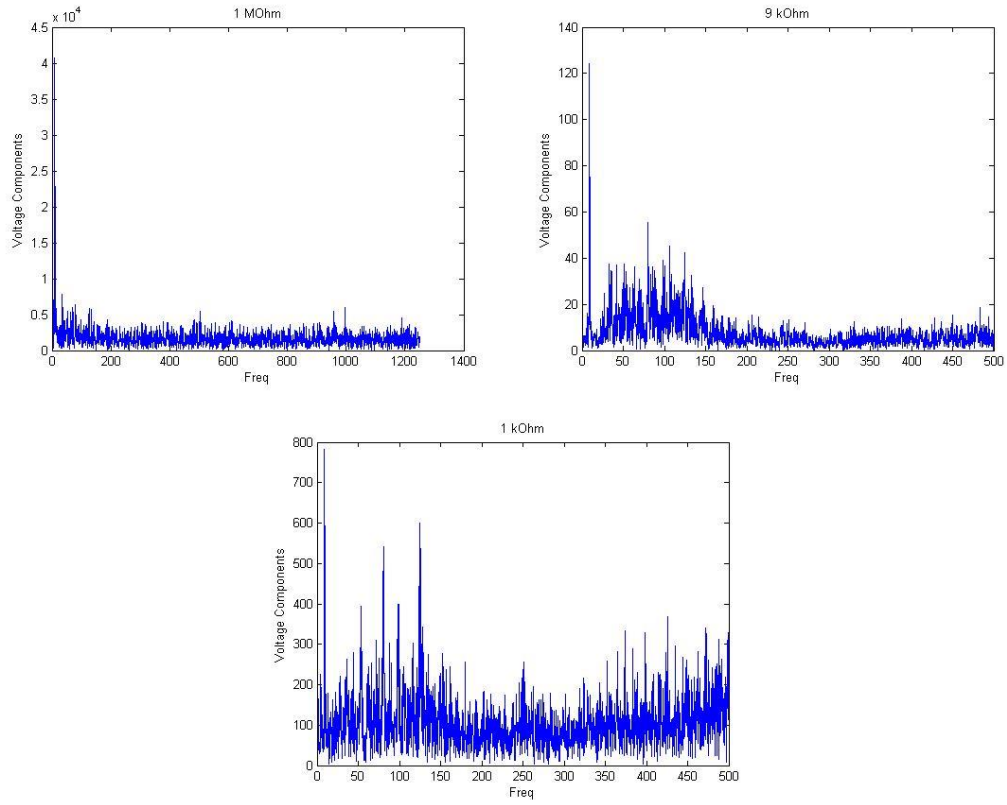

Figure 7-3: Fast Fourier Transform of the voltage time signal from the bistable cantilever's piezoelectric patch at the indicated resistances

Thus, the actual power output resulting from the flapping of the laminate must be lower than the nominal values. In terms of feasibility, however, it has been shown that it is possible to snap a bistable cantilever through using the wind. While in the windtunnel, θ_W was limited due to the cross-sectional area of the windtunnel, in outdoor operation, this would not be a limitation. Also, here a Smart Materials 2814-P2 MFC patch was used with active dimensions of 28 x 14 mm. A larger piezoelectric patch could be used to increase power output.

7.2 Train Excitation Tests

The tests done in the following section were carried out in collaboration with Perpetuum Ltd. at their Hampshire site. In the previous chapters, the objective was the variation of design parameters to investigate the relationships of the various parameters to the energy harvesting capability of the harvesters. Here, the harvesters are selected with consideration of several practical requirements and constrains, and a power output goal of 10 mW was set.

1. It is advantageous for the harvesters to be physically small. The space which is available with the bogey for installation of an energy harvesting device is limited.

2. In order to specify the accompanying equipment such as transmitters (such as the one seen in chapter 2 figure 2-2) and transducers, a worst case scenario lower bound of power output must be determined.

3. It is also useful for similar reasons to establish an upper bound of what the maximum power output might be as this will affect other design considerations for the overall device.

4. It is important to establish whether or not the bistable laminate energy harvesters are mechanically robust enough to withstand the acceleration levels encountered on exceptionally rough sections of track.

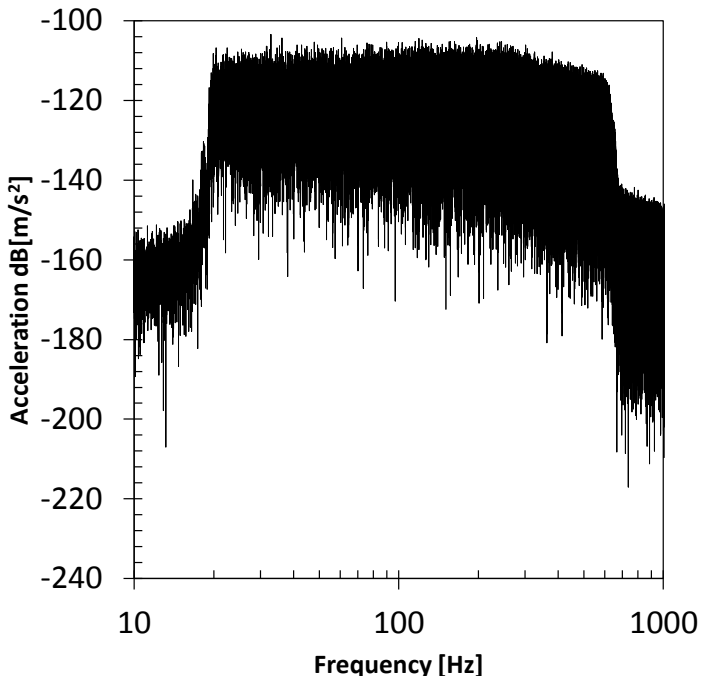

Figure 7-4: Frequency Content of Train Excitation

To address these first two points, two bistable laminate energy harvesters were designed and built. A saltire laminate and a square laminate 150x150 mm were manufactured, similar to those in chapter 4, figure 4-2. Because of their smaller size, they were unable to accommodate a large MFC patch as this would excessively increase stiffness, and therefore a Smart Materials 2814-P2 MFC with an active area of 28x14 mm was used. The stacking sequence for both was $[0^{\circ}_{\mathrm{MFC}}/0^{\circ}/90^{\circ}]_{\mathrm{T}}$. These harvesters were mounted to an electromechanical shaker set to produce an excitation pattern based on sampled train data. The frequency content of the excitation is shown in figure 7-4.

As shown in figure 7-4, there is no dominant frequency around which a device might be optimized. The excitation frequencies are effectively a flat band rolling on at 20 Hz and rolling off at about 600 Hz. The RMS acceleration is 108 m/s^2, or 11 g. The frequency content of the voltages from the piezoelectric patches of the harvesters are shown in figures 7-5a, and b.

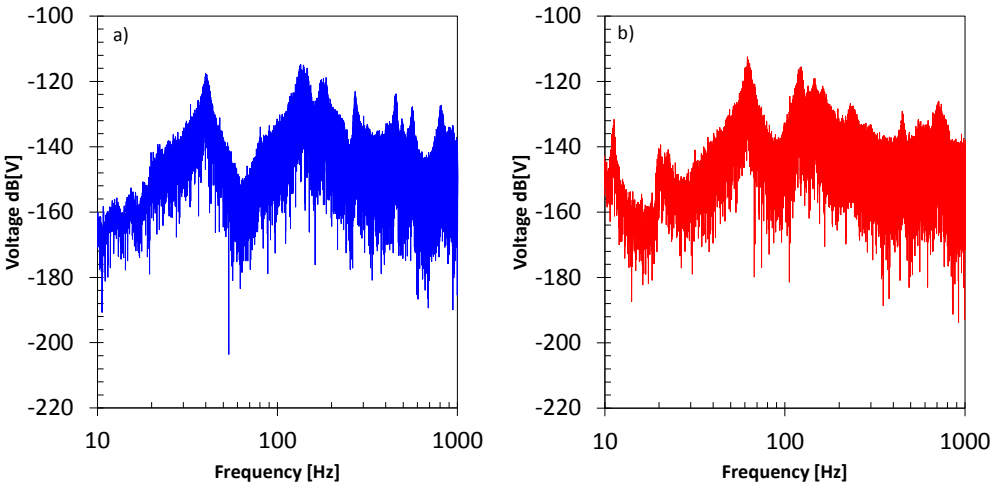

Figure 7-5: Frequency content of voltage for a) saltire and b) square

The power output for both harvesters was calculated based on the RMS voltage over the 62-second time record. The saltire's power output was 0.46 mW and the power output of the square harvester was 0.43 mW. These power values are less than those reported in chapter 4 because the active area of the piezoelectric patches is less. As can be seen in figures 7-5, both harvesters show several peaks throughout the frequency band. Interestingly, the square's response has a small peak at 11 Hz, which is outside the excitation's frequency bandwidth. In both cases, the highest peak corresponds to the natural frequency of the respective devices. The saltire laminate is able to produce more power than the square harvester because the peaks throughout the frequency band outside of the primary resonance peak are taller than the square's. As shown in chapters 4 and 5, the square bistable laminate energy harvesters can behave essentially like a linear device at low levels of excitation, and do not start to exhibit strong nonlinear characteristics until a certain acceleration threshold is crossed. In chapter 4, the saltire laminate showed nonlinear behavior such as snap-through at acceleration levels lower than the square. Thus, it logically follows that in this forcing situation, the saltire's broad-band performance is superior.

These experiments have shown that energy can indeed by harvested by bistable laminate energy harvesters from realistic excitation patterns. The increased nonlinearity of the saltire behavior was advantageous in improving the energy harvesting behavior by allowing the device to have more activity at a broader range of frequencies. The worst case scenario's lower power output bound was established to be in the mid-hundreds of micro-watts.

In order to address design points 3 and 4, 2 more laminates were prepared. A $[-30^{\circ}_{\mathrm{MFC}}/0^{\circ}/30^{\circ}]_{\mathrm{T}}$, and $[0^{\circ}_{\mathrm{MFC}}/0^{\circ}/45^{\circ}]_{\mathrm{T}}$ similar to those of chapter 5 were built at 200x200 mm square. It was clear that harvesters with nonlinear characteristics were superior in terms of the energy harvesting capability. The $[-30^{\circ}_{\mathrm{MFC}}/0^{\circ}/30^{\circ}]_{\mathrm{T}}$ was built, rather the $[0^{\circ}_{\mathrm{MFC}}/0^{\circ}/30^{\circ}]_{\mathrm{T}}$, of chapter 5. The MFC was tilted at an angle such that the long side of the MFC patch was perpendicular to the 2^{nd} ply angle. This was done in order to flatten the laminate and reduce its stiffness slightly. As before, the laminate was bistable before the addition of the MFC, but would not statically hold the two separate shapes afterwards. The $[0^{\circ}_{\mathrm{MFC}}/0^{\circ}/45^{\circ}]_{\mathrm{T}}$, was chosen because it was slightly stiffer than the $[-30^{\circ}_{\mathrm{MFC}}/0^{\circ}/30^{\circ}]_{\mathrm{T}}$, and therefore might have more power output due to higher strain transduction efficiency between the laminate substrate and the patch. These harvesters were subjected to a harsher vibration pattern than the saltire and the square. The excitation's frequencies appear in figure 7-6.

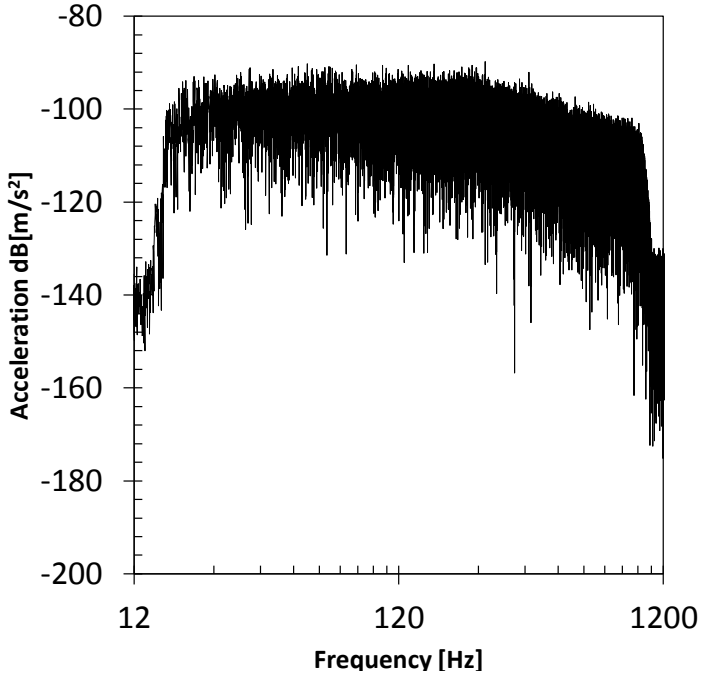

Figure 7-6: Frequency Content of endurance run of worst 0.1 % of Train Excitation

As shown in figure 7-6, the frequency band begins at 20 Hz as before, but continues on to about 1 kHz before rolling off. The RMS acceleration here is 129 $\frac{\mathrm{m}}{\mathrm{s}^2}$, or 13.1 g. This excitation pattern was designed to replicated the conditions of the worst 0.1% of the vibrations seen by trains and thus is used to test for the resilience of the harvesters. The power output of the $[-30^{\circ}_{\mathrm{MFC}}/0^{\circ}/30^{\circ}]_{\mathrm{T}}$ and the $[0^{\circ}_{\mathrm{MFC}}/0^{\circ}/45^{\circ}]_{\mathrm{T}}$ harvesters subjected to this vibrational pattern were 13.7 mW and 12.7 mW, respectively, thus attaining the goal set. The frequencies of their responses are shown in figures 7-7.

Again, the highest peaks are seen at the natural frequencies. Both harvesters have a few peaks throughout the frequency band. The trend of the energy harvesting behavior is similar

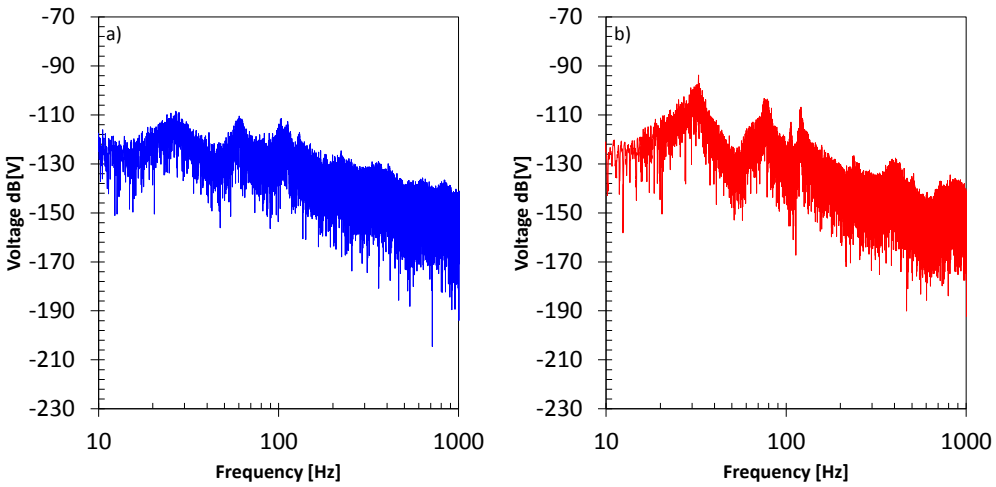

Figure 7-7: Frequency content of voltage for a) $[-30^{\circ}_{\mathrm{MFC}}/0^{\circ}/30^{\circ}]_{\mathrm{T}}$ and b) $[0^{\circ}_{\mathrm{MFC}}/0^{\circ}/45^{\circ}]_{\mathrm{T}}$

to the behavior of the saltire and the square. The acceleration threshold of the $[0^{\circ}_{\mathrm{MFC}}/0^{\circ}/45^{\circ}]_{\mathrm{T}}$ for the onset of nonlinear behavior will be the higher of the two. Because of this, the peaks of the $[0^{\circ}_{\mathrm{MFC}}/0^{\circ}/45^{\circ}]_{\mathrm{T}}$ tend to be sharper and taller than those of the $[-30^{\circ}_{\mathrm{MFC}}/0^{\circ}/30^{\circ}]_{\mathrm{T}}$. As before, the gains in energy harvesting performance come about because the overall voltage level is higher, on average, throughout. This set of experiments has shown that the laminates were able to survive heightened excitation levels. It has also established that the best-case-scenario of power output is in the teens of milli-watts. Chapter 2 table 2.1 gives the power demands of several types of sensors. The power demands of temperature, light, humidity, and vibration sensors are given to be 21.101, 21.181, 22.161, and 23.25 mW, respectively. If it is assumed that the energy harvester are able to make 10 mW of power available for the sensors continuously, this is approximately half the power output required to operate any of these sensors. This means that with an energy storage unit and management system, it should be feasible to produce sufficient power to run these sensors at a rate of about one reading every five seconds.

7.3 Conclusions

This chapter has demonstrated the feasibility of harvesting energy from non harmonic sources. Energy was successfully harvested from both the wind and a train bogey excitation pattern. In the case of the cantilever in the wind, in practice, a larger cantilever with more area to catch the wind could be built as well as some sort of vane mechanism to ensure that the cantilever is as perpendicular as possible with the direction of the wind. For the bistable laminates harvesting energy from the train bogies, it was seen that the harvesters with the greatest degree of nonlinearity had the highest performance.

This major findings of this chapter can be summarized:

- It is possible to harvest energy from nonharmonic sources such as wind, and the excitation spectra associated with train bogies
- While snap-through was indeed observed for the cantilever, the power outputs are exaggerated due to ingress of electrical noise from the wind tunnel's fan motor
- While the windspeed velocities required were relatively high, here the size of the cantilever was constrained by the cross-sectional dimensions of the windtunnel which would not apply in a practical situation
- Four design considerations were set forth for energy harvesters geared towards harvesting energy from the vibrations of train bogies and were addressed. The minimum power was shown to be on the order of hundreds of micro-watts for a small harvester, with a maximum of teens of milli-watts, depending on the design of the harvester. The goal of harvesting 10 mW was achieved. Furthermore, the harvesters survived the excitation pattern associated with the top 0.1% of harshness

Chapter 8

Conclusions and Future Directions

8.1 Summary of main conclusions

This thesis presents research on bistable laminate vibrational energy harvesters using piezoelectric transduction. Harvesters of both the centrally supported plate type and clamped free cantilever type were built and tested on a frequency and acceleration controlled electromagnetic shaker rig. The objective of this research has been to develop energy harvesters capable of operating over a broad range of frequencies. The aim of the bistable harvesters studied in this thesis has been to unlock potential sources of vibrational energy which are not able to be effectively exploited by linear harvesting systems. The novel contributions of the substantive chapters are set out below.

Chapter 3 compares the performance of a linear system against an equivalent linear counterpart. Several design parameters were also examined. It showed that while the peak power level fell by nearly half, the power bandwidth quadrupled. This implies that there may be a tradeoff between peak power and broadness of response. This chapter also showed that at this scale, the self-mass was such that changing the orientation of the harvester from vertical to horizontal had little effect. The addition of a small 4.1 gram mass showed high sensitivity to proof mass. The acceleration required to cause snap-through was lowered from 5g to 4g, but with a power decrease of approximately $\frac{1}{2}$. The sensitivity of the power output with respect to load resistance showed that changes of natural frequency resulting from softening were not substantial enough to require an active resistance tuning system as a matter of priority.

Chapter 4 investigated bistable plates for energy harvesting. The planiform shape was altered in order to study the relationship between material removed and harvested power. Removal of material was shown to reduce the acceleration required to induce snap through from greater than 11g for a square-shaped harvester to 7g for a saltire-shaped harvester. The laminates were modeled using an analytical approach. The predicted out-of-plane displacement

of the static shapes was shown to be within just over 16% of agreement with experimental profilometry measurements. The laminates were modeled using an analytical approach and it was shown that the major nonlinear dynamical features experimentally observed were present in the model. The model successfully exhibited softening, differences of natural frequency between the two stable states, snap-through, and subharmonic and superharmonic frequency content. The removal of material caused the natural frequency to decrease, showing that the harvester's mass was being reduced more quickly than stiffness.

Chapter 5 studied the relationship of power output and the second ply angle as another route to tailor the response of plate type harvesters. Reducing the relative ply angle from 90° to smaller angles reduced stiffness, causing the natural frequencies to reduce. The acceleration required for snap-through was reduced from greater than 7g for the $[0^{\circ}_{\mathrm{MFC}}/0^{\circ}/90^{\circ}]_{\mathrm{T}}$ to 4g for the $[0^{\circ}_{\mathrm{MFC}}/0^{\circ}/30^{\circ}]_{\mathrm{T}}$, and 2g for the $[0^{\circ}_{\mathrm{MFC}}/0^{\circ}/20^{\circ}]_{\mathrm{T}}$. The broadness of the $[0^{\circ}_{\mathrm{MFC}}/0^{\circ}/30^{\circ}]_{\mathrm{T}}$ was double that of the $[0^{\circ}_{\mathrm{MFC}}/0^{\circ}/90^{\circ}]_{\mathrm{T}}$. The gradual emergence of nonlinearity was also studied. The increase of superharmonic activity in the $[0^{\circ}_{\mathrm{MFC}}/0^{\circ}/30^{\circ}]_{\mathrm{T}}$ with respect to increasing acceleration was presented. The increase of the damping ratio with respect to increasing acceleration was also enumerated.

Chapter 6 revisited bistable cantilevers. A pair of magnets were placed in repulsion such that the gap distance between them was adjustable in order to control the contribution of the magnetic dual potential well to the overall dynamics of the system. The arrangement allowed for the tradeoff between broadness and peak power to be leveraged within a parametric space. The natural frequency was adjustable within a 6 Hz band, and snap-through was observed as low as 2g. It was shown that higher acceleration levels benefited from closer magnetic gap distances.

Chapter 7 presented a practical demonstration of a bistable cantilever to harvest energy from the wind and bistable plates to harvest energy from train bogeys. In both cases, energy was successfully harvested. Snap-through was observed in the cantilever, showing feasibility as a solid-state wind energy conversion device. The plates for harvesting from train frequency spectra were designed with four practical considerations in mind. The harvesters were shown to be able to withstand the excitation of the bogeys. The bounds of performance were shown to be between the mid-hundreds of micro-watts to the teens of milliwatts.

8.2 Future work

If the eventual final objective is the development of a deployable energy harvesting power unit to provide electrical power to run devices, several avenues of research should be explored to further the understanding of the design parameters, dynamic characteristics, and develop the accompanying hardware for the complete device. Chapter 3 showed how different modes of vibration resulted in different power outputs. Furthermore, the non-orthogonal layups of the pates of Chapter 5 exhibited significant twist at some frequencies. An investigation into the strain fields of these different vibrational modes, and the best piezoelectric patch location and orientation to exploit these modes may yield substantial power gains. Investigations into how to

move the frequencies associated with these preferred modes into required frequency bands could be carried out. This could be done by adjusting a number of design parameters such as making the plies thinner by, attaching proof masses at nodal points, or using different substrate materials than carbon fiber. Other fiber-matrix systems with different stiffnesses, thermal expansion coefficients and cure temperatures could give more options.Completely different manufacturing approaches such as residual thermal strain on thin 3D printed metal pieces would result in structures similar to that seen in figure 2-17. These options would expand the design space, providing options for designers and engineers. This thesis explored only MFC-type piezoelectric patches utilizing PZT fibers for transduction. The main reason for this was because of the physically robust packaging and availability. While the d_{33} is high at 593 pC/N, it is also stiff, having a Young's modulus of 40 GPa. Another candidate material is the piezoelectric polymer PVDF. While the d_{33} is less at -33 pC/N, the stiffness is also one order of magnitude less at 2.7 GPa. Additionally, PVDF and other piezoelectric polymers are orthotropic, which would decrease the natural frequency discrepancy effected when the patch is adhered on. PVDF is also able to be cut into arbitrary shapes giving another dimension in the design space. In order to advance the fidelity of the models used to predict the behavior of bistable energy harvesters, as well as to understand the bistable laminates' dynamics more in-depth, two phenomenon should be investigated further. Chapter 4 suggests that the strain energy of the bistable system should be investigated not only as a function of strain, but also as a function of strain rate. Chapter 6 showed the presence of hysteresis in the bistable cantilever. It would be useful to see the strain, and strain rate dependency of this phenomenon, and understand its relation to damping. The empirical model derived in this chapter could be expanded by including piezoelectric transduction. Also, only the transverse forces from the magnet were considered. Increasing the number of degrees of freedom to capture the longitudinal force vectors should increase the accuracy of the model. The approach of using an analytical model as well as an empirical model should be maintained. Once the model is refined such that it can accurately predict power outputs given the laminate design parameters such as ply angle, shape, and piezoelectric patch orientation, material parameters, and arbitrary vibrational input, it would be highly informative to interface the model with an optimizer to obtain the optimal parametric set for the excitation input. In order to build the complete energy harvesting device with the bistable laminate as the power unit, several other components will need to be designed. A physically robust case, and mounting hardware will need to be designed such that the vibrations to be harvested are not attenuated before exciting the bistable laminate. An energy storage unit such as a supercapacitor will need to be specified, as well a rectification and conditioning circuitry so that the power provided is suitable for the devices to be powered. All this will require a power management unit which will likely run on a microcontroller. Once the prototype is built, it can be tested in situ.

Appendix 1: Electrical Characterization with Respect to Strain ε and Strain Rate $\frac{\mathrm{d}\varepsilon}{\mathrm{d}t}$

A property of piezoelectric materials in general is that their voltage is proportional to strain and that current is proportional to the strain rate. Given the way that a plate-type harvester is supported by a central bolt, the displacement of the carbon substrate should correspond to the strain undergone by the piezo. Therefore, if the velocity is the rate of change of displacement with respect to time, the velocity of the same point should relate to the current developed by the piezo. Thus, under an open circuit, the voltage of a piezoelectric material will be maximized, but the power output will be zero because there will be no flow of current. An example of this can be seen in figure figure A.1 a) where the amplitude of the voltage waveform over the resistance value range is shown. Similarly, under short-circuit conditions, electrical current will flow, but because there is no voltage, no power will be produced in this situation either. At the indicated resistances of figure figure A.1, the harvester was excited harmonically at 1g and the displacement, velocity, and voltage of the harvester were all recorded. Upon reaching steady state, sine waves were fit to the data using a least squares method to determine the coefficients required for a regression fit–generally $f(t) = A_0 \sin(2\pi f t + \phi)$. Here, A_0 is the amplitude of the waveform, $2\pi f$ is the frequency term, t is time, and ϕ is the phase angle. The phase term of the voltage was then subtracted by the phase term of the displacement and the velocity.

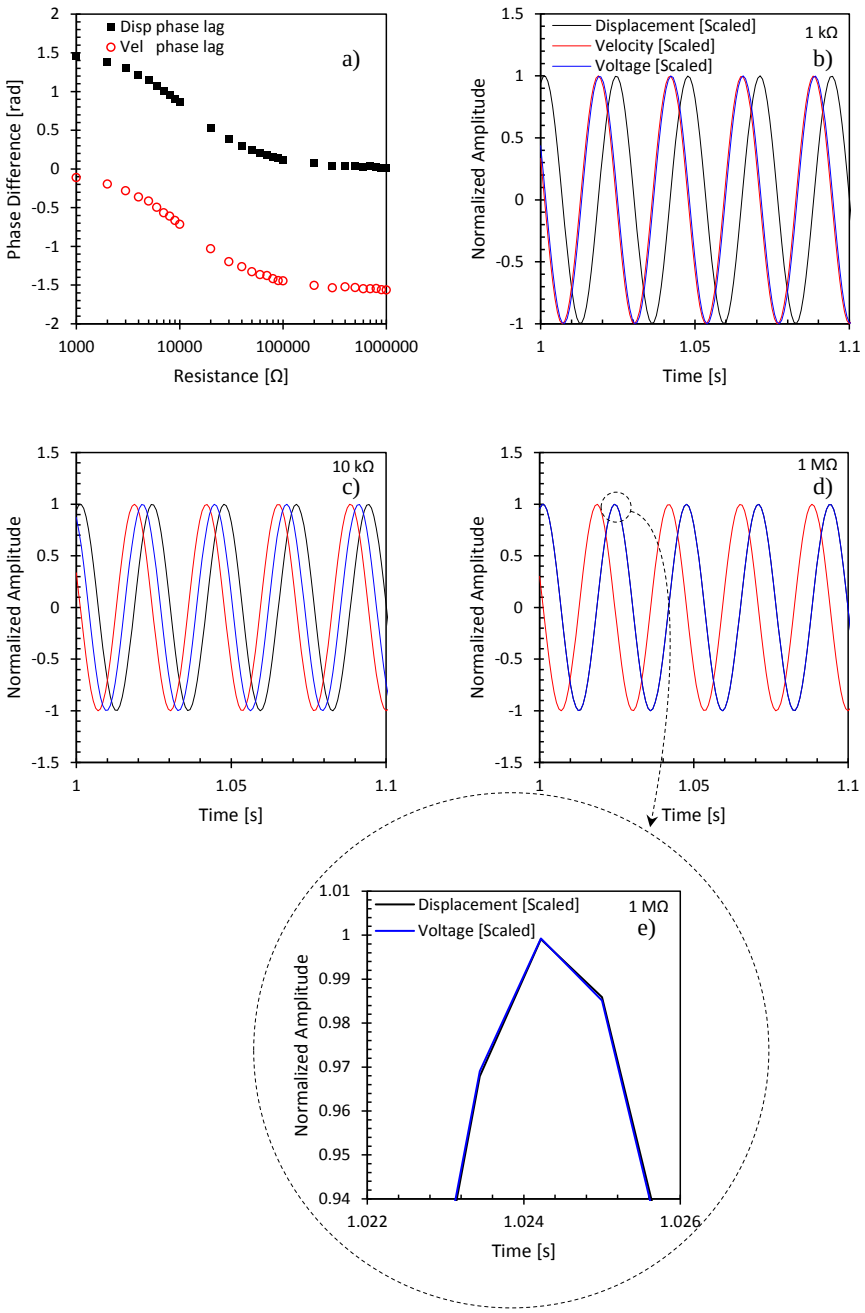

Figure A.1: a) phase change of voltage signal relative to voltage and displacement b) voltage in phase with velocity at approximately short circuit condition c) voltage signal is shown to be equally off-phase with respect to displacement and velocity near impedance matching condition d) voltage is in phase with displacement near open-circuit conditions e) voltage inset of d) to show overlap of lines

This phase angle difference is seen in figure figure A.1. As shown, the voltage is nearly in phase with velocity at the lowest resistance. This is expected as this resistance approximates a

short circuit condition. Thus, the low voltage, as seen in figure figure A.1 shows that because the voltage is low, the current must be high. The phase difference at this resistance between the voltage and displacement is $\frac{\pi}{2}$. This lead and lag can be seen in the time domain graph of figure A.1.

At 10kΩ, near the impedance matching resistance value, as seen in figure figure A.1 the peak of the voltage nearly coincides with the point where velocity and displacement intersect suggesting that the absolute value of the lag and lead of the voltage with respect to these two quantities is equal in the case of optimal load resistance. Finally, at high resistance, the trend is the opposite of that observed at low resistance where now the displacement is in phase with voltage and out of phase $\frac{\pi}{2}$ with velocity.

Conference Papers

Conference Paper 1:

Presented at: European Conference on Application of Polar Dielectrics—July 7-11, 2014 Vilnius, Lithuania

Title: Manufacture and characterization of piezoelectric broadband energy harvesters based on asymmetric bistable cantilever laminates

Authors: P. Harris, W. Skinner, C. R. Bowen, H. A. Kim

CONTENT WITHHELD DUE TO COPYRIGHT

Conference Paper 2:

Presented at: American Society for Composites 29th Technical Conference, 16th US-Japan Conference on Composite Materials & ASTM-D30 Meeting—September 8-10, 2014 La Jolla, California, USA

Title: Manufacture and Characterisation of Piezoelectric Broadband Energy Harvesters Based on Asymmetric Bistable Laminates

Authors: P. Harris, C. R. Bowen, H. A. Kim

CONTENT WITHHELD DUE TO COPYRIGHT

Conference Paper 3:

Presented at: SPIE Defense + Commercial Sensing—April 17-21, 2016 Baltimore, Maryland, USA

Title: A composite beam with dual bistability for enhanced vibration energy harvesting

Authors: P. Harris, G. Litak, C. R. Bowen, M. H. Arafa

Link: http://proceedings.spiedigitallibrary.org/proceeding.aspx?articleid=2524621

CONTENT WITHHELD DUE TO COPYRIGHT

Journal Papers

Journal Paper 1:

Ferroelectrics 466(1) 14-20. 2014

Title: Piezoelectric Fibres Integrated into Structural Composites

Authors: C. R. Bowen, M. Watson, D. N. Betts, P. Harris, M. Bertin, H. A. Kim

Link: http://www.tandfonline.com/doi/abs/10.1080/00150193.2014.894842

CONTENT WITHHELD DUE TO COPYRIGHT

Journal Paper 2:

Ferroelectrics 480(1) 67-76. 2015

Title: Manufacture and Characterisation of Piezoelectric Broadband Energy Harvesters Based on Asymmetric Bistable Cantilever Laminates

Authors: P. Harris, W. Skinner, C. R. Bowen, H. A. Kim

Link: http://www.tandfonline.com/doi/full/10.1080/00150193.2015.1012447?src=recsys

CONTENT WITHHELD DUE TO COPYRIGHT

Journal Paper 3:

Journal of Multifunctional Composites 2(3) 113-123. 2014

Title: Manufacture and Characterisation of Piezoelectric Broadband Energy Harvesters Based on Asymmetric Bistable Laminates

Authors: P. Harris, C. R. Bowen, H. A. Kim

Link: http://www.dpi-journals.com/index.php/JMC/article/viewFile/551/422

CONTENT WITHHELD DUE TO COPYRIGHT

Journal Paper 4:

Journal Paper 4: The European Physical Journal Plus 131(4). 2016

Title: Dynamics of a vibrational energy harvester with a bistable beam: voltage response identification by multiscale entropy and "0-1" test

Authors: P. Harris, C. R. Bowen, H. A. Kim, G. Litak

Link: http://orca.cf.ac.uk/91338/1/art%253A10.1140%252Fepjp%252Fi2016-16109-4.pdf

CONTENT WITHHELD DUE TO COPYRIGHT

Journal Paper 5:

Applied Mechanics and Materials 849 95-105. 2016

Title: Recurrence Plot and Recurrence Quantification of the Dynamic Properties of Cross-Shaped Laminated Energy Harvester

Authors: P. Harris, G. Litak, J. Iwaniec, C. R. Bowen

Link: https://www.scientific.net/AMM.849.95

CONTENT WITHHELD DUE TO COPYRIGHT

Journal Paper 6:

(Accepted by Materials Today: Proceedings)

Title: Non-orthogonal laminates for energy harvesting

Authors: P. Harris, C. R. Bowen

Link: http://www.materialstoday.com/proceedings

CONTENT WITHHELD DUE TO COPYRIGHT

Journal Paper 7:

Journal Paper 7: European Physical Journal B: Condensed Matter and Complex Systems. 90(1). 2017

Title: Output response identification in a multistable system for piezoelectric energy harvesting

Authors: P. Harris, M. H. Arafa, G. Litak, C. R. Bowen, J. Iwaniec

Link: https://link.springer.com/article/10.1140/epjb/e2016-70619-y

CONTENT WITHHELD DUE TO COPYRIGHT

Bibliography

[1] Joseph A. Paradiso and Thad Starner. Energy scavenging for mobile and wireless electronics. *Pervasive Computing*, 4(1):18–27, 2005.

[2] Lars Jarup and Carl Gustaf Elinder. Incidence of renal stones among cadmium exposed battery workers. *British Journal of Industnial Medicine*, 50:598–602, 1993.

[3] Terry I. Mohammed, Ivan Chang-Yen, and Isaac Bekele. Lead pollution in east trinidad resulting from lead recycling and smelting activities. *Environmental Geochemistry and Health*, 18(3):123–128, 1996.

[4] Tim Nedwed and Dennis A. Clifford. A survey of lead battery recycling sites and soil remediation processes. *Waste Management*, 17(4):257–269, 1998.

[5] Peter Svete, Radmila Milacic, and Boris Pihlar. Partitioning of zn, pb and cd in river sediments from a lead and zinc mining area using the bcr three-step sequential extraction procedure. *Journal of Environmental Monitoring*, 3:586–590, 2001.

[6] Matthew M. Matlock, Brock S. Howerton, and David A. Atwood. Chemical precipitation of lead from lead battery recycling plant wastewater. *Industrial and Chemical Engineering Research*, 41(6):1579–1582, 2002.

[7] Amer Hammami, Nathalie Raymond, and Michel Armand. Lithium-ion batteries: Runaway risk of forming toxic compounds. *Nature*, 424:635–636, 2003.

[8] Faheem Shah, Tasneem Gul Kazi, Hassan Imran Afridi, Naeemullah, and Sadaf Sadia Arain. Exposures of lead to adolescent workers in battery recycling workshops and surrounding communities. *Journal of Exposure Science and Environmental Epidemiology*, 22:649–653, 2012.

[9] Minh Quyen Le, Jean-Fabien Capsal, Mickael Lallart, Yoann Hebrard, Andre Van Der Ham, Nicolas Reffe, Lionel Geynet, and Pierre-Jean Cottinet. Review on energy harvesting for structural health monitoring in aeronautical applications. *Progress in Aerospace Sciences*, 79(147-157), 2015.

[10] Cian Ó Mathúna, Terence Ó Donnell, Rafael V. Martinez-Catala, James Rohan, and Brendan Ó Flynn. Energy scavenging for long-term deployable wireless sensor networks. *Talanta*, 75(3):613–623, 2008.

[11] C. R. Bowen and M. H. Arafa. Energy harvesting technologies for tire pressure monitoring systems. *Advanced Energy Materials*, 5(7), 2014.

[12] W. S. Wang, T. Ó Donnell, M. Hayes N. Wang, B. Ó Flynn, and C. Ó Mathuna. Design considerations of sub-mw indoor light energy harvesting for wireless sensor systems. *ACM Journal on Emerging Technologies in Computing Systems*, 6(2), 2010.

[13] J W Matiko, N J Grabham, S P Beeby, and M J Tudor. Review of the application of energy harvesting in buildings. *Measurement Science and Technology*, 25(1), 2013.

[14] Sidney B. Lang. Pyroelectricity: From ancient curiosity to modern imaging tool. *Physics Today*, 58(8):31–36, 2005.

[15] Gael Sebald, Daniel Guyomar, and Amen Agbossou. On thermoelectric and pyroelectric energy harvesting. *Smart Materials and Structures*, 18(12), 2009.

[16] Mengying Xie, Daniel Zabek, Chris Bowen, Mostafa Abdelmageed, and Mustafa Arafa. Wind-driven pyroelectric energy harvesting device. *Smart Materials and Structures*, 25(12).

[17] D. Zabek, J.M. Taylor, and C.R. Bowen. *Performance of thin film polyvinylidenefluoride (PVDF) for pyroelectric energy harvesting*, pages 1–4. IEEE, 2014.

[18] C. R. Bowen, J. Taylor, E. LeBoulbar, D. Zabek, A. Chauhan, and R. Vaish. Pyroelectric materials and devices for energy harvesting applications. *Energy & Environmental Science*, 7(12):3836–3856, 2014.

[19] A. K. Batra and M. D. Aggarwal. *Pyroelectric Materials Infrared Detectors, Particle Accelerators, and Energy Harvesters*. SPIE, Bellingham, Washington, USA, 2013.

[20] Daniel Zabek, John Taylor, Emmanuel Le Boulbar, and Chris Bowen. Micropatterning of flexible and free standing polyvinylidene difluoride (pvdf) films for enhanced pyroelectric energy transformation. *Advanced Energy Materials*, 5(8), 2015.

[21] G. Jeffrey Snyder. *Thermoelectric Energy Harvesting*, book section 11, pages 325–336. Springer, 2009.

[22] S.B. Riffat and Xiaoli Ma. Thermoelectrics: a review of present and potential applications. *Applied Thermal Engineering*, 23(8):913–935, 2003.

[23] Miguel Fisac, Francesc X. Villasevil, and Antonio M. Lopez. Design of a thermoelectric generator with fast transient response. *Renewable Energy*, 81:658–663, 2015.

[24] Andrew Avent and Chris Bowen. Principles of thermoacoustic energy harvesting. *The European Physical Journal Special Topics*, 224:2967–2992, 2015.

[25] Wei Wang, Junyi Cao, Shengxi Zhou, and Jing Lin. Bistable energy harvesting from human motion. In *27th Conference on Mechanical Vibration and Noise*, volume 8. ASME, 2015.

[26] Yang Bai, Hana Hughes, Pavel Tofel, and Tim W. Button. Fabrication and characterization of vibration and wind energy harvesters using multilayer free-standing piezoelectric thick films. *Journal of Microelectronics and Electronic Packaging*, 12(4):181–188, 2015.

[27] Y. Bai, Z. Havranek, P. Tofel, C. Meggs, H. Hughes, and T.W. Button. Nonlinear piezoelectric devices for broadband air-flow energy harvesting. *The European Physical Journal Special Topics*, 224(14-15):2675–2685, 2015.

[28] Shuguang Li, Jianping Yuan, and Hod Lipson. Ambient wind energy harvesting using cross-flow fluttering. *Journal of Applied Physics*, 109(2):4, 2011.

[29] Hailing Fu and Eric M. Yeatman. A miniaturized piezoelectric turbine with self-regulation for increased air speed range. *Applied Physics Letters*, 107(24), 2015.

[30] L Wang and F G Yuan. Vibration energy harvesting by magnetostrictive material. *Smart Materials and Structures*, 17(4), 2008.

[31] Samuel C. Stanton, Alper Erturk, Brian P. Mann, and Daniel J. Inman. Nonlinear piezoelectricity in electroelastic energy harvesters: Modeling and experimental identification. *Journal of Applied Physics*, 108(77), 2010.

[32] Sukhdeep Kaur, Einar Halvorsen, Oddvar Sorasen, and Eric M. Yeatman. Characterization and modeling of nonlinearities in in-plane gap closing electrostatic energy harvester. *Journal of Microelectromechanical Systems*, 24(6):2071 –2082, 2015.

[33] Dibin Zhu and Steve Beeby. *Energy Harvesting Systems Principles, Modeling and Applications*. Springer, 2011.

[34] Paul D. Mitcheson, Eric M. Yeatman, G. Kondala Rao, Andrew S. Holmes, and Tim C. Green. Energy harvesting from human and machine motion for wireless electronic devices. *Proceedings of the IEEE*, 96(9):1457–1486, 2008.

[35] S P Beeby, M J Tudor, and N M White. Energy harvesting vibration sources for microsystems applications. *Measurement Science and Technology*, 17(12):175–195, 2006.

[36] Pranay Podder, Andreas Amann, and Saibal Roy. A bistable electromagnetic micropower generator using fr4-based folded arm cantilever. *Sensors and Actuators A: Physical*, 227:39–47, 2015.

[37] Dibin Zhu, Stephen Roberts, Thomas Mouille, Michael J Tudor, and Stephen P Beeby. General model with experimental validation of electrical resonant frequency tuning of electromagnetic vibration energy harvesters. *Smart Materials and Structures*, 21(10), 2012.

[38] Eric Yeatman and Paul Mitcheson. *Energy Harvesting and Power Delivery*, book section 6, pages 237 –272. Springer-Verlag London, London, 2014.

[39] Jan Tichy, Jiri Erhart, Erwin Kittinger, and Jana Privratska. *Fundamentals of Piezoelectric Sensorics Mechanical, Dielectric, and Thermodynamical Properties of Piezoelectric Materials*, volume 2010. Springer, 2010.

[40] Jan Holterman and Pim Groen. *An Introduction to Piezoelectric Materials and Applications*. Stichting Applied Piezo, The Netherlands, 2013.

[41] S. Sreenivasa Prasath and A. Arockiarajan. Analytical, numerical and experimental predictions of the effective electromechanical properties of macro-fiber composite (mfc). *Sensors and Actuators A: Physical*, 214:31–44, 2014.

[42] S. Sreenivasa Prasath and A. Arockiarajan. Effect of interphase and thermal environment on the effective properties of macro-fiber composites (mfc). *Composites Part B*, 75:327–335, 2015.

[43] M Karimi, R Tikani, S Ziaei-Rad, and HR Mirdamadi. Experimental and theoretical studies on piezoelectric energy harvesting from low-frequency ambient random vibrations. *Proceedings of the Institution of Mechanical Engineers, Part C: Journal of Mechanical Engineering Science*, 0(0):1–13, 2015.

[44] C. R. Bowen, H. A. Kim, P. M. Weaver, and S. Dunn. Piezoelectric and ferroelectric materials and structures for energy harvesting applications. *Energy & Environmental Science*, 7(1):25–44, 2014.

[45] Henry A. Sodano, Daniel J. Inman, and Gyuhae Park. Comparison of piezoelectric energy harvesting devices for recharging batteries. *Journal of Intelligent Material Systems and Structures*, 16(10):799–807, 2005.

[46] E Hasler, L Stein, and G Harbauer. Implantable physiological power supply with pvdf film. *Ferroelectrics*, 60(1):277–282, 1984.

[47] James Roscow, John Taylor, and Chris Bowen. Manufacture and characterization of porous ferroelectrics for piezoelectric energy harvesting applications. *Ferroelectrics*, 498(1):40–46, 2016.

[48] J. Roscow, Y. Zhang, J. Taylor, and C.R. Bowen. Porous ferroelectrics for energy harvesting applications. *The European Physical Journal Special Topics*, 224(14):2949–2966, 2015.

[49] Jaehwan Kim Heung Soo Kim, Joo-Hyong Kim. A review of piezoelectric energy harvesting based on vibration. *International Journal of Precision Engineering and Manufacturing*, 12(6):1129–1141, 2011.

[50] Henry A. Sodano, Daniel J. Inman, and Gyuhae Park. A review of power harvesting from vibration using piezoelectric materials. *The Shock and Vibration Digest*, 36(3):197–205, 2004.

[51] Ryan L. Harne. Theoretical investigations of energy harvesting efficiency from structural vibrations using piezoelectric and electromagnetic oscillators. *The Journal of the Acoustical Society of America*, 132(1):162–172, 2012.

[52] G. Poulin, E. Sarraute, and F. Costa. Generation of electrical energy for portable devices comparative study of an electromagnetic and a piezoelectric system. *Sensors and Actuators A: Physical*, 116(3):461–471, 2004.

[53] E Lefeuvre J Wei and F Costa H Mathias. Interface circuit for vibration energy harvesting with adjustable bias voltage. In *he 15th International Conference on Micro and Nanotechnology for Power Generation and Energy Conversion Applications*, volume 660, 2015.

[54] Hongwei Song, Xuegong Huang, Xuezheng Jiang, and Jiong Wang. The synchronized switch harvesting circuit on inductor based on piezoelectricity, April 2011 2011.

[55] Matthias Heymanns and Peter Hagedorn. Optimal impedance load of a bistable energy harvester. *Proceedings in Applied Mathematics and Mechanics*, 15(1):249 – 250, 2015.

[56] E. Lefeuvre, A. Badel, C. Richard, L. Petit, and D. Guyomar. A comparison between several vibration-powered piezoelectric generators for standalone systems. *Sensors and Actuators A: Physical*, 126(2):405–416, 2006.

[57] Elie Lefeuvre, Gael Sebald, Daniel Guyomar, Mickael Lallart, and Claude Richard. Materials, structures and power interfaces for efficient piezoelectric energy harvesting. *Journal of Electroceramics*, 22(1-3):171–179, 2007.

[58] Lihua Tang, Yue Han, James Hand, and Ryan L. Harne. Exploring the roles of standard rectifying circuits on the performance of a nonlinear piezoelectric energy harvester. In Gyuhae Park, editor, *Active and Passive Smart Structures and Integrated Systems 2016*, volume 9799. SPIE, 2016.

[59] P. Harris, W. Skinner, C. R. Bowen, and H. A. Kim. Manufacture and characterisation of piezoelectric broadband energy harvesters based on asymmetric bistable cantilever laminates. *Ferroelectrics*, 480(1):67–76, 2015.

[60] Dongna Shen, Jung-Hyun Park, Joo Hyon Noh, Song-Yul Choe, Seung-Hyun Kim, Howard C. Wikle III, and Dong-Joo Kim. Micromachined pzt cantilever based on soi structure for low frequency vibration energy harvesting. *Sensors and Actuators A: Physical*, 154(1):103–108, 2009.

[61] R Elfrink, T M Kamel, M Goedbloed, S Matova, D Hohlfeld, Y van Andel, and R van Schaijk. Vibration energy harvesting with aluminum nitride-based piezoelectric devices. *Journal Of Micromechanics and Microengineering*, 19(9), 2009.

[62] Hyun J Song, Young-Tai Choi, Norman M Wereley, and Ashish Purekar. Comparison of monolithic and composite piezoelectric material-based energy harvesting devices. *Journal of Intelligent Material Systems and Structures*, 25(13), 2014.

[63] Dibin Zhu, Michael J Tudor, and Stephen P Beeby. Strategies for increasing the operating frequency range of vibration energy harvesters: a review. *Measurement Science and Technology*, 21(2), 2009.

[64] I N Ayala-Garcia, D Zhu, M J Tudor, and S P Beeby. A tunable kinetic energy harvester with dynamic over range protection. *Smart Materials and Structures*, 19(11), 2010.

[65] Mohamed O. Mansour, Mustafa H. Arafa, and Said M. Megahed. Resonator with magnetically adjustable natural frequency for vibration energy harvesting. *Sensors and Actuators A: Physical*, 163(1):297–303, 2010.

[66] Xiaoming Wu, Jianhui Lin, Seiki Kato, Kai Zhang, Tianling Ren, and Litian Liu. A frequency adjustable vibration energy harvester. In *PowerMEMS 2008+ microEMS2008*, pages 245–248, 2015.

[67] I.N. Ayala-Garcia, P.D. Mitcheson, E.M. Yeatman, D. Zhu, J. Tudor, and S.P. Beeby. Magnetic tuning of a kinetic energy harvester using variable reluctance. *Sensors and Actuators A: Physical*, 189:266–275, 2013.

[68] Dibin Zhu, Stephen Roberts, Michael J. Tudor, and Stephen P. Beeby. Design and experimental characterization of a tunable vibration-based electromagnetic micro-generator. *Sensors and Actuators A: Physical*, 158(2):284–293, 2010.

[69] Noha A. Aboulfotoh, Mustafa H. Arafa, and Said M. Megahed. A self-tuning resonator for vibration energy harvesting. *Sensors and Actuators A: Physical*, 201:328–334, 2013.

[70] Lei Gu and Carol Livermore. Passive self-tuning energy harvester for extracting energy from rotational motion. *97*, 8, 2010.

[71] Lindsay M. Miller, Pit Pillatsch, Einar Halvorsen, Paul K. Wright, Eric M. Yeatman, and Andrew S. Holmes. Experimental passive self-tuning behavior of a beam resonator with sliding proof mass. *Journal of Sound and Vibration*, 332(26):7142–7152, 2013.

[72] Christian Peters, Dominic Maurath, Wolfram Schock, Florian Mezger, and Yiannos Manoli. A closed-loop wide-range tunable mechanical resonator for energy harvesting systems. *Journal of Micromechanics and Microengineering*, 19(9), 2009.

[73] Cheng Luo and Heath F. Hofmann. Wideband energy harvesting for piezoelectric devices with linear resonant behavior. *IEEE Transactions on Ultrasonics, Ferroelectrics, and Frequency Control*, 58(7):1294–1301, 2011.

[74] Jing-Quan Liu, Hua-Bin Fang, Zheng-Yi Xu, Xin-Hui Mao, Xiu-Cheng Shen, Di Chen, Hang Liao, and Bing-Chu Cai. A mems-based piezoelectric power generator array for vibration energy harvesting. *Microelectronics Journal*, 39(5):802–806, 2008.

[75] Stephen P Beeby, Leran Wang, Dibin Zhu, Alex S Weddell, Geoff V Merrett, Bernard Stark, Gyorgy Szarka, and Bashir M Al-Hashimi. A comparison of power output from linear and non-linear kinetic energy harvesters using real vibration data. *Smart Materials and Structures*, 22(7), 2013.

[76] A Cammarano, S A Neild, S G Burrow, and D J Inman. The bandwidth of optimized nonlinear vibration-based energy harvesters. *Smart Materials and Structures*, 23(5), 2014.

[77] R. Ramlan, M. J. Brennan, B. R. Mace, and I. Kovacic. Potential benefits of a non-linear stiffness in an energy harvesting device. *Nonlinear Dynamics*, 59(4):545–558, 2010.

[78] Helios Vocca, Igor Neri, Flavio Travasso, and Luca Gammaitoni. Kinetic energy harvesting with bistable oscillators. In Umberto Desideri Yan and Jinyue, editors, *Third International Conference on Applied Energy*, volume 97, pages 771–776. Applied Energy, 2012.

[79] Mohammed F. Daqaq, Ravindra Masana, Alper Erturk, and D. Dane Quinn. On the role of nonlinearities in vibratory energy harvesting: A critical review and discussion. *Applied Mechanics Reviews*, 66(4), 2014.

[80] Gael Sebald, Hiroki Kuwano, Daniel Guyomar, and Benjamin Ducharne. Experimental duffing oscillator for broadband piezoelectric energy harvesting. *Smart materials and structures*, 20(10), 2011.

[81] Gael Sebald, Hiroki Kuwano, Daniel Guyomar, and Benjamin Ducharne. Simulation of a duffing oscillator for broadband piezoelectric energy harvesting. *Smart materials and structures*, 20(7), 2011.

[82] A. Erturk and D.J. Inman. Broadband piezoelectric power generation on high-energy orbits of the bistable duffing oscillator with electromechanical coupling. *Journal of Sound and Vibration*, 330(10):2339–2356, 2011.

[83] Dhiman Mallick, Andreas Amann, and Saibal Roy. A nonlinear stretching based electromagnetic energy harvester on fr4 for wideband operation. *Smart Materials and Structures*, 24(1), 2014.

[84] Einar Halvorsen. Fundamental issues in nonlinear wideband-vibration energy harvesting. *Physical Review E*, 87(4), 2013.

[85] Yang Bai, Carl Meggs, and Tim W. Button. Investigation of using free-standing thick-film piezoelectric energy harvesters to develop wideband devices. *International Journal of Structural Stability and Dynamics*, 14(8), 2014.

[86] M S M Soliman, E M Abdel-Rahman, E F El-Saadany, and R R Mansour. A wideband vibration-based energy harvester. *Journal Of Micromechanics and Microengineering*, 18(11), 2008.

[87] D S Nguyen, E Halvorsen, G U Jensen, and A Vogl. Fabrication and characterization of a wideband mems energy harvester utilizing nonlinear springs. *Journal of Micromechanics and Microengineering*, 20(12), 2010.

[88] Cuong Phu Le, Einar Halvorsen, Oddvar Sorasen, and Eric M Yeatman. Wideband excitation of an electrostatic vibration energy harvester with power-extracting end-stops. *Smart Materials and Structures*, 22(7), 2013.

[89] D Zhu and S P Beeby. A broadband electromagnetic energy harvester with a coupled bistable structure. In *The 13th International Conference on Micro and Nanotechnology for Power Generation and Energy Conversion Applications*, volume 476. IOP Publishing, 2013.

[90] D Zhu, D C Arthur, and S P Beeby. A miniature coupled bistable vibration energy harvester. In *The 14th International Conference on Micro and Nanotechnology for Power Generation and Energy Conversion Applications*, volume 557. IOP Publishing Ltd., 2014.

[91] A. Erturk, J. Hoffmann, and D. J. Inman. A piezomagnetoelastic structure for broadband vibration energy harvesting. *Applied Physics Letters*, 94(25), 2009.

[92] Bruce Alphenaar Ji-Tzuoh Lin. Enhancement of energy harvested from a random vibration source by magnetic coupling of a piezoelectric cantilever. *Journal of Intelligent Material Systems and Structures*, 21(13):1337–1341, 2010.

[93] Lihua Tang, Yaowen Yang, and Chee-Kiong Soh. Improving functionality of vibration energy harvesters using magnets. *Journal of Intelligent Material Systems and Structures*, 23(13):1433–1449, 2012.

[94] Zhiyang Zhou, Weiyang Qin, and Pei Zhu. Improve efficiency of harvesting random energy by snap-through in a quad-stable harvester. *Sensors and Actuators A: Physical*, 243:151–158, 2016.

[95] Yuefeng Cui and Matthew Santer. Characterisation of tessellated bistable composite laminates. *Composite Structures*, 137:93–104, 2016.

[96] Yuefeng Cui and Matthew Santer. Highly multistable composite surfaces. *Composite Structures*, 124, 2015.

[97] Pilkee Kim and Jongwon Seok. Dynamic and energetic characteristics of a tri-stable magnetopiezoelastic energy harvester. *Mechanism and Machine Theory*, 94:41–63, 2015.

[98] Junyi Cao, Shengxi Zhou, Wei Wang, and Jing Lin. Influence of potential well depth on nonlinear tristable energy harvesting. *Applied Physics letters*, 106(17), 2015.

[99] Z. Wu, R. L. Harne, and K. W. Wang. Vibration energy harvesting using multi-stable two degree of freedom nonlinear dynamics. In *ASME 2013 International Design Engineering Technical Conferences and Computers and Information in Engineering Conference, IDETC/CIE 2013*, volume 8. ASME, 2013.

[100] S. Daynes, C. G. Diaconu, K. D. Potter, and P.M. Weaver. Bistable prestressed symmetric laminates. *Journal of Composite Materials*, 44(9):1119–1137, 2010.

[101] Yang Zhu and Jean Zu. A magnet-induced buckled-beam piezoelectric generator for wideband vibration-based energy harvesting. *Journal of Intelligent Material Systems and Structures*, 25(13), 2014.

[102] Grzegorz Litak, Andrzej Rysak, Marek Borowiec, Michael Scheffler, and Joachim Gier. Vertical beam modal response in a broadband energy harvester. *Proceedings of the Institution of Mechanical Engineers Part K: Journal of Multi-body Dynamics*, 0(0):1–12, 2016.

[103] Chunbo Lan, Weiyang Qin, and Wangzheng Deng. Energy harvesting by dynamic unstability and internal resonance for piezoelectric beam. *Applied Physics Letters*, 107(9), 2015.

[104] Weiqun Liu, Adrien Badel, Fabien Formos, Yipeng Wu, Nabil Bencheikh, and Amen Agbossou. A wideband integrated piezoelectric bistable generator: Experimental performance evaluation and potential for real environmental vibrations. *Journal of Intelligent Material Systems and Structures*, 26(7):872–877, 2015.

[105] Benjamin Todd, Brian D. Jensen, Stephen M. Schultz, and Aaron R. Hawkins. Design and testing of a thin-flexure bistable mechanism suitable for stamping from metal sheets. *Journal of Mechanical Design*, 132(7), 2010.

[106] T. E. Bruns, O. Sigmund, and D. A. Tortorelli. Numerical methods for the topology optimization of structures that exhibit snap-through. *INTERNATIONAL JOURNAL FOR NUMERICAL METHODS IN ENGINEERING*, 55(10):1215–1237, 2002.

[107] R. Masana and M. F. Daqaq. Energy harvesting in the super-harmonic frequency region of a twin-well oscillator. *Journal of Applied Physics*, 111(4), 2012.

[108] E Kebadze, S.D Guest, and S Pellegrino. Bistable prestressed shell structures. *International Journal of Solids and Structures*, 41(11-12):2801–2820, 2004.

[109] Zi Chen, Qiaohang Guo, Carmel Majidi, Wenzhe Chen, David J. Srolovitz, and Mikko P. Haataja. Nonlinear geometric effects in mechanical bistable morphing structures. *Physical Review Letters*, 109(11), 2012.

[110] S. Daynes, K.D. Potter, and P.M. Weaver. Bistable prestressed buckled laminates. *Composites Science and Technology*, 68(15-16):3431–3437, 2008.

[111] Mengying Xie, Kean C. Aw, and Wei Gao. A multi-layered polydimethylsiloxane structure for application in low-excitation, broadband and low frequency energy harvesting. *Sensors and Actuators A: Physical*, 222:140–148, 2015.

[112] Zheng Zhang, Helong Wu, Gangfei Ye, Jie Yang, Sritawat Kitipornchai, and Guozhong Chai. Experimental study on bistable behaviour of anti-symmetric laminated cylindrical shells in thermal environments. *Composite Structures*, 144:24–32, 2016.

[113] Diana A. Galletly and Simon D. Guest. Bistable composite slit tubes. i. a beam model. *International Journal of Solids and Structures*, 41(16-17):4517–4533, 2004.

[114] Zheng Zhang, Helong Wua, Xiaoqiao He, Huaping Wu, Yumei Bao, and Guozhong Chai. The bistable behaviors of carbon-fiber/epoxy anti-symmetric composite shells. *Composites Part B: Engineering*, 47:190–199, 2013.

[115] Christopher Rhys Bowen, Peter F. Giddings, Aki I. T. Salo, and Hyunsun Alicia Kim. Modeling and characterization of piezoelectrically actuated bistable composites. *IEEE Transactions on Ultrasonics, Ferroelectrics, and Frequency Control*, 58(9):1737–1750, 2011.

[116] Michael W. Hyer. Some observations on the cured shape of thin unsymmetric laminates. *Journal of Composite Materials*, 15:175–194, 1981.

[117] Michael W. Hyer. The room-temperature shapes of four-layer unsymmetric cross-ply laminates. *Journal of Composite Materials*, 16:318–340, 1982.

[118] Marie-Laure Dano and Michael W. Hyer. Thermally-induced deformation behavior of unsymmetric laminates. *International Journal of Solids and Structures*, 35(17):2101–2120, 1998.

[119] W. J. Jun and C. S. Hong. Effect of residual shear strain on the cured shape of unsymmetric cross-ply thin laminates. *Composites Science and Technology*, 38(1):55–67, 1989.

[120] Christopher J. Brampton, David N. Betts, Christopher R. Bowen, and H. Alicia Kim. Sensitivity of bistable laminates to uncertainties in material properties, geometry and environmental conditions. *Composite Structures*, 102:276–286, 2013.

[121] David N. Betts, Aki I.T. Salo, Christopher R. Bowen, and Hyunsun A. Kim. Characterisation and modelling of the cured shapes of arbitrary layup bistable composite laminates. *Composite Structures*, 92(7):1694–1700, 2009.

[122] Maenghyo Cho, Min-Ho Kim, Heung Soap Choi, Chung Hwa Chung, Kyu-Jong Ahn, and Yong Sung Eom. A study on the room-temperature curvature shapes of unsymmetric laminates including slippage effects. *Journal of Composite Materials*, 32(5):460–482, 1998.

[123] Jong-Gu Lee, Junghyun Ryu, Seung-Won Kim, Je-Sung Koh, Kyu-Jin Cho, and Maenghyo Cho. Effect of initial tool-plate curvature on snap-through load of unsymmetric laminated cross-ply bistable composites. *Composite Structures*, 122:82–91, 2015.

[124] Alex Brinkmeyer, Sergio Pellegrino, and Paul M. Weaver. Effects of long-term stowage on the deployment of bistable tape springs. *Journal of Applied Mechanics*, 83(1), 2015.

[125] Andres F. Arrieta, Izabela K. Kuder, Tobias Waeber, and Paolo Ermanni. Variable stiffness characteristics of embeddable multi-stable composites. *Composites Science and Technology*, 97:12–18, 2014.

[126] Andres F. Arrieta, Izabela K. Kuder, Mathias Rist, Tobias Waeber, and Paolo Ermanni. Passive load alleviation aerofoil concept with variable stiffness multi-stable composites. *Composite Structures*, 116:235–242, 2014.

[127] Izabela K. Kuder, Andres F. Arrieta, Mathias Rist, and Paolo Ermanni. Static design of a selective compliance morphing wing profile based on integrated variable stiffness bi-stable components. In *ASME 2014 Conference on Smart Materials, Adaptive Structures and Intelligent Systems*, volume 1. ASME, 2014.

[128] Izabela K. Kuder, Andres F. Arrieta, and Paolo Ermanni. Design space of embeddable variable stiffness bi-stable elements for morphing applications. *Composite Structures*, 122:445–455, 2015.

[129] Izabela K Kuder, Andres F Arrieta, Mathias Rist, and Paolo Ermanni. Aeroelastic response of a selectively compliant morphing aerofoil featuring integrated variable stiffness bi-stable laminates. *Journal of Intelligent Material Systems and Structures*, online, 2016.

[130] M.-L. Dano and M.W. Hyer. Sma-induced snap-through of unsymmetric fiber-reinforced composite laminates. *International Journal of Solids and Structures*, 40(22):5949–5972, 2003.

[131] Hao Li, Fuhong Dai, and Shanyi Du. Numerical and experimental study on morphing bi-stable composite laminates actuated by a heating method. *Composites Science and Technology*, 72(14):1767–1773, 2012.

[132] Christopher J. Brampton, Christopher R. Bowen, Samuel T. Buschhorn, Jeonyoon Lee, Simon G. Pickering, Brian L. Wardle, and Hyunsun A. Kim. Actuation of bistable laminates by conductive polymer nanocomposites for use in thermal-mechanical aerosurface de-icing systems. In *55th AIAA/ASME/ASCE/AHS/ASC Structures, Structural Dynamics, and Materials Conference*. AIAA, 2014.

[133] Marc R. Schultz and Michael W. Hyer. Snap-through of unsymmetric cross-ply laminates using piezoceramic actuators. *Journal of Intelligent Material Systems and Structures*, 25(13):795–814, 2003.

[134] C. R. Bowen, R. Butler, R. Jervis, H. A. Kim, and A. I. T. Salo. Morphing and shape control using unsymmetrical composites. *Journal of Intelligent Material Systems and Structures*, 18(1):89–98, 2007.

[135] David N. Betts, H. Alicia Kim, and Christopher R. Bowen. Optimization of stiffness characteristics for the design of bistable composite laminates. *AIAA JOURNAL*, 50(10):2211–2218, 2012.

[136] Stephen Daynes and Paul Weaver. Analysis of unsymmetric cfrp-metal hybrid laminates for use in adaptive structures. *Composites: Part A*, 41(11):1712–1718, 2010.

[137] A.F. Arrieta, G. Spelsberg-Korspeter, P. Hagedorn, S.A. Neild, and D.J. Wagg. Low order model for the dynamics of bi-stable composite plates. *Journal of Intelligent Material Systems and Structures*, 22(17):2025–2043, 2011.

[138] Andres F. Arrieta, Simon A. Neild, and David J. Wagg. On the cross-well dynamics of a bi-stable composite plate. *Journal of Sound and Vibration*, 330(14):3424–3441, 2011.

[139] Andres F. Arrieta, Peter Hagedorn, Alper Erturk, and Daniel J. Inman. Electromechanical modelling and experiments of a bistable plate for nonlinear energy harvesting. In *ASME 2010 Conference on Smart Materials, Adaptive Structures and Intelligent Systems*. American Society of Mechanical Engineers.

[140] A. F. Arrieta, S. A. Neild, and D. J. Wagg. Nonlinear dynamic response and modeling of a bi-stable composite plate for applications to adaptive structures. *Nonlinear Dynamics*, 58(1-2):259–272, 2009.

[141] Cezar G. Diaconu, Paul M. Weaver, and Andres F. Arrieta. Dynamic analysis of bi-stable composite plates. *Journal of Sound and Vibration*, 322(4-5):987–1004, 2009.

[142] D.N. Betts, C.R. Bowen, H.A. Kim, N. Gathercole, C.T. Clarke, and D.J. Inman. Nonlinear dynamics of a bistable piezoelectric composite energy harvester for broadband application. *THE EUROPEAN PHYSICAL JOURNAL*, 222(7):1553–1562, 2013.

[143] Sergio P Pellegrini, Nima Tolou, Mark Schenk, and Just L Herder. Bistable vibration energy harvesters: A review. *Journal of Intelligent Material Systems and Structures*, 24(11):1303–1312, 2012.

[144] R L Harne and K W Wang. A review of the recent research on vibration energy harvesting via bistable systems. *Smart Materials and Structures*, 22(2), 2013.

[145] David N. Betts, H. Alicia Kim, and Christopher R. Bowen. Preliminary study of optimum piezoelectric cross-ply composites for energy harvesting. *Smart Materials Research*, 2012, 2012.

[146] David N. Betts, H. Alicia Kim, Christopher R. Bowen, and Daniel J. Inman. Optimization of piezoelectric bistable composite plates for broadband vibrational energy harvesting, March 2012 2012.

[147] A. F. Arrieta, P. Hagedorn, A. Erturk, and D. J. Inman. A piezoelectric bistable plate for nonlinear broadband energy harvesting. *Applied Physics Letters*, 97(10):104102–1–3, 2010.

[148] David N. Betts, Christopher R. Bowen, Daniel J. Inman, Paul M. Weaver, and H. Alicia Kim. Investigation of geometries of bistable piezoelectric-laminate plates for vibration-based energy harvesting, May 2014 2014.

[149] Peter Harris, Grzegorz Litak, Joanna Iwaniec, and Christopher Bowen. Recurrence plot and recurrence quantification of the dynamic properties of cross-shaped laminated energy harvester. *Applied Mechanics and Materials*, 849, 2016.

[150] S. Mehdi Tavakkoli, Paul M. Weaver, Christopher R. Bowen, Daniel J. Inman, and H. Alicia Kim. An analytical study on piezoelectric bistable laminates with arbitrary shapes for energy harvesting. In et al A.L. Arajo, C.A. Mota Soares, editor, *7th ECCOMAS Thematic Conference on Smart Structures and Materials*. IDMEC 2015, 2015.

[151] Samer Tawfik, Xinyuan Tan, Serkan Ozbay, and Erian Armanios. Anticlastic stability modeling for cross-ply composites. *Journal of Composite Materials*, 41(11):1325–1338, 2007.

[152] David N. Betts, Christopher R. Bowen, H. Alicia Kim, Robert A. Guyer, Pierre-Yves Le Bas, and Daniel J. Inman. Modelling the dynamic response of bistable composite plates for piezoelectric energy harvesting, January 2014 2014.

[153] M. S. Taki, R. Tikani, S. Ziaei-Rad, and A. Firouzian-Nejad. Dynamic responses of cross-ply bi-stable composite laminates with piezoelectric layers. *Archive of Applied Mechanics*, 86(6):1003–1018, 2016.

[154] David N. Betts, Christopher R. Bowen, H. Alicia Kim, Nicholas Gathercole, Christopher T. Clarke, and Daniel J. Inman. Investigation of bistable piezo-composite plates for broadband energy harvesting, March 2013 2013.

[155] Andres F. Arrieta, Tommaso Delpero, and Paolo Ermanni. Analytical electromechanical model of cantilevered bi-stable composites for broadband eenergy harvesting, September 16-18, 2013 2013.

[156] Andres F. Arrieta, Tommaso Delpero, Andrea Bergamini, and Paolo Ermanni. A cantilevered piezoelectric bi-stable composite concept for broadband energy harvesting, 2013.

[157] Hao Li, Fuhong Dai, and Shanyi Du. Broadband energy harvesting by exploiting nonlinear oscillations around the second vibration mode of a rectangular piezoelectric bistable laminate. *Smart Materials and Structures*, 24(4), 2015.

[158] C. R. Bowen, M. Watson, D. N. Betts, P. Harris, M. Bertin, and H. A. Kim. Piezoelectric fibres integrated into structural composites. *Ferroelectrics*, 466(1):14–20, 2014.

[159] P. Harris, C. Bowen, and H. A. Kim. Manufacture and characterisation of piezoelectric broadband energy harvesters based on asymmetric bistable laminates. In Hyonny Kim, Daniel Whisler, Zhi M. Chen, Chiara Bisagni, Masamichi Kawai, and Ronald Krueger, editors, *16th US-Japan Conference on Composite Materials*. DEStech Publications, 2014.

[160] Peter Harris, Chris R. Bowen, and H. Alicia Kim. Manufacture and characterisation of piezoelectric broadband energy harvesters based on asymmetric bistable laminates. *Journal of Multifunctional Composites*, 2(3):113–123, 2014.

[161] P. Harris, W. Skinner, C. R. Bowen, and H. A. Kim. Manufacture and characterisation of piezoelectric broadband energy harvesters based on asymmetric bistable cantilever laminates, 2014.

[162] Peter Harris, Grzegorz Litak, Chris R. Bowen, and Mustafa Arafa. A composite beam with dual bistability for enhanced vibration energy harvesting. In Nibir K. Dhar; Achyut K. Dutta, editor, *SPIE Defense and Commercial Sensing*, volume 9865. SPIE, 2016.

[163] P.D. Mitcheson, P. Miao, B.H. Stark, E.M. Yeatman, A.S. Holmes, and T.C. Green. Mems electrostatic micropower generator for low frequency operation. *Sensors and Actuators A: Physical*, 115(2-3):523–529, 2004.

[164] P. Glynne-Jones, M.J. Tudor, S.P. Beeby, and N.M. White. An electromagnetic, vibration-powered generator for intelligent sensor systems. *Sensors and Actuators A: Physical*, 110(1-3):344–349, 2004.

[165] Shashank Priya. Advances in energy harvesting using low profile piezoelectric transducers. *Journal of Electroceramics*, 19(1):167–184, 2007.

[166] Michael W. Hyer. Calculations of the room-temperature shapes of unsymmetric laminates. *Journal of Composite Materials*, 15:296–310, 1981.

[167] Christopher R Bowen, David N Betts, Peter F Giddings, AIT Salo, and H Alicia Kim. A study of bistable laminates of generic lay-up for adaptive structures. *Strain*, 48(3):235–240, 2012.

[168] Smart Materials.

[169] Igor Neri, Flavio Travasso, Riccardo Mincigrucci, Helios Vocca, Francesco Orfei, and Luca Gammaitoni. A real vibration database for kinetic energy harvesting application. *Journal of Intelligent Material Systems and Structures*, 23(18):2095–2101, 2012.

[170] J.P. Hou and C. Ruiz. Measurement of the properties of woven cfrp t300/914 at different strain rates. *Composites Science and Technology*, 60(15):2829–2834, 2000.

[171] Howard F. Wolfe and Cynthia A. Shroyer. Large amplitude nonlinear response of flat aluminum, and carbon fiber plastic beams and plates. Report, Air Force Materiel Command, 1992-1993.

[172] David Wagg and Simon Neild. *Nonlinear Vibration with Control For Flexible and Adaptive Structures*, volume 218 of *Solid Mechanics and Its Applications*. Springer, 2010.

[173] D. A. Hall. Review nonlinearity in piezoelectric ceramics. *Journal of Materials Science*, 36(19):4575–4601, 2001.

[174] A. Lei, R. Xu, A. Thyssen, A.C. Stoot, T. L. Christiansen, K. Hansen, R. Lou-Moller, E.V. Thomsen, and K. Birkelund. Mems-based thick film pzt vibrational energy harvester, 2011.

[175] A. Rajasekaran, A. Hande, and D. Bhatia. Buck-boost converter based power conditioning circuit for low excitation vibrational energy harvesting, 2008.

[176] Elie Lefeuvre, David Audigier, Claude Richard, and Daniel Guyomar. Buck-boost converter for sensorless power optimization of piezoelectric energy harvester. *IEEE Transactions on Power Electronics*, 22(5):2018 – 2025, 2007.

[177] Na Kong, Dong Sam Ha, Alper Erturk, and Daniel J. Inman. Resistive impedance matching circuit for piezoelectric energy harvesting. *Journal of Intelligent Material Systems and Structures*, 21(13):1293–1302, 2010.

[178] Libo Ren and Azar Parvizi-Majidi. A model for shape control of cross-ply laminated shells using a piezoelectric actuator. *Journal of Composite Materials*, 40(14):1271–1285, 2006.

[179] Grant A. Vogl and Michael W. Hyer. Natural vibration of unsymmetric cross-ply laminates. *Journal of Sound and Vibration*, 330(20):4764–4779, 2011.

[180] Yi-Yuan Yu. *Vibrations of Elastic Plates Linear and Nonlinear Dynamical Modeling of Sandwiches, Laminated Composites, and Piezoelectric Layers.* Springer-Verlag, New York, 1996.

[181] Sydney Henry Gould. *Variational Methods for Eigenvalue Problems: An Introduction to the Methods of Rayleigh, Ritz, Weinstein, and Aronszajn.* Dover Publications, inc, New York, 1995.

[182] A.F. Arrieta, D.J. Wagg, and S.A. Neild. Dynamic snap-through for morphing of bi-stable composite plates. *Journal of Intelligent Material Systems and Structures*, 22(2):103–112, 2011.

[183] Andres F. Arrieta, Onur Bilgen, Michael I. Friswell, and Paolo Ermanni. Modelling and configuration control of wing-shaped bi-stable piezoelectric composites under aerodynamic loads. *Aerospace Science and Technology*, 29(1):453–461, 2013.

[184] A. F. Arrieta, T. Delpero, A. E. Bergamini, and P. Ermanni. Broadband vibration energy harvesting based on cantilevered piezoelectric bi-stable composites. *Applied Physics Letters*, 102, 2013.

[185] Junuthula Naraimha Reddy. *Theory and Analysis of Elastic Plates and Shells, Second Edition.* Taylor and Francis, Philadelphia, Pennsylvania, 1999.

[186] Hexcel.

[187] Peter Harris, Grzegorz Litak, Joanna Iwaniec, and Christopher R Bowen. Recurrence plot and recurrence quantification of the dynamic properties of cross-shaped laminated energy harvester. *Applied Mechanics and Materials*, 849, 2016.

[188] D. N. Betts, H. A. Kim, C. R. Bowen, and D. J. Inman. Optimal configurations of bistable piezo-composites for energy harvesting. *Applied Physics Letters*, 100(11):114104–1–4, 2012.

[189] M. Borowiec, A. Rysak, D.N. Betts, C.R. Bowen, H.A. Kim, and G. Litak. Complex response of a bistable laminated plate: Multiscale entropy analysis. *The European Physical Journal Plus*, 129(211), 2014.

[190] Andres F. Arrieta, Paolo Ermanni, Daniel J. Inman, and M. Amin Karami. Elastically bi-stable heartbeat powered energy harvester, 2014.

[191] D. J. Inman. *Engineering Vibrations 3rd ed.* Prentice Hall, 1994.

[192] A. Syta, C. R. Bowen, H. A. Kim, A. Rysak, and G. Litak. Experimental analysis of the dynamical response of energy harvesting devices based on bistable laminated plates. *Meccanica*, 50(8):1961–1970, 2015.